Dissertation

Christian Günz

Combined Dielectric-Constant Gas Thermometry and Expansion Experiments – Virial Coefficients of Argon

Physikalisch-Technische Bundesanstalt

Thermodynamik
PTB-Th-12
Braunschweig, Juni 2021

Christian Günz

Combined Dielectric-Constant Gas Thermometry and Expansion Experiments – Virial Coefficients of Argon

Fakultät Maschinenbau
fortschritt studieren

RUHR UNIVERSITÄT BOCHUM

RUB

Combined Dielectric-Constant Gas Thermometry and Expansion Experiments - Virial Coefficients of Argon

Dissertation
zur
Erlangung des Grades
Doktor-Ingenieur

der

Fakultät für Maschinenbau
der Ruhr-Universität Bochum

von

Christian Günz
aus Erlabrunn

Bochum 2020

Dissertation eingereicht am: 15. Dezember 2020

Tag der mündlichen Prüfung: 01. März 2021

Erster Referent: Prof. Dr.-Ing. R. Span

Zweiter Referent: Prof. Dr.-Ing. M. Richter

Danksagung

Ich möchte mich an dieser Stelle bei allen Menschen bedanken, die mich während meiner Zeit als Doktorand unterstützt haben und so die Fertigstellung dieser Arbeit erst ermöglicht haben.

Mein besonderer Dank gilt hier zunächst meinem Mentor Dr. Christof Gaiser, der dieses interessante Thema aufgeworfen hat und mir nicht nur mit gutem Rat, sondern auch tatkräftiger Unterstützung zur Seite stand. Seine ansteckende Euphorie für die Methode war mir immer wieder eine Quelle der Motivation.

Bei Prof. Dr.-Ing. Roland Span und Prof. Dr.-Ing. Markus Richter möchte ich mich recht herzlich für die universitäre Betreuung und Begutachtung der Arbeit, sowie für die fachlichen Diskussionen und Hinweise, bedanken. Darüber hinaus sei den Mitarbeiterinnen und Mitarbeitern für die freundschaftliche Aufnahme am Lehrstuhl für Thermodynamik der Ruhr-Universität Bochum gedankt.

Weiterer Dank gilt der gesamten Arbeitsgruppe 7.43 „Kryo- und Primärthermometrie" der Physikalisch-Technischen Bundesanstalt, in der Ich die Arbeit angefertigt habe. In kollegialer Atmosphäre wurde mir hier stets die notwendige Unterstützung zuteil.

Ein großes Dankeschön sei hiermit auch dem gesamten Team des Technischen Gerätebaus der Physikalisch-Technischen Bundesanstalt Berlin ausgesprochen, das ausgehend von meinem 3D-Modell die Apparatur gezeichnet, gefertigt, gereinigt und entscheidende Komponenten charakterisiert hat.

Schließlich möchte ich mich besonders herzlich bei meinen Freunden, meiner Familie und vor allem meiner Frau und meinem Sohn bedanken, die in dieser Zeit oft auf mich verzichten mussten und mich doch unentwegt unterstützt haben. Vielen Dank Irene, dass du mir den Rücken freigehalten hast!

Contents

Contents

List of abbreviations

ADC **A**nalog-to-**D**igital **C**onverter

AGT **A**coustic **G**as **T**hermometry

CSPRT **C**apsule type **S**tandard **P**latinum **R**esistance **T**hermometer

CVGT **C**onstant-**V**olume **G**as **T**hermometry

DCGT **D**ielectric-**C**onstant **G**as **T**hermometry

EMPIR **E**uropean **M**etrology **P**rogramme for **I**nnovation and **R**esearch

EOS **E**quation **O**f **S**tate

FCI **F**ull **C**onfiguration **I**nteraction

FEM **F**inite **E**lement **M**ethod

GUM **G**uide to the **U**ncertainty of **M**easurements

ITS-90 **I**nternational **T**emperature **S**cale of 1990

NIST **N**ational **I**nstitute of **S**tandards and **T**echnology

NMI **N**ational **M**etrology **I**nstitute

PEEK **P**oly**E**ther **E**ther **K**etone

ppm **P**arts **P**er **M**illion

PRT **P**latinum **R**esistance **T**hermometer

PTB **P**hysikalisch-**T**echnische **B**undesanstalt

QED **Q**uantum **E**lectro **D**ynamics

QMS **Q**uadrupole **M**ass **S**pectrometer

RIGT **R**efractive **I**ndex **G**as **T**hermometry

RUS **R**esonant **U**ltrasound **S**pectroscopy

SI **S**ysteme **I**nternational d'unites

8

List of virial coefficients

$b_{\mathrm{CM}}(T)$ 2$^{\mathrm{nd}}$ Mosotti virial coefficient
$c_{\mathrm{CM}}(T)$ 3$^{\mathrm{rd}}$ Mosotti virial coefficient
$b_{\epsilon}(T)$ 2$^{\mathrm{nd}}$ dielectric virial coefficient
$c_{\epsilon}(T)$ 3$^{\mathrm{rd}}$ dielectric virial coefficient
$B(T)$ 2$^{\mathrm{nd}}$ density virial coefficient
$C(T)$ 3$^{\mathrm{rd}}$ density virial coefficient
$D(T)$ 4$^{\mathrm{th}}$ density virial coefficient
$E(T)$ 5$^{\mathrm{th}}$ density virial coefficient
$B_p(T)$ 2$^{\mathrm{nd}}$ pressure virial coefficient
$C_p(T)$ 3$^{\mathrm{rd}}$ pressure virial coefficient
$D_p(T)$ 4$^{\mathrm{th}}$ pressure virial coefficient
$E_p(T)$ 5$^{\mathrm{th}}$ pressure virial coefficient
$B_{\mathrm{DCGT}}(T)$ 2$^{\mathrm{nd}}$ DCGT virial coefficient
$C_{\mathrm{DCGT}}(T)$ 3$^{\mathrm{rd}}$ DCGT virial coefficient
$D_{\mathrm{DCGT}}(T)$ 4$^{\mathrm{th}}$ DCGT virial coefficient
$E_{\mathrm{DCGT}}(T)$ 5$^{\mathrm{th}}$ DCGT virial coefficient

List of fit and working equation coefficients

A_1 1$^{\mathrm{st}}$ DCGT working equation coefficient
A_2 2$^{\mathrm{nd}}$ DCGT working equation coefficient
A_3 3$^{\mathrm{rd}}$ DCGT working equation coefficient
A_4 4$^{\mathrm{th}}$ DCGT working equation coefficient
A_1^* 1$^{\mathrm{st}}$ DCGT fit coefficient
A_2^* 2$^{\mathrm{nd}}$ DCGT fit coefficient
A_3^* 3$^{\mathrm{rd}}$ DCGT fit coefficient
A_4^* 4$^{\mathrm{th}}$ DCGT fit coefficient
D_0 1$^{\mathrm{st}}$ dielectric expansion fit coefficient
D_1 2$^{\mathrm{nd}}$ dielectric expansion fit coefficient
D_2 3$^{\mathrm{rd}}$ dielectric expansion fit coefficient
K_0 1$^{\mathrm{st}}$ Burnett expansion fit coefficient
K_1 2$^{\mathrm{nd}}$ Burnett expansion fit coefficient
K_2 3$^{\mathrm{rd}}$ Burnett expansion fit coefficient
K_3 4$^{\mathrm{th}}$ Burnett expansion fit coefficient
V_1 1$^{\mathrm{st}}$ expansion working equation coefficient
V_2 2$^{\mathrm{nd}}$ expansion working equation coefficient
V_3 3$^{\mathrm{rd}}$ expansion working equation coefficient
V_4 4$^{\mathrm{th}}$ expansion working equation coefficient
V_5 5$^{\mathrm{th}}$ expansion working equation coefficient

Contents

List of symbols

A_0	ideal area of the piston cylinder assembly of the pressure balance
A_{eff}	effective area of the piston cylinder assembly of the pressure balance
A_ϵ	molar polarizability
A_μ	molar magnetizability
c_p	thermal capacity at constant pressure
c_V	thermal capacity at constant volume
$C(p)$	capacitance of a gas filled capacitor at pressure p
E	module of elasticity
$\boldsymbol{E}_{\text{ext}}$	external electric field
$\boldsymbol{E}_{\text{int}}$	internal electric field
f	Mossotti-term
F_{ratio}	ratio of Mosotti-terms
g	local gravimetrical constant
h	Planck constant
k	Boltzmann constant
m	mass
M	molar mass
n	refractive index
N	number of particles
N_{A}	Avogadro constant
p	pressure
p_{res}	residual pressure of the pressure balance
P_{ratio}	ratio of pressures
$\boldsymbol{P}_\alpha$	Polarizability
Q	ideal apparatus constant ($Q = (V_{\text{A}} + V_{\text{DA}} + V_{\text{B}} + V_{\text{DB}})/(V_{\text{A}} + V_{\text{DA}})$)
Q_{A}	ratio of volumes at T_{GHS} and T_{iso} in the measuring part ($Q_{\text{A}} = V_{\text{DA}}/V_{\text{A}}$)
Q_{B}	ratio of volumes at T_{GHS} and T_{iso} in the expansion part ($Q_{\text{B}} = V_{\text{DB}}/V_{\text{B}}$)
Q^*	ratio of the volumes of measuring and expansion cells at T_{iso} ($Q^* = V_{\text{A}}/V_{\text{B}}$)
$Q_{\Delta T}$	apparent apparatus constant
R	molar gas constant
t	temperature in °C
T	thermodynamic temperature in K
T_{iso}	measuring temperature as ITS-90 temperature
T_{GHS}	temperature of the gas-handling system as ITS-90 temperature
T_{ratio}	ratio of the measuring and gas-handling system temperature ($T_{\text{ratio}} = T_{\text{iso}}/T_{\text{GHS}}$)
u	uncertainty of a property
V	volume
Z	compressibility factor

List of greek symbols

α_0	static electric dipole polarizability
α_{th}	linear coefficient of thermal expansion
$(\alpha + \beta)$	thermal expansion coefficient of the pressure balance
β_{Digi}	temperature sensitivity coefficient of the Digiquartz pressure sensor
β_Q	slope of the temperature dependence of the apparent apparatus constant $Q_{\Delta T}$
γ	relative change of capacitance, DCGT measuring quantity ($\gamma = \epsilon_{\text{r}} - 1 + \epsilon_{\text{r}}\kappa_{\text{eff}}p$)
Δ	difference of two values
$\Delta\alpha(r)$	trace of the interaction induced polarizability tensor
ϵ	dielectric constant ($\epsilon = \epsilon_0\epsilon_{\text{r}}$)
ϵ_0	vacuum permittivity
ϵ_{r}	relative dielectric permittivity
$\varphi(r)$	angle independent interaction potential
κ_{eff}	effective compressibility of the capacitor
κ_{vol}	isothermal bulk compressibility
λ	pressure deformation coefficient
μ	working quantity of DCGT ($\mu = \frac{\gamma}{\gamma+3}$)
μ_{P}	Poisson ratio
μ_{r}	relative magnetic permeability
ρ	mass density
ρ_{m}	molar particle density
ρ_{N}	number particle density

List of subscripts

A	measuring volume at measuring temperature
B	expansion volume at measuring temperature
corr	corrected property
DA	measuring volume at gas-handling system temperature
DB	expansion volume at gas-handling system temperature
DCGT	Dielectric-constant gas thermometry
Digi	Digiquartz pressure sensor (either Digi_1 or Digi_2)
GHS	gas-handling system
ideal	under idealized conditions, for an ideal gas
iso	constant (measuring) temperature
meas	measured property
MC	Monte-Carlo
pb	pressure balance
r	relative

1. Introduction

Natural scientists and engineers use a broad variety of methods to determine the thermophysical properties of fluids. In this thesis, the potential of **D**ielectric-**C**onstant **G**as **T**hermometry (DCGT) as a complementary method for the determination of density and dielectric virial coefficients of gases is explored. This method of primary thermometry has already been successfully used to determine combinations of density and dielectric virial coefficients, the so called DCGT virial coefficients [1–3]. The drawback of this approach is the impossibility to distinguish between both contributions since capacitance and pressure data is utilized in combination. That is why these experiments are coupled with Burnett and dielectric expansion experiments where pressure and capacitance ratios are defined by repeated expansion of gas from one into another volume [4–6]. From these ratios, the independent density and dielectric virial coefficients can be determined without the need to assess the absolute particle density. Both methods typically require large experimental setups whose manual operation is time consuming. In this thesis, a new compact apparatus was developed that combines both experimental approaches, whereas the expansions are fully automated.

To validate the performance of the device, measurements with argon were carried out at the four temperatures $253.898\,\text{K}$, $273.161\,\text{K}$, $296.126\,\text{K}$ and $302.913\,\text{K}$. The valuation of the results is ensured by detailed uncertainty budgets, which were assigned in accordance with the **G**uide to the **U**ncertainty of **M**easurements (GUM), as well as by comparison to the relevant literature values. Unless stated otherwise, uncertainties in this thesis are given as standard uncertainties with the corresponding coverage factor $k = 1$ [7]. The achieved combined relative standard uncertainties are between $0.15\,\%$ and $0.3\,\%$ for the second DCGT virial coefficient (B_{DCGT}) and $1.5\,\%$ to $2.5\,\%$ for the third DCGT virial coefficient (C_{DCGT}). For the evaluation of the expansion data, two cases were studied. First, a free fit was applied to the data resulting in combined relative standard uncertainties in the order of $1.5\,\%$ to $2.5\,\%$ for the second density virial coefficient (B) and $25\,\%$ to $35\,\%$ for the second dielectric virial coefficient (b_ϵ). In a second approach, the volume ratio defining the expansions was precisely measured with helium and used as a constraint in the fit. This way the uncertainties can be lowered by roughly a factor of two resulting in uncertainties of less than $1\,\%$ for $B(T)$ and in the order of $15\,\%$ for b_ϵ. The experimental results agree among themselves and in comparison to the established literature mostly on the level of the standard uncertainty but always for the expanded standard uncertainty (coverage factor $k = 2$). It should be mentioned that the assessment of the dielectric virial coefficients is experimentally challenging since they are typically two orders of magnitude smaller than the density virial coefficients. Still, they gain relevance especially due to the advances in optical measurements. To the knowledge of

the author, this work is the first in almost three decades that attempts to precisely measure the dielectric virial coefficients of argon as a function of temperature including a detailed uncertainty budget. Due to the small absolute value of b_ϵ, the uncertainty of the second density virial coefficient can actually be further lowered to the order of $0.5\,\%$ and less if it is calculated by $B = B_{\mathrm{DCGT}} + b_\epsilon$.

That is why the gained results are not only used to validate the performance. They are part of two **E**uropean **M**etrology **P**rogramme for **I**nnovation and **R**esearch (EMPIR) projects dedicated to advances in gas metrology, a field that became particularly interesting after the redefinition of the **S**ysteme **I**nternational d'unites (SI) in 2019. Both projects and further motivation of the work is given in the short next chapter 2.

The theoretical background of the virial coefficients and the used working equations of the methods are presented in chapter 3. A substantial amount of work was required to derive new working equations for the expansion experiments. While these experiments are typically carried out at isothermal conditions, the demand for automation in this thesis required to stabilize the pressure sensors and valves of the gas-handling system at ambient temperature while the measuring temperature is varied. Taking the resulting dead volumes at different temperatures as well as the deformation of the cells under pressure into account, results in long but at the same time well-structured working equations. A discussion on the required fit orders for the evaluation of the data is carried out as well.

Further details on the design and construction of the apparatus as well as the used measuring equipment is presented in chapter 4. This includes the concept of thermal stabilization as well as a comprehensive investigation of the used cylindrical capacitors. Since the potential of this method to be used by non **N**ational **M**etrology **I**nstitute (NMI)s is to be explored as well, commercially available measuring equipment was used exclusively. It will be shown that for the virial coefficients, the main contributions to uncertainty arise from statistical scattering of pressure and capacitance. In contrast, the uncertainties of their absolute values as well as the uncertainty of the absolute temperature are of secondary importance.

The final averaged results of a total of 19 isotherms measured with argon and the corresponding uncertainty budgets are presented in chapter 5. Besides the virial coefficients, this chapter also includes results from the classical DCGT data evaluation in form of the molar polarizability A_ϵ, thermodynamic temperatures and effective compressibilities κ_{eff} of the used capacitors. The more precise determination of the virial coefficients from the expansion experiments with a constraint fit is based on a precise assessment of the volume ratio between the cells. The determination of this ratio with relative uncertainty on the level of $5\,\mathrm{ppm}$ was carried out by measurements with helium.

Recommendations for the improvement of the method and a discussion of the potential for this method to be used in a more commercial fashion is based on the uncertainty budgets of chapter 5 and presented in the summary 6.

2. The role of the virial coefficients for gas metrology

Equation **O**f **S**tate (EOS) play an undeniably big role in many fields of science, technology and industry offering a broad variety of aspects to motivate this work. For instance, the apparatus presented in this thesis can contribute important measurements for hydrogen and hydrogen mixtures. This potential future energy carrier is of special interest in regards of the german "Energiewende", "Power-to-Gas" and emerging hydrogen technologies. The different output quantities that can be obtained with just one measurement also make this device desirable for the solely purpose of determining highly precise gas properties. However, one field that will particularly benefit not only from this new measuring concept but also from the results presented in chapter 5 of this thesis is gas metrology. Here, a measuring gas with precisely known properties is used to asses other physical properties as for instance temperature T, pressure p, density ρ or the refractive index n. Linking the thermodynamic properties is ensured by an EOS with the simplest one being the ideal gas equation. The most precise ones are reference EOS that are typically explicit in the Helmholtz free energy. They cover a broad temperature and pressure range, are valid for different phases and allow to calculate a variety of properties by partial differentiation. Furthermore, they can include numerous pure substances and predict the p-ρ-T behavior of their mixtures. A very prominent and important reference EOS is the GERG2008 that was developed for natural gas containing up to 21 pure substances [8]. However, the complexity of these EOS is a disadvantage for practical gas metrology. Often, only a certain pressure range at one temperature for one pure substance is of interest. There are several other EOS as for instance relatively compact two parameter equations like the EOS of Van-der-Waals, Redlich-Kwong or Peng-Robinson and several modifications of them. They all have their certain fields of application but in gas metrology the virial EOS, which will be introduced in detail in section 3.1, is certainly favored. Its two big benefits are, first, that as well only a limited set of parameters, namely the density virial coefficients, are required to precisely describe the p-ρ-T behavior of the gas. They are the factors of a polynomial in particle density. Secondly, the required number of these coefficients can be adapted to the required pressure range. This is visualized in figure 2.1 where the relative overall correction to the ideal gas pressure as well as the individual contributions of the different virial coefficients are shown for argon at a temperature of 296 K.

The overall relative correction is dominated by the second density viral coefficient B defining the linear correction. Quadratic and cubic contributions in the correction due to the third and fourth density viral coefficients C and D first gain relevance at higher pressures. De-
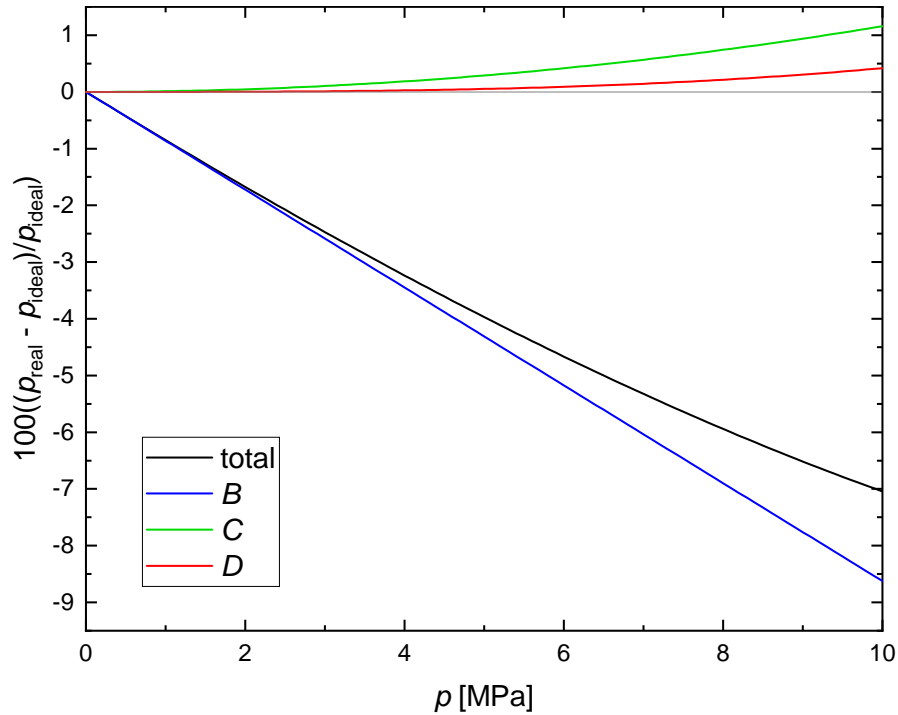
Figure 2.1.: Relative correction of the pressure of an ideal gas in percent for argon at a temperature of $296\,\mathrm{K}$. The different contributions to the total correction are shown as well with B, C and D denoting the contributions based on the second, third and fourth density virial coefficients.

pending on the absolute pressure and the uncertainty demands of an experiment, the number of included virial coefficients can thus be adapted. At low pressures, just one parameter, namely B, may potentially already be sufficient to evaluate experiments. Another aspect that may explain the popularity of this EOS in gas metrology is the structure as a polynomial enabling fairly easy data fitting. Furthermore, the derivation of working equations often include the expansion into a Taylor series, which is of polynomial character as well. Generally, the virial coefficients are temperature dependent, but since experiments of metrological character are typically carried out at isothermal conditions this is not an issue. Instead, it offers the possibility to determine the virial coefficients at certain temperatures with high precision and use the gas at this temperature as reference gas or for calibration purposes. This could for instance be useful at the fix point temperatures of the **I**nternational **T**emperature **S**cale of 1990 (ITS-90) (see section 4.4 for more details on the ITS-90).

Especially after the overworking of the SI on the 20th of May 2019, some of the corresponding gas metrological measurement methods became strikingly attractive for the direct realization of units. Generally, the seven base units do no longer rely on artifacts like the Ur-kilogram or triple point cells. Instead, they have been linked to natural constants that do not change over time. The implementation of this new SI and especially the progress in gas metrology is supported by a variety of projects in the frame of the EMPIR. Two of them benefit directly from the apparatus presented in this thesis and the measured results. The first, "Real K", explores methods for the realization of the unit of temperature, the kelvin,

which is now defined by the Boltzmann constant k rather than by the triple point of water. In the second project, "Quantum Pascal", the goal is to study and develop dielectric and optical methods that can be used as primary pressure standards with competitive uncertainties compared to established mechanical methods. An aspect that is equal in both projects is the desire to promote argon as a measuring gas instead of the typically used helium. Helium has the big advantage that due to its simple atomic structure its properties can be calculated with very low uncertainties by *ab initio* methods. In fact, these uncertainties cannot be obtained experimentally at this point. However, the drawback is that the dielectric and optical measuring effect is very low due to the low polarizability. On the one hand this makes experiments vulnerable to impurities, on the other hand it requires very accurate and, thus, expensive measuring equipment to achieve low uncertainties. These drawbacks could be ovcerome by using argon whose polarizability is a factor of eight higher. It fulfills almost all other demands to a metrological measuring gas like non toxicity, non flammability and availability in high purity at moderate prices. Unfortunately, it will be also shown in the next chapter that calculation of its properties are rather demanding because of the more complex atomic structure. That is why both projects aim to further develop these calculations. The work of the theoreticians is supported by accurately measured density and dielectric virial coefficients, which are presented in chapter 5 of this thesis. Further information on the underlying principals of the calculations will be given in sections 3.1.1 and 3.1.3. Both projects will be briefly summarized in the following, whereas further contributions of this thesis will be emphasized.

2.1. Project: "Realising the redefined kelvin"

Prior to the before mentioned redefinition of the kelvin, traceability to this unit was realized exclusively by the use of temperature scales, as for instance the currently valid ITS-90. Now, certain methods of primary thermometry are included in the *Mise en Pratique* as direct realizations of the kelvin. Room for innovation and development in the future has been created and further methods may be included. Though the direct realization of the kelvin appears strikingly attractive, the methods included are bulky, complicated and rather expensive. Therefore, this project "Real-K" aims in two directions. On the one hand it shall be ensured that the currently used temperature scale ITS-90 can be further used until primary methods of thermometry can compete. NMIs, institutes and consumers world wide have established and are used to a metrological infrastructure based on this temperature scale. Changes and acceptance of these will thus take time. On the other hand the long time goal is to establish a number of primary thermometry methods that may be used practically for the realization and especially dissemination of the kelvin. Currently included methods are radiation thermometry based on the Planck law for temperatures above 1235 K, Johnson noise thermometry based on the noise voltage of thermally moved charge carriers in a suitable measuring resistor and a variety of gas thermometric methods based on the gas law, namely **A**coustic **G**as **T**hermometry (AGT), DCGT and **R**efractive **I**ndex **G**as

Thermometry (RIGT) covering the important temperature range from several kelvin up to several hundred kelvin. On the one hand the potential of DCGT to be used at temperatures above the triple point of water as a practical primary thermometer is explored with this apparatus. On the other hand precisely measured density virial coefficients also contribute important input for the other gas thermometric methods. This is particularly true for argon which could be used to perform relative primary thermometry with lower demands to the measuring equipment for the dissemination of the kelvin.

2.2. Project: "Towards quantum-based realisations of the pascal"

This second project "Quantum Pascal" is dedicated to the realization of the unit of pressure, the pascal. Pressures are typically realized by their mechanical definition of force per unit area. The most precise pressure measurement devices are either u-tube manometers filled with mercury or pressure balances with piston cylinder assemblies that can reach relative uncertainties in the order of 1 ppm [9]. Scientists at **N**ational **I**nstitute of **S**tandards and **T**echnology (NIST) were the first to seriously discuss the idea of an alternative pressure standard based on dielectric measurements in 1998 [10]. The basic idea is identical to the DCGT principle, which will be introduced in more detail in section 3.2. The dielectric constant of the measuring gas is measured with a capacitor and the density is calculated by the Clausius-Mosotti equation (see section 3.1.3 for further details). The pressure is then calculated from the density with an EOS. Precise knowledge of the polarizability as well as the dielectric and density virial coefficients are required in this process which is why helium was proposed as the measuring gas. Still, by that time the uncertainties of these properties were limiting the reachable pressure uncertainties to more than 20 ppm. Profiting from the tremendous progress made in the calculation of *ab initio* properties of helium since then, Gaiser *et al.* have recently proven that this principle has actually the potential to be a pressure standard with competitive uncertainties in the order of a few ppm [11]. The idea was also captured by Pendrill who adapted it to refractometry and optical methods in 2004 after the improvements in lasers and optics of that time [12]. Instead of measuring the dielectric constant of a gas, the refractive index n is measured. If the refractivity and the refractive virial coefficients of the measuring gas are known, the particle density can be calculated with the Lorentz-Lorenz equation (see appendix D). Work in this field is recently rising with several groups working on the topic [13–16]. Besides the already mentioned drawbacks of helium, an additional problem occurs for these optical experiments. The small helium atom tends to permeate into certain glasses which can cause errors due to deformation and changes of length that are harmful especially in optical experiments. The permeation can also lead to outgassing which causes drifts and errors in the measurement signal at quasi stable conditions.

This is where the "Quantum Pascal" project pursues the recent considerations into two directions. Firstly, a variety of methods including primarily Fabry-Pérot based refractometers but also microwave resonators, Rayleigh scattering, DCGT and absorption spectroscopy is

investigated for its potential to realize pressures in the broad range from 1 Pa up to 3 MPa. Secondly, the potential of argon as measuring gas is explored and improved by big efforts in the field of *ab initio* calculations of the polarizability and the dielectric virial coefficients including their frequency dependence. The relation between the static and the dynamic properties is shown in appendix D. It is important to emphasize that the frequency corrections to the static values are typically only in the order of a few percent. Furthermore, these corrections can be calculated with reasonable uncertainties allowing to utilize the dielectric virial coefficients of argon that are determined in this thesis also for the optical experiments.

3. Theoretical background

The apparatus presented in this thesis combines three different methods for the determination of real gas properties. Namely DCGT for the determination of the molar polarizability A_ϵ and DCGT virial coefficients (B_{DCGT}, C_{DCGT},...), the classic Burnett method for the determination of density virial coefficients (B, C,...) and a respective dielectric expansion method for the determination of dielectric virial coefficients (b_ϵ, c_ϵ,...). First, a short introduction on these properties and the corresponding declarations used throughout this thesis are given. As discussed in the previous chapter, *ab initio* calculations of the quantities play a major role for primary metrology. Therefore, the underlying principles and the current state-of-the-art is shortly summarized for each of them. After this, the principles and working equations for the tree different methods are presented. The lengthy derivations of the equations is mainly transferred to the appendix, while in this chapter only the starting equations and final results are given. In the appendix, the virial coefficients are written as B, C, *et cetera* without indicating the temperature dependence ($B(T)$, $C(T)$ *et cetera*) to ease readability. The derivations for the expansion methods including different corrections typically follow the same pattern which is why the principle is explained exemplary in section 3.3.1 for the ideal case and in section 3.3.2 for corrections. In case of the expansion experiments, the corrections due to the gas volume at different temperatures are only shown for the second virial coefficients. The derivations for the higher virials are getting exponentially complex, require further approximations and are, thus, content of future work. Results for the third virial coefficients are, therefore, only given for the DCGT virial coefficients and the results at room temperature where only the deformation of the cells requires correction.

3.1. Ideal and real gas

In an ideal gas, relations between pressure p and molar particle density ρ_{m} are derived from the assumption that the gas particles haven an infinitely small volume and may only conduct elastic scattering with other particles and the walls of the vessels containing it. These assumptions lead to the well known ideal gas equation:

$$p = \rho_{\text{m}} RT \tag{3.1}$$

In this formula, $R = N_{\text{A}} k$ is the molar gas constant, N_{A} is the Avogadro constant, k is the Boltzmann constant and T is the thermodynamic temperature. Equation (3.1) describes the behavior of highly diluted real gases to some extend, but deviations from experimental results

increase with rising particle densities. On the one hand this is due to the increasing effect of the volume of the particles themselves. On the other hand multi particle scattering needs to be taken into account. To describe his experimental data, one way to describe a real gas was empirically introduced by Kammerlingh Onnes. He developed an expansion in terms of the particle density with the corresponding factors being the density virial coefficients explained in the next section.

3.1.1. Density and pressure virial coefficients

To properly describe real gas behavior, the density virial expansion includes correction terms to the ideal gas in form of temperature dependent factors $B(T)$, $C(T)$, $D(T)$, $E(T)$... that take multi particle interaction into account. They are multiplied with powers of the particle density and are referred to as density virial coefficients of second, third, fourth and fifth... order. The order also indicates the number of particles whose interactions are considered. The biggest correction to the ideal gas, thus, arises from the second virial coefficient $B(T)$ taking into account two particle interaction.

$$p = \rho_{\mathrm{m}} RT \left(1 + B\left(T\right)\rho_{\mathrm{m}} + C\left(T\right)\rho_{\mathrm{m}}^2 + D\left(T\right)\rho_{\mathrm{m}}^3 + E\left(T\right)\rho_{\mathrm{m}}^4 + ... \right) \tag{3.2}$$

In some works, the term in brackets is referred to as compressibility factor *Z*.

$$Z = \left(1 + B\left(T\right)\rho_{\mathrm{m}} + C\left(T\right)\rho_{\mathrm{m}}^2 + D\left(T\right)\rho_{\mathrm{m}}^3 + E\left(T\right)\rho_{\mathrm{m}}^4 + ... \right) \tag{3.3}$$

For the derivation of the working equations used in this thesis, it is more convenient to work with an expansion in the experimentally accessible pressure rather than in particle density.

$$p = \rho_{\mathrm{m}} RT \left(1 + B_p\left(T\right)p + C_p\left(T\right)p^2 + D_p\left(T\right)p^3 + E_p\left(T\right)p^4 + ... \right) \tag{3.4}$$

In equation 3.4, $B_p\left(T\right)$, $C_p\left(T\right)$, $D_p\left(T\right)$, $E_p\left(T\right)$, ... denote the pressure virial coefficients of second, third, fourth, fifth, ... order respectively. A general relation between these two types of virial coefficients of any order was derived by Putnam and Killpatrick by means of functional theory [17]. Essentially, a comparison of the compressibility factors of equations 3.2 and 3.4, while replacing the pressure *p* with equation 3.2, is carried out. Comparing the factors of powers of the particle density is shown in Appendix A and reveals the following simple relations for the orders relevant in this thesis:

$$B\left(T\right) = B_p\left(T\right) \cdot RT$$
$$C\left(T\right) = C_p\left(T\right) \cdot (RT)^2 + (B\left(T\right))^2$$
$$D\left(T\right) = D_p(T) \cdot (RT)^3 + 3C(T)B(T) - 2(B(T))^3$$
$$E\left(T\right) = E_p\left(T\right) \cdot (RT)^4 + 2(C\left(T\right))^2 + 4B\left(T\right)D\left(T\right) - 10(B(T))^2 C\left(T\right) + 5(B(T))^4$$

$$(3.5)$$

The theoretical background of equation 3.2 will be introduced to the required extend since it is the basis for *ab initio* calculations of the virial coefficients. State-of-the-art calculations are introduced while their discussion and comparison to the experimental results of this thesis is carried out in section 5.6.1. The extensive derivation of equation 3.2 is for instance comprehensively described in [18] in two different manners. One option is to use the classical virial theorem while the other one starts with the partition function. The latter is summarized in appendix C since it can be easily adapted to include quantum mechanical considerations, which is also shown in the appendix.

As shown there, a closed-form solution resulting from classical mechanics can be derived for the second density virial coefficient for the assumption of an angle independent potential, which is valid for noble gases:

$$B'(T) = -2\pi \int_0^\infty \left(\exp\left(\frac{-\varphi(r)}{kT} \right) - 1 \right) r^2 dr \tag{3.6}$$

Here, $\varphi(r)$ is the interaction potential between two particles separated by distance r. The prime indicates that these are the microscopic rather than the molar virial coefficients. The conversion is simply carried out by $B(T) = B'(T) \cdot N_A$ with N_A being the Avogadro constant. It can be shown that this formula can be adapted to include quantum mechanics (see appendix C as well) and then may be written as:

$$B'(T) = \lambda^3 \left(\pm 2^{-\frac{5}{2}} - 2^{\frac{3}{2}} \sum_l (2l+1) \sum_n e^{\left(-\frac{E_{nl}}{kT} \right)} - \right.$$
$$\left. \frac{2^{\frac{3}{2}}}{\pi} \sum_l (2l+1) \int_0^\infty e^{\left(-\frac{\hbar^2 \kappa^2}{2\mu_m kT} \right)} \left(\frac{d\delta_l}{d\kappa} \right) d\kappa \right) \tag{3.7}$$

In this formula, $\mu_m = m_1 m_2/(m_1 + m_2)$ is the reduced mass, $\lambda = h/(2\pi mkT)^{1/2}$ is the thermal wavelength and $\kappa = (2\mu_m E_n)^{\frac{1}{2}}/\hbar$. E_{nl} are the discrete energy states of the system, $\delta_l(\kappa)$ is the phase-shift of the energy states, which is caused by scattering, and the summation is carried out over the angular momentum l of the two particle system. The Planck constant is denoted by h and $\hbar = h/(2\pi)$. Equation 3.7 is applicable for Bose and Fermi spin statistics. In Boson statistics (for instance helium-4), the first term has

a negative sign and the summation is only carried out over even values of l. For Fermi statistics (for instance helium-3), the ideal term has a positive sign and the summation is only carried out over odd values of l. This selection of angular momenta is a consequence of the quantum mechanical restriction that wave functions of bosons are symmetrical while the one for fermions have to be antisymmetrical. The different contributions in formula 3.7 are the ideal term, the term for weakly bound particles and the last term which takes collisions between two particles into account. In principal $B(T)$ may be calculated now. However, there are three major challenges. First of all, the potential in equation 3.6 describing the interaction between the particles needs to be known very precisely and from *ab initio* considerations as well. In equation 3.7, the potential is implicitly included by E_{nl} and $\delta_l(\kappa)$. Secondly, the energy levels E_n need to be calculated, which requires to solve the Schrödinger equation. In most cases, two different approaches are chosen in this case. Either the theory of coupled clusters is applied or, where possible, the full configuration interaction (FCI) is taking into account all available excited states making it generally more precise. Last but not least, the calculation itself contains to solve complicated integrals. These integrals tend to get more complicated with higher orders. Additionally, already the third virial coefficient requires the solution of a three-body problem, which does not have a general closed-form solution any more. This accounts for the derivation of the potential as well, whereas here another challenge lies in the inclusion of quantum mechanics.

Due to its comparably simple atomic structure, helium has been extensively used for calculations. Considerable progress was made in preparation for the redefinition of the SI, since it was for instance used as a measuring gas for the determination of the Boltzmann constant [19]. To ensure independence from other experiments, the required properties had to be calculated exclusively *ab initio* and with reliable as well as sufficiently low uncertainties. By that time, two highly accurate potentials were used to calculate the virial coefficients. One from a group of the university of Rostock [20] and one from a group from the university of Warsaw [21]. Though independent and different potentials were used, the agreement between both calculations is excellent. Deviations are well within the uncertainty given in [21] indicating a certain reliability of the computations. In 2017, the polish group improved their helium pair potential again by one order of magnitude [22]. It was recently used to recalculate the virial coefficients of helium-3 and helium-4 [23]. The latest adaptions to the potential and the influence on the virial coefficients are presented in a submission to Physical Review A, which is accepted but not yet published [24].

As explained in the previous text, the calculation of the higher virial coefficients is much more complicated. The first calculation of the third virial coefficient based on a real three-body potential was carried out by Garberoglio et al. in 2009 [25]. They used a path integral method for the calculation of the virial coefficients and refined the values by including spin statistics in 2011 [26]. To include the quantum mechanical contributions to the classical formulation, perturbation theory was used. Resulting terms were incorporated into existing potentials to different orders. For the higher virial coefficients, most precise values were computed by Shaul et al. [27, 28]. It shall be noted that currently the uncertainties of the
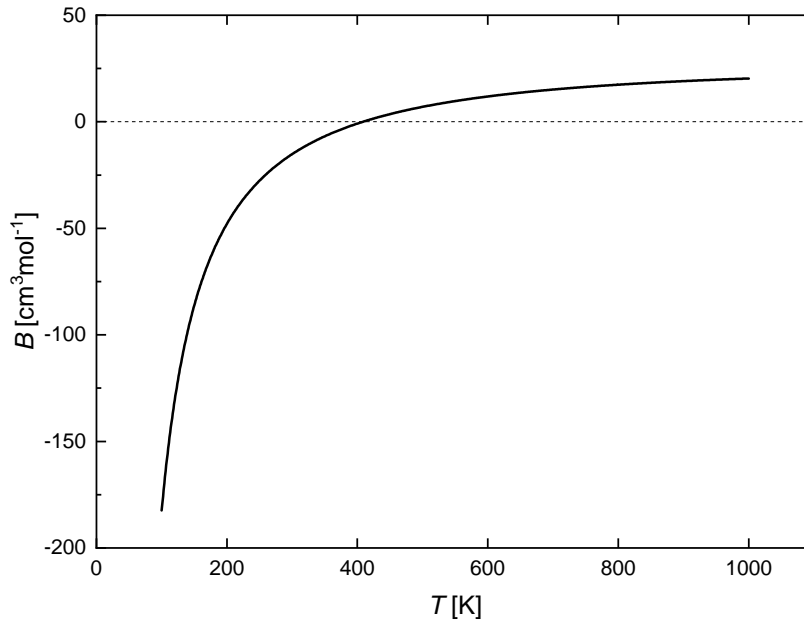
Figure 3.1.: Temperature dependence of the second density virial coefficient of argon as calculated by Jäger *et al.* [29].

computed values for helium are at least one order of magnitude lower than the most precise experimental determinations.

For argon, the situation is different. Here, experimental values are yet more precise than the calculated ones. This is simply due to the more complex atomic structure with 18 protons and electrons making computations of the potential and the virial coefficients much harder. Calculations for $B(T)$, $C(T)$ and $D(T)$ were carried out by Jäger *et al.* [29] and Wiebke *et al.* [30], whereas the potential used by Wiebke *et al.* is not independent from [29]. Furthermore, exact values of $B(T)$ are given in [31] and *ab initio* values for $C(T)$ are published in [32]. The values are summarized in section 5.6.1.

In general, the virial coefficients are temperature dependent. The behavior shown in figure 3.1 for the second density virial coefficient of argon can be qualitatively explained. For lower temperatures, the molecules move slowly and tend to spend more time associated to other molecules. This is leading to a lower pressure compared to the ideal gas, which is why the sign of $B(T)$ is negative. For higher temperatures, scattering becomes a dominant factor. Energetic collisions lead to a pressure, which is above the one of an ideal gas.

3.1.2. Polarizability and the Clausius-Mosotti equation

A relation to the particle density of a gas cannot only be established by the pressure but also by dielectric properties. A key property in this case is the electric dipole polarizability, which describes the reaction of an atom or molecule to an external electric field $\boldsymbol{E}_{\text{ext}}$ [33]. Protons and electrons of the molecule are interacting with the field, get torn into the corresponding directions and create an internal electric field of opposite direction. The macroscopic behavior of the gas can then be expressed by means of the polarizability $\boldsymbol{P}_\alpha$:

$$\boldsymbol{E}_{\text{ext}} + \frac{\boldsymbol{P}_\alpha}{\epsilon_0} = \epsilon_{\text{r}}\boldsymbol{E}_{\text{ext}} \tag{3.8}$$

In this formula $\epsilon_r = \epsilon/\epsilon_0$ is the relative permittivity and ϵ is the dielectric constant of the gas. For non polar gases and for a system of N particles, the polarizability $\boldsymbol{P}_\alpha$ is given by:

$$\boldsymbol{P}_\alpha = \rho_N \alpha_0 \boldsymbol{E}_{\text{int}} \tag{3.9}$$

ρ_N denotes the particle density, α_0 is the static electric dipole polarizability of the molecules and $\boldsymbol{E}_{\text{int}}$ is the average internal electric field influencing the individual particles. At this point, the question is what the relation between the internal and the external electric field is. Lorentz was able to derive an expression for non polar gases by considering a virtual sphere filled with a homogeniously polarized matter. Placing the sphere in an homogenous electric field $\boldsymbol{E}_{\text{ext}}$ results in in the so called Lorentz field $\boldsymbol{E}_{\text{L}} = \boldsymbol{E}_{\text{ext}} + \boldsymbol{E}_{\text{Sphere}}$ inside the sphere. $\boldsymbol{E}_{\text{Sphere}}$ results from the induced charges on the surface of the sphere and can be calculated by $\boldsymbol{E}_{\text{Sphere}} = \boldsymbol{P}_\alpha/(3\epsilon_0)$. In combination with equations 3.8 and 3.9 the Clausius-Mosotti equation can be derived:

$$\frac{\epsilon_{\text{r}} - 1}{\epsilon_{\text{r}} + 2} = \rho_{\text{N}} \frac{\alpha_0}{3\epsilon_0} = \rho_{\text{m}} A_\epsilon \tag{3.10}$$

In this formula, A_ϵ denotes the molar polarizability used for the molar notation of the equation. The Term $\frac{\epsilon_{\text{r}}-1}{\epsilon_{\text{r}}+2}$ in equation 3.10 will be referred to as the Mosotti Term in this thesis. This equation is derived for static electric fields, which is a valid assumption for the capacitance bridge operating at a frequency of $1000\,\text{Hz}$ used in this thesis. For optical experiments as for instance performed in the "Quantum Pascal" project described in 2.2, a formula including the frequency needs to be used. In this case, the assessed refractive index n can be related to the particle density by the so called Lorentz-Lorenz equation for electrodynamics. Since the refractive index is related to the relative electric permittivity by $n^2 = \epsilon_{\text{r}}\mu_{\text{r}}$ where μ_{r} is the relative magnetic permeability, the formula is very similar to the Clausius-Mosotti equation. A brief summary of the formula, the refractivity and the refractive index virial coefficients is given in appendix D.

The importance of precise knowledge of the dipole polarizability can be illustrated by considering gases at low densities. Neglecting higher order terms and corrections, it becomes clear that the polarizability relates pressures p and temperature T to the dielectric constant by a linear relation:

$$(\epsilon_{\text{r}} - 1)kT = 4\pi\alpha_0 p \tag{3.11}$$

This formula essentially holds its linear character also for optical measurements of the refractive index.

Due to the same reasons layed out in subsection 3.1.1, calculations of the polarizability for helium were refined in preparation for the redefinition of the SI in 2017 [19]. It will be shown in section 3.2 that this was particularly required for DCGT and RIGT experiments. Different highly accurate calculations were carried out by the group from the University of Warsaw [34, 35] with relative uncertainties of less than 0.2 ppm. In a current publication, these calculations were further improved by performing relativistic **Q**uantum **E**lectro **D**ynamics (QED) calculations including the finite nuclear mass [36]. The relative uncertainty was again lowered to 0.1 ppm. Experimentally, these uncertainties cannot be achieved at this point. The most accurate measurement was carried out by Gaiser *et al.* with the setup used for the determination of the Boltzmann constant and resulted in a relative uncertainty in the order of 2 ppm [37].

In the same publication, the currently most precise experimental value for argon with a relative uncertainty in the order of 2 ppm was published. At this point calculations of the polarizability for argon are scarce, and due to the complex electron structure, relative uncertainties are about three orders of magnitude higher than the experiment [38, 39]. However, one goal of the projects described in chapter 2 is to further improve these calculations for argon.

3.1.3. Dielectric virial coefficients

Similar to the elucidations given in section 3.1.1, the interactions between multiple particles have to be taken into account for the Clausius-Mosotti equation 3.10 as well. In terms of the dielectric properties these contributions are multipoles. In analogy to equation 3.2, the Clausius-Mosotti equation 3.10 is expanded in terms of the molar particle density with the corresponding factors being the temperature dependent dielectric virial coefficients $b_\epsilon\,(T)$, $c_\epsilon\,(T)$,... of second, third,... order:

$$\frac{\epsilon_\mathrm{r} - 1}{\epsilon_\mathrm{r} + 2} = A_\epsilon \rho_\mathrm{m} \left(1 + b_\epsilon\,(T)\,\rho_\mathrm{m} + c_\epsilon\,(T)\,\rho_\mathrm{m}^2 + ...\right) \tag{3.12}$$

It shall be noted that in some works the dielectric virial coefficients are differently defined by $\frac{\epsilon_\mathrm{r}-1}{\epsilon_\mathrm{r}+2} = A_\epsilon \rho_\mathrm{m} + b_\epsilon^*(T)\rho_\mathrm{m}^2 + c_\epsilon^*(T)\rho^3 + ...$ However, in this thesis the definition by equation 3.12 is used exclusively, and formulas from other literature sources have been adapted accordingly. Again, it is advantageous for the derivation of further working equations to develop this equation in powers of the Mosotti-term $f = \frac{\epsilon_\mathrm{r}-1}{\epsilon_\mathrm{r}+2}$ rather than the molar particle density:

$$f = A_\epsilon \rho_\mathrm{m} \left(1 + b_\mathrm{CM}\,(T)\,f + c_\mathrm{CM}\,(T)\,f^2 + ...\right) \tag{3.13}$$

3. Theoretical background

In equation 3.13, $b_{\mathrm{CM}}(T)$, $c_{\mathrm{CM}}(T)$,...denote the Mosotti virial coefficients of respective orders. The relation to the dielectric virial coefficients can be established in analogy to the pressure virial coefficients and is shown in appendix B.

$$b_\epsilon(T) = b_{\mathrm{CM}}(T) A_\epsilon$$
$$c_\epsilon(T) = b_\epsilon(T)^2 + c_{\mathrm{CM}}(T) A_\epsilon^2 \tag{3.14}$$

Since the electric field only causes minor perturbations to the system, the dielectric virial coefficients are generally around two orders of magnitude smaller than the density virial coefficients. Therefore, they are here only considered up to the third order.

The theoretical background of the expansion of the Clausius-Mosotti equation for non polar gases was carried out by Buckingham in 1955 [40]. He investigated the possible perturbations considering two different effects. On the one hand a neighbor molecule may influence the polarizability of a molecule, on the other hand moments induced by the neighboring molecules may induce additional moments in the neighbor molecule as well. The derived formula for the second dielectric virial coefficient which may be used for calculations of this property is:

$$b'_\epsilon = \frac{2\pi}{3\epsilon_0} \int_0^\infty \Delta\alpha(r) \exp\left(\frac{\varphi(r)}{kT}\right) \tag{3.15}$$

In this equation, $\Delta\alpha(r)$ denotes the trace of the interaction induced polarizability tensor. The prime indicates that it is the microscopic second dielectric virial coefficient valid for the expansion in particle density rather than in molar particle density. Conversion is carried out by $b_\epsilon(T) = b'_\epsilon(T) \cdot N_{\mathrm{A}}$. Due to the distortions, the polarizability is not a scalar quantity anymore but a tensor. For the further discussions, the polarizability is split into contributions parallel $\alpha_\parallel$ and perpendicular $\alpha_\perp$ to the interatomic axis resulting in [6].

$$\Delta\alpha(r) = \frac{\alpha_\parallel(r) + 2\alpha_\perp(r)}{3} - 2\alpha_0 \tag{3.16}$$

Furthermore, the polarizabilities α_0 of two unperturbed atoms is subtracted, which illustrates that the dipole induced polarizability tensor $\Delta\alpha(r)$ only includes additional contributions resulting from the interaction between both particles. Finally, an expression for $\Delta\alpha(r)$ can be retrieved under the assumption of point dipoles [6] in the so called dipole induced dipole model [40]:

$$\Delta\alpha(r) = \frac{4\alpha_0}{r^6} \tag{3.17}$$

The rapid decay due to the power of ten to the minus six with the interatomic distance is another verification for the smallness of the dielectric virial coefficients. Unfortunately,

calculations carried out with this simple expression do not agree with experimental results since long- and short range interactions are neglected in the dipole induced dipole model. The expression of the trace of the polarizability tensor given in equation 3.17 will always produce positive values for b_ϵ, while for instance helium has a negative value at ambient temperatures and below [3]. Therefore, quantum mechanical contributions have to be taken into account especially for light atoms and low temperatures. The first quantum mechanical expression for b_ϵ derived by Hill in 1958 [41] unfortunately did not converge to the semiclassical result for high temperatures. Moszynski *et al.* have shown that this was caused by approximating the internal electric field E_{int} with the external electric field E_{ext} [42]. They corrected the derivation by using the Lorentz equation relating external E_{ext} and internal electric field E_{int} and achieved this quantum mechanical expression:

$$b'(T) = \frac{kT}{3\epsilon_0} \left(\frac{\partial^2 B'(T, \boldsymbol{E}_{\text{ext}})}{\partial^2 \boldsymbol{E}_{\text{ext}}} \right) \tag{3.18}$$

However, in the most recent publications, two different approaches based on the semiclassical formula 3.15 but with quantum mechanical corrections are followed [43, 44]. These new computations are based on previously determined highly precise and quantum mechanical calculations of the interaction induced polarizabilities $\Delta\alpha(r)$ and pair potentials referenced in these publications. Results were obtained for helium as well as for argon. Further publications containing results on both gases are [45] and [46], whereas the first has to be highlighted due to the fact that they used a **F**ull **C**onfiguration **I**nteraction (FCI) approach. Theoretical computations for helium were also carried out by [34] and [47]. For argon, the group from Rostock presented a publication in 2010 [48].

The last time experimental work on the dielectric virial coefficients of helium and argon was performed is already three decades ago. Achtermann *et al.* and Huot *et al.* performed experiments on both gases in the early nineties [6, 49, 50]. Lallemand and Vidal also published results for both gases in 1977. Their work is of particular interest because they were going to very high pressures of 1000 MPa [51].

3.2. Theory of dielectric constant gas thermometry

DCGT is a method of primary thermometry that was first realized by Gugan and Michel in 1980 in England [52]. At PTB it is established since the beginning of the 1990s. A comprehensive review on the method can be found in reference [53]. Like in any other method of primary thermometry, a direct link between measurable quantities and temperature is required. For gas thermometers, the basis of all working equations is the ideal gas equation 3.1, whereas the different types differ in the way the hard to assess molar particle density ρ_{m} is determined. A short overview of alternative methods is given in subsection 3.2.1. In case of the DCGT, ρ_{m} is determined by measuring the dielectric constant ϵ_{r} with a capacitor and utilizing the virial expansion of the Clausius-Mosotti equation 3.10. A schematic

3. Theoretical background
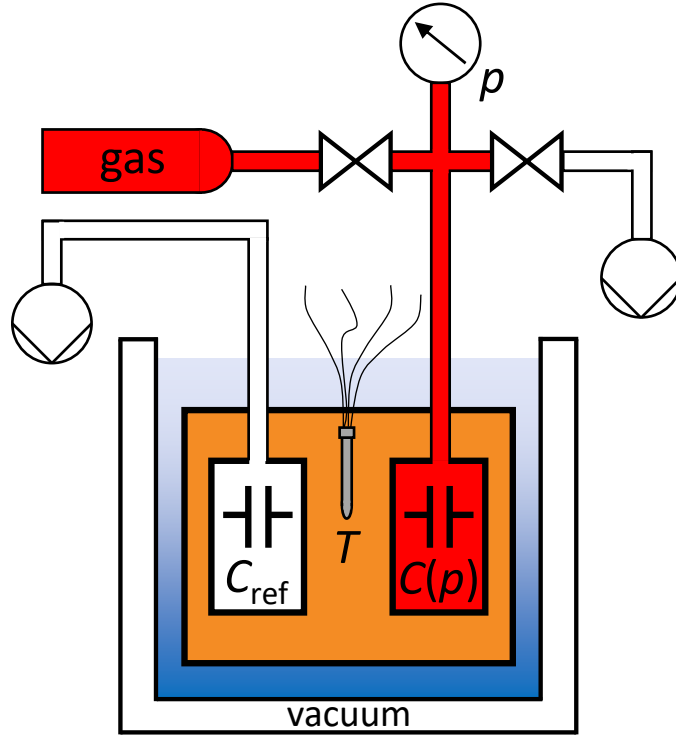
Figure 3.2.: Schematic view of a DCGT setup. The measuring cells are inside a massive copper block of temperature T that is submerged in a thermostat. Including a separate reference capacitor C_{ref} is optional but required for capacitance measurements of highest accuracy (see also section 4.3).

experimental setup is shown in figure 3.2.

For an ideal capacitor, the relative change in capacitance $C(p)$ at a pressure p with respect to the capacitance at vacuum $C(0)$ is connected to the dielectric constant ϵ_{r} by:

$$\frac{C(p) - C(0)}{C(0)} = \epsilon_{\text{r}} - 1 \tag{3.19}$$

For an ideal gas and an ideal capacitor without deformation, the dielectric constant from equation 3.19 can be used to assess the particle density with the Clausius-Mosotti equation 3.10. A working equation can then be derived by combination with the ideal gas law 3.1:

$$\frac{\epsilon_{\text{r}} - 1}{\epsilon_{\text{r}} + 2} = A_\epsilon \frac{p}{RT} \tag{3.20}$$

With this ideal formula, two measurements, one at vacuum and and one at pressure p, are sufficient for the determination of the thermodynamic temperature T. However, for a real experimental setup, the deformation of the capacitor under pressure needs to be taken into account, which is ensured by an effective compressibility κ_{eff}

$$\frac{C(p) - C(0)}{C(0)} = \epsilon_{\mathrm{r}} - 1 + \epsilon_{\mathrm{r}}\kappa_{\mathrm{eff}}p = \gamma \tag{3.21}$$

γ is the measured relative change of capacitance. Details on the determination of the effective compressibility, its influence on the capacitance measurement and the dependence on the capacitor type are given in section 5.1.1. Furthermore, the previously introduced deviations from the real gas in form of density and dielectric virial coefficients (equations 3.2 and 3.12) need to be taken into account. Initially, the working equation was derived for the determination of thermodynamic temperatures in the range between $4.2\,\mathrm{K}$ and $27.1\,\mathrm{K}$ [2, 52]. Effects of the deformation of the capacitor under pressure could therefore be neglected in the higher orders but have to be included for temperatures above $50\,\mathrm{K}$ and for the determination of virial coefficients [1, 53]. The derivation of the DCGT working equation used in this thesis is layed out in reference [1]. The extensive derivation of both working equations is carried out in appendix E. Basically, equations 3.2 and 3.12 need to be combined. To obtain a linear expression of p over powers of the dielectric measurement, the Clausius-Mosotti equation being in the denominator needs to be expanded into a Taylor series where powers higher than the order of two are truncated. The resulting equation can be simplified by defining a DCGT-working variable $\mu = \frac{\gamma}{\gamma+3}$ and is:

$$\begin{aligned}
p &= A_1\mu\left(1 + A_1 A_2\mu + A_1^2 A_3\mu^2 + A_1^3 A_4\mu^3 + ...\right) \\
A_1 &= \frac{1}{\frac{A_\epsilon}{RT} + \frac{\kappa_{\mathrm{eff}}}{3}} \\
A_2 &= \frac{1}{RT}(B(T) - b_\epsilon(T)) - \frac{\kappa_{\mathrm{eff}}}{3}\left(1 + \frac{B(T)}{A_\epsilon}\right) \\
A_3 &= \frac{1}{(RT)^2}\left[C(T) - c_\epsilon(T) - 2b_\epsilon(T)(B(T) - b_\epsilon(T))\right] \\
&\quad + \frac{\kappa_{\mathrm{eff}}}{3}\frac{1}{RT}\left[2A_\epsilon - 3(B(T) - b_\epsilon(T)) - \frac{1}{A_\epsilon}(2(B(T) - b_\epsilon(T))^2 + C(T))\right] \\
A_4 &= \frac{1}{(RT)^3}\left[D(T) - d_\epsilon(T) - 3b_\epsilon(T)C(T) - 2B(T)c_\epsilon(T)+\right. \\
&\quad \left. 5b_\epsilon(T)c_\epsilon(T) + 5(b_\epsilon(T))^2 B(T) - 2(b_\epsilon(T))^3\right] + \\
&\quad \frac{\kappa_{\mathrm{eff}}}{(RT)^2}\left[4A_\epsilon(B(T) - b_\epsilon(T)) - 2(B(T) - b_\epsilon(T))^2-\right. \\
&\quad \left. 6b_\epsilon(T)(B(T) - b_\epsilon(T)) + 3(C(T) - c_\epsilon(T))\right] + \\
&\quad \frac{\kappa_{\mathrm{eff}}}{(RT)^2}\frac{1}{A_\epsilon}\left[6b_\epsilon(T)(B(T) - b_\epsilon(T))^2 + (B(T) - b_\epsilon(T))(3c_\epsilon(T) - 5C(T))\right]
\end{aligned} \tag{3.22}$$

This form of the working equation allows to retrieve the temperature T from a series of isothermal pressure and capacitance measurements by evaluation of the constant fit coefficient A_1 without the need to know the virial coefficients. But it is also possible to retrieve other information from A_1. The same procedure has been used to determine the Boltzmann

constant for the redefinition of the SI by measurements at the triple point of water. From the molar gas constant $R = kN_A$, the Boltzmann-constant k was determined by using the Avogadro constant N_A [19]. Another option is to determine the effective compressibility κ_{eff} of a capacitor with a well known reference gas. Most important for the measurements presented in this thesis is the possibility to determine the molar polarizability A_ϵ, which is required to evaluate the dielectric virial coefficients from the expansion experiments (see section 3.4).

Evaluation of the higher fit coefficients of equation 3.22 allows to retrieve information on the virial coefficients as well. Since both, pressure and capacitance information is used, only sums and products of density and dielectric virial coefficients can be examined without the possibility to differ between them. Instead, the so called DCGT virial coefficients are defined.

$$
\begin{aligned}
B_{\text{DCGT}}(T) =& B(T) - b_\epsilon(T) \\
C_{\text{DCGT}}(T) =& C(T) - c\epsilon(T) - 2b_\epsilon(T)\left(B(T) - b_\epsilon(T)\right) \\
D_{\text{DCGT}}(T) =& D(T) - d_\epsilon(T) - 3b_\epsilon(T)C(T) - 2B(T)c_\epsilon(T)+ \\
& 5b_\epsilon(T)c_\epsilon(T) + 5(b_\epsilon(T))^2 B(T) - 2(b_\epsilon(T))^3 \\
& ...
\end{aligned}
\tag{3.23}
$$

If either the dielectric or density virial coefficient is known, the other one can in principle be calculated from the DCGT virial coefficient. However, since the dielectric virials are typically two orders of magnitude smaller than the density virial coefficients, their determination is only possible with large uncertainties by this method. This is further discussed in section 3.4. There has been a number of publications where DCGT and density virial coefficients of noble gases were retrieved from DCGT data, such as references [1–3, 54].

3.2.1. Alternative methods of gas thermometry

This subsection gives a short comparison of other gas thermometric methods that are currently part of the ITS-90 and its *Mise en Pratique* as well as their potential for the determination of virial coefficients. A detailed overview can be found in reference [55]. As mentioned before, all gas thermometers are based on the ideal gas equation 3.1 but differ in the form that the molar particle density ρ_{m} is determined.

In **C**onstant-**V**olume **G**as **T**hermometry (CVGT), the particle density is assessed by determination of the (constant) volume of the measuring chamber and the number of gas particles introduced in this chamber. The volume is typically determined by dimensional measurements or pycnometrically. The number of gas particles is typically assessed by measuring the weight of the cylinder containing the gas before and after filling the thermometer. Very accurate temperature measurements were for instance carried out by Berry to establish the low temperature scale NPL-75 for the temperature range from $2.6\,\text{K}$ to $27.1\,\text{K}$ [56]. The method is still used as an interpolation instrument in the low temperature range of the ITS-90 while it is typically not used as a primary thermometer at this point. The main

reason is the challenging determination of the absolute volume, which results in comparably high uncertainties. A viable option to reduce the uncertainty of the volume could be the assessment with microwave resonances, which is typically carried out in AGT measurements. That is why a certain potential for the direct determination of the density virial coefficients, especially in the low temperature range, can be assigned.

An AGT utilizes the relation between the speed of sound u_0 and the thermodynamic temperature of a gas, which is given by:

$$u_0 = \left(\frac{c_p}{c_V} \frac{RT}{M} \right)^{\frac{1}{2}} \tag{3.24}$$

where $\frac{c_p}{c_V}$ is the ratio between the specific heat capacity at constant pressure p and at constant volume V while M is the molar mass of the measuring gas. A comprehensive overview of the method is given in [31]. In analogy to the density and dielectric virial coefficients, the speed of sound of a real gas u is given by a virial expansion:

$$u^2 = u_0^2(1 + B_u(T)p + C_u(T)p^2 + ...) \tag{3.25}$$

with $B_u(T)$, $C_u(T)$,... being the acoustic virial coefficients. Since pressure does only play a role as a second order effect, the uncertainties achievable with AGT are currently the lowest compared to other primary thermometry methods. This thermometer has been widely used by the NMIs of France, Great Britain and Italy for the determination of the Boltzmann-constant for the redefinition of the unit kelvin and the new SI. Though AGT features the lowest uncertainties with less than 1 ppm for the determination of the Boltzmann constant, the relation between the acoustic virial coefficients and the density virial coefficients is more complicated limiting the potential to be used for the determination of the latter [57]:

$$B_u(T) = 2B(T) + 2\left(\frac{c_p}{c_V} - 1 \right) T \left(\frac{dB}{dT} \right) + \frac{\left(\frac{c_p}{c_V} - 1 \right)^2}{\frac{c_p}{c_V}} T^2 \frac{d^2B}{dT^2} \tag{3.26}$$

The principle of a RIGT is very similar to the DCGT, but instead of the dielectric constant the refractive index n of a gas is measured [58]. The working equation is very similar in structure but based on the Lorentz-Lorenz equation D.1 (see appendix D), which turns into the Clausius-Mosotti equation for vanishing frequencies. Due to the similarity, these two thermometers form the group of polarizing gas thermometry. RIGT is typically performed in two different manners. Originally, interferometers were used to assess the refractive index of the measuring gas at optical wavelengths. This is accompanied by a variety of experimental challenges. First, the demands to understand the deformation of the measuring equipment under pressure are enormous and difficult. This problem is increased by the fact that the

used optical materials are often highly anisotropic. The same accounts for the influence of thermal gradients that change the dimensions of the refractometers. Therefore, typically calibration measurements are performed, for instance with helium. As mentioned in section 2.2, the drawback of helium is its permeation into certain optical materials, which again complicates these calibrations. There are further experimental challenges in the mechanical construction when higher gas pressures are targeted. That is why May *et al.* proposed to use quasi-spherical cavity resonators to measure the refractive index in the microwave range in 2004 [59]. Measurements up to 7 MPa have already been demonstrated [60]. The intended unideal shape of the resonator as a triaxial ellipsoid splits up the otherwise triply-degenerate eigen-frequencies of an ideal cavity, which allows to assess the frequencies with high precision. Relative uncertainties for the determination of the Boltzmann constant were in the order of 10 ppm, whereas one of the main uncertainty contributions is again the deformation of the cavity under pressure. Still, this method is in principle also promising for the determination of coupled density and refractive index virial coefficients. The latter are nearly equal to the dielectric virial coefficients for the low frequencies of microwaves. Still, it should be mentioned that in contrast to electrostatic experiments the very small magnetic polarizability A_μ needs to be taken into account for these experiments. May *et al.* actually used this aspect to determine the magnetic susceptibility of oxygen by coupled measurements analyzing the gas simultaneously in a quasi-spherical cavity resonator and a capacitor [61].

3.3. The Burnett method

To determine the density virial coefficients, it is in principle possible to measure ratios of pressure and particle density, which can then be fitted by a polynomial equation to obtain the coefficients the way they are defined in equation 3.2. As mentioned before, the particle density is typically difficult to measure. Burnett had the idea to assess particle density ratios rather than to determine the absolute particle density in 1936 [4]. The working principle, data evaluation as well as progress made since then are presented in the next section. The disadvantage of this original approach is that a highly precise pressure measurement typically has to be realized with a differential pressure membrane separating the isothermal measuring vessels from bulky pressure standards like mercury u-tube manometers or pressure balances at ambient conditions. This requires time consuming manual operation and only offers limited potential for automation. Therefore, an approach was made by Sakoda *et al.* in 2012 to use an absolute pressure transducer, which is kept at a constant temperature different from the measuring temperature [62, 63]. In subsection 3.3.3, their work as well as the derivation of the final working equation used in this thesis will be presented.

Generally, the popularity of the Burnett method dropped after improvements in magnetic suspension couplings allowed the development of very accurate sinker densimeters in the middle eighties [64]. A comprehensive overview of of these instruments is, for instance, given in [65] and [66]. They can directly measure the density of a fluid by applying the buoyancy principle to one or more appropriate sinkers located inside the fluid at a certain

pressure and temperature. The selected sinker is linked to an accurate balance outside the thermalized experimental volume by the magnetic coupling. If two sinkers of same mass and surface area (and ideally same surface material) but different volumes are used, many distorting effects, for instance buoyant forces on the suspension and wires of the sinkers or adsorption, vanish [67]. The density of the fluid can then be determined from the measured mass difference divided by the volume difference of the sinkers. Relative uncertainties for the density measurement in the order $0.01\,\%$ ($k = 2$) can typically be achieved. Recently, the potential of the method has been further developed to investigate sorption effects at the dew point, which is particularly interesting for gas mixtures since the composition of the fluid phase changes [68, 69]. Therefore, specially designed sinkers with equal mass and volume but different surface area were used. The drawback of these sinkers is that the uncertainty of the determined densities rises, which is why a four-sinker densimeter for the investigation of sorption effects combined with a precise measurement of density was developed [70].

3.3.1. Ideal Burnett expansion

In its simplest form, a Burnett apparatus consist of two volumes kept at constant temperature T_{iso} that are separated by an expansion valve V_{exp} as depicted in figure 3.3. Volume V_A is filled by opening valve V_{in} and the initial pressure is measured while V_{exp} is closed and volume V_B is evacuated. Then, the gas is expanded into V_B by opening valve V_{exp}. The pressure is measured again before V_{exp} is closed and cell B is evacuated by opening V_{out}. This process is repeated until a sufficient number of measuring points has been taken. In the original publication by Burnett an error prone iterative approach including two extrapolations was used to evaluate the data [4]. It is shortly summarized here, since it will be required in section 3.3.3 for the evaluation of strategies reported in the literature to include dead volumes at temperatures different from the measuring temperature [4, 62].
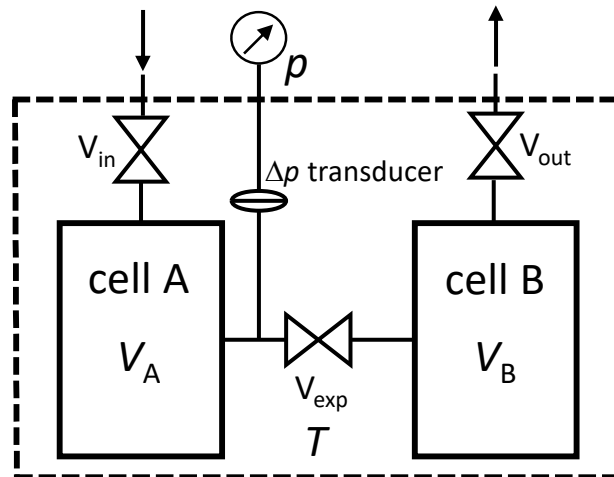

Figure 3.3.: A simple Burnett apparatus with two volumes V_A and V_B separated by an expansion valve V_{exp}. Components inside the thermostat (dashed line) are thermally stabilized to temperature T. The pressure measurement at ambient conditions is enabled by a differential pressure transducer.

3. Theoretical background

From equation 3.2, the ratio of pressures $\frac{p_r}{p_{r+1}}$ before and after expansion $r+1$ relate by:

$$\frac{p_r}{p_{r+1}} = \frac{V_A + V_B}{V_A}\frac{Z_r}{Z_{r+1}} = Q\frac{Z_r}{Z_{r+1}} \tag{3.27}$$

where Q is the apparatus constant, which is defined only by the volumes of the vessels. After an infinite number of expansions, the gas will be highly diluted reaching ideal gas behavior resulting in compressibility factors of $Z_r = Z_{r+1} = 1$, as defined in equation 3.3. Thus, extrapolating the values of $\frac{p_r}{p_{r+1}}$ over p_r to $p_r = 0$ results directly in Q as the intercept with the Y-axis. Generalizing equation 3.27 results in:

$$\prod_{r=0}^{j}\frac{p_r}{p_{r+1}} = \prod_{r=0}^{j} Q_r\frac{Z_r}{Z_r+1} \tag{3.28}$$

Utilizing, again, the fact that $Z_r = 1$ after an infinite number of expansions, the initial compressibility factor Z_0 can be determined for the known starting pressure p_0 by an extrapolation of the products $p_r Q_1 Q_2...Q_r$ over p_r towards $p_r = 0$. The intermediate compressibility factors Z_r may then be calculated by equation 3.28. Fitting Z_r either over p_r or $\rho_r = \frac{p_r}{Z_r RT}$ with a polynomial of appropriate order, the pressure or density virial coefficients are the respective fit coefficients. The benefit of this routine is that corrections to the apparatus constant Q_r, for instance due to pressure caused deformations, can be easily implemented for each pressure p_r. The role of the apparatus constant is extensively discussed in section 5.2. Anyway, this iterative approach is mostly not used anymore. The data evaluation was topic of numerous papers throughout the years, whereas the current standard procedure is to directly fit a polynomial equation to the ratios $\frac{p_r}{p_{r+j}}$ over p_r [71, 72]. For an ideal setup, as depicted in 3.3, it is shown in appendix F.1 that the following equation can be retrieved neglecting the deformation of the cells under pressure:

$$\begin{aligned}
\frac{p_r}{p_{r+j}} =& Q^j + (Q^j - 1)\frac{B(T)}{RT}\cdot p_r + \frac{(Q^j - Q^{-j})}{(RT)^2}(C(T) - (B(T))^2)\cdot p_r^2 + \\
& \frac{1}{(RT)^3}\left[\left(\frac{1}{Q^j} - \frac{1}{Q^{2j}}\right)(B(T)C(T) - (B(T))^3) + \right. \\
& \left. \left(Q^j - \frac{1}{Q^{2j}}\right)(D(T) - 3C(T)B(T) - 2(B(T))^3)\right]\cdot p_r^3 + ...
\end{aligned} \tag{3.29}$$

Fitting equation 3.29 with a polynomial of the required order $\frac{p_r}{p_{r+j}} = K_0 + K_1\cdot p_r + K_2\cdot p_r^2 + K_3\cdot p_r^3...$ leads to the following relations for the properties of interest:

$$Q = K_0^{\frac{1}{j}}$$

$$B(T) = \frac{K_1 RT}{Q^j - 1} = \frac{K_1 RT}{K_0 - 1}$$

$$C(T) = \frac{K_2 (RT)^2}{Q^j - Q^{-j}} + (B(T))^2$$

$$D(T) = \frac{K_3 (RT)^3 - \left(Q^{-j} - Q^{-2j}\right)\left(B(T)C(T) - (B(T))^3\right) + 3C(T)B(T) + 2(B(T))^3}{Q^j - Q^{-2j}}$$

$$(3.30)$$

The order of the polynomial is of key importance for the data evaluation and basically predefined by the magnitude of the virial coefficients. Since the influence of the higher orders rises with pressure, one has to carefully estimate which is the highest order that contributes significantly and select the order of the fit accordingly. This opens the conflict that on the one hand lower fit orders have lower uncertainties, but may on the other hand deliver wrong results if the order is too low. Furthermore, the number of data points has to be sufficient to apply higher fit orders. A detailed discussion of the fit orders required and used in this thesis is given in section 3.6. Typically, j is chosen to be 1, which means that consecutive measurement values are used to calculate the ratios. Equation 3.30 illustrates one important advantage of the Burnett method. Complicated volume measurements are not required, since the apparatus constant Q is directly determined from the fit coefficients. Burnett and several others used a smart experimental design with double walled vessels, where pressure is applied from the inside as well as from the outside [4]. This way, the influence of deformation is reduced to the volume change due to compression and was neglected allowing to utilize this formula.

3.3.2. Isothermal Burnett expansion with deformation

For the work carried out in this thesis, it is beneficial to include the pressure deformation of the measuring cells directly in the working equation, which is used to fit the data. Again, the isothermal expansion from the filled cell A with volume $V_A(1 + \lambda_A p)$ into evacuated cell B with volume $V_B(1 + \lambda_B p)$ is considered. λ_A and λ_B are the pressure deformation coefficients of cell A and cell B respectively, whereas V_A and V_B now denote the corresponding volumes without pressure deformation. The following derivation is carried out utilizing the pressure virial coefficients defined in equation 3.4. With the number of particles being the same at expansion r and after expansion $r + 1$, the starting point for the derivation is:

$$\frac{p_r V_A (1 + \lambda_A p_r)}{(1 + B_p(T)p_r + C_p(T)p_r^2 + D_p(T)p_r^3 ...)} = \frac{p_{r+1}(V_A(1 + \lambda_A p_{r+1}) + V_B(1 + \lambda_B p_{r+1}))}{(1 + B_p(T)p_{r+1} + C_p(T)p_{r+1}^2 + D_p(T)p_{r+1}^3 ...)}$$

$$(3.31)$$

Solving this equation and similar ones in the sections ahead always follows the same pat-

tern. The starting equation is defined utilizing the conservation of the number of particles before and after the expansion. Then, the measured quantity after the expansion, in this case p_{r+1}, is replaced by introducing the ratio $P_{\text{ratio},r} = \frac{p_r}{p_{r+1}}$. The resulting equation is solved for the ratio $P_{\text{ratio},r}$ and the result is rearranged as a power series of p_r. This expression is fitted with a polynomial and the target quantities are retrieved from the fit coefficients. The equations generally become very complex with higher orders or by including more corrections which is why all derivations were carried out utilizing the program Mathematica 12.0 (Wolfram Research). The further steps to solve equation 3.31 are shown in appendix F.2 with the final result being:

$$
\begin{aligned}
P_{\text{ratio},r} = & Q + (Q-1)\left(\frac{B(T)}{RT} + \frac{1}{Q}(\lambda_\text{B} - \lambda_\text{A}(Q+1))\right) \cdot p_r + \\
& \left[\frac{C(T) - B^2(T)}{(RT)^2}\left(Q - \frac{1}{Q}\right) + Q\lambda_\text{A}\left(\lambda_\text{A} - \frac{B(T)}{RT}\right) + \right. \\
& \left. \frac{1}{Q}\left(\frac{B(T)}{RT}\left(\frac{\lambda_\text{A}}{Q} + \lambda_\text{B}\left(1 - \frac{1}{Q}\right)\right) - \left(\frac{\lambda_\text{A}}{Q} + \lambda_\text{B}\left(1 - \frac{1}{Q}\right)\right)^2\right)\right] \cdot p_r^2 + ..
\end{aligned}
\tag{3.32}
$$

Fitting equation 3.32 with a polynomial of the required order $\frac{p_r}{p_{r+1}} = K_0 + K_1 \cdot p_r + K_2 \cdot p_r^2 + ...$ leads to the following relations for the properties of interest:

$$
\begin{aligned}
Q = & K_0 \\
B(T) = & \frac{K_1 RT}{K_0 - 1} - \frac{RT}{Q}(\lambda_\text{B} - \lambda_\text{A}(Q+1)) \\
C(T) = & \frac{(RT)^2}{Q - \frac{1}{Q}}\left[K_2 - Q\left(\lambda_\text{A}^2 - \frac{\lambda_\text{A} B(T)}{RT}\right) - \right. \\
& \left. \frac{1}{Q}\left(\frac{B}{RT}\left(\frac{\lambda_\text{A}}{Q} + \lambda_\text{B}\left(1 - \frac{1}{Q}\right)\right) - \left(\frac{\lambda_\text{A}}{Q} + \lambda_\text{B}\left(1 - \frac{1}{Q}\right)\right)^2\right)\right] + (B(T))^2
\end{aligned}
\tag{3.33}
$$

For vanishing deformations, these coefficients are equal to the ones given in equation 3.30. To compare the final working equation used in this work to the result shown here, the derivation was repeated with the additional volumes and deformation coefficients of the gas-handling system shown schematically in figure 3.5. The results are included in appendix F.2 as well. Further discussion and details on how the deformation was determined in this work is given in section 4.1.4.

The isothermal Burnett method was used widely until the nineteen eighties to determine density virial coefficients of pure fluids but also mixtures [73–77]. High precision measurements were for instance carried out by Waxman and Hastings at NIST with argon and krypton [78]. A number of highly accurate measurements by Jaeschke and Co-workers is referenced in the GERG2004 monograph [79]. Further work on different natural gas mixtures was published in 1997 by Hwang *et al.* [80]. As already explained in the introduction of this chapter, the method became less popular with the rise of highly precise densimeters [65].

3.3.3. Burnett expansion with dead volumes at different temperature

The group around Sakoda still further developed the method by application of an absolute pressure transducer placed outside of the thermostat, instead of using a differential pressure transducer simplifying the experimental effort [62, 81, 82]. This way, automated experiments at high pressures and temperatures are possible. The challenge is that the pressure transducer has to be kept at a constant temperature which is different from the measurement temperature introducing a dead volume at different temperature. Their experimental setup is shown in figure 3.4.
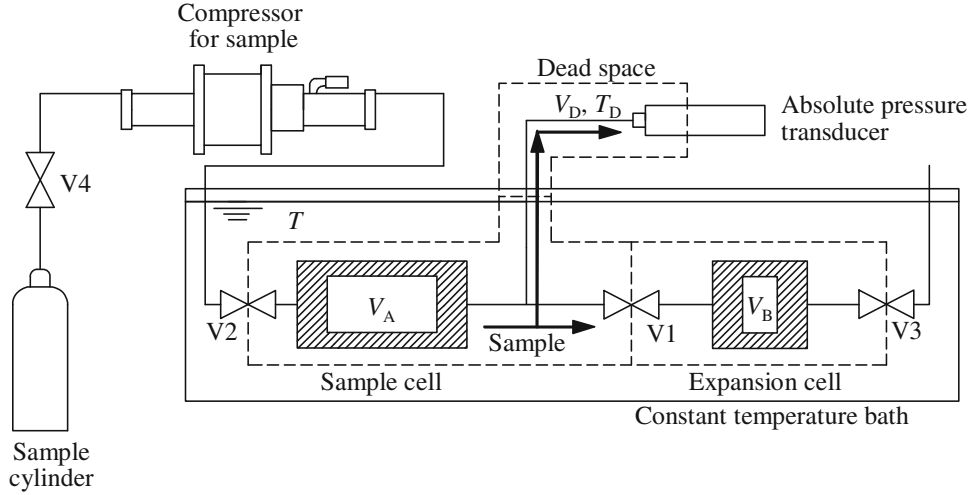
Figure 3.4.: This picture of the experimental setup used by Sakoda *et al.* was taken from the reference [62].

To evaluate the data, the authors adapted the iterative approach of the ideal expansion presented in section 3.3.1. Since the additional Volume V_D is included as dead space at a temperature T_D, first, an overall apparatus constant Q_r was defined by:

$$Q_r = (1 + Q_{\text{B}}) \frac{1 + \frac{Q_{\text{D}}}{1 + Q_{\text{B}}} \frac{T}{T_{\text{D}}} \frac{Z_{r+10}}{Z_{\text{D},r+1}}}{1 + Q_{\text{D}} \frac{T}{T_{\text{D}}} \frac{Z_r}{Z_{\text{D},r+1}}} \tag{3.34}$$

Where $Q_{\text{D}} = \frac{V_{\text{D}}}{V_{\text{A}}}$ and $Q_{\text{B}} = \frac{V_{\text{B}}}{V_{\text{A}}}$ are ratios defined by the volumes. To evaluate the data, they first carried out calibration measurements with a well known reference gas, in their case nitrogen, to determine Q_{D} and Q_{B}. From the measured pressure ratios, the compressibility factor Z_r is first determined neglecting the different temperature T_{D} in V_{D} by the iterative approach described in subsection 3.3.1. Next, the apparatus constant $Q_{r,\text{initial}}$ is calculated by formula 3.34 with initial values for Q_{B} and Q_{D}, while the compressibility factors for the dead volume $Z_{\text{D},r}$ and $Z_{\text{D},r+1}$ are calculated from an EOS. $Q_{r,\text{initial}}$ is used to determine Z_0 and Z_r by the iterative approach for the standard Burnett method. These values are, in turn, used to recalculate $Q_{r,\text{new}}$ by equation 3.34, which is then compared to the initial value

3. Theoretical background

$Q_{r,\text{initial}}$. In case the deviation is larger than the tolerance, the recalculated value of $Q_{r,\text{new}}$ is used as new $Q_{r,\text{initial}}$ value and the process is repeated. These iterations are carried out until the deviation between $Q_{r,\text{initial}}$ and $Q_{r,\text{new}}$ are smaller than the specified tolerance. This way, Q_r can be determined together with the corresponding compressibility factors and, thus, average density. Though Q_r is now known, the individual values of Q_D and Q_B still have to be determined. This is realized by performing a non-linear least squares fit algorithm. The sum of squares are calculated for the differences between the particle density ρ_N determined from Q_r and the one calculated by an EOS for the corresponding temperatures. The fitting is carried out via the derivatives $\frac{\partial \rho_N}{\partial Q_B}$ and $\frac{\partial \rho_N}{\partial Q_D}$ by adapting the amount of particles N_B and N_D in the different parts of the system. These values are then used to recalculate the particle density. This process is repeated until the measured particle density and the one from the EOS coincide. With the now fix numerical values for Q_B and Q_D, the pressure ratios from an unknown gas may be evaluated. The first temperature to be measured is T_D to assess Z_D.

To avoid the iterative approach, a new working equation has been derived in this work, which allows to directly fit the data. Furthermore, dead volumes at different temperatures are not only considered for the sample but also for the expansion part of the system. This is due to the design of the apparatus, which is schematically shown in figure 3.5 and explained in more detail in section 4.1.
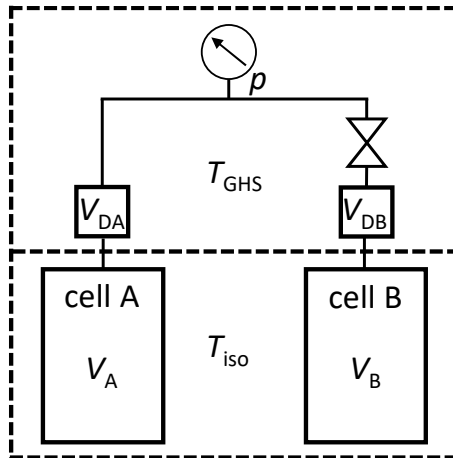
Figure 3.5.: Simplified scheme of the volumes and two different thermal regimes (separated by the dashed line) of the current apparatus.

While the measuring cells A and B are stabilized at the temperature T_{iso}, the dead volumes V_{DA} and V_{DB} of the gas-handling system and the pressure measurement are stabilized at the temperature T_{GHS}. For the derivation, it is assumed that the temperature change at the border in between both temperature regimes can be described by a step function leading to the starting equation:

$$\frac{p_r V_A}{T_{\text{iso}}(1 + B_{p,\text{iso}}p_r + C_{p,\text{iso}}p_r^2 + ...)} + \frac{p_r V_{DA}}{T_{\text{GHS}}(1 + B_{p,\text{GHS}}p_r + C_{p,\text{GHS}}p_r^2 + ...)} =$$
$$\frac{p_{r+1}(V_A + V_B)}{T_{\text{iso}}(1 + B_{p,\text{iso}}p_{r+1} + C_{p,\text{iso}}p_{r+1}^2 + ...)} + \frac{p_{r+1}(V_{DA} + V_{DB})}{T_{\text{GHS}}(1 + B_{p,\text{GHS}}p_{r+1} + C_{p,\text{GHS}}p_{r+1}^2 + ...)}$$

$$(3.35)$$

The further steps of the derivation are carried out in appendix F.3. A closed solution can only be obtained if virial coefficients of order three and higher are neglected. In this case, a solution is given by:

$$\frac{p_r}{p_{r+1}} = K_0 + K_1 p_r + K_2 p_r^2 + ...$$
$$K_0 = 1 + \frac{T_{\text{iso}}V_{DB} + T_{\text{GHS}}V_B}{T_{\text{iso}}V_{DA} + T_{\text{GHS}}V_A} = Q_{\Delta T}$$
$$\frac{K_1}{K_0 - 1} = \frac{B_{\text{iso}}}{RT_{\text{iso}}}\left(\frac{1}{1 + \frac{T_{\text{iso}}}{T_{\text{GHS}}}\frac{V_{DA}}{V_A}} - \frac{1}{1 + \frac{T_{\text{iso}}}{T_{\text{GHS}}}\frac{V_{DB}}{V_B}} + \frac{1}{1 + \frac{T_{\text{iso}}}{T_{\text{GHS}}}\frac{(V_{DA}+V_{DB})}{(V_A+V_B)}}\right) +$$
$$\frac{B_{\text{GHS}}}{RT_{\text{GHS}}}\left(1 - \frac{1}{1 + \frac{T_{\text{iso}}}{T_{\text{GHS}}}\frac{V_{DA}}{V_A}} + \frac{1}{1 + \frac{T_{\text{iso}}}{T_{\text{GHS}}}\frac{V_{DB}}{V_B}} - \frac{1}{1 + \frac{T_{\text{iso}}}{T_{\text{GHS}}}\frac{(V_{DA}+V_{DB})}{(V_A+V_B)}}\right)$$

$$(3.36)$$

The solution given here is valid to calculate the second density virial cofficient since including higher orders in the starting equation would as well only contribute to higher orders. The coefficient K_0 results in the ideal apparatus constant Q, which was defined in equation 3.30, if T_{GHS} approaches T_{iso}. That is why K_0 is treated as an artificial, temperature dependent apparatus constant $Q_{\Delta T}$ similar to the one used by Sakoda *et al.* (see equation 3.34). This analogy is also used to derive a descriptive expression for the calculation of the second density virial coefficient by calculating $\frac{K_1}{K_0-1}$, again in analogy to the ideal case described in equation 3.30. Instead of using absolute volumes and temperatures, it is beneficial to express equation 3.36 utilizing the following volume and temperature ratios, which are used throughout this thesis:

$$T_{\text{ratio}} = \frac{T_{\text{iso}}}{T_{\text{GHS}}}$$

$$Q_{\text{A}} = \frac{V_{\text{DA}}}{V_{\text{A}}}$$

$$Q_{\text{B}} = \frac{V_{\text{DB}}}{V_{\text{B}}}$$

$$Q^* = \frac{V_{\text{A}}}{V_{\text{B}}} \tag{3.37}$$

$$Q = \frac{V_{\text{A}} + V_{\text{B}} + V_{\text{DA}} + V_{\text{DB}}}{V_{\text{A}} + V_{\text{DA}}} = 1 + \frac{1}{Q^*}\frac{(1+Q_{\text{B}})}{(1+Q_{\text{A}})}$$

$$Q_{\Delta T} = 1 + \frac{1}{Q^*}\frac{1+T_{\text{ratio}}Q_{\text{B}}}{1+T_{\text{ratio}}Q_{\text{A}}} = Q + (Q-1)\frac{(Q_{\text{A}}-Q_{\text{B}})(1-T_{\text{ratio}})}{(1+Q_{\text{B}})(1+T_{\text{ratio}}Q_{\text{A}})}$$

With these ratios, the term for the second virial coefficient of equation 3.36 can be expressed as:

$$\frac{K_1}{K_0 - 1} = \frac{B_{\text{iso}}}{RT_{\text{iso}}}\left(\frac{1}{1+T_{\text{ratio}}Q_{\text{A}}} - \frac{1}{1+T_{\text{ratio}}Q_{\text{B}}} + \frac{1}{1+T_{\text{ratio}}\frac{Q^*Q_{\text{A}}+Q_{\text{B}}}{Q^*+1}}\right) +$$

$$\frac{B_{\text{GHS}}}{RT_{\text{GHS}}}\left(1 - \frac{1}{1+T_{\text{ratio}}Q_{\text{A}}} + \frac{1}{1+T_{\text{ratio}}Q_{\text{B}}} - \frac{1}{1+T_{\text{ratio}}\frac{Q^*Q_{\text{A}}+Q_{\text{B}}}{Q^*+1}}\right) \tag{3.38}$$

3.3.4. Final working equation of the Burnett expansion

To evaluate the measured data in this thesis, the pressure deformation as well as the dead volumes at a different temperature have to be considered at the same time. In analogy to previous sections and using the same declarations, the starting point for the derivation is:

$$\frac{p_r V_{\text{A}}(1+\lambda_{\text{A}}p_r)}{T_{\text{iso}}(1+B_{p,\text{iso}}p_r+C_{p,\text{iso}}p_r^2+...)} + \frac{p_r V_{\text{DA}}(1+\lambda_{\text{GHS}}p_r)}{T_{\text{GHS}}(1+B_{p,\text{GHS}}p_r+C_{p,\text{GHS}}p_r^2+...)} =$$

$$\frac{p_{r+1}(V_{\text{A}}(1+\lambda_{\text{A}}p_{r+1})+V_{\text{B}}(1+\lambda_{\text{B}}p_{r+1}))}{T_{\text{iso}}(1+B_{p,\text{iso}}p_{r+1}+C_{p,\text{iso}}p_{r+1}^2+...)} + \frac{p_{r+1}(V_{\text{DA}}+V_{\text{DB}})(1+\lambda_{\text{GHS}}p_{r+1})}{T_{\text{GHS}}(1+B_{p,\text{GHS}}p_{r+1}+C_{p,\text{GHS}}p_{r+1}^2+...)} \tag{3.39}$$

In this equation $\lambda_{\text{DA}} = \lambda_{\text{DB}} = \lambda_{\text{GHS}}$ is used, since the gas-handling system is made of the same tubing. The further derivation is carried out in appendix F.4, whereas the final result used for the evaluation of the pressure data in this thesis is:

$$\frac{p_r}{p_{r+1}} = K_0 + K_1 p_r + K_2 p_r^2 + ...$$

$$K_0 = Q_{\Delta T}$$

$$\frac{K_1}{K_0 - 1} = \frac{B_{\text{iso}}}{RT_{\text{iso}}} \left[\frac{1}{1 + T_{\text{ratio}}Q_A} - \frac{1}{1 + T_{\text{ratio}}Q_B} + \frac{1}{1 + T_{\text{ratio}}\frac{(Q_B + Q_A Q^*)}{(1+Q^*)}} \right] +$$

$$\frac{B_{\text{GHS}}}{RT_{\text{GHS}}} \left[1 - \frac{1}{1 + T_{\text{ratio}}Q_A} + \frac{1}{1 + T_{\text{ratio}}Q_B} - \frac{1}{1 + T_{\text{ratio}}\frac{(Q_B + Q_A Q^*)}{(1+Q^*)}} \right] +$$

$$\lambda_B \left[\frac{1}{Q_{\Delta T}} \left(\frac{1}{1 + T_{\text{ratio}}Q_B} \right) \right] +$$

$$\lambda_A \left[\left(\frac{1}{Q_{\Delta T}} - 1 \right) \frac{Q^*}{1 + T_{\text{ratio}}Q_B} - \frac{1}{1 + T_{\text{ratio}}Q_A} \right] +$$

$$\lambda_{\text{GHS}} \left[\frac{1}{Q_{\Delta T}} \frac{1}{\left(1 + \frac{1}{T_{\text{ratio}}Q_B}\right)} - \frac{1}{1 + \frac{1}{T_{\text{ratio}}Q_A}} + \left(\frac{1}{Q_{\Delta T}} - 1 \right) \frac{Q_A Q^*}{Q_B + \frac{1}{T_{\text{ratio}}}} \right]$$

$$(3.40)$$

This equation exhibits a certain elegance. The terms including the density virial coefficients are identical to the ones retrieved in the previous section for the case of two different temperature regimes neglecting the deformation (equation 3.38). The terms including the deformations can be compared to the ones for the isothermal case depicted in appendix F.2 in equation F.14. The isothermal equation there gives the result shown here if the ideal apparatus constant Q is replaced with the apparent apparatus constant $Q_{\Delta T}$ and if the volume ratios Q_A and Q_B are multiplied with the temperature ratio T_{ratio}. Equation 3.40 thus exactly represents both cases derived separately in the two previous sections. A further evaluation of this final working equation and a comparison to the equations for the dielectric expansion, which will be retrieved in the next section, is carried out in section 3.5.

3.4. Dielectric expansion experiments

After Buckingham *et al.* developed the theoretical basis for the relation between dielectric properties and particle densities of fluids in the nineteen fifties [40, 83], interest in the determination of the very small second dielectric virial coefficient rised. First experimental attempts were made by measuring the dielectric constant and pressure together with a determination of the particle density from an EOS. This is in principal the same as to evaluate the measured values by means of the following formula, which can simply be derived by substituting the particle density in the Clausius-Mosotti equation 3.12 with the pressure virial expansion 3.4:

$$\frac{\epsilon_r - 1}{\epsilon_r + 2} = A_\epsilon \left(\frac{p}{RT} \right) + (b_\epsilon(T) - A_\epsilon B_p(T)) \left(\frac{p}{RT} \right)^2 + ... \tag{3.41}$$

3. Theoretical background

Measured dielectric constants and pressures can be fitted and $b_\epsilon(T)$ can be determined from the linear term when the second density virial coefficient is known. The key problem is that uncertainties in the order of few percent in $B(T)$ already lead to uncertainties in the order of $100\,\%$ in $b_\epsilon(T)$ due to $b_\epsilon(T)$ being roughly two orders of magnitude smaller [84]. A new approach was undertaken in 1960 by Johnston and co-workers [85]. They adapted the Burnett method presented in the previous section 3.3 to dielectric measurements by equipping a measuring vessel with a plate capacitor. Their ideal approach is presented in the next section 3.4.1. Compared to the Burnett method, much more experimental modifications were implemented through the time to reach acceptable uncertainties for the small dielectric virial coefficients. An overview about these efforts is given in appendix G.2. Non of the previously carried out works did include dead volumes at different temperatures as required for the data evaluation in this thesis. These issues and the corresponding working equations are discussed in the following sections.

3.4.1. Ideal dielectric expansion

Johnston, Orcutt and Cole carried out dielectric measurements with Burnett like expansions and published results for the dielectric virial coefficients of several gases in 1962 and 1965 [5, 86]. The experimental setup is equal to the Burnett setup shown in figure 3.3 with the difference that a capacitor is included in volume V_A. The derivation of the working equation for this ideal system, neglecting the deformation of the vessels under pressure, follows the routine presented in 3.3.1 for the density virial coefficients and is shown in appendix G.1. The starting equation is based on the Clausius-Mosotti equation 3.12 with the final result being:

$$F_{\text{ratio},r} = \frac{f_r}{f_{r+j}} = Q^j + \frac{(Q^j - 1)}{A_\epsilon} b_\epsilon(T) f_j + \frac{(Q^j - Q^{-j})}{A_\epsilon^2} \left(c_\epsilon(T) - b_\epsilon^2(T) \right) f_j^2 + ... \quad (3.42)$$

In this equation, the ratios of the Mosotti-terms after r and $r + j$ expansions $F_{\text{ratio},r}$ are plotted over the initial Mosotti term f_r. The data is then fitted with a polynomial of the required order $F_{\text{ratio},r} = D_0 + D_1 \cdot f_r + D_2 \cdot f_r^2 + ...$ which gives the following relations:

$$
\begin{aligned}
Q &= D_0^{\frac{1}{j}} \\
b_\epsilon(T) &= \frac{D_1 A_\epsilon}{Q^j - 1} \\
c_\epsilon(T) &= \frac{D_2 A_\epsilon^2}{Q^j - Q^{-j}} + b_\epsilon^2(T)
\end{aligned}
\quad (3.43)
$$

There are two key challenges of this method. One is the determination of the apparatus constant Q, which has to be carried out with a relative uncertainty of a few **P**arts **P**er **M**illion (ppm) to achieve relative uncertainties for $b_\epsilon(T)$ in the order of percent. This topic is discussed in more detail in section 5.2. Experimental adaptions intended to target this

issue are summarized in appendix G.2. The other challenge is that the dielectric virials always appear in combination with the molar polarizability A_ϵ, which has to be determined by additional experiments in case no reliable literature values are available. In previous methods, rough determinations of A_ϵ were carried out from a pressure measurement after the expansion cycles had finished. In the setup presented in this thesis, A_ϵ is directly determined from the DCGT data evaluation with relative uncertainties in the order of 25 ppm (see sections 3.2 and 5.1.3 for details).

3.4.2. Isothermal dielectric expansion with deformation

In analogy to section 3.3.2, another working equation, which includes the deformation of the vessels, is derived. The starting equation is formulated using the Mosotti virial coefficients defined in equation 3.13:

$$\frac{f_r V_A (1 + \lambda_A p_r)}{A_\epsilon \left(1 + b_{CM}(T) f_r + c_{CM}(T) f_r^2 + ...\right)} = \frac{f_{r+1} \left(V_A (1 + \lambda_A p_{r+1}) + V_B (1 + \lambda_B p_{r+1})\right)}{A_\epsilon \left(1 + b_{CM}(T) f_{r+1} + c_{CM}(T) f_{r+1}^2 + ...\right)}$$

(3.44)

The further derivation is carried out in appendix G.3 with the final result being:

$$F_{\text{ratio},r} = Q + (Q-1) \left(\frac{b_\epsilon(T)}{A_\epsilon} + \frac{RT}{A_\epsilon} \frac{1}{Q} (\lambda_B - \lambda_A (Q+1)) \right) \cdot f_r +$$
$$\left[\frac{c_\epsilon(T) - b_\epsilon^2(T)}{A_\epsilon^2} \left(Q - \frac{1}{Q} \right) + \frac{Q \lambda_A RT}{A_\epsilon^2} (\lambda_A RT - b_\epsilon(T)) + \right.$$
$$\left. \frac{(RT)^2}{Q A_\epsilon^2} \left(\frac{b_\epsilon(T)}{RT} \left(\frac{\lambda_A}{Q} + \lambda_B \left(1 - \frac{1}{Q} \right) \right) - \left(\frac{\lambda_A}{Q} + \lambda_B \left(1 - \frac{1}{Q} \right) \right)^2 \right) \right] \cdot f_r^2 + ..$$

(3.45)

In this final equation, the pressure p_r was replaced by the ideal term $p_r = \frac{f_r RT_{\text{iso}}}{A_\epsilon}$ for two reasons. First, the formulas derived in this thesis should also be applicable to experiments that eventually do not feature an *in situ* pressure measurement. More important, the impressive similarity in structure to the formulas derived for the Burnett expansion will be lost if the pressure is not replaced. This aspect is emphasized in section 3.5. Fitting equation 3.45 with a polynomial of the required order $F_{\text{ratio},r} = D_0 + D_1 \cdot f_r + D_2 \cdot f_r^2 + ...$ leads to the following relations for the properties of interest:

$$Q = D_0$$

$$b_\epsilon(T) = A_\epsilon \left(\frac{D_1}{D_0 - 1} - \frac{RT}{A_\epsilon} \frac{1}{Q} (\lambda_B - \lambda_A(Q + 1)) \right)$$

$$c_\epsilon(T) = \frac{A_\epsilon^2}{Q - \frac{1}{Q}} \left[A_2 - \frac{Q\lambda_A RT}{A_\epsilon^2} (\lambda_A RT - b_\epsilon) - \right.$$

$$\left. \frac{(RT)^2}{QA_\epsilon^2} \left(\frac{b_\epsilon}{RT} \left(\frac{\lambda_A}{Q} + \lambda_B \left(1 - \frac{1}{Q} \right) \right) - \left(\frac{\lambda_A}{Q} + \lambda_B \left(1 - \frac{1}{Q} \right) \right)^2 \right) \right] + b_\epsilon^2(T) \tag{3.46}$$

A comparison with the coefficients given in equation 3.43 shows that the results are the same for vanishing pressure deformation. Further discussion and details on how the deformation was determined in this work is given in section 4.1.4.

3.4.3. Dielectric expansion with dead volumes at different temperature

To evaluate the data, which is generated with the setup used in this thesis (see figure 3.5), a working equation that includes dead volumes at a different temperature needs to be derived. The starting equation is layed out utilizing the Mosotti virial coefficients defined by equation 3.13:

$$\frac{f_{r,\text{iso}} V_A}{1 + b_{\text{CM,iso}} f_{r,\text{iso}} + c_{\text{CM,iso}} f_{r,\text{iso}}^2 + ...} + \frac{f_{r,\text{GHS}} V_{DA}}{1 + b_{\text{CM,GHS}} f_{r,\text{GHS}} + c_{\text{CM,GHS}} f_{r,\text{GHS}}^2 + ...} =$$

$$\frac{f_{r+1,\text{iso}} (V_A + V_B)}{1 + b_{\text{CM,iso}} f_{r+1,\text{iso}} + c_{\text{CM,iso}} f_{r+1,\text{iso}}^2 + ...} + \frac{f_{r+1,\text{GHS}} (V_{DA} + V_{DB})}{1 + b_{\text{CM,GHS}} f_{r+1,\text{GHS}} + c_{\text{CM,GHS}} f_{r+1,\text{GHS}}^2 + ...} \tag{3.47}$$

The challenge with equation 3.47 is that, on the one hand, the different temperatures are not directly included at this point. On the other hand, unlike the pressure, the capacitance is different for the two different temperature regimes. Thus, the Mossoti-term $f_{r,\text{iso}}$ for T_{GHS} is an additional unknown quantity. To solve this problem, the Mosotti-terms for the temperatures T_{GHS} are derived from the DCGT data evaluation. Taking into account the second order virial coefficients, the following relations are valid:

$$p(T_{\text{iso}}) = \frac{1}{\frac{A_\epsilon}{RT_{\text{iso}}} + \frac{\kappa_{\text{eff}}}{3}} \mu_{\text{iso}} \left(1 + \frac{B_{\text{DCGT,iso}}}{A_\epsilon} \mu_{\text{iso}} \right)$$

$$p(T_{\text{GHS}}) = \frac{1}{\frac{A_\epsilon}{RT_{\text{GHS}}} + \frac{\kappa_{\text{eff}}}{3}} \mu_{\text{GHS}} \left(1 + \frac{B_{\text{DCGT,GHS}}}{A_\epsilon} \mu_{\text{GHS}} \right) \tag{3.48}$$

The pressure is approximately equal $p(T_{\text{iso}}) \approx p(T_{\text{GHS}})$ in both temperature regimes neglecting the small head correction. Thus, a link between the capacitance ratios at T_{iso} and T_{GHS} can be established. The further steps are carried out in appendix G.4. The final result is displayed here by means of the already defined ratios and the fit coefficients used for the

evaluation of the data:

$$F_{\text{ratio},r} = D_0 + D_1 \cdot f_r + D_2 \cdot f_r^2 + ...$$

$$D_0 = Q_{\Delta T}$$

$$\frac{D_1}{D_0 - 1} = \frac{b_{\epsilon,\text{iso}}}{A_\epsilon} \left[\frac{1}{1 + T_{\text{ratio}}Q_{\text{A}}} - \frac{1}{1 + T_{\text{ratio}}Q_{\text{B}}} + \frac{1}{1 + T_{\text{ratio}}\frac{(Q_{\text{B}} + Q_{\text{A}}Q^*)}{(1+Q^*)}} \right] +$$

$$\frac{b_{\epsilon,\text{GHS}}}{A_\epsilon} T_{\text{ratio}} \left[1 + \frac{1}{1 + T_{\text{ratio}}Q_{\text{B}}} - \frac{1}{1 + T_{\text{ratio}}Q_{\text{A}}} - \frac{1}{1 + T_{\text{ratio}}\frac{(Q_{\text{B}} + Q_{\text{A}}Q^*)}{(1+Q^*)}} \right] +$$

$$\frac{(B_{\text{DCGT,iso}} - T_{\text{ratio}}B_{\text{DCGT,GHS}})}{A_\epsilon} \left[\left(\frac{1}{Q_{\Delta T}^2} - 1 \right) \left(\frac{1}{1 + \frac{1}{T_{\text{ratio}}Q_{\text{A}}}} + \frac{Q_{\text{A}}Q^*}{\frac{1}{T_{\text{ratio}}} + Q_{\text{B}}} \right) + \right.$$

$$\left. \frac{1}{Q_{\Delta T}^2} \left(\frac{1}{1 + \frac{1}{T_{\text{ratio}}Q_{\text{B}}}} + \frac{\frac{Q_{\text{B}}}{Q^*}}{\frac{1}{T_{\text{ratio}}} + Q_{\text{A}}} \right) \right]$$

$$(3.49)$$

3.4.4. Final working equation of the dielectric expansion

The main corrections to the ideal case of the dielectric expansion experiments introduced in section 3.4.1 were described in the previous two sections. For the final data evaluation, they have to be considered together. Starting point is the modified starting equation 3.47 of the previous section for the case of dead volumes which is extended by incorporating the pressure correction terms (e.g. $(1 + \lambda_{\text{A}}p_r)$) to the volumes. As argued in in section 3.4.2, the pressure is replaced by the ideal approximation $p_r = \frac{f_{r,\text{iso}}RT_{\text{iso}}}{A_\epsilon}$ for the starting pressure. Since the pressure is equal in both thermal regimes, it is not necessary to include $f_{r,\text{GHS}}$. On the expansion side of this equation, the pressure has to be approximated by $p_{r+1} = \frac{f_{r,\text{iso}}RT_{\text{iso}}}{Q_{\Delta T}A_\epsilon}$ instead of $p_{r+1} = \frac{f_{r,\text{iso}}RT_{\text{iso}}}{F_{\text{ratio},r}A_\epsilon}$, to obtain a solvable equation. For the second order of the dielectric virial coefficient this results in:

$$\frac{f_{r,\text{iso}}V_A\left(1+\lambda_A\frac{f_{r,\text{iso}}RT_{\text{iso}}}{A_\epsilon}\right)}{(1+b_{\text{CM,iso}}f_{r,\text{iso}})} - \frac{f_{r,\text{iso}}\left(V_A\left(1+\lambda_A\frac{f_{r,\text{iso}}RT_{\text{iso}}}{Q_{\Delta,T}A_\epsilon}\right)+V_B\left(1+\lambda_B\frac{f_{r,\text{iso}}RT_{\text{iso}}}{Q_{\Delta T}A_\epsilon}\right)\right)}{F_{\text{ratio,iso}}(1+b_{\text{CM,iso}}\frac{f_{r,\text{iso}}}{F_{\text{ratio,iso}}})} =$$

$$\frac{\left(\frac{T_{\text{iso}}}{T_{\text{GHS}}}\cdot\frac{f_{r,\text{iso}}}{F_{\text{ratio,iso}}}+\frac{B_{\text{DCGT,iso}}T_{\text{iso}}T_{\text{GHS}}-B_{\text{DCGT,GHS}}T_{\text{iso}}^2}{T_{\text{GHS}}^2 A_\epsilon}\cdot\frac{f_{r,\text{iso}}^2}{Q_{\Delta T}^2}\right)V_{DA}\left(1+\lambda_{\text{GHS}}\frac{f_{r,\text{iso}}RT_{\text{iso}}}{Q_{\Delta T}A_\epsilon}\right)}{\left(1+b_{\text{CM,GHS}}\left(\frac{T_{\text{iso}}}{T_{\text{GHS}}}\cdot\frac{f_{r,\text{iso}}}{F_{\text{ratio,iso}}}+\frac{B_{\text{DCGT,iso}}T_{\text{iso}}T_{\text{GHS}}-B_{\text{DCGT,GHS}}T_{\text{iso}}^2}{T_{\text{GHS}}^2 A_\epsilon}\cdot\frac{f_{r,\text{iso}}^2}{Q_{\Delta T}^2}\right)\right)}+$$

$$\frac{\left(\frac{T_{\text{iso}}}{T_{\text{GHS}}}\cdot\frac{f_{r,\text{iso}}}{F_{\text{ratio,iso}}}+\frac{B_{\text{DCGT,iso}}T_{\text{iso}}T_{\text{GHS}}-B_{\text{DCGT,GHS}}T_{\text{iso}}^2}{T_{\text{GHS}}^2 A_\epsilon}\cdot\frac{f_{r,\text{iso}}^2}{Q_{\Delta T}^2}\right)V_{DB}\left(1+\lambda_{\text{GHS}}\frac{f_{r,\text{iso}}RT_{\text{iso}}}{Q_{\Delta T}A_\epsilon}\right)}{\left(1+b_{\text{CM,GHS}}\left(\frac{T_{\text{iso}}}{T_{\text{GHS}}}\cdot\frac{f_{r,\text{iso}}}{F_{\text{ratio,iso}}}+\frac{B_{\text{DCGT,iso}}T_{\text{iso}}T_{\text{GHS}}-B_{\text{DCGT,GHS}}T_{\text{iso}}^2}{T_{\text{GHS}}^2 A_\epsilon}\cdot\frac{f_{r,\text{iso}}^2}{Q_{\Delta T}^2}\right)\right)}-$$

$$\frac{\left(\frac{T_{\text{iso}}}{T_{\text{GHS}}}\cdot f_{r,\text{iso}}+\frac{B_{\text{DCGT,iso}}T_{\text{iso}}T_{\text{GHS}}-B_{\text{DCGT,GHS}}T_{\text{iso}}^2}{T_{\text{GHS}}^2 A_\epsilon}\cdot f_{r,\text{iso}}^2\right)V_{DA}\left(1+\lambda_{\text{GHS}}\frac{f_{r,\text{iso}}RT_{\text{iso}}}{A_\epsilon}\right)}{\left(1+b_{\text{CM,GHS}}\left(\frac{T_{\text{iso}}}{T_{\text{GHS}}}\cdot f_{r,\text{iso}}+\frac{B_{\text{DCGT,iso}}T_{\text{iso}}T_{\text{GHS}}-B_{\text{DCGT,GHS}}T_{\text{iso}}^2}{T_{\text{GHS}}^2 A_\epsilon}\cdot f_{r,\text{iso}}^2\right)\right)}$$

$$\tag{3.50}$$

The further derivation is carried out in appendix G.5 with the final result being:

$$\frac{D_1}{D_0-1} = \frac{b_{\text{iso}}}{A_\epsilon}\left[\frac{1}{1+T_{\text{ratio}}Q_A}-\frac{1}{1+T_{\text{ratio}}Q_B}+\frac{1}{1+T_{\text{ratio}}\frac{(Q_B+Q_AQ^*)}{(1+Q^*)}}\right]+$$

$$\frac{b_{\text{GHS}}}{A_\epsilon}\cdot T_{\text{ratio}}\left[1+\frac{1}{1+T_{\text{ratio}}Q_B}-\frac{1}{1+T_{\text{ratio}}Q_A}-\frac{1}{1+T_{\text{ratio}}\frac{(Q_B+Q_AQ^*)}{(1+Q^*)}}\right]+$$

$$\lambda_B\cdot\frac{RT_{\text{iso}}}{A_\epsilon}\left[\frac{1}{Q_{\Delta T}}\left(\frac{1}{1+T_{\text{ratio}}Q_B}\right)\right]+$$

$$\lambda_A\cdot\frac{RT_{\text{iso}}}{A_\epsilon}\left[\left(\frac{1}{Q_{\Delta T}}-1\right)\left(\frac{Q^*}{1+T_{\text{ratio}}Q_B}\right)-\frac{1}{1+T_{\text{ratio}}Q_A}\right]+$$

$$\lambda_{\text{GHS}}\cdot\frac{RT_{\text{iso}}}{A_\epsilon}\left[\frac{1}{Q_{\Delta T}}\left(\frac{1}{1+\frac{1}{T_{\text{ratio}}Q_B}}+\frac{Q^*Q_A}{\frac{1}{T_{\text{ratio}}}+Q_B}\right)-\right.$$

$$\left.\frac{1}{1+\frac{1}{T_{\text{ratio}}Q_A}}-\frac{Q^*Q_A}{\frac{1}{T_{\text{ratio}}}+Q_B}\right]+$$

$$\frac{(B_{\text{DCGT,iso}}-T_{\text{ratio}}B_{\text{DCGT,GHS}})}{A_\epsilon}\left[\left(\frac{1}{Q_{\Delta T}^2}-1\right)\left(\frac{1}{1+\frac{1}{T_{\text{ratio}}Q_A}}+\frac{Q_AQ^*}{\frac{1}{T_{\text{ratio}}}+Q_B}\right)+\right.$$

$$\left.\frac{1}{Q_{\Delta T}^2}\left(\frac{1}{1+\frac{1}{T_{\text{ratio}}Q_B}}+\frac{\frac{Q_B}{Q^*}}{\frac{1}{T_{\text{ratio}}}+Q_A}\right)\right]$$

$$\tag{3.51}$$

3.5. Evaluation of the final working equations

The derived working equations of the previous three sections offer the possibility to directly fit the experimental data, without the need to correct it for either deformation of the cells,

dead volumes at different temperatures or both effects. This novel approach for expansion experiments may be of importance not only for this work but for other groups that perform similar work or intend to do so as well. The derivations for these expansion experiments were carried out strictly separating Burnett and dielectric expansions. However, summarizing equations 3.38, 3.40, 3.49 and 3.51 as done in the following reveals aesthetic similarities. The working equations for the case of dead volumes neglecting the deformation may be written as:

$$
\begin{aligned}
\left(\frac{K_1}{K_0 - 1}\right) \cdot RT_{\text{iso}} =& B_{\text{iso}} \cdot V_1 + B_{\text{GHS}} T_{\text{ratio}} \cdot (1 - V_1) \\
\left(\frac{D_1}{D_0 - 1}\right) \cdot A_\epsilon =& b_{\epsilon,\text{iso}} \cdot V_1 + b_{\epsilon,\text{GHS}} T_{\text{ratio}} \cdot (1 - V_1) + \\
& (B_{\text{DCGT,iso}} - T_{\text{ratio}} B_{\text{DCGT,GHS}}) \cdot V_5
\end{aligned}
\tag{3.52}
$$

The final working equations, which additionally include the deformation of the cells under pressure, can be expressed by:

$$
\begin{aligned}
\left(\frac{K_1}{K_0 - 1}\right) \cdot RT_{\text{iso}} =& B_{\text{iso}} \cdot V_1 + B_{\text{GHS}} T_{\text{ratio}} \cdot (1 - V_1) + \\
& RT_{\text{iso}} \left(\lambda_{\text{B}} \cdot V_2 + \lambda_{\text{A}} \cdot V_3 + \lambda_{\text{GHS}} \cdot V_4\right) \\
\left(\frac{D_1}{D_0 - 1}\right) \cdot A_\epsilon =& b_{\epsilon,\text{iso}} \cdot V_1 + b_{\epsilon,\text{GHS}} T_{\text{ratio}} \cdot (1 - V_1) + \\
& RT_{\text{iso}} \left(\lambda_{\text{B}} \cdot V_2 + \lambda_{\text{A}} \cdot V_3 + \lambda_{\text{GHS}} \cdot V_4\right) + \\
& (B_{\text{DCGT,iso}} - T_{\text{ratio}} B_{\text{DCGT,GHS}}) \cdot V_5
\end{aligned}
\tag{3.53}
$$

whereas the coefficients of equations 3.52 and 3.53 are given by:

$$
\begin{aligned}
V_1 =& \left[\frac{1}{1 + T_{\text{ratio}} Q_{\text{A}}} - \frac{1}{1 + T_{\text{ratio}} Q_{\text{B}}} + \frac{1}{1 + T_{\text{ratio}} \frac{(Q_{\text{B}} + Q_{\text{A}} Q^*)}{(1 + Q^*)}}\right] \\
V_2 =& \left[\frac{1}{Q_{\Delta T}} \left(\frac{1}{1 + T_{\text{ratio}} Q_{\text{B}}}\right)\right] \\
V_3 =& \left[\left(\frac{1}{Q_{\Delta T}} - 1\right)\left(\frac{Q^*}{1 + T_{\text{ratio}} Q_{\text{B}}}\right) - \frac{1}{1 + T_{\text{ratio}} Q_{\text{A}}}\right] \\
V_4 =& \left[\frac{1}{Q_{\Delta T}}\left(\frac{1}{1 + \frac{1}{T_{\text{ratio}} Q_{\text{B}}}} + \frac{Q^* Q_{\text{A}}}{\frac{1}{T_{\text{ratio}}} + Q_{\text{B}}}\right) - \frac{1}{1 + \frac{1}{T_{\text{ratio}} Q_{\text{A}}}} - \frac{Q^* Q_{\text{A}}}{\frac{1}{T_{\text{ratio}}} + Q_{\text{B}}}\right] \\
V_5 =& \left[\left(\frac{1}{Q_{\Delta T}^2} - 1\right)\left(\frac{1}{1 + \frac{1}{T_{\text{ratio}} Q_{\text{A}}}} + \frac{Q_{\text{A}} Q^*}{\frac{1}{T_{\text{ratio}}} + Q_{\text{B}}}\right) + \frac{1}{Q_{\Delta T}^2}\left(\frac{1}{1 + \frac{1}{T_{\text{ratio}} Q_{\text{B}}}} + \frac{\frac{Q_{\text{B}}}{Q^*}}{\frac{1}{T_{\text{ratio}}} + Q_{\text{A}}}\right)\right]
\end{aligned}
\tag{3.54}
$$

The multiplication of the processed fit coefficients with RT_{iso} or A_ϵ on the left side of equations 3.52 and 3.53 accounts for the derivation of the working equations utilizing the

pressure and Mosotti virial coefficients rather than the targeted density and dielectric virial coefficients. This step was already used in the description of the ideal systems in equations 3.30 and 3.43. The two equations 3.52 taking into account dead volumes but neglecting the pressure deformation of the cells only differ in structure by a term that includes the second DCGT virial coefficients. This additional term is required for the evaluation of the capacitance data since the dielectric constant at the gas-handling system temperature is not measured directly, in contrast to the pressure, which is approximately equal in both thermal regimes. Taking the effect of deformation into account in equations 3.53 results in an additional term which is actually the same for the Burnett and the dielectric expansion. This surprises to some extend, since the pressure in the terms describing the deformation was replaced in the derivation utilizing the ideal assumption $p = \frac{fRT_{\mathrm{iso}}}{A_\epsilon}$. This step reappears if the right hand side of equations 3.53 is divided again by the factors of the left hand side RT_{iso} or A_ϵ respectively. In this case, the factor RT_{iso} before the deformation term of the density viral coefficients simply cancels out while the factor of the dielectric expansion turns into $\frac{RT_{\mathrm{iso}}}{A_\epsilon} = \frac{p}{f}$.

3.6. Fit routine and fit orders

The evaluation of the measured data requires to fit polynomials to the measured points for all three methods. The data treatment was carried out in Microsoft Excel, but instead of using the Excel fit function "RGP" a least squares fit routine that was implemented as a macro in VBA (Virtual Basic for Applications) was used. This routine was programmed in the working group based on the routine proposed by Björck [87], which is described as well in Hall *et al.* [71, 72]. The fitting is carried out by means of orthogonal polynomials utilizing modified Gram-Schmidt orthogonalization and a conversion back to a standard polynomial when finished. The motivation for this was to reliably understand how the uncertainty of the fit coefficients is determined. It should be mentioned, that in case of the polynomials used in this thesis no deviations to coefficients obtained by the "RGP" function can be reported. This also accounts for the derived uncertainties of the fit coefficients.

A second very important aspect is the question which order of the polynomial is the best to fit the data. On the one hand lower fit orders are more stable under statistical scattering of the data points and will result in lower uncertainties, but on the other hand the fit will result in systematically wrong results in case the fit order is too low. If the number of fit parameters is too big, the results will be distorted from the correct values as well since statistically scattered data will be described by physically meaningless higher fit coefficients [29]. In principal, the question that needs to be answered is which is the highest virial coefficient (or fit order) that significantly contributes to the result for the selected density and thus pressure or dielectric constant range. Since argon is a well investigated gas, it can be concluded from the literature that for the DCGT evaluation and the Burnett expansions the fifth density virial coefficient $E(T)$ probably needs to be taken into account for the highest pressures of 7 MPa, while for the dielectric expansion it is sufficient to include

the third dielectric virial coefficient $c_\epsilon(T)$ [1]. Additional information for the required fit order can be obtained by investigation of the fit residuals for systematic deviations. This is exemplified in figure 3.6 for the averaged Burnett and dielectric expansion data of argon at the triple point of water. These results will be presented in sections 5.3 and 5.4. In (a), the absolute difference between the measured pressure ratios and the ones calculated from the fit coefficients is plotted. Different fit orders were probed, whereas the highest included virial coefficient is indicated in the legend of the diagram. A truncation of the fit function after the third density virial coefficient $C(T)$ is obviously not sufficient to described the data. On the other hand, inclusion of the fifth density virial coefficient $E(T)$ does not further improve the replication of the data in comparison to truncation after $D(T)$. It is concluded that the scattering of the data in this work is too high to resolve the influence of $E(T)$ which is reported in the literature [1]. That is why $D(T)$ is selected as the highest order, which is included in the evaluation of the data. The same arguments can be applied to the dielectric expansion in (b). Here, it is approved that a function which is truncated after the third dielectric virial coefficient $c_\epsilon(T)$ describes the data sufficiently .

(a) Burnett expansion

(b) dielectric Expansion
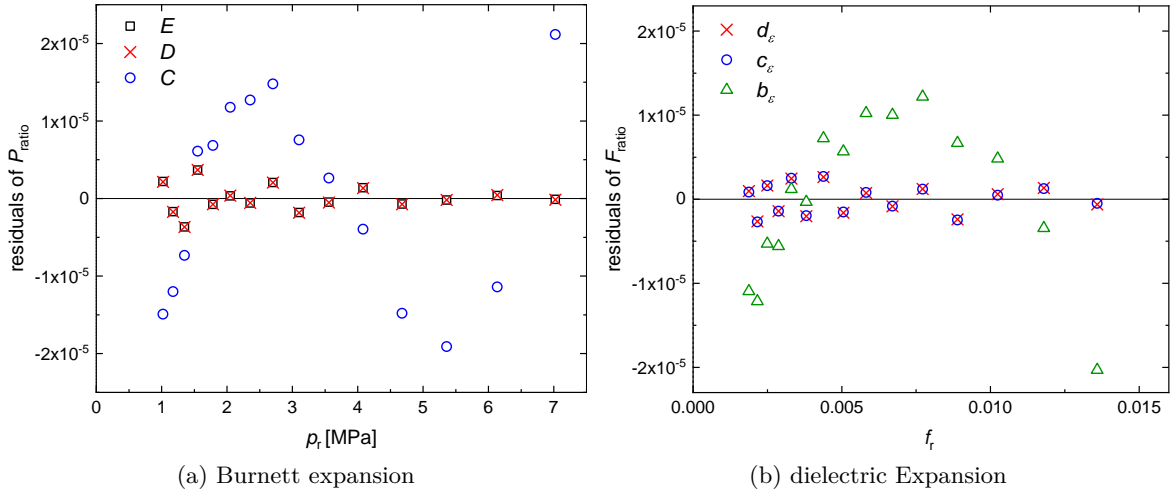
Figure 3.6.: Absolute values of the fit residuals of the pressure ratios (a) and the ratios of Mosotti-terms (b) for argon at the triple point of water. The legend indicates the highest virial coefficient that was included in the fit of the measured data.

In the literature, different approaches to the problem of the fit order are discussed by the evaluation of p-ρ-T data of argon, which was measured with densimetry by Gilgen *et al.* [67]. In the original publication, all data sets were fitted with a polynomial including orders up to the fifth virial coefficient, whereas only values for the second and third virial coefficient were published. The data was reevaluated by Tegeler *et al.* in a more sophisticated approach based on a procedure described by Nowak *et al.* [88–90]. The parameters of the fit function were reduced by truncation after the third density virial coefficient. Then, the included data sets were reduced starting from higher densities until the retrieved second and third density virial coefficients would describe the densities within the uncertainty of the measurement. A second approach was carried out by Jäger *et al.* [29]. They used computed

higher virial coefficients to constraint the data, which allowed them to also use fit functions with fewer parameters but at the same time to include data sets with higher densities. For the temperature range that is interesting for the work carried out in this thesis (250 K to 310 K), the relative differences in the second denstiy virial coefficient are typically less than 0.5 %. The relative change in the third density virial coefficient is in the order of 1 % for the evaluation by Tegeler *et al.* and exceeds several percent for the approach by Jäger *et al.*. These deviations are within the uncertainty specified by Gilgen *et al.*. Still, they show that especially for the higher virial coefficients significantly different results can be obtained depending on the fit order.

4. Experimental background
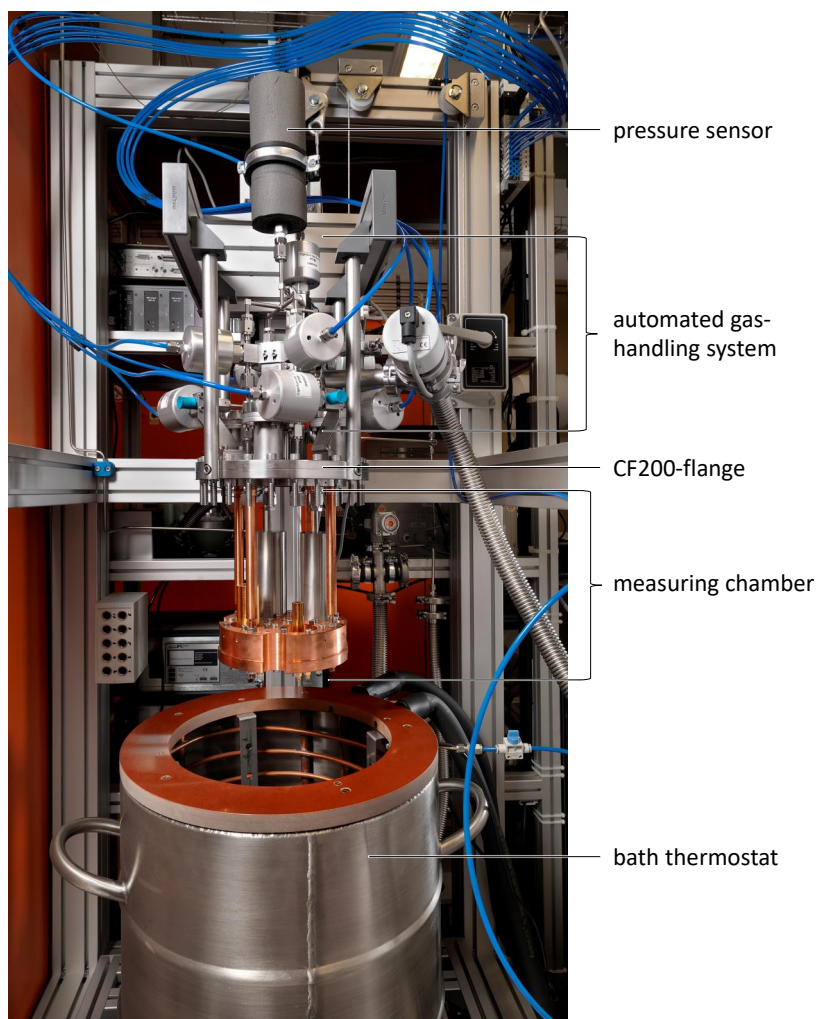
Figure 4.1.: The newly designed apparatus and its main components which will be explained in the following sections.

This chapter comprehensively covers the design of the apparatus developed, built and validated in this thesis taking the considerations of the previous chapter 3 into account. Key requirements that influenced the construction were the possibility for automation, use of commercial measurement equipment, a very compact design and the potential to be used for experiments with hydrogen and carbon dioxide. The temperature operating range was anticipated to be from $230\,\mathrm{K}$ to $360\,\mathrm{K}$ for pressures up to $7\,\mathrm{MPa}$. The concept of the apparatus was published in [91]. Improvements made since then as well as a detailed description are

given in the following. The potential of this method to be used as a compact and more commercial system is discussed in the summary 6. Details on the used measurement equipment for pressure, capacitance and temperature are given in sections 4.2, 4.3 and 4.4. Commercial hard- and software identified throughout this thesis does not imply recommendation or endorsement by **P**hysikalisch-**T**echnische **B**undesanstalt (PTB), nor does it imply that identified equipment is the best for this purpose.

4.1. Design of the apparatus

An overview of the different components building up the new device can be seen in figure 4.1 The measuring system is constructed around a CF-200 flange, which can be better seen in figure 4.2. The lower part containing the measurement cells can be closed with a CF-200 stainless steel vacuum chamber. On top of the flange, a gas-handling system and the pressure sensors (a second sensor was installed right next to the one shown in the picture) are located. This upper part of the system is shielded by an acrylic glass hood with a Peltier cooler and fan (not shown in figure 4.1). These parts form the central measurement system and are mounted to a sled moving vertically on a frame operated by a hand winch. This way, the system can be lowered down into a liquid bath thermostat, which is mounted on wheels so it can be moved to the side for repairs. Details on the concept for the thermostatization of the system are given in subsection 4.1.1. The footprint of the entire system is less than $1\,\mathrm{m}^2$. Due to the space requirements, controllers, data acquisition and a pressure balance for calibration were fitted inside shelves behind the system.

The central elements of the measuring system can be seen in the cross section in figure 4.2. To the CF-200 flange, a massive plate (thickness $50\,\mathrm{mm}$) made from highly conductive oxygen free copper is attached via four copper poles with a diameter of $15\,\mathrm{mm}$. The copper plate serves as thermal anchor for the system. Four measurement chambers made from stainless steel (X5CrNi18-10) and equipped with the capacitors are bolted to it from below. Further details on the used capacitors is given in section 4.1.3. The cells are custom produced with a wall thickness of $6\,\mathrm{mm}$ but have a standard CF-40 copper seal to incorporate the bases of the capacitors. Instead of two cells, which would be sufficient to perform standard expansion experiments, four cells were installed for several reasons. First, as shown in the DCGT principle in figure 3.2, capacitance measurements of highest precision require to use a highly stable reference capacitor (see section 4.3). This leaves three cells, which still allows to perform expansion experiments in the cyclic manner described in appendix G.2. Experiments of this kind have not been performed yet but are considered to be explored in the future. Lastly, having four cells (or three if one is used as the capacitance reference) allows to adapt the actual volume ratios of the expansions. Since for argon at least the fourth density virial coefficient $D(T)$ needs to be considered for pressures of $7\,\mathrm{MPa}$, a minimum of 12 data points with sufficient uncertainties is required to fit the data. Considering that the uncertainties of the pressure sensors drastically rises below $1\,\mathrm{MPa}$ (see section 4.2), the volumes of the measuring cells were selected as follows. Three of them (C1, C2 and C3) have

the same effective volume of $145.46\,\mathrm{cm}^3$ while the cell containing capacitor C4 has a volume of $67.09\,\mathrm{cm}^3$. Expanding the gas from the tree larger cells C1 to C3 into cell C4 allows to record 16 data points at an excellent spacing for the fit routines. The different volumes of the system retrieved from dimensional measurements are summarized in table 4.1.
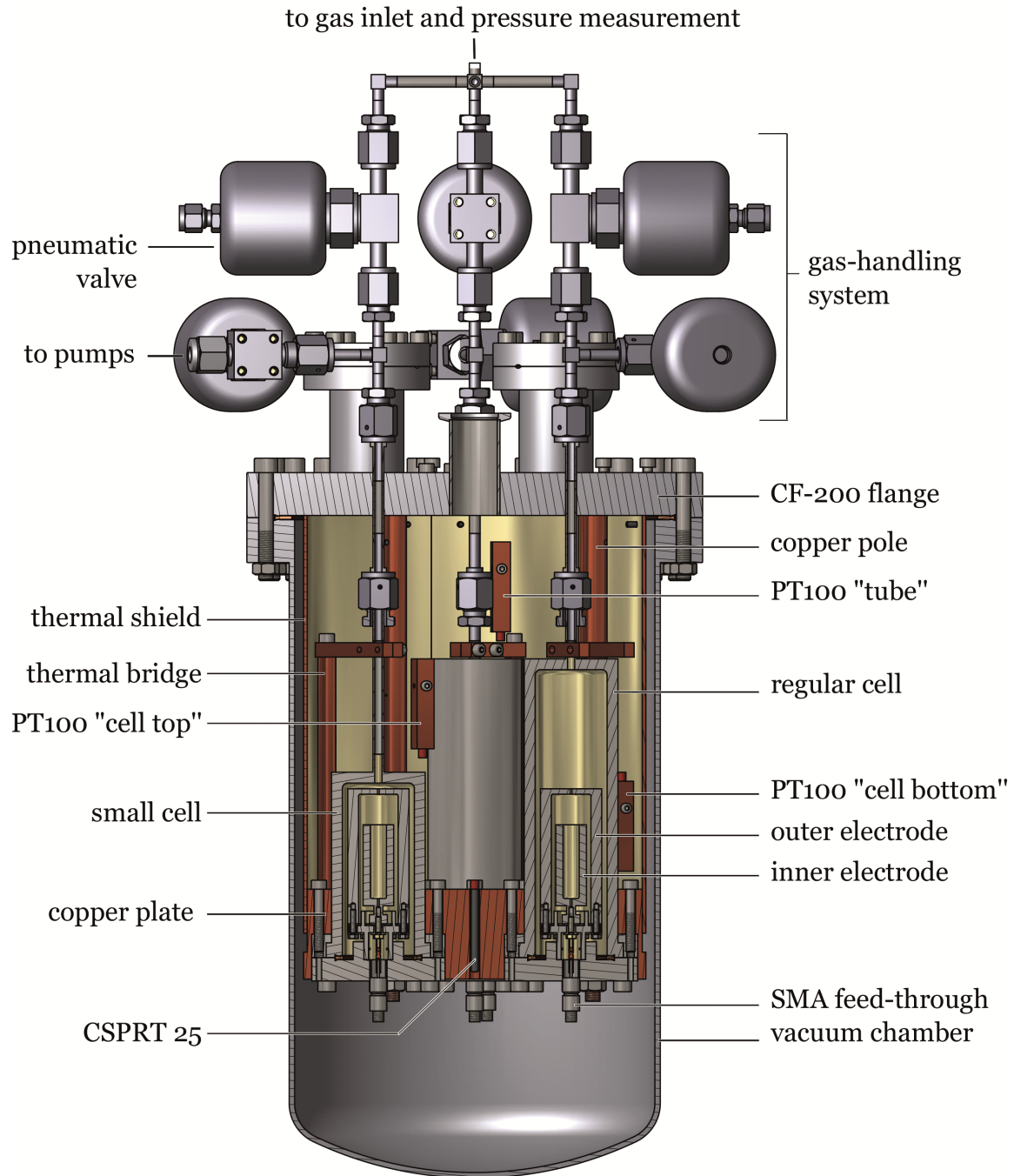

Figure 4.2.: Cross section of the central measuring chamber and its main components.

From the volumes given in table 4.1, the ratios defined in equation 3.37 used for the final evaluation of the expansion experiments as described in section 4.6 can be calculated and are $Q^* = 6.504$ $Q_A = 0.021$, $Q_B = 0.047$ and $Q = 1{,}152$. These ratios are obviously not

component	volume [cm^3]	T_{iso}	T_{GHS}	assigned to
cells C1 to C3	145.46	x		V_{A}
cells C1 to C3	3.16		x	V_{DA}
cell C4	67.09	x		V_{B}
cell C4	3.16		x	V_{DB}
GHS	16.69		x	V_{DA}

Table 4.1.: Volumes of the different parts of the system and their temperature. Volumes given for cells C1 to C3 are the volume per individual cell. The border between the two thermal regimes is chosen at the edge of the thermostating fluid. Components of the cells assigned to T_{GHS} are between the edge of the thermostating fluid and the opened halve of the "Gas" valves (see figure 4.4). GHS abbreviates the dead volume of the gas-handling system including the pressure sensors starting at the closed halve of the "Gas" valves.

accurate enough to be used in the final data evaluation. Details on the determination of the precise ratios from the fit of the data is given in section 5.2.

4.1.1. Thermal stabilization

There are strict requirements for thermal stabilization in this setup. All measurements have to be taken at isothermal conditions since deviations cause changes in the particle density and, thus, in the output quantities. Essentially, the experience gathered within the scope of the Boltzmann project of PTB has been transferred to this much smaller setup [92]. The fluid bath shown in figure 4.1 has a volume of 60 l and incorporates a pipe coil made of copper, which is connected to a Lauda proline RP1840 refrigeration bath circulator. In addition, an electrical heater coupled to a Fluke 2100 temperature controller is installed at the bottom of the bath. Circulation and temperature homogeneity of the fluid (water for temperatures above the triple point of water, water and ethanol for temperatures of the triple point of water and less) is ensured by small air bubbles that are induced under the electrical heater. The temperature distribution and stability within the fluid bath was measured with five PT100 temperature sensors located in different positions. For the experiments at the triple point of water and at higher temperatures, the standard deviations of the temperatures in the bath were less than 5 mK. Temperature differences in vertical direction were typically less than 30 mK while no lateral temperature gradients were observed. The experiments at 253 K had to be carried out without the use of the Fluke 2100 temperature controller. The operating range was limited to temperatures above 263 K because the linearized Hart 2611 thermistor probe was used. That is why the standard uncertainty of the measured bath temperatures rised to the level of 20 mK.

Further improvement of the temperature stability inside the measuring chamber is achieved by mounting the measuring cells with the incorporated capacitors to a massive copper plate with a thickness of 5 cm. It is mechanically and thermally connected to the CF-200 flange with 4 symmetrically located copper rods with a diameter of 15 mm. Additionally, four electric heaters are installed in the copper plate at the contact points with the copper rods.

They are linked to another temperature controller (model: PTC 10, Stanford Research Systems), which utilizes a PT100 thermometer located close to the center of the copper plate for temperature regulation. In figure 4.3, the temperature stability of the system is demonstrated by plotting the temperature measured with the 25 Ω **C**apsule type **S**tandard **P**latinum **R**esistance **T**hermometer (CSPRT) for each data point of the expansion starting with a pressure of 7 MPa at point 1. One random isotherm for each temperature was selected. This impressively shows that the temperature is extremely stable during the course of an isotherm lasting around ten days. The standard deviation of the temperature is less than 0.2 mK for all isotherms at each temperature.

(a) isotherm 2

(b) isotherm 6

(c) isotherm 14
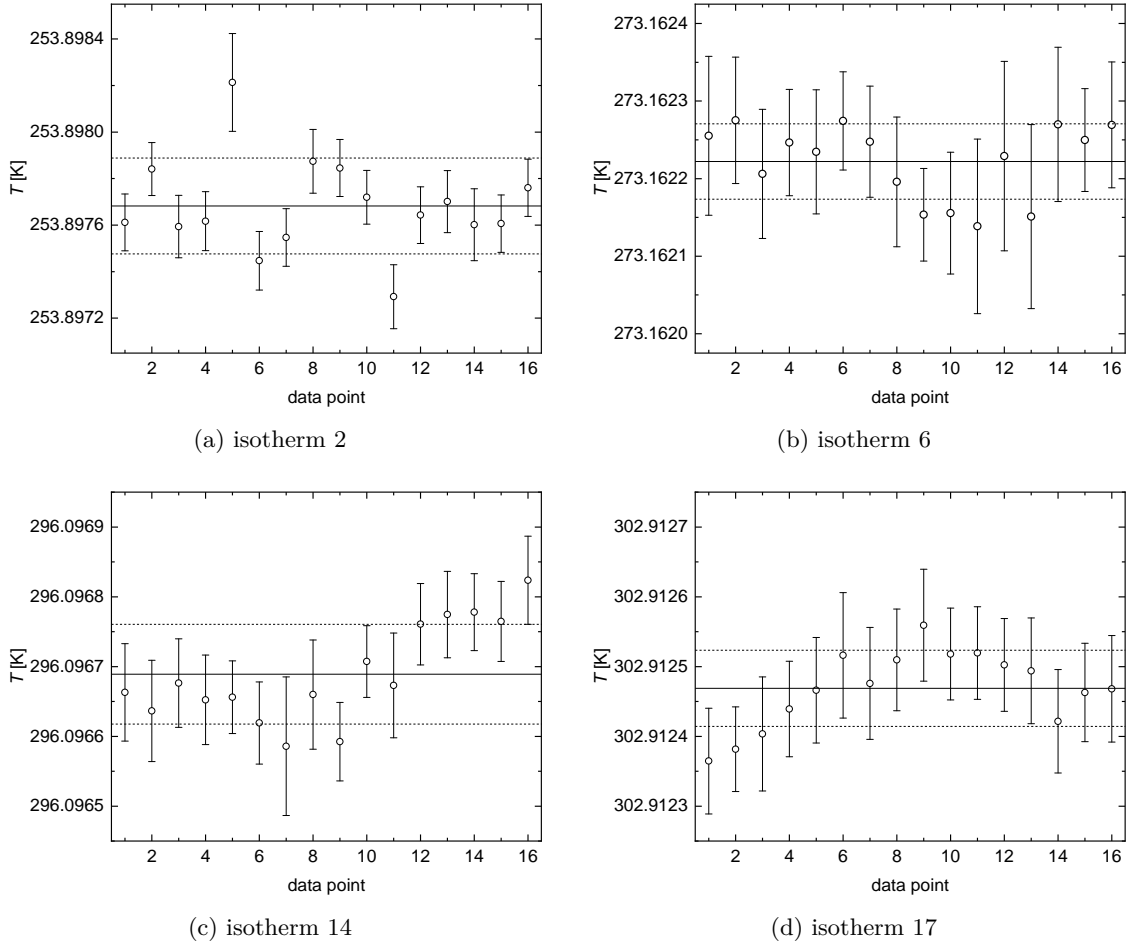
(d) isotherm 17

Figure 4.3.: Examples of the temperature stability of the central copper plate during an isotherm measurement for each temperature. The isotherm numbers are defined in table 5.1. Data point 1 corresponds to the starting pressure of 7 MPa. At each data point, the temperature was measured for 2 hours with the error bars indicating the corresponding standard uncertainty of these averaged temperatures. The solid lines indicate the average value of the temperature over the whole isotherm measurement, while the dashed line shows the corresponding standard deviation.

Though the temperature of the copper plate is regulated to a more than satisfying degree,

there are temperature gradients over the measuring chambers resulting from the thermal conduction and the lower temperature of the CF-200 flange. To diminish the gradients, additional thermal bridges made from copper (see figure 4.2) were installed. They link the connection tubes of the measuring cells directly to the copper plate. The temperature distribution in the system was then measured with calibrated, highly stable PT100 resistance thermometers whose measuring positions are indicated in figure 4.2. The gradients over the measuring chambers were decreased to a level of less than 10 mK (measured temperature difference between the upper end of the measuring cell and the copper plate) for measurements at the triple point of water and above. Due to the higher standard deviation of the fluid bath temperature at 253 K, the average bath temperature had to be lowered leading to higher gradients in the order of 30 mK in this case. These effects are taken into account in the uncertainty budget for the temperature measurement in section 4.4. They primarily influence the DCGT data evaluation of temperatures and molar polarizabilities rather than the determination of the virial coefficients.

For the data evaluation of the expansion experiments, a system with two different temperatures is considered making the temperature stabilization of the gas-handling system rather important as well. Therefore, the tubing of the gas-handling system shown in figures 4.1 and 4.2 was wrapped in electrical heating tape controlled by the second channel of the temperature controller (model: PTC 10, Stanford Research Systems, USA) and a small PT100 sensing element mounted inside a little copper block mechanically strapped to the middle of the gas-handling system. Additionally, the tubes are wrapped in thermal insulation. The temperature of the gas-handling system T_{GHS} was then checked with another PT100 thermometer. Since the temperature is measured rather punctually this way, a conservative uncertainty of 100 mK is assigned to the absolute value of T_{GHS}. It will be shown in chapter 5 that due to the comparably small volume of the gas-handling system in comparison to the measuring volume the influence on the final results is not dominant. Changes in temperature can also be measured with the internal thermometers of the two pressure sensors (model: Digiquartz 9000 2K, paro scientific, USA) while they are not suitable for the determination of absolute temperature. To minimize the influence of changing room temperature, a box shielding the tubing and pressure sensors was constructed from acrylic glass. On top of the box, a Peltier cooler ventilator was installed. This is beneficial for the temperature stabilization and is required to perform measurements above ambient temperature since the pressure sensors have to be kept at a constant temperature. While the standard uncertainties of the temperatures at the individual data points is typically less than 10 mK, the differences between these data points are larger. The standard uncertainty of the gas-handling system temperature over the whole isothermal measurement is in the order of 30 mK. This is assigned to the influence of the changing room temperature $((21 \pm 1)\,°\mathrm{C})$. A plot prepared in analogy to figure 4.3 but showing the temperature instability of the gas-handling system is shown in appendix H. These temperature differences need to be corrected for the data evaluation of the expansion experiments, which is described in more detail in section 4.7.

4.1.2. The gas-handling system

The gas-handling system is of special importance in two regards. First, it shall enable the expansion experiments but furthermore, these experiments have to be automated, which is described in detail in section 4.6. A schematic drawing of the gas-handling system is shown in figure 4.4. Utilizing the valves "Gas1" to "Gas4" as well as "Vac1" to "Vac4', gas can be expanded from any cell into any other cell while each one can be evacuated individually. Used are pneumatically driven membrane valves (manufacturer swagelok). Connections of the high pressure side (thin lines in figure 4.4) are established with electropolished stainless steel tubing (outer diameter 6 mm; inner diameter 4 mm) and mainly $\frac{1}{4}$ inch VCR connectors (manufacturer: swagelok). On the vacuum side (thick lines in figure 4.4), stainless steel corrugated tubes with different diameters and KF connectors are used. After one of the sapphire insulation washers of the capacitors (see section 4.1.3 for details) broke due to the mechanical stress upon the expansion of the gas, special VCR snubber gaskets containing a stainless steel filter body (pore size 5 μm) were incorporated next to the "Gas" valves. This ensures that the cells still can be evacuated properly through the "Vac" valves while the gas slowly expands when the "Gas" valves are opened. The gas-handling system is layed out to meet the requirements of german safety regulations regarding working with hydrogen by using metal seals. Further details on the gas-handling system is given in section 4.6 with regard to the automation of the experiments.
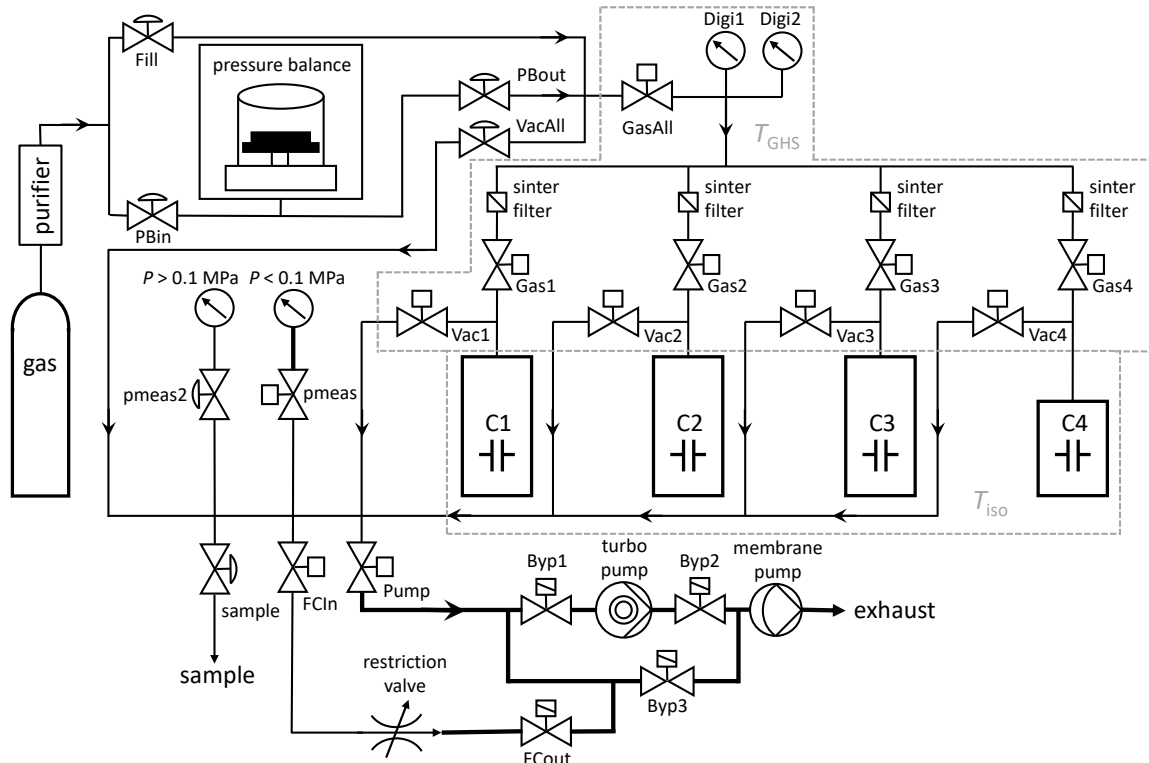

Figure 4.4.: Schematic drawing of the gas-handling system and the relevant components. Thin lines indicate high pressure tubing, while thick lines indicate vacuum tubing. Both thermal regimes are indicated by the grey dashed lines.

4.1.3. Design and characterization of the capacitors

To achieve sufficient uncertainties in the dielectric measurements, relative changes in capacitance in the order of 50 ppb need to be detected. This requires extreme mechanical stability of the capacitors under pressure and over time.

A well studied calculable capacitor type proposed by Thompson and Lampard is the cross capacitor [93]. Though the geometry of the electrodes may be rather arbitrary, a practical setup could be constructed of 4 symmetrically and axially aligned rods (see figure 4.5(a)). In case the capacities per unit length C_1 and C_2 defined between opposite rods are approximately equal, the mean capacitance $C_x \equiv (C_1 + C_2)/2$ is referred to as cross capacitance per unit length [94]:

$$C_x = \frac{\epsilon_0}{\pi} \ln 2 \left(1 + \frac{\ln 2}{8} \left(\frac{C_1 - C_2}{C_x} \right)^2 + ... \right) \approx 1.9535 \frac{\text{pF}}{\text{m}} \tag{4.1}$$

From equation 4.1, it can be seen that minor differences in the two capacities only cause second order effects, which is why the cross capacitance C_x is very insensitive to thin films on the surface of the electrodes. Therefore, this capacitor type has been used as an impedance standard for the realization of the electric units ohm and farad prior to the realization with the quantum hall effect and would in principle be beneficiary for the precise measurement of dielectric constants [95, 96]. To achieve absolute capacities in the order of 10 pF, which are favorable for the available capacitance measuring equipment, the rods would require an impracticable length in the order of 5 m. A much more compact and, thus, more applicable version are toroidal cross capacitors described and used in [94, 97]. As depicted in figure 4.5(b), the cross capacitance is, in this case, defined between inner and outer ring electrodes and top and bottom electrodes.


(a) (b)
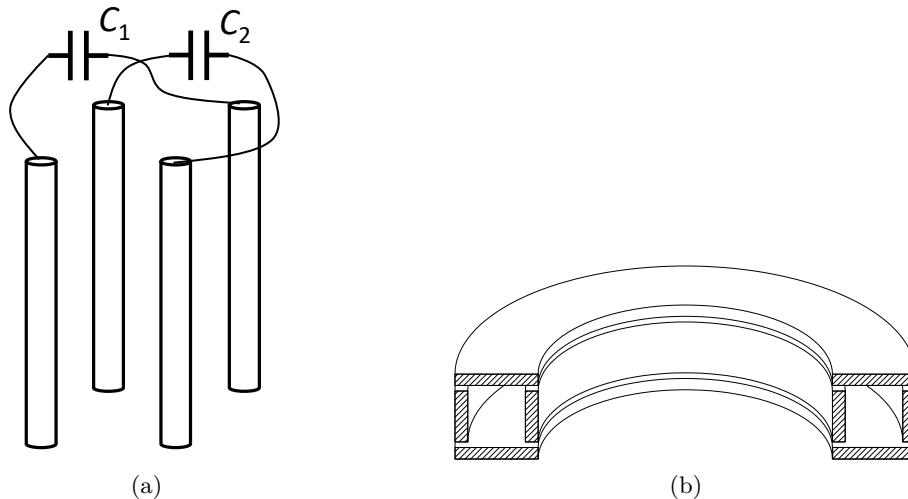
Figure 4.5.: Two practical realizations of a cross capacitor: a) A rod capacitor with four axially aligned rods. b) Cross section of a toroidal cross capacitor as used by Buckley *et al.* [94].

The toroidal cross capacitor used by Schmidt and Moldover had a diameter of roughly 10 cm, while its vacuum capacitance was still less than 1 pF [97]. Reaching higher absolute capacitances can be achieved by stacking several toroidal cross capacitors and connecting them in parallel. The drawback is a very complicated construction accompanied by a relatively large volume. Prototypes of these stacked capacitors made from tungsten carbide were tested in the frame of the Boltzmann-project at PTB but unfortunately did not perform satisfactorily under high pressure cycling. Another problem mentioned by Schmidt and Moldover is the long time required to reach thermal equilibrium in vacuum [97]. They reported an exponential decay constant of 7 hours in vacuum.

That is why, finally, in the Boltzmann-project as well as in this apparatus, cylindrical capacitors were used. They have been used at PTB successfully for more than 25 years and proven to be extremely reliable even under high pressures while being compact and simple structured [2, 19]. The capacitance in vacuum is calculated by the formula:

$$C = 2\pi\epsilon_0 \frac{l}{\ln \frac{R_2}{R_1}} \tag{4.2}$$

Where l denotes the length of the capacitor and R_2 and R_1 are the radii of the inner and outer electrode respectively. For this thesis, a new type of cylindrical capacitor based on experiences gained in the working group has been designed and is shown in figure 4.6. Compared to previous designs, the outer electrode is longer and encloses the inner electrode functioning as electromagnetic shield additionally. The inner electrode is shorter and hollow on the inside to reduce imperfectness due to stray fields ranging to the shielding outer electrode. A visualization of the electric field is depicted in figure 4.9 in section 4.1.4. The base of the capacitor has been designed as simple as possible to ease **F**inite **E**lement **M**ethod (FEM) simulations of the deformation under pressure. Furthermore, it shields the electrical connection of inner and outer electrode. Therefore, it was possible to lay out the electrical connection of the electrodes to the mounting base as a plug connection while in previous designs soldering was required. Electrodes and mounting base are made of non-magnetic stainless steel (1.4122/X39CrMo17-1) while c-axis oriented, highly parallel sapphire spacers (thickness 1 mm) and **P**oly**E**ther **E**ther **K**etone (PEEK) bushings insulate them electrically [91]. The capacitor base is haltered by a custom made CF-40 flange, which is a further development of the design published in [19]. Two SMA feed throughs are included in the flange to electrically contact the electrodes.

Another advantage of the cylindrical design is that the deformation of the capacitor under pressure can be derived from simple formulas. The deformation in radial direction cancels out leaving only the compression of the inner electrode in axial direction. Therefore, the effective compressibility κ_{eff}, which was introduced in formula 3.21, is given by:

$$\kappa_{\text{eff}} = \frac{1}{3}\kappa_{\text{vol}} \tag{4.3}$$

4. Experimental background
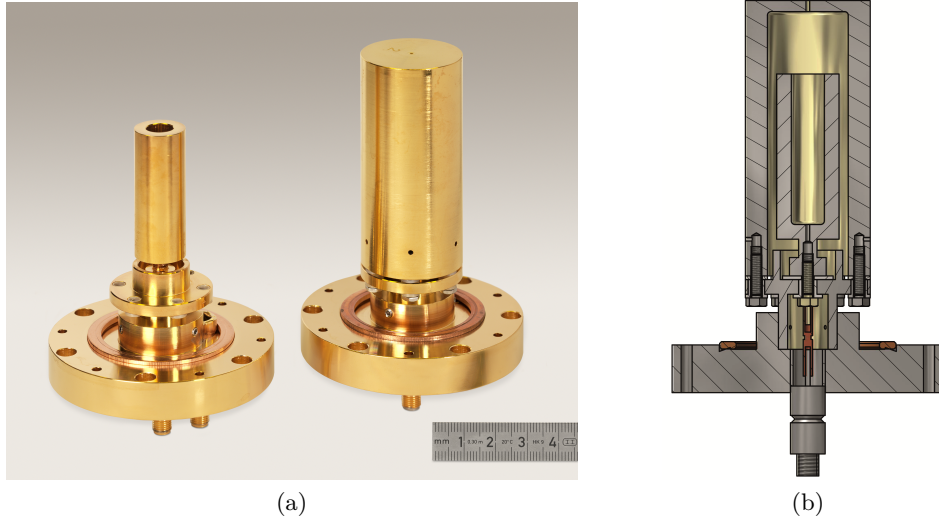
Figure 4.6.: The cylindrical capacitors developed in this thesis: a) Picture of the capacitor without and with the outer electrode. b) Cross section of a capacitor.

for an isotropic material. In this formula, κ_{vol} is the isothermal bulk compressibility of the electrode material. To assess the compressibility, the elastic constants as well as their temperature dependance were measured by **R**esonant **U**ltrasound **S**pectroscopy (RUS). In this well established method, precisely manufactured parallelepipeds of the material under investigation are haltered on two corners by piezoelectric transducers. The sample is then excited with a frequency sweep with one transducer while the other one detects the transmitted signal. The eigen-frequencies can be extracted from the transmitted spectrum and the elastic constants can be determined under the assumption of a crystal structure of the material and from the exact dimensions of the sample. Finally, the bulk module B_{bulk} is determined and used to calculate the effective adiabatic compressibility $\kappa_{\text{eff,ad}} = \frac{1}{3B_{\text{bulk}}}$. This value has to be converted to the isothermal conditions of the experiments carried out here by [98]:

$$\kappa_{\text{eff}} = \kappa_{\text{eff,ad}} \left(1 + 3\alpha_{\text{th}} T_{\text{iso}} \gamma_{\text{G}}\right) \tag{4.4}$$

where α_{th} is the linear coefficient of thermal expansion and γ_{G} is the Grüneisenparameter:

$$\gamma_{\text{G}} = \frac{3\alpha_{\text{th}} B_{\text{bulk}}}{c_p \rho} \tag{4.5}$$

In this formula, ρ is the mass density and c_p denotes the specific heat capacity at constant pressure. Fortunately, the steel of the electrodes has been investigated very thoroughly in preparation of the Boltzmann project at PTB [99]. The linear coefficient of thermal expansion α_{th} was measured in an accredited calibration laboratory to be $\alpha_{\text{th}} = 9.92 \times 10^{-6}\,\text{K}^{-1}$ with a
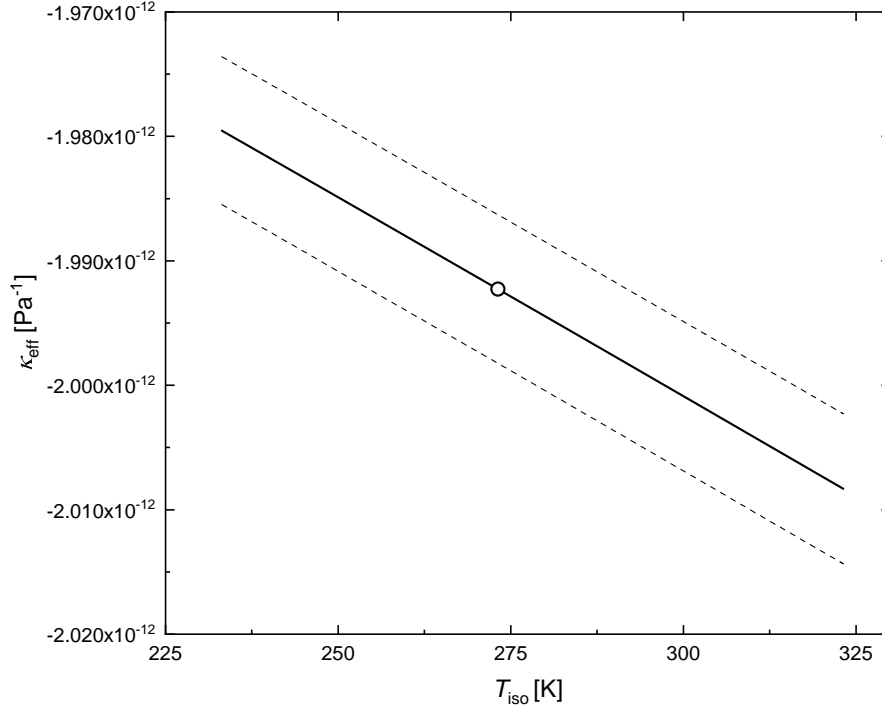
Figure 4.7.: Temperature dependance of the effective compressibility of the capacitors calculated from comprehensive RUS measurements utilizing the value published by Fellmuth *et al.* as base value [99]. The dashed lines indicate the combined relative standard uncertainties of 0.3 %.

relative standard uncertainty of 1.51 % at a temperature of 20 °C. The specific heat capacity at constant pressure was determined by the working group to be $c_p =$478.0 J kg^{-1} K^{-1} with a relative standard uncertainty of 1.5 %. A very accurate value of $\kappa_{\text{eff,ad}}=-1.9809 \times 10^{-12}$ Pa^{-1} with a relative standard uncertainty of 0.14 % at a temperature of 273.15 K was published by PTB in 2011 [99] and is used here as base value. To determine the compressibility at different temperatures, RUS measurements were performed between -40 °C and 50 °C to assess the temperature dependence of the elastic constants and thus $\kappa_{\text{eff,ad}}$. The results are best described by a linear function in temperature with the relative residuals at each point being less than 20 ppm. The final values of κ_{eff} of the capacitors plotted in figure 4.7 were calculated utilizing the highly accurate value of Fellmuth *et al.* at 273.15 K while the slope was determined from the additional RUS measurements. These final values include a small correction due to the c-axis oriented sapphire spacers. The effective compressibility κ_{eff} at a certain temperature is then calculated by:

$$\kappa_{\text{eff}} = -1.9923 \cdot 10^{-12} \, \frac{1}{\text{Pa}} - 3.198 \cdot 10^{-16}(T_{\text{iso}} - 273.15 \text{ K}) \, \frac{1}{\text{KPa}} \tag{4.6}$$

In principle, the corrections to the very accurate value at 273.17 K are small and also the properties required for the conversion from adiabatic to isothermal conditions are known

4. Experimental background

with small uncertainties. The uncertainties calculated in accordance with the established formalisms of error propagation stated in the GUM and the formulas given above, thus, result in only slightly higher values compared to the low uncertainty of κ_{eff} at $273.15\,\mathrm{K}$. However, the capacitors are complex geometrical objects that may not always behave ideally. To assess an uncertainty that can be assigned to the values calculated by formula 4.6, additional FEM simulations of the capacitor were carried out on the one hand. The previously described mechanical constants were used as input parameters to simulate the deformation and resulting changes of capacitance under pressure. The disagreement between the formula and the FEM simulations is on a solid level of less than $1\,\%$. It is assumed that the two different geometries, which are used, are causing the remaining differences.

(a) C1

(b) C2

(c) C3

(d) C4
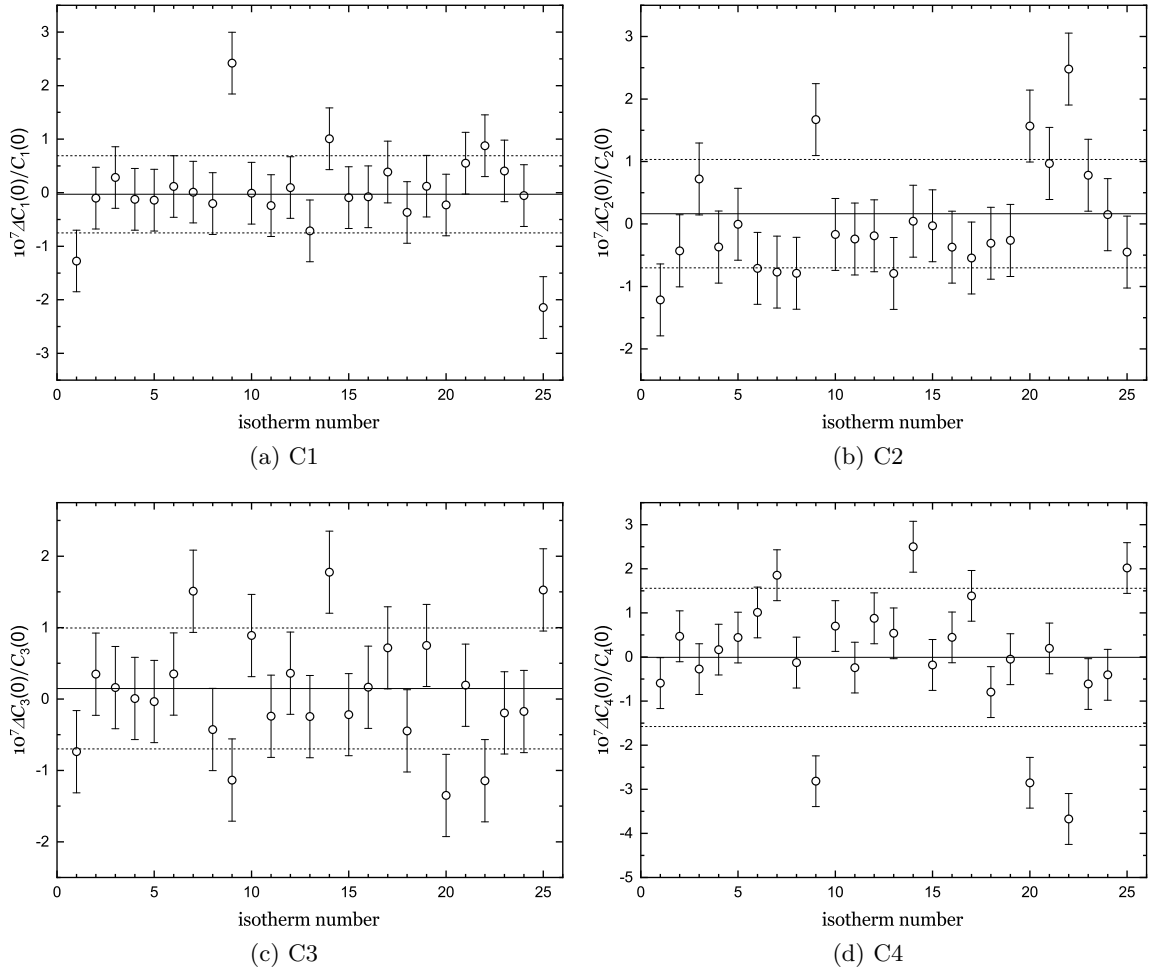
Figure 4.8.: Test of the stability of the vacuum reference value of the indicated capacitors. The black circles indicate the relative difference of the vacuum value of the capacitance before and after the corresponding expansion isotherm. The error bars represent the combined standard uncertainty for each data point calculated from the type A contribution (average of 30 measuring points) and the standard uncertainty of the assessed capacitance ratio (see section 4.3 for details). The solid line marks the average value while the dotted lines are the upper and lower boundary of the standard uncertainty of averaging the data points.

	C$_1$	C$_2$	C$_3$	C$_4$
$\Delta C(0)$	-0.3×10^{-8}	1.6×10^{-8}	1.5×10^{-8}	0.1×10^{-8}
u($\Delta C(0)$)	7.2×10^{-8}	8.7×10^{-8}	8.5×10^{-8}	15.7×10^{-8}

Table 4.2.: Average values and standard uncertainties of the relative differences of the vacuum capacitance before and after the expansion.

On the other hand information on the stability and deformation of the capacitors can also be retrieved from the experimental results. First, the capacitance values before and after the expansion in vacuum are required for the evaluation of the data and should be equal. The measured relative differences ΔC are plotted for the four used capacitors in figure 4.8. If the capacitors are stable under pressure changes, the average value of these deviations should ideally be zero while their scattering would represent the uncertainty of the capacitance ratio measurement. The average values and corresponding standard uncertainties are summarized in table 4.2. While zero lies well within the standard uncertainty of the average values, only the standard uncertainties of capacitors C$_1$ to C$_3$ agree with the stated uncertainty of the capacitance ratio measurement in section 4.3. C$_4$ features a standard uncertainty that is a factor of two larger than the expected value. Therefore, further investigations presented in section 5.1.1 were carried out. Essentially, it was proven that capacitor C$_4$ is not fully stable under pressure cycling. This is most likely due to the fact that all expansion were carried out by expanding into cell 4. Also, the automated evacuation procedure induces stress on the capacitor. Still, the capacitor was not changed for several reasons. First, there are still three fully functional capacitors that can be used to average the data. Furthermore, changing the capacitor without changing the evacuation routine would most likely lead to a damage of C$_4$ again. Most important, it is shown in section 5.2 that the volume ratios of the cells needs to be assessed with uncertainties in the order of few ppm. To evaluate the data retrieved in this thesis, it is ,thus, of crucial importance to not change these ratios. Instead, the changing zero capacitance is included as a linear drift for all capacitors. Further investigation of the effective compressibility of the capacitors and especially C$_4$ is carried out in section 5.1.1. Based on these observations, the relative uncertainty of κ_{eff} is set to $1.0\,\%$ for C$_1$ to C$_3$. The relative uncertainty of C$_4$ needs to be further increased to $2.5\,\%$.

4.1.4. Deformation of the measurement cells

As worked out in the previous chapter, the deformation of the measurement cells is important for the correction of the expansion experiments. To precisely determine the pressure deformation coefficients λ_A and λ_B of the measuring and expansion volume, two different approaches were used. On the one hand FEM simulations were performed using the software "COMSOL Multiphysics$^{\text{TM}}$". On the other hand analytical considerations for ideal cylinders were taken into account. In both cases, the elastic constants of the used steel (1.4301/X5CrNi18-10) are required as input parameters. To assess them, the results of RUS measurements, which were performed with this type of steel in the working group, were utilized. The results display the average of twelve different samples, which were measured

(a) electric field   (b) deformation
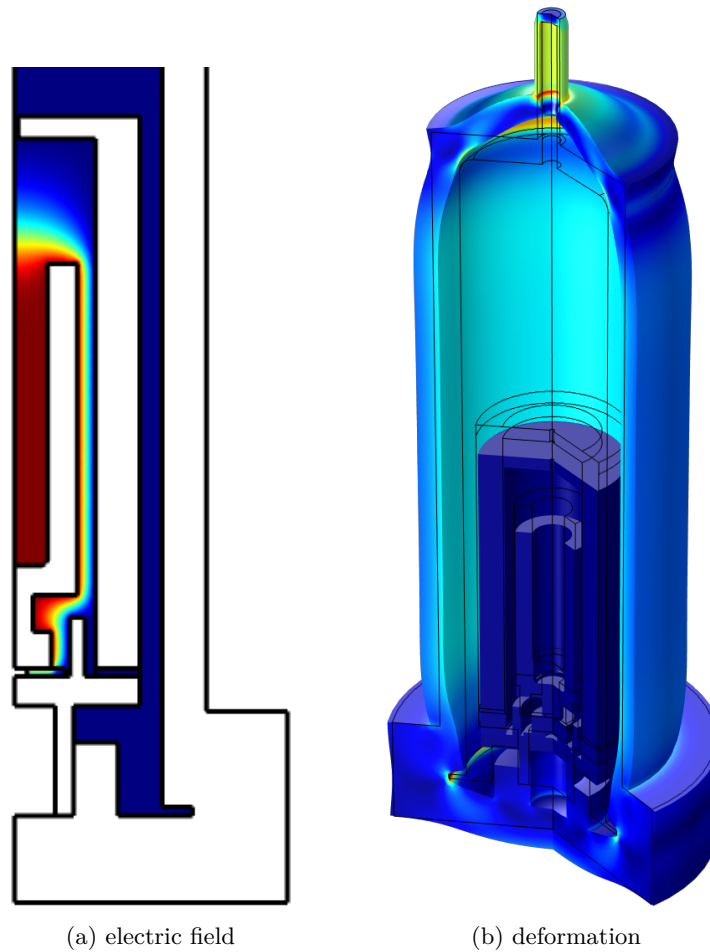
Figure 4.9.: FEM simulation of the measuring cell and the capacitor. a) Rotational symmetric electric field of the capacitor in the two dimensional cross cut. b) Schematic visualization of the deformation of the measuring cell and the capacitor under pressure.

at ambient temperature. The module of elasticity was determined to be $E =199.99\,\text{GPa}$, whereas the relative standard deviation of the 12 samples was $0.5\,\%$. The Poisson ratio μ_P is 0.2845 with the corresponding relative standard deviation being $1\,\%$.

The deformation of the regular measuring cell with an incorporated capacitor is schematically shown in figure 4.9 b). The corresponding FEM models were created for the regular and the smaller cell using the rotational symmetry neglecting the holes of the PEEK bushings that insulate the bolts holding the outer electrode. The sapphire washers used for the insulation were modeled as layers with the corresponding thickness of $1\,\text{mm}$. The results of these simulations are shown in table 4.3

In the literature, a variety of equations is used to estimate the deformation of cylindrical cells (see for instance [62, 100] and references within these). Since the ratio between the inner diameter and the thickness of the wall is $\frac{40\,\text{mm}}{6\,\text{mm}} = 6.7$, Lamés theorem for thick cylinders is applied. Based on stress and strain, the relative change of volume per pressure $\frac{\Delta V}{Vp}$ can

be calculated for a cylindrical measuring cell with closed ends that is exposed to internal pressure only by [62]:

$$\frac{\Delta V}{V p} = \frac{1}{E} \frac{1}{\left(\frac{r_o}{r_i}\right)^2 - 1} \left(2 \left(\frac{r_o}{r_i}\right)^2 (1 + \mu_P + 3(1 - 2\mu_P)) \right) \tag{4.7}$$

where $r_o = 26\,\mathrm{mm}$ and $r_i = 20\,\mathrm{mm}$ are the outer and inner radii of the cell, respectively. The result is at this point equal for both cells. To calculate the final pressure deformation coefficients, the volume and the compression of the capacitor under pressure need to be taken into account. These two corrections are separated in table 4.3 to demonstrate their influence. Neglecting the compression of the capacitor will already result in a relative deviation of λ_A of 4.3 % and even 7.0 % for λ_B. The agreement between the coefficients obtained by both methods is very good considering the complex base of the measuring cell. The relative deviations are in the order of only 0.3 %. Since the upper and lower end of the cell deform quite differently under pressure (see figure 4.9 b)), the results obtained by the FEM simulations are selected in this thesis. In addition to the values shown in table 4.3, the pressure deformation of the gas-handling system λ_{GHS} was estimated to be $2.81 \times 10^{-11}\,\mathrm{Pa}^{-1}$ from the used tubing. In principle, the low uncertainties of the elastic constants would allow to assign a comparably low uncertainty. Since the temperature dependence of the elastic constants is not known and since the FEM model is still a simplification of the complex construction, a more conservative relative standard uncertainty of 5 % is estimated here.

	λ_A [Pa^{-1}]	λ_B [Pa^{-1}]
empty cell (equation 4.7)	4.08×10^{-11}	4.08×10^{-11}
cell with capacitor (only volume)	5.76×10^{-11}	7.84×10^{-11}
cell with capacitor and its compression	6.01×10^{-11}	8.39×10^{-11}
FEM	5.99×10^{-11}	8.36×10^{-11}

Table 4.3.: Assessment of the pressure deformation coefficients by analytical means and in comparison to the value obtained from FEM modeling.

4.2. Pressure measurement

The assessment of pressure is one of the most prominent tasks in experiments with gases. For the typical pressure range of several MPa covered in this experiment, the most precise measuring devices besides toxic and bulky mercury manometers are pressure balances. It has been shown that they can achieve relative uncertainties of 1 ppm for pressures up to 7 MPa [9]. Their working principle can be directly derived from the definition of the pressure as force per area. A piston rotating in a cylinder and centered by the gas flowing around it may be loaded with cylindrical mass discs and kept floating on the gas column. The automated Ruska 2465 pressure balance and its main components used in this experiment are shown in figure 4.10. First, the standard bell jar was replaced by an acrylic glas version. This allowed

4. Experimental background
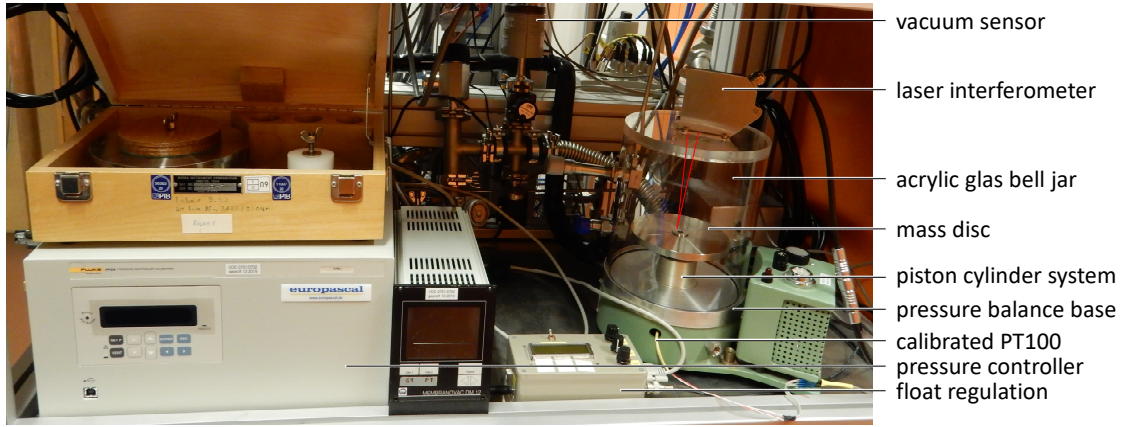
Figure 4.10.: The automated pressure balance and its main components used for the calibration of the digital pressure sensors.

to install a laser interferometer on top of the bell jar which measures the level of the floating masses. This information is processed by a small two point control unit based on an Arduino programmable PC connected to the PPC4 A7MU pressure controller from Europascal. The lower level, upper level and sensitivity can be set with three potentiometers. If the slowly sinking piston approaches the lower limit, the pressure controller is instructed to increase the pressure for a certain time depending on the sensitivity and checks the new level until the upper level is reached. This way the masses can be kept floating automatically. During the pressure regulation, the "Gas all" valve (see figure 4.4) connecting the measuring system with the pressure balance is closed. On the one hand this prevents potential impurities from the pressure controller to contaminate the measuring system to some extend. On the other hand the systems remains isolated in case the automation fails for some reason. Measurements were exclusively carried out in absolute mode evacuating the bell jar. Firstly, this way the buoyant effect of the otherwise present air can be excluded. Secondly, fluctuations of the ambient pressure, which would serve as a reference in gauge mode do not influence the measurement. The residual pressure p_{res} in the bell jar is measured with a capacitance manometer from MKS (type: Baratron 626C.1, maximum pressure: 13.3 Pa, relative uncertainty: 0.25 % of reading). The pressure of the pressure balance p_{pb} can be calculated by equation 4.8:

$$p_{\text{pb}} = \frac{g \left(\sum m_i + V_{\text{pb}}\rho_i \right)}{A_0 \left[1 + (\alpha + \beta)(t_{\text{pb}} - 20\ ^\circ\text{C}) \right] (1 + \lambda_{\text{pb}}p)} + p_{\text{res}} + \sum g h_i \rho_i \qquad (4.8)$$

The denominator term denotes the effective area $A_{\text{eff}} = A_0 \left[1 + (\alpha + \beta)(t_{\text{pb}} - 20\ ^\circ\text{C}) \right] (1 + \lambda_{\text{pb}}p)$ of the piston cylinder assembly. Key to achieving lowest uncertainties is the characterization of the ideal effective are A_0 by dimensional measurements or from cross floating comparisons. Temperature and pressure corrections have to be applied by the material parameters $(\alpha + \beta)$ and the coefficient λ_{pb} taking pressure deformation into account. The masses m_i used in this thesis were calibrated at PTB with relative uncertainties of less than 1 ppm ($k = 1$). To calculate the weight force, the local gravitational constant g needs to be

pressure balance	"Ruska 4"	"Ruska 5"	"Ruska 6"
serial number	V1408	C-619	G203
maximum pressure	7×10^6 Pa	7×10^5 Pa	3.5×10^6 Pa
V_{pb} in 10^{-6} m^3	0	-1.55 ± 0.02	0
A_0 in 10^{-5} m^2	$0.838\,757 \pm 0.000\,019$	$8.395\,842 \pm 0.000\,097$	$1.679\,560 \pm 0.000\,024$
$(\alpha + \beta)$ in 10^{-6} °C^{-1}	9.1 ± 1.0	9.1 ± 1.0	9.1 ± 1.0
λ_{pb} in 10^{-6} MPa^{-1}	0.9 ± 2.2	0	-1.25

Table 4.4.: Parameters of the three piston cylinder assemblies used for the investigation of the Digiquartz sensors.

well known as well since it depends on altitude, mass distribution and several other aspects of the surrounding area. The value used in this thesis $g = (9.812\,701\,0 \pm 0.000\,000\,1)$ m s^{-2} was measured in a calibration laboratory around 15 m away at the same altitude. In addition to the masses, some pistons are constructed in a way that gas volume described by the parameter V_{pb} increases the total mass load. Values of the introduced parameters for the three different tungsten carbide piston cylinder assemblies used are given in table 4.4. Finally, the hydrostatic pressure of the measuring gas is leading to a correction typically referred to as hydrostatic head correction. Since the pressure needs to be assessed at a different altitude and at a different temperature than the pressure balance, the height differences h_i and corresponding densities of the gas ρ_i for the different gas temperatures need to be determined.

A key requirement for expansion experiments is to maintain constant volumes. In previous setups, this was typically ensured by using highly accurate differential pressure diaphragms separating the measuring volumes from mercury manometers or pressure balances. These are very sensitive instruments suitable to measure low pressure differences. Their operation requires to set pressure on both sides carefully and simultaneously. Together with the manually operated pressure balances this complicates the automation in this work. That is why two commercially available pressure sensors (model: 9000-2K Digiquartz, manufacturer: Paro Scientific) with a working range up to 13.8 MPa were used in this work for the expansion isotherms. They will be referred to as "Digi$_1$" and "Digi$_2$" in the following.

Paro Scientific specifies a relative uncertainty of 100 ppm full scale for the pressure, which is certainly not sufficient for the targeted uncertainties. To overcome this limit, both sensors were calibrated at the pressure department of PTB in Braunschweig in a first step. Though the sensors technically reached relative expanded uncertainties of 25 ppm of the reading, it was not possible to work with them practically for two reasons. On the one hand the "zero" value of the sensor under vacuum that has to be subtracted from the measured pressure tends to drift. It can take more than a day until the indicated pressure appears to be stable. On the other hand the sensors are very sensitive to temperature changes. Both effects are well known [101] and, therefore, corrected by the manufacturer in the characteristic function to a level that allows to reach the claimed uncertainty level. Although the sensors are temperature stabilized together with the other components of the gas-handling system, they have slightly different temperatures depending on the measuring temperature. Furthermore,

(a) Digi1 (b) Digi2
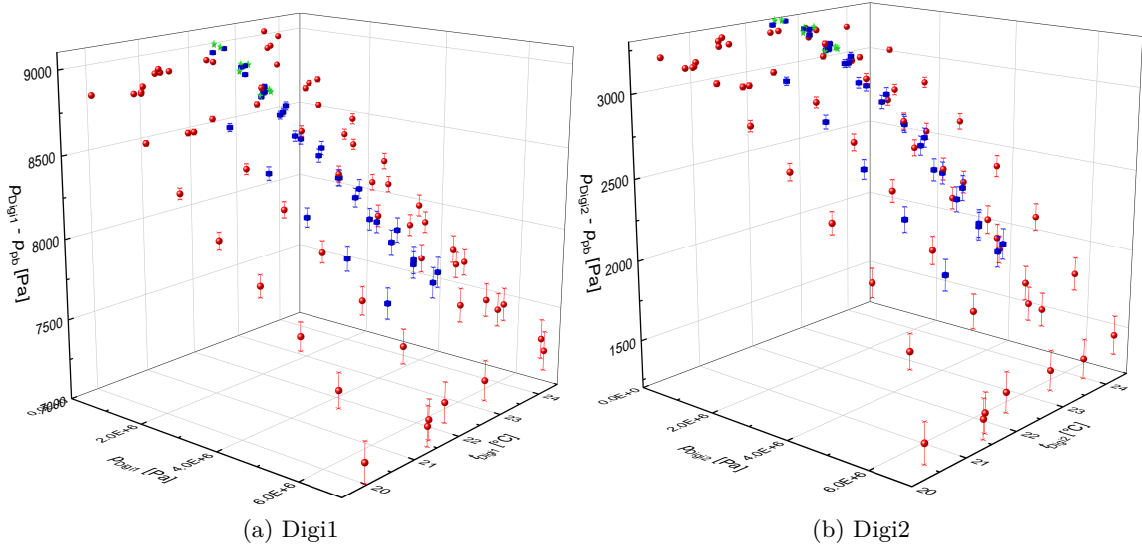
Figure 4.11.: Three dimensional plot of the absolute pressure difference between the pressure sensors and the three piston cylinder assemblies "Ruska 4" (red dots), "Ruska 5" (green stars) "Ruska 6" (blue cubes) specified in table 4.4. The error bars include uncertainties of the pressure balances and the standard uncertainty of the Digiquartz sensors during each measurement.

the temperature slightly changes depending on whether the system is connected to the pressure balance or isolated during the expansion cycles. Therefore, extensive comparisons with three different pressure balances, whose characteristics are summarized in table 4.4 were carried out to investigate the temperature dependence of the measured pressure value and to investigate the reachable uncertainty.

The results of these measurements are shown in figure 4.11. Plotted is the absolute difference between the pressure of the pressure balance p_{pb} and the value shown by the Digiquartz sensors (without correction of the vacuum value) as a function of the sensor temperature t_{Digi} and the pressure value indicated by the Digiquartz.

Upon the closer investigation it became evident that the pressurized sensors typically reach reproducible and stable values within hours instead of days. Thus, it is assumed that the poor zero performance is a temperature effect due to low thermal conduction without the measuring gas. Therefore, in a second attempt, the definition of an absolute characteristic surface from the points plotted in figure 4.11 was intended. While Digi$_1$ can be sufficiently described by a characteristic plane, Digi$_2$ features a curvature that can be described by including a (temperature independent) quadratic term. Unfortunately, the deviations in the lower pressure range still exceeded several ten ppm using this attempt.

That is why a calibration procedure of the Digiquartz sensors was included in each isothermal expansion. In the beginning the pressure balance equipped with the "Ruska 4" high pressure piston cylinder assembly is used to calibrate the Digiquartz sensors when filling the system at a pressure of 7 MPa. After the expansion cycles are finished, a second calibration with the same pressure balance is performed at 1 MPa. A detailed description of the com-
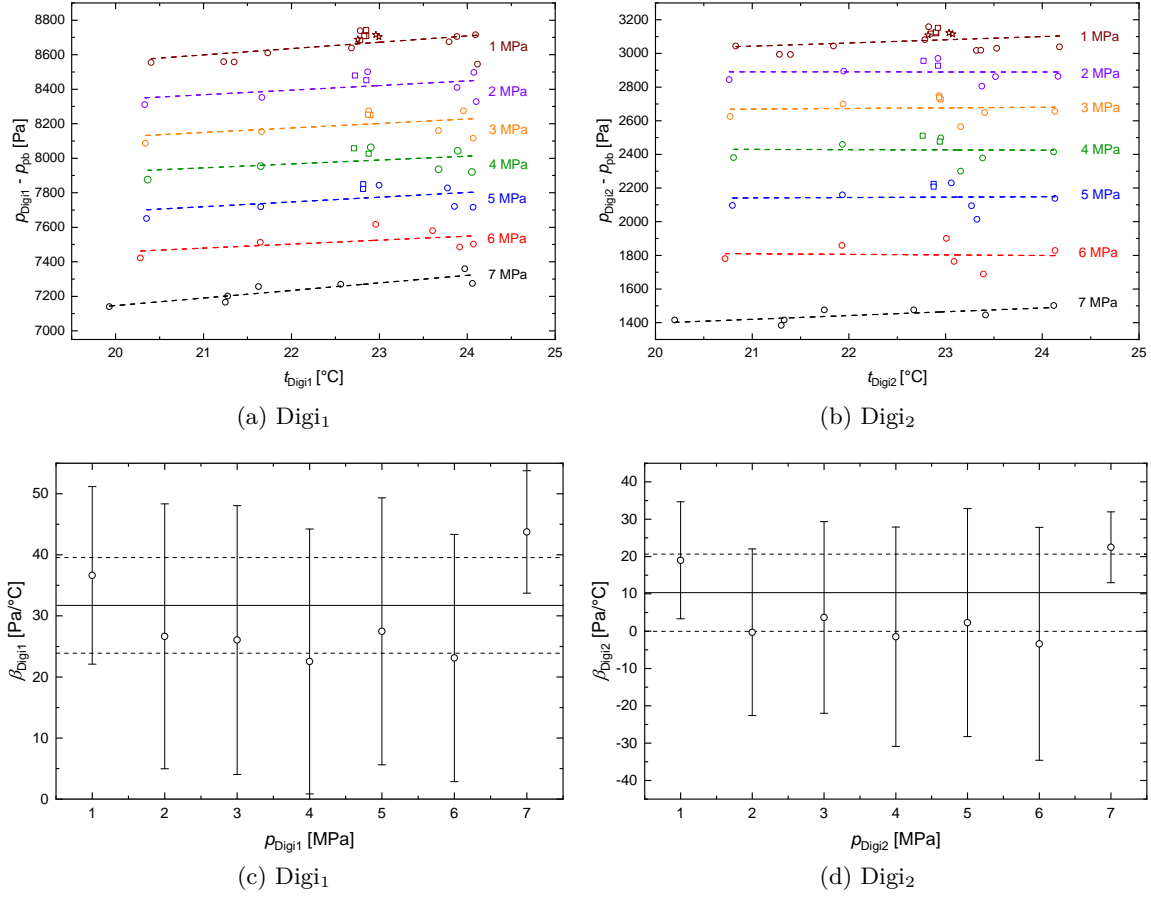
Figure 4.12.: (a) and (b) show the data points of figure 4.11 displayed in the Δp-t_{Digi} plane to assess the temperature dependance of the absolute pressure deviation. The data sets are categorized in the labeled pressures and were measured with "Ruska 4" (open circles), "Ruska 5" (open stars) and "Ruska 6" (open squares). The dashed lines are linear fits applied to the constant pressure data. Their slopes are plotted as a function of pressure in (c) and (d) together with the standard uncertainties of the fit. In (c) and (d) solid lines mark the mean average value of the slope while the dashed line is the standard deviation of the average value.

plete measuring routine will be given in section 4.6. To determine a suitable characteristic surface from only these two calibration points, the temperature dependence of the pressure correction needs to be extracted separately. Therefore, linear temperature coefficients as illustrated in figure 4.12 were retrieved by analyzing the three dimensional plots of figure 4.11 again in the Δp-t_{Digi} plane. From these plots, a pressure dependance of the temperature sensitivity is neither reportable for Digi_1 nor Digi_2. Thus, the individual slopes were determined by linear fitting of the distinct pressures and plotted together with their standard error from the fit in plots 4.12 (c) and (d). The pressure independent temperature sensitivities are $\beta_{\text{Digi}_1} = (31.73 \pm 7.83)\,\text{Pa}\,°\text{C}^{-1}$ for Digi_1 and $\beta_{\text{Digi}_2} = (10.31 \pm 10.35)\,\text{Pa}\,°\text{C}^{-1}$ for Digi_2. The second requirement is that the characteristic curve is linear. The plane character in figure 4.11 (a) indicates that this can be well assumed for Digi_1. Further investigations approving the linearity are presented in figure I.1 of appendix I. As already shown in figure 4.11, Digi_2

4. Experimental background

exhibits a quadratic rather than a linear characteristic curve, which cannot be fixed by only two calibration points. A more detailed plot of the quadratic contribution is also shown in appendix I in figure I.2. Fortunately, this quadratic coefficient is independent of temperature and was determined to be $c_{\mathrm{Digi_2}} = (-1.66 \pm 0.12) \times 10^{-11}\,\mathrm{Pa}^{-1}$ from the comparisons to the pressure balances. This reduces the free parameters of the quadratic characteristic curve leaving two, which are defined by the two calibration points before and after the expansion cycle.
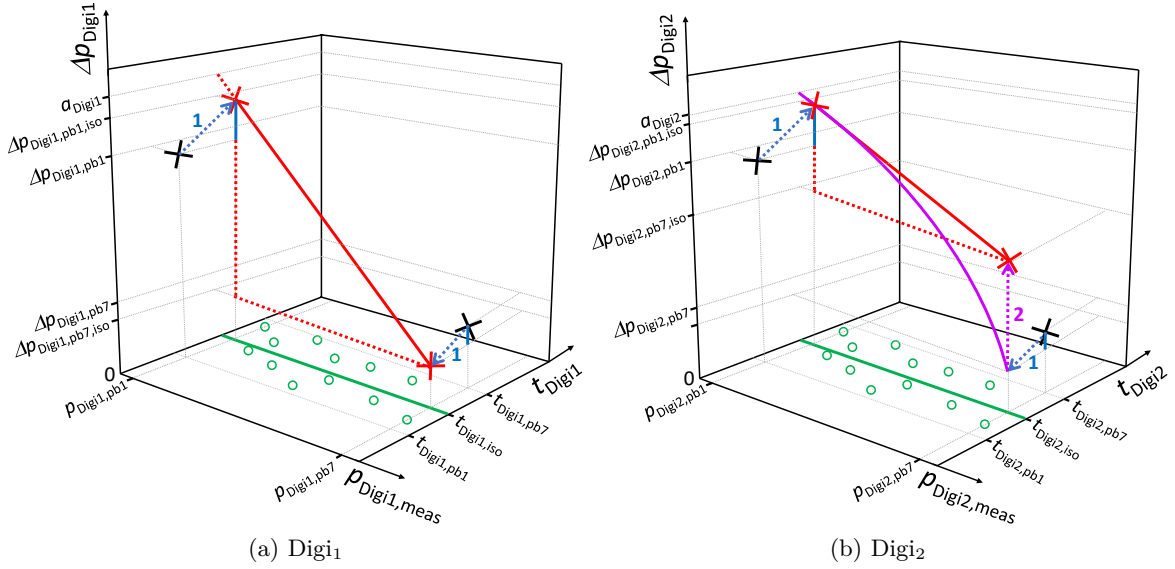
(a) $\mathrm{Digi_1}$ (b) $\mathrm{Digi_2}$

Figure 4.13.: Schematic principle of the calibration of (a) $\mathrm{Digi_1}$ and (b) $\mathrm{Digi_2}$. The black crosses denote the two pressure balance calibration points. They are corrected to the average Digiquartz temperature $t_{\mathrm{Digi,iso}}$ (indicated by the solid green line) in step **1**, which is illustrated by the blue arrows. For $\mathrm{Digi_1}$, a sufficient characteristic linear function (solid red line) in the Δp_{Digi}-$p_{\mathrm{Digi,meas}}$ plane is now fixed by the two corrected values (red crosses). $\mathrm{Digi_2}$ has an overall quadratic characteristic function (purple line) in the Δp_{Digi}-$p_{\mathrm{Digi,meas}}$ plane. This requires to perform a **2**nd correction illustrated by the purple arrow to obtain the linear part (solid red line) of the characteristic function, which is then also fixed by the two red crosses. Further explanations and the corresponding equations are given in the text.

The calibration routine of the pressure sensors is schematically illustrated in figure 4.13 in a three dimensional model, similar to the plots in figure 4.11. Essentially, the procedure can be visualized for $\mathrm{Digi_1}$ by a plane whose slope in the $t_{\mathrm{Digi_1}}$ direction is defined by $\beta_{\mathrm{Digi_1}}$ (blue dotted line), which was, therefore, retrieved in figure 4.12. The slope and intercept of the plane in the $p_{\mathrm{Digi,meas}}$ direction (solid red line) needs to be assessed by the two pressure balance calibration points (black crosses). The behavior of $\mathrm{Digi_2}$ is more complex due to the quadratic contribution and will be discussed later. The goal is to fix the plane (or surface for $\mathrm{Digi_2}$) by calibration so that Δp_{Digi} can be determined at each data point to calculate the final and corrected Digiquartz pressures by:

$$p_{\text{Digi}_1} = p_{\text{Digi}_1,\text{meas}} - \Delta p_{\text{Digi}_1}$$
$$p_{\text{Digi}_2} = p_{\text{Digi}_2,\text{meas}} - \Delta p_{\text{Digi}_2}$$

(4.9)

Therefore, the average value of the sensor temperature $t_{\text{Digi}_1,\text{iso}}$ or $t_{\text{Digi}_2,\text{iso}}$ during the isothermal measurement is calculated from the individual data points (green circles) as indicated by the solid green line. Starting point of the calibration are the two pressure balance measurements at $7\,\text{MPa}$ and $1\,\text{MPa}$ marked by the two black crosses. The corresponding pressures of the Digiquartz are defined as $p_{\text{Digi}_1,\text{pb7}}$ and $p_{\text{Digi}_1,\text{pb1}}$, whereas the sensor temperatures are $t_{\text{Digi}_1,\text{pb1}}$ and $t_{\text{Digi}_1,\text{pb7}}$. The difference to the pressure of the pressure balance p_{pb1} and p_{pb7} is the required correction Δp_{Digi_1} and Δp_{Digi_2} at these conditions:

$$\Delta p_{\text{Digi}_1,\text{pb1}} = p_{\text{Digi}_1,\text{pb1}} - p_{\text{pb1}}$$
$$\Delta p_{\text{Digi}_1,\text{pb7}} = p_{\text{Digi}_1,\text{pb7}} - p_{\text{pb7}}$$
$$\Delta p_{\text{Digi}_2,\text{pb1}} = p_{\text{Digi}_2,\text{pb1}} - p_{\text{pb1}}$$
$$\Delta p_{\text{Digi}_2,\text{pb7}} = p_{\text{Digi}_2,\text{pb7}} - p_{\text{pb7}}$$

(4.10)

The defined differences in equation 4.10 need to be corrected to the average sensor temperatures $t_{\text{Digi}_1,\text{iso}}$ and $t_{\text{Digi}_2,\text{iso}}$ indicated by the solid green line since the slope of the temperature dependence is already fixed by β_{Digi_1} and β_{Digi_2}. This correction **1** is indicated by the blue dotted arrows, whereas the magnitude of the correction is visualized by the solid blue lines. For Digi_1, these two corrected data points (red crosses) are sufficient to fix the linear characteristic function (solid red line) in the Δp_{Digi_1}-$p_{\text{Digi}_1,\text{meas}}$ plane. Digi_2 has a quadratic characteristic function in this plane, which is illustrated by the solid purple line in figure 4.13 (b). This requires to perform a **2**nd correction, which is indicated by the purple arrow. The quadratic contribution is subtracted to obtain the linear part (solid red line), which is now also fixed by the corrected calibration points (red crosses). The application of these corrections yields:

$$\Delta p_{\text{Digi}_1,\text{pb1},\text{iso}} = \Delta p_{\text{Digi}_1,\text{pb1}} + \beta_{\text{Digi}_1}\left(t_{\text{Digi}_1,\text{iso}} - t_{\text{Digi}_1,\text{pb1}}\right)$$
$$\Delta p_{\text{Digi}_1,\text{pb7},\text{iso}} = \Delta p_{\text{Digi}_1,\text{pb7}} + \beta_{\text{Digi}_1}\left(t_{\text{Digi}_1,\text{iso}} - t_{\text{Digi}_1,\text{pb7}}\right)$$
$$\Delta p_{\text{Digi}_2,\text{pb2},\text{iso}} = \Delta p_{\text{Digi}_2,\text{pb1}} + \beta_{\text{Digi}_2}\left(t_{\text{Digi}_2,\text{iso}} - t_{\text{Digi}_2,\text{pb1}}\right) - c_{\text{Digi}_2}p_{\text{Digi}_2,\text{pb1}}^2$$
$$\Delta p_{\text{Digi}_2,\text{pb7},\text{iso}} = \Delta p_{\text{Digi}_2,\text{pb7}} + \beta_{\text{Digi}_2}\left(t_{\text{Digi}_2,\text{iso}} - t_{\text{Digi}_2,\text{pb7}}\right) - c_{\text{Digi}_2}p_{\text{Digi}_2,\text{pb7}}^2$$

(4.11)

The solid red lines, which are now fixed by the two corrected calibration points (red crosses) for both sensors, may be described by the intercept a_{Digi_1} (a_{Digi_2}) and the slope b_{Digi_1} (b_{Digi_2}):

$$
\begin{aligned}
a_{\text{Digi}_1} &= \Delta p_{\text{Digi}_1,\text{pb1},\text{iso}} - b_{\text{Digi}_1} p_{\text{Digi}_1,\text{pb1}} \\
b_{\text{Digi}_1} &= \frac{\Delta p_{\text{Digi}_1,\text{pb7},\text{iso}} - \Delta p_{\text{Digi}_1,\text{pb1},\text{iso}}}{p_{\text{Digi}_1,\text{pb7}} - p_{\text{Digi}_1,\text{pb1}}} \\
a_{\text{Digi}_2} &= \Delta p_{\text{Digi}_2,\text{pb1},\text{iso}} - b_{\text{Digi}_2} p_{\text{Digi}_2,\text{pb1}} \\
b_{\text{Digi}_2} &= \frac{\Delta p_{\text{Digi}_2,\text{pb7},\text{iso}} - \Delta p_{\text{Digi}_2,\text{pb1},\text{iso}}}{p_{\text{Digi}_2,\text{pb7}} - p_{\text{Digi}_2,\text{pb1}}}
\end{aligned}
\tag{4.12}
$$

This way the characteristic plane of Digi_1 and surface of Digi_2 is well defined. The corrections Δp_{Digi_1} and Δp_{Digi_2} can be retrieved for any measured pressure $p_{\text{Digi},\text{meas}}$ and sensor temperature t_{Digi} as demanded in the beginning of this explanation in equation 4.9. The final pressures p_{Digi_1} and p_{Digi_2} of the sensors during the isothermal measurement are then calculated by:

$$
\begin{aligned}
p_{\text{Digi}_1} &= p_{\text{Digi}_1,\text{meas}} - (a_{\text{Digi}_1} + b_{\text{Digi}_1} p_{\text{Digi}_1,\text{meas}}) + \beta_{\text{Digi}_1} \left(t_{\text{Digi}_1,\text{iso}} - t_{\text{Digi}_1} \right) \\
p_{\text{Digi}_2} &= p_{\text{Digi}_2,\text{meas}} - (a_{\text{Digi}_2} + b_{\text{Digi}_2} p_{\text{Digi}_2,\text{meas}} + c_{\text{Digi}_2} p_{\text{Digi}_2,\text{meas}}^2) + \\
&\quad \beta_{\text{Digi}_2} \left(t_{\text{Digi}_2,\text{iso}} - t_{\text{Digi}_2} \right)
\end{aligned}
\tag{4.13}
$$

To test the validity and assign an uncertainty to this procedure, the following efforts were made. Essentially, the comparisons to the pressure balances described previously were performed either by starting at zero pressure adding mass discs till the highest pressure was reached or starting at the highest pressure with reducing the mass. The pressure sensors are in most cases not evacuated in between the assessment of the data points, which is comparable to the expansion cycles described in section 4.6. To test the procedure, characteristic curves were assigned to the Digiquartz sensors with the highest and lowest pressure measured with the pressure balance in each individual measurement. The Digiquartz values at the intermediate pressures were then calculated by equation 4.13 and compared to the values of the pressure balance. The corresponding relative deviations plotted in figure 4.14 are on a level which is mostly below 10 ppm at 1 MPa and 5 ppm at 7 MPa. This estimation of uncertainty is shown as dashed line. A second aspect that needs to be taken into account for the final uncertainty budget is to distinguish between strictly statistical contributions and these of systematic origin. To estimate the statistical contribution, the differences between consecutive points was analyzed for the individual measurements. Based on this investigation, a constant statistical uncertainty of 5 ppm for the entire pressure range is assigned. Another systematic component of 8.6 ppm is added at 1 MPa, so that combining both components results in the dashed line plotted in figures 4.14 (a) and (b).

An additional cross check can be performed by direct comparison of the pressure difference between Digi_1 and Digi_2. Differences should be of statistical origin exclusively. In figure 4.15, two different cases are shown. The first plot shows the relative deviations of the calculated pressures for the measurements with the pressure balances. The second case summarizes
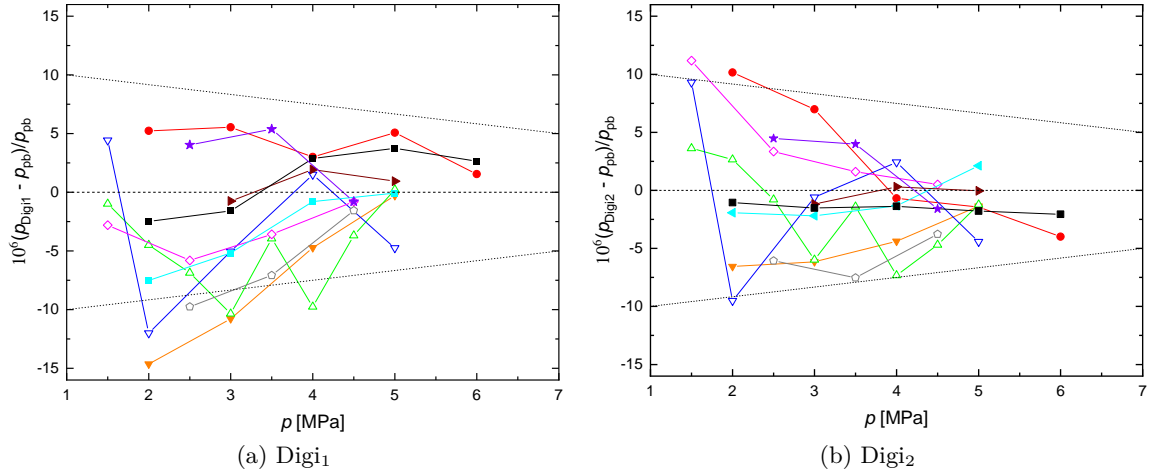
Figure 4.14.: Relative differences between the pressures of the pressure balance and the ones derived from the Digiquartz sensors in ppm utilizing equation 4.13. Solid symbols denote experiments with the "Ruska 4" and open symbols with the "Ruska 6" piston cylinder assembly. Equal symbols denote one measurement run. The dashed lines denote the assigned uncertainty of the Digiquartz sensors for the interpolation of pressures between the two pressure balance calibration points.

the relative differences of the two pressure sensors for different isothermal measurements with argon at four temperatures (see table 5.1 in chapter 5). The deviations are below 10 ppm in both cases and certainly within the combined uncertainty that is assigned to the Digiquartz sensors. While the deviations in (a) appear to be of statistical origin only, a systematic characteristic occurs in (b). This is assigned to the influence of the quadratic term $c_{\mathrm{Digi_2}}$ of $\mathrm{Digi_2}$. Eventually, also a characteristic curve including more parameters may be required to describe the behavior of $\mathrm{Digi_2}$ better but this is not an option here. However, since $c_{\mathrm{Digi_2}}$ was obtained from the measurements with the pressure balances it is not further adapted. Furthermore, the deviations are very well within the assigned combined standard uncertainties, which is taken as additional indication that the procedure of the calibration of the Digiquartz sensors is valid.

Assignment of an uncertainty to the pressure measurement is complex, on the one hand, due to the procedure shown above. On the other hand three different categories of uncertainty need to be distinguished to correctly calculate the error propagation in chapter 5. The different contributions are organized in table 4.5 following the calibration procedure. Uncertainties of category I are those causing identical relative deviations at the two calibration points as, for instance, the uncertainty of the effective Area A_0 of the pressure balance. Category II are contributions that also influence the calibration points but not equally. Category III are contributions that cause statistical scattering of the interpolation of the pressures. This subdivision is important since these categories are differently processed in the final error propagation of the results. Contributions of category I cancel completely for the determination of pressure ratios. These of category II influence the slope of the characteristic function and have a minor influence influence on the ratios. Contributions of category III need to be

(a) pressure balance calibration   (b) isothermal measurements
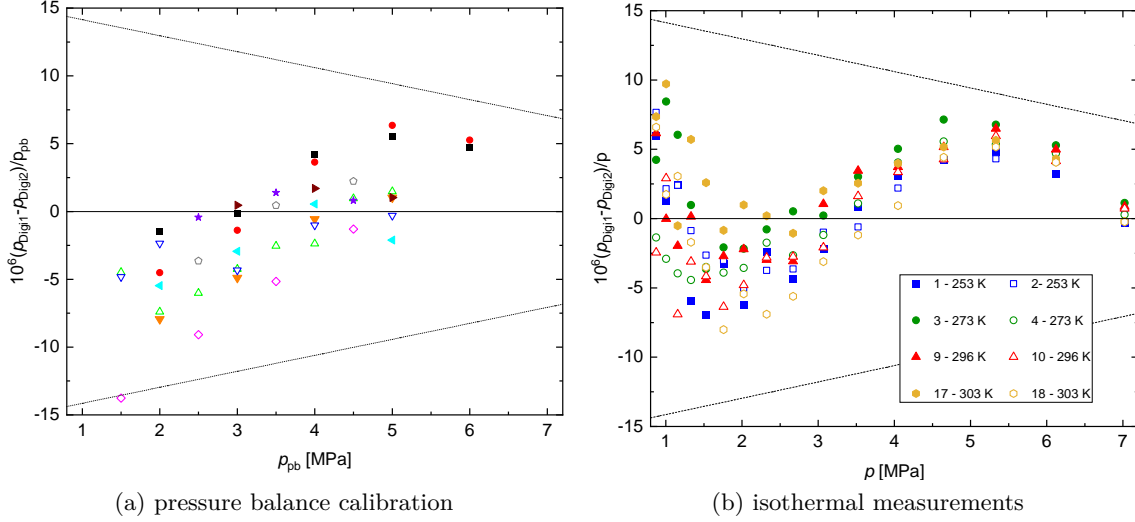
Figure 4.15.: Relative differences between the pressures of the Digiquartz sensors for a) the measurements with the pressure balance and b) for selected expansion isotherms. In (a), solid symbols denote experiments with the "Ruska 4" and open symbols with the "Ruska 6" piston cylinder assembly. Equal symbols denote the same measurements as in figure 4.14. The numbers of the isotherms in plot (b) are defined in table 5.1. Dashed lines in both plots mark the combined uncertainty for the difference of the pressure sensors.

evaluated by Monte-Carlo simulations. Further details on this topic is given in the sections covering the uncertainty budgets in chapter 5.

The largest contribution for the calibration is the uncertainty of the effective area A_0 of the piston cylinder assembly at $20\,°C$ and zero pressure. The second contribution of category I is based on the uncertainty of the temperature coefficient $(\alpha + \beta)$, which will be the same for both calibration points. All the following contributions are of category II and, thus, different at both points. These are the uncertainty of the temperature measurement for the correction of A_{eff}, the resolution of the pressure balance and the uncertainties of the used mass discs. The contribution of the head correction is dominated by the height differences of the floating piston due to the automation of the pressure balance described in the beginning of this section. The uncertainty contribution due to the correction to the average Digiquartz temperature by equation 4.11 is different for both sensors since the utilized coefficients β_{Digi} are different for both sensors. Contributions that are neglected since they are less than $0.01\,\mathrm{ppm}$ are the uncertainty of the pressure distortion λ_{pb}, the gravitational constant g and the residual pressure p_{res}.

The second source of uncertainty is the interpolation of the pressures between the two pressure balance calibration points. As already explained above, the overall contribution is divided into a pressure independent purely statistical contribution of $5\,\mathrm{ppm}$ (component interpolation 1) and another systematic contribution (component interpolation 2), which is described by the linear function $u[\mathrm{ppm}] = 8.60 - 8.60/6(p_{\mathrm{Digi}}10^{-6}\ \mathrm{Pa}^{-1} - 1)$. The resolution of the pressure sensors is already included in the statistical component. For Digi_2, an

pressure balance calibration

component	category	at 7 MPa [ppm]	at 1 MPa [ppm]
A_0	I	10.05	10.05
$(\alpha + \beta)$	I	2.00	2.00
t correction of A_{eff}	II	0.45	0.45
p balance resolution	II	0.33	2.30
mass discs m_i	II	1.25	0.70
head correction 1	II	1.94	1.94
correction to $t_{\mathrm{Digi_{1,iso}}}$	II	0.34	2.37
correction to $t_{\mathrm{Digi_{2,iso}}}$	II	0.44	3.11
interpolation of pressures			
component	category	at 7 MPa [ppm]	at 1 MPa [ppm]
interpolation 1	III	5.00	5.00
interpolation 2	II	0.00	8.60
$c_{\mathrm{Digi_2}}$	II	1.00	3.50
head correction 2	II	0.20	0.20
head correction 3	II	0.23	0.23
correction to $t_{\mathrm{Digi_{1,iso}}}$	II	0.12	0.84
correction to $t_{\mathrm{Digi_{2,iso}}}$	II	0.15	1.04
Digi$_1$ combined		**11.66**	**14.84**
Digi$_2$ combined		**11.70**	**15.39**

Table 4.5.: Overview of the uncertainty contributions to the pressure measurement at 7 MPa and at 1 MPa. Head correction 1 is carried out between the Digiquartz sensors and the pressure balance. Head corrections 2 and 3 are between the Digiquartz sensors and the measuring cells. Interpolation 1 is a constant statistical contribution, while interpolation 2 is a systematic contribution of the pressure sensor at 1 MPa. The combined standard uncertainties are valid for the assessment of the indicated absolute pressures with the Digiquartz sensors during the expansions. In case rectangular distributions were given, these were converted to standard uncertainties [7]. Further information on the contributions and an explanation of the categories is given in the text.

additional component arising from the uncertainty of the quadratic contribution described by $c_{\mathrm{Digi_2}}$ needs to be taken into account. A Monte-Carlo simulation was performed in which $c_{\mathrm{Digi_2}}$ was scattered by Gaussian distributed random numbers that were multiplied with the corresponding standard deviation. For each scattering, the characteristic function of a fix pressure balance data set was calculated and the resulting interpolated pressures were saved. After 500 simulations the standard deviations of the pressures were retrieved. The resulting contribution in ppm is best described by the function $3.5 - 2.5/6(p_{\mathrm{Digi}}10^{-6}\mathrm{Pa}^{-1} - 1)$. The influence at 7 MPa is 1 ppm which increases linearly to 3.5 ppm at 1 MPa. Further contributions to the isothermal measurements arise from the head correction between the pressure sensors and the measuring cells for the two different temperature regimes. This component is dominated by the uncertainty of the length measurement and, thus, taken into category II. Finally,the correction of each individual reported pressure value at a certain Digiquartz temperature needs to be corrected to $t_{\mathrm{Digi,iso}}$ (see equation 4.13).

4.3. Capacitance measurement

As explained in section 3.2, the dielectric constant is determined from the relative change γ of capacitance when filling a capacitor with gas. An assessment of absolute capacitance is not required. The most precise capacitance bridges used at PTB work by comparing the measuring capacitor C_X to a presumably constant reference capacitance C_N as depicted in the simplified circuit diagram in figure 4.16 [102].
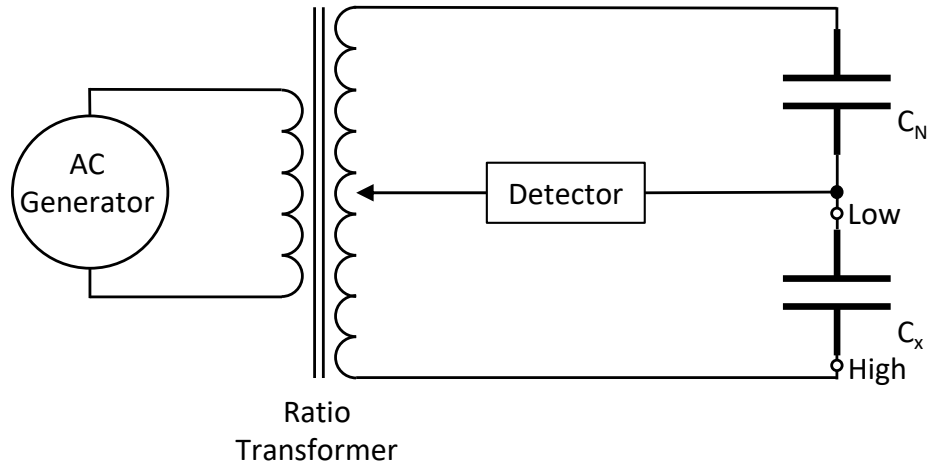
Figure 4.16.: Simplified circuit diagram of a capacitance bridge with a ratio transformer neglecting ohmic resistances of the leads and parasitic capacities of the cables. C_N is the reference capacitor, while C_X denotes the unknown capacitance. Low and High indicate the connectors of the AH 2500 bridge.

The bridge is balanced if no voltage drop is measured by the detector (typically a lock-in amplifier is used) along the middle path. A more detailed analysis of the working principle is given in [102, 103] and reveals the complexity of these measurements. Ohmic and non ohmic contributions have to be balanced by additional resistance decades, capacitors and the so called Wagner balance. By utilizing a custom built 9-decade inductive voltage divider as ratio transformer and a sinusoidal measuring voltage of $70.71\,\text{V}_{\text{RMS}}$ at a frequency of $1000\,\text{Hz}$, it is possible to measure relative changes of capacitance with a relative uncertainty in the order of 2×10^{-9}, which was required to determine the Boltzmann constant k with a relative uncertainty of $1.9\,\text{ppm}$ [19, 102]. Another requirement to achieve these specifications is a symmetrical circuit, which means that reference and measuring capacitance should be more or less equal. In current DCGT setups (see figure 3.2), this is achieved by placing two capacitors of identical construction in separated but closely located pressure vessels isothermally stabilized. While one acts as reference capacitor remaining evacuated, the other is filled with gas, thus, being the measuring capacitor. The required manual operation of this bridge is time consuming and offers very limited potential for automation or digital data acquisition, which is a key requirement for the apparatus designed in this work. That is why the most precise commercially available capacitance measurement bridge (manufacturer: Andeen Hagerling, model: AH2500 Option E) is used. It is an actual bridge in the sense

component	as specified	standard uncertainty
resolution	0.119 ppm	0.034 ppm
temperature sensitivity	±0.021 ppm/K	0.012 ppm
instability of C_N	±0.516 ppm/year	0.011 ppm
combined $\frac{C_X}{C_N}$		0.038 ppm
combined $\frac{C(p)}{C(0)}$		**0.054 ppm**

Table 4.6.: Contributions to the uncertainty for the measurement of capacitance ratios with the AH2500 Option E capacitance bridge. The second column lists the contributions as specified by the manual, while column three shows the converted contributions required for the current measurements. Details on their calculation is given in the text. The first listed combined uncertainty is the square root of the quadrature sum of the listed contributions. It is valid for the ratio of an unknown capacitance to the internal reference capacitor, while the second represents the combined uncertainty of a ratio of two unknown capacities as required in this work.

that it utilizes a ratio transformer for a comparative measurement, as layed out in figure 4.16 as well. In contrast to the custom built bridge, it incorporates highly stable temperature controlled fused-silica reference capacitors and uses a measuring voltage of up to $15\,\mathrm{V_{RMS}}$ with a frequency of 1000 Hz. Balancing of the bridge is automatically ensured with sets of relays and is carried out in less than one second. Schmidt and Moldover already reported in reference [97] that this bridge is capable of measuring capacitance ratios much better than with the specified accuracy of 3 ppm. To assess an uncertainty for the measurement of capacitance ratios, the following considerations have to be taken into account. First, it is important to visualize that though the bridge provides absolute capacitance values as an output quantity, it measures capacitance ratios R_C with respect to the internal reference capacitor C_N:

$$\frac{C(p)}{C(0)} = \frac{R_C(p)C_N}{R_C(0)C_N} \tag{4.14}$$

Equation 4.14 illustrates not only that the absolute value of C_N is not of significant importance since it cancels out. Uncertainty contributions to C_N that are of systematic nature and, thus, constant cancel out as well. Fortunately, the manual of the used bridge comprehensively describes the specifications, which allows to select the ones required for the assessment of capacitance ratios. They are summarized in table 4.6. The contribution arising from the difference in non-linearity was calculated but is negligible since all measured capacities are in the small capacitance range between 10 pF and 11 pF.

The listed specified contributions all have a rectangular distribution. In accordance with the GUM, the corresponding relative standard deviation is calculated by dividing the half width of the interval by $\sqrt{3}$. The contribution resulting from the temperature sensitivity was calculated with the instability of the temperature in the laboratory, which is less than ±1 K. Drifting of the reference capacitance C_N is only important for the time one isothermal
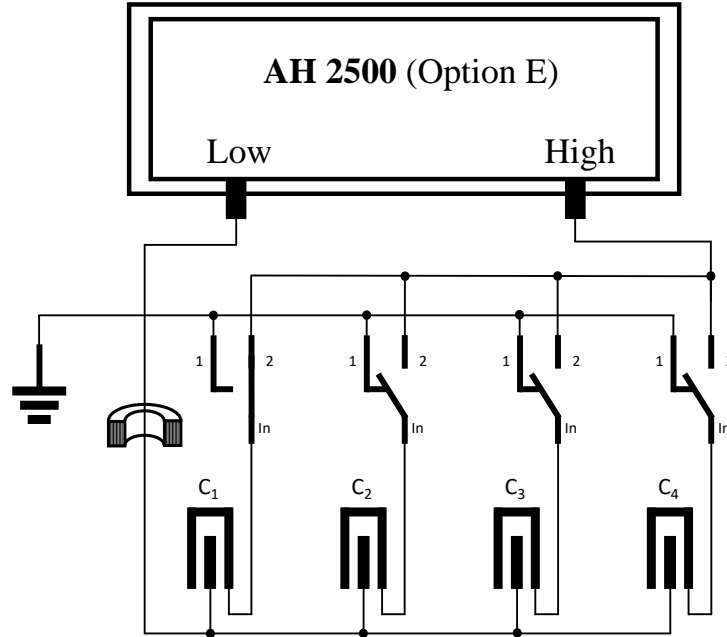
Figure 4.17.: Circuit diagram of the capacitance measurement. Capacitor C1 is measured, while the outer electrodes of C2, C3 and C4 are grounded. All cables have coaxial shields.

measurement takes. This is typically less than two weeks resulting in the contribution shown in column three. From these contributions, the relative standard uncertainty of the assessed capacitance ratio is determined to be $u_r \left(\frac{C(p)}{C(0)} \right) = 5.4 \times 10^{-8}$.

In total, four capacitors have to be measured with the capacitance bridge. As depicted in the circuit diagram in figure 4.17, four 12 Vdc SMA relays (manufacturer: Teledyne) with coaxial shields are used to switch between the outer electrodes connected to the the high port (relay position 1) of the capacitance bridge. The remaining three outer electrodes, which are not measured, are connected to ground (position 2). The inner electrodes of all four capacitors are interconnected and directly attached to the low port of the bridge. All cabling is established with coaxial shielding leading to a three terminal configuration for the capacitance measurement. The insulation resistance was verified to be beyond $30\,\text{G}\Omega$ for all connections. Between the electrodes and the close by located relays, low noise coaxial cable being less sensitive to mechanical stress and SMA connectors are used. The connection between the bridge and the relays is established with BNC connectors and a special coaxial cable with a low ground capacitance of only $43.3\,\text{pF/m}$ compared to typically $100\,\text{pF/m}$ for regular $50\,\Omega$ cable. The shielding ensures that noise cannot couple to the very sensitive capacitance measurement. However, ground loop currents in these shields can cause measuring errors, stray magnetic fields and sensitivity to background noise as well. That is why typically highly permeable toroidal cores, so called chokes, are used to suppress these currents in specific places by winding the cable around the choke [104]. In case of the used Andeen Hagerling bridge, the lead going to the "Low" connector is part of the middle arm (see circuit
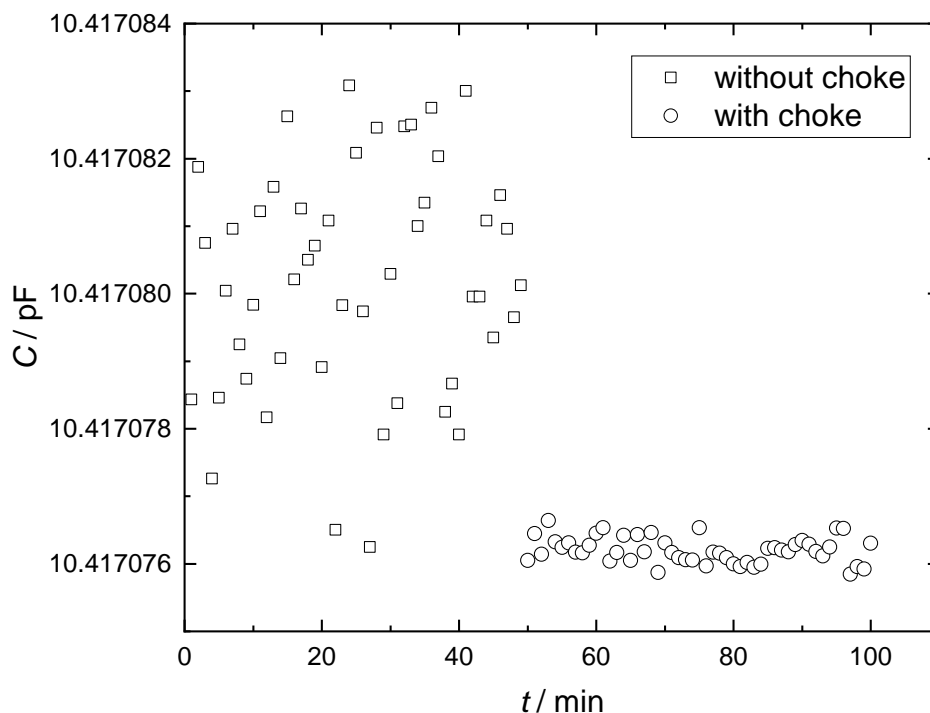
Figure 4.18.: Capacitance of capacitor C1 (evacuated, $T = 296.147\,\text{K}$) measured with and without a choke in the cable connected to the low port of the capacitance bridge.

diagram in figure 4.16) and, thus, explicitly vulnerable to noise which is why a choke has been included in the corresponding cable suppressing currents in the shield. The importance of this step is illustrated in the graph in figure 4.18 showing the measured capacitance for the evacuated capacitor C1 at a temperature of $296.147\,\text{K}$. The average value of the capacitance is lowered from $10.417\,080\,2\,\text{pF}$ to $10.417\,076\,2\,\text{pF}$, which corresponds to a relative change of 3.87×10^{-7} and is well within the bridges specified accuracy of $3\,\text{ppm}$. Furthermore, the scattering is significantly reduced by one order of magnitude from a relative standard deviation of 1.64×10^{-7} to 1.84×10^{-8}, which is the level that can be reported for almost all data points. Both effects are a consequence of currents induced by the ground capacitances and inductances of the lead and are well described in reference [104].

4.4. Temperature measurement

Temperature is obviously the key property of thermometry. Since primary thermometers for the determination of thermodynamic temperature are difficult, expensive and complex, temperature scales approximating the thermodynamic temperatures based on more manageable measurement principles were introduced. The currently valid temperature scale is the

4. Experimental background

ITS-90 [105]. All temperature values given in this thesis are ITS-90 temperatures unless stated otherwise (for instance for the thermodynamic temperatures determined by DCGT). The ITS-90 is based on a series of highly reproducible fix points linked to specific material properties with defined (ideally thermodynamic) temperatures in combination with methods to interpolate between them. In the temperature range between the triple point of hydrogen ($T_{90} = 13.8033\,\mathrm{K}$) and the freezing point of silver ($T_{90} = 1234.93\,\mathrm{K}$), standard **P**latinum **R**esistance **T**hermometer (PRT)s are used for interpolation. This transfers the problem of temperature measurement to a measurement of resistance. Therefore, two main components have to be considered for the determination of the temperature and the uncertainty that may be assigned to it. On the one hand the sensing thermometer is calibrated with a specific uncertainty. On the other hand the uncertainty of the resistance measurement by the used resistance bridge needs to be taken into account.

The most precise resistance measurement bridges work with ac voltages based an a Wheatstone bridge measurement principle with an inductive voltage divider similar to the system described for the capacitance measurement in section 4.3. These best commercially available transformer bridges used at PTB and other NMIs to calibrate resistance thermometers achieve relative uncertainties in the order of 2×10^{-8} for the measurement of resistance ratios and are traceable to the national standards at PTB. Though these bridges work in an automated fashion and enable a digital data acquisition, they typically need quite some time to balance. That is why in this work a "microK70" (manufacturer: Isotech) with the corresponding sample switch "microsKanner" employing dc voltages in combination with an extremely accurate **A**nalog-to-**D**igital **C**onverter (ADC) converter was used. It enables faster measuring while featuring a low uncertainty as well. In contrast to the previously described true bridge principle, this instrument can be visualized by a high accuracy voltmeter with a switch to measure the voltage drop over the reference resistor and the unknown resistance alternatingly with the same measuring current. The key innovative element of this bridge described in [106] is the ADC converting the measured voltages to a processable digital signal. It is based on a Σ-Δ ADC, which works with a feed back loop that compares the approximately generated digital signal from a simple ADC to the analog input signal with a high accuracy digital-to-analog converter. The difference of both signals is processed by a series of integrators and filters. To quantize the analog input signal, oversampling is used, which in combination with the integrators leads to spreading of the noise over a broad frequency range while the required signal only has a relatively small bandwidth that is digitally filtered leading to highly precise values. Reducing this noise can be achieved by increasing the sampling rate which has the drawback that the performance of the used elements drops. Instead, the "mircoK70" works with four integrators and a higher resolution using a 5 bit ADC. The corresponding highly accurate 5 bit digital-to-analog converter of the feedback loop uses pulse width modulation. The output signal has, thus, a fixed amplitude but a variable pulse width, which transfers the problem of generating accurate voltages to a problem of accurate timing. A $120\,\mathrm{kHz}$ clock is the timer of the system. With these modifications, a full accuracy measurement can be carried out in $100\,\mathrm{ms}$. The relative uncertainty specified

by the manufacturer for the assessed ratio of resistances is 0.07 ppm for the whole range and 0.017 ppm for ratios between 0.95 and 1.05. Traceability of this circuit to the national standard is, however, not possible. Verification of the specified uncertainties is, thus, only possible by comparison to resistance networks probing certain resistance ratios.

Since the bridge itself is only capable of assessing the ratio of two resistances, the absolute resistance of the thermometer is determined by comparison to a highly stable reference resistor. Though the "microK70" inhibits several internal reference resistors, typically calibrated, external reference resistors which are temperature stabilized inside an enclosure are used. In this work, a $25\,\Omega$ reference resistor (manufacturer: Tinsley Instrumentation Ltd, type: 5685A, $R=(25.000\,188\,0 \pm 0.000\,002\,1)\,\Omega$) was used to measure the $25.5\,\Omega$ CSPRT, and another $100\,\Omega$ reference resistor (manufacturer: Tinsley Instrumentation Ltd, type: 5685A, $R=(99.999\,660 \pm 0.000\,021)\,\Omega$) was used to measure the PRTs used for the assessment of the temperature differences inside the measuring chamber. Their calibration is traceable to the national standard at PTB. The assigned uncertainty includes a contribution of the stability for the entire time of the measuring period, whose results are shown here. This component was estimated from the documented development of resistance over time of the normal reference resistors.

To practically achieve lowest uncertainties, a four terminal configuration is required to connect the PRTs to the bridge. This ensures that the resistance of the interconnecting wires cancel out. Furthermore, the wiring of the thermometers was carried out following experiences from low temperature experiments where extreme care has to be taken to prevent heat flow to the system and PRT sensing elements. Therefore, 12 thin copper wires (diameter 0.2 mm) were glued together to form a strap, which was then winded and glued around a copper bobbin (diameter 10 mm, length 40 mm) that is bolted to the central copper plate. From there, the wires are soldered to a compact plate with 4-pin connectors to connect the thermometers. In total, four bobbins are installed allowing to connect up to 12 thermometers.

The CSPRT (manufacturer: Hart Scientific, type: 5695, serial number: 9507), which was used to determine the ITS-90 temperatures in this work, was calibrated by measurements at the triple point of water (273.16 K), the triple point of mercury (234.3156 K) and the melting point of gallium (302.9146 K). Temperatures, which are measured with the CSPRT in this range, have an uncertainty of 0.35 mK ($k = 1$) including minor contributions from the used resistance bridge and the reference resistor. However, the temperature differences, which were measured inside the system (see section 4.1.1), have to be taken into account as well. Since the measuring capacitors are located in the lower quarter of the measuring cells, the temperature difference over the cell is divided by a factor of 4 and added to the uncertainty of the temperature measurement. For measurements at the triple point of water and above, the uncertainty is, therefore, increased to 3 mK. For the measurements at 253 K, the gradients over the cells were larger due to the reasons described in section 4.1.1. In this case, the uncertainty of the temperature measurement is increased to 7.5 mK.

The second type of thermometers used for the temperature controller and for the assessment of the temperature differences inside the system are highly stable, hand selected PRTs

with a resistance of $100\,\Omega$. They were calibrated inside the apparatus developed in this thesis as well. Therefore, eight holes surrounding the centered $25.5\,\Omega$ CSPRT were drilled in the copper plate shown in figure 4.2 with a maximum lateral distance to the CSPRT of $15\,\text{mm}$ as calibration positions. Due to the high thermal conductivity of copper, temperature gradients across the plate can be neglected for these small distances. The thermometers were then distributed to the positions described in section 4.1.1. Their primary use is the assessment of temperature differences rather than the measurement of absolute temperature. The uncertainty that can be assessed for this purpose is based on repeatability, stability and hysteresis. Taking these effects into account, an uncertainty of $3\,\text{mK}$ for the assessment of temperature differences can be assigned.

4.5. Sample purity

The used gases (argon and helium) were ordered from Linde AG with a specified purity of 6.0 (99.9999 %) corresponding to an impurity level of less than $1\,\text{ppm}$. An additional helium gas purifier (type VICI HP2) from Valco Instruments Co. Inc. equipped with a non-evaporable getter alloy (zirconium, vanadium and iron) designed for the purification of noble gases was installed in line. According to the specifications, total inlet traces of $10\,\text{ppm}$ H_2O, H_2, O_2, N_2, NO, NH_3, CO and CO_2 are reduced to a level of less than $10\,\text{ppb}$.

To minimize adsorption to the walls, the used tubes are electro polished and high purity VCR components from the manufacturer Swagelok were used. The inside of the measuring chambers as well as the metal parts of the capacitors were gold plated to smoothen the surfaces and reduce adsorbtion. The gold plating of the custom made CF-40 flanges, which are the base the capacitors are mounted to, introduced an impurity problem. Though the incorporated SMA feed throughs were thoroughly sealed before the gold plating, the ceramic insulation was polluted leading to a reduced insulation resistance but also to slow out gassing and virtual leaks. To solve this issue, the flanges were mounted to left over measuring chambers and evacuated directly with a turbo pump stand while being heated to a temperature of $120\,°\text{C}$ for several days until the monitored pressure was less than $1 \times 10^{-6}\,\text{mbar}$ and the insulation resistance was beyond $30\,\text{G}\Omega$. After this procedure, the flanges were installed with the capacitors and thoroughly flushed with gas at high pressures.

A **Q**uadrupole **M**ass **S**pectrometer (QMS) (GAM400, InProcess Instruments) developed and calibrated to verify the purity of noble gases for the Boltzmann project at PTB was used to control samples of the measuring gas [19]. This particularly includes traces of other noble gases, which are not extracted by the gas purifier. In the performed measurements, the concentrations of other noble gases were very well below the specified level of $1\,\text{ppm}$.

4.6. Measurement procedure and automation

As emphasized in the previous chapters, automation of experiments is one of the key requirements for modern measuring devices. That is why the data acquisition from the measure-

ment equipment is carried out with two personal computers and a program developed by the working group in "LabVIEW" (National Instruments). It captures the averaged values of capacitance, different pressures and different temperatures synchronized one times per minute and stores them in a text file for each measuring instrument. This program runs independently from the second LabVIEW program controlling the expansions. The latter controls three relay cards with 8 relays each, which, in turn, are used to select the capacitor and to control pneumatic valves that, thereupon, switch the membrane valves of the gas handling and vacuum system (see schematic drawing of the gas-handling system in figure 4.4). Further details will be given later in the text.

Every isotherm measurement was carried out by the same routine, whereas each data point in the following description corresponds to an averaging time of two hours with 30 minutes per capacitor. First, the vacuum values $C(0)$ of the four capacitors are measured, before the chambers are filled with the measuring gas to a pressure slightly above 7 MPa. After thermal equilibrium is reached, the connecting valves "PBin", "PBout" and "GasAll" to the pressure balance (see schematic drawing of the gas-handling system in figure 4.4) are opened. The starting pressure of 7 MPa, which is ideally the same for all measurements, is established with the automated pressure balance. Furthermore, the measurement with the pressure balance marks the first calibration point for the characteristic function of the pressure sensors, as described in section 4.2. Then, the "GasAll" valve is closed defining the starting number of atoms in the system, and the LabVIEW program controlling the expansions is started. This program, whose flow diagram is shown in figure 4.19, is repeated for each expansion, whereas the number of the expansions is defined at the start of the routine. Capacitor C1 is measured until the thermal equilibrium is reached. The required waiting time is adapted to each expansion step independently and, typically, varies from 10 hours in the beginning to 5 hours for the smaller pressure steps by the end of the isothermal measurement. During this waiting time, the measured capacitor C1 offers an excellent instrument to control the thermal equilibrium. As long as the temperature changes, the length of the inner electrode changes resulting in a characteristic drift of the capacitance signal that can, actually, be resolved with the capacitance bridge. Before the other capacitors are measured, a check is performed to ensure that the data acquisition with the first LabVIEW program is working by comparison of the last date the text storage files were changed to the current time. The data acquisition can be restarted optionally. Then, the expansion starts by closing valve "Gas4" and evacuation of cell 4. This process is divided into three different steps. First, the high pressure is carefully lowered to less than 1×10^5 Pa by utilizing a bypass to the pump branch, which includes a restriction valve (open valves "FCIn" and "FCout") to reduce the pressure at the inlet of the membrane pump. If the pressure is less than 1×10^5 Pa, the membrane pump is used to evacuate the system directly via the valves "Pump" and "Byp3" until the pressure is low enough to utilize the turbo molecular pump (open valves "Byp1" and "Byp2"). Cell4 is evacuated to a pressure of less than 0.01 Pa before the corresponding vacuum valve "Vac4" is closed. Then, the gas is expanded into cell4 by opening the "Gas4" valve and measuring capacitor C1 starts again. This cycle is repeated until the defined number of expansions is
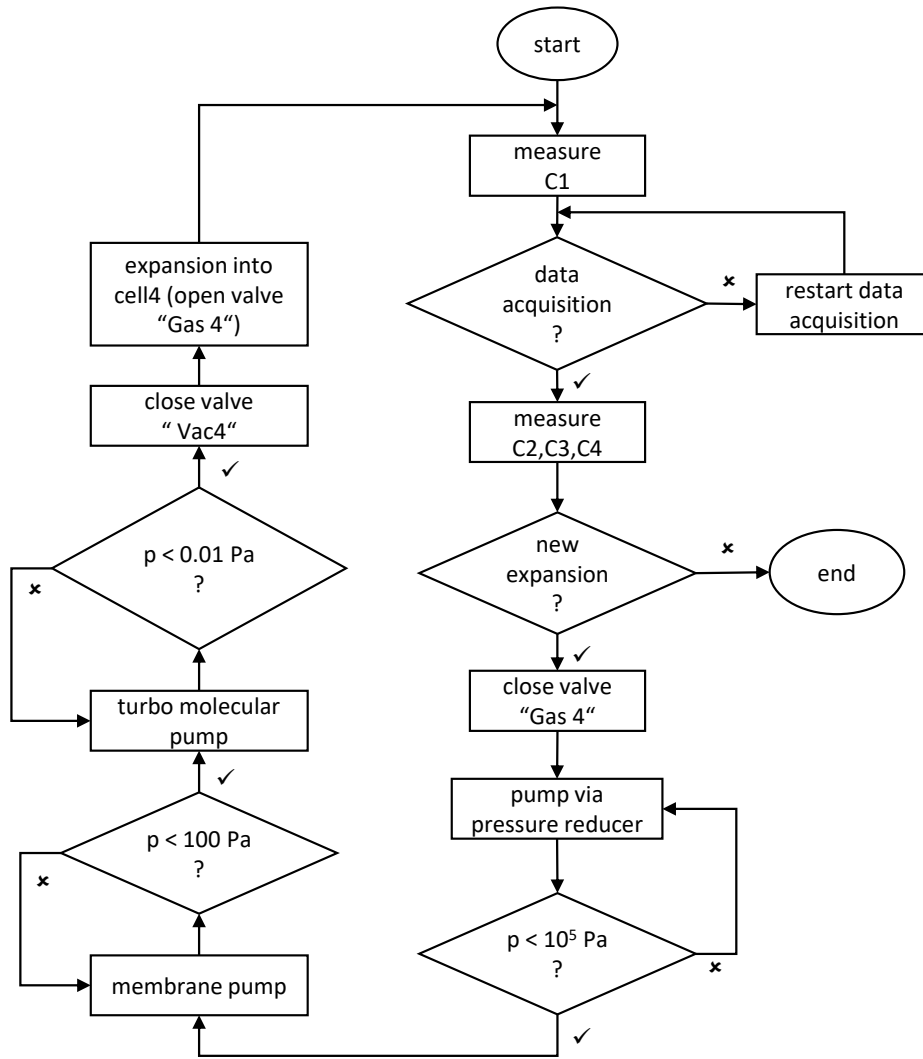
Figure 4.19.: Flowchart of the program used to automate the expansions.

performed. The number is selected in a way, that the last measured pressure is close to 1 MPa, which corresponds to 16 expansions for measurements with argon and 15 for measurements with helium. When the expansions have finished, a second measurement with the pressure balance at a pressure of 1 MPa is performed to obtain the second calibration point for the Digiquartz sensors. Finally, the entire system is evacuated and the zero capacitance of the four capacitors is measured after thermal equilibrium is reached. The time required to perform one isothermal measurement by the routine described above is typically in the order of two weeks.

4.7. Correction to isothermal conditions

The working equations derived in chapter 3 rely on the assumption of isothermal regimes. For the DCGT evaluation, this requires to correct either the pressure or the capacitance data to the average temperature T_{iso} of the isotherm. In this case, the measured pressures p_{meas}

were corrected by:

$$p_{\text{corr}} = p_{\text{meas}} \frac{T_{\text{iso}}}{T_{\text{meas}}} \tag{4.15}$$

Due to the impressive thermal stability of the central measuring system reported in section 4.1.1, the resulting corrections are minor and do typically not exceed the level of a few pascal. Instabilities of the gas-handling system temperature only play a negligible role by means of small differences in the head correction.

The situation is different for the expansion experiments. In this case, the working equations are based on the assumption of particle conservation before and after the measurement. Furthermore, the distribution of these particles in the system is treated by the assumption of two stable thermal regimes. As already emphasized, the thermal stability of the measuring cells is sufficient to comply with this assumption. In contrast, it was shown in section 4.1.1 that the temperature of the gas-handling system tends to change during the course of the isothermal measurement. This causes changes in the distribution of the particles between both thermal regimes, which are not anymore correctly described by the previously introduced assumptions. To correct these deviations, it is crucial to rely on the temperature of the gas-handling system (and the measuring cells) at the moment the interconnecting valve between measuring and expansion volume is closed. In this moment, the particle ratio of the expansion step is defined for the corresponding temperature ratio T_{ratio} between both thermal regimes. The strategy followed in this thesis is to generate pairs of data sets which are corrected to the temperature of this defining moment. The interconnecting valve is closed directly after measuring capacitor C_4. Therefore, the reference temperatures are the average temperatures during the 30 minute measuring period of capacitor C_4. The correction applied to the capacities C_1 to C_3 (and the corresponding pressure) prior to the expansion is rather small since the corresponding time differences are less than two hours. The correction of the values after the expansion is more prominent since the time required to reach the thermal equilibrium of the measuring chambers is in the order of several hours. From these values, the ratios of the Mosotti-terms F_{ratio} and pressures P_{ratio} required for the evaluation of the expansion experiments are calculated. A consequence of this procedure is that the same measured pressure and capacitance values of one data point are corrected twice, and eventually differently, depending on whether they are in the numerator or denominator of the ratio. The influence of this temperature correction is visualized in figure 4.20 (a) for the ratio of Mosotti terms at $296\,\text{K}$. The scattering of the ratios is clearly reduced, although the relative corrections, which are plotted in 4.20 (b), are only in the order of a few ppm. Furthermore, it will be shown in sections 5.3 and 5.4 that statistical scattering is the main source of uncertainty for the determination of the virial cofficients by means of free fits. For the example shown in figure 4.20, the relative difference between the second dielectric virial coefficient determined by the corrected and uncorrected data points is in the order of $7\,\%$, though the relative corrections shown in (b) rarely exceed $5\,\text{ppm}$. It is assumed

that the correction has an uncertainty of 20 % which corresponds to a relative uncertainty of P_{ratio} and F_{ratio} of 1 ppm due to the instability of T_{GHS}. This component is included in the uncertainty budgets in the corresponding sections 5.3 and 5.4 for the evaluation of the expansion experiments.

(a) capacitance ratios   (b) corrections
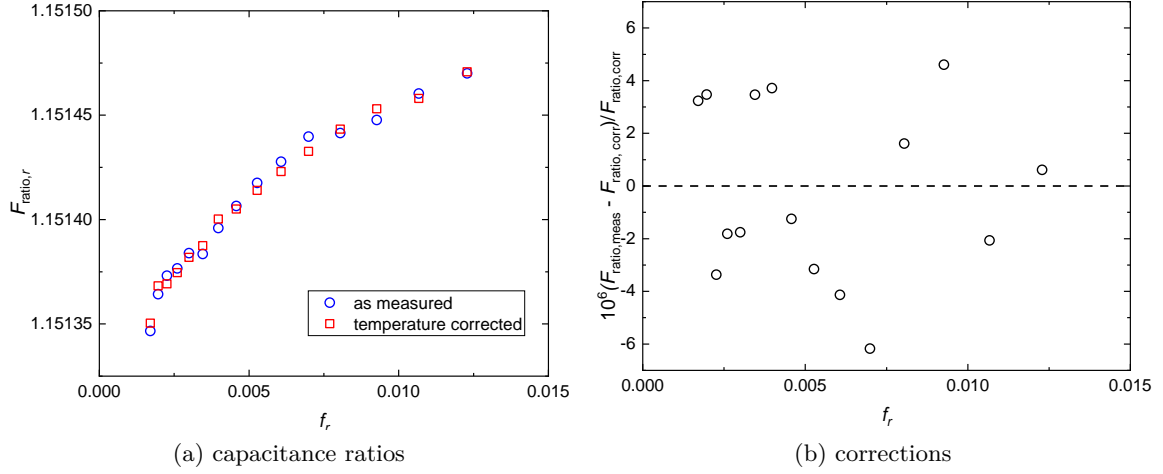
Figure 4.20.: Influence of the correction to the gas-handling system temperature described in the text by the example of isotherm number 9 measured at 296 K (see table 5.1 for further details). Shown in (a) are the averaged ratios of the Mosotti-terms F_{ratio}, which are fitted over the initial Mosotti-term for the evaluation of the dielectric expansion experiments before and after the correction. In (b), the relative changes in F_{ratio} caused by the corrections are shown in ppm.

5. Results

This thesis presents the results of a total of 24 isothermal measurements carried out at four different temperatures with argon and helium. They are numbered and summarized in table 5.1 to ease discussions.

argon

number	T_{iso} [K]	T_{GHS} [K]	number	T_{iso} [K]	T_{GHS} [K]
1	253.8977	294.150	10	296.1474	296.369
2	253.8973	294.056	11	296.1472	296.320
3	273.1617	295.757	12	296.1472	296.164
4	273.1618	295.715	13	296.0967	295.612
5	273.1621	296.072	14	296.0967	295.366
6	273.1622	295.821	15	296.0968	295.939
7	273.1612	295.504	16	302.9125	296.169
8	273.1588	294.704	17	302.9125	296.244
9	296.1475	296.484	18	302.9129	296.268

helium

number	T_{iso} [K]	T_{GHS} [K]	number	T_{iso} [K]	T_{GHS} [K]
19	273.1616	295.146	22	296.1475	296.287
20	296.1474	296.680	23	296.1469	296.162
21	296.1476	295.078	24	296.1462	296.054

Table 5.1.: Summary of the performed measurements used for the data evaluation in this thesis.

Each of the isotherms was measured by the automated procedure described in section 4.6. For each data point, the pressure was determined as average value of the two pressure sensors. It was shown in section 4.2 that both sensors have different working characteristics and, thus, different contributions to their uncertainty. Since it can be seen from table 4.5 that these differences in uncertainty are only minor, no weighing was applied. The same accounts for the capacities, where unweighed average values of the working variables μ retrieved from the four individual capacitors are used. It was worked out in section 4.3 that the effective compressibility of capacitor number 4 is higher than the others, but it will be shown in the uncertainty considerations of this chapter that this component is not a dominating contribution to the uncertainty of the final results. For the expansion experiments, the pressure ratios P_{ratio} and ratios of Mosotti-terms F_{ratio} have to be averaged independently and can not be recalculated from the averaged pressure and capacitance values due to the complex correction to the appropriate gas-handling system temperature described in section 4.7.

In this chapter, the summarized results are presented rather than all individual measurements. Individual isotherms will be referenced when appropriate. Furthermore, the evaluation of the data is focused on argon, while the measurements with helium serve for cross checks and calibration purposes. All uncertainties are given as standard uncertainties ($k = 1$) unless stated otherwise, whereas the individual contributions are considered to be not correlated.

In the next three sections, results based on the evaluation by means of DCGT (5.1), the Burnett (5.3) and the dielectric expansion (5.4) are shown. Since all determined properties and their uncertainty are based on different fit coefficients, each of these sections start with an overview of the fit coefficients and their uncertainty analysis, which is partially based on Monte-Carlo simulations. After that, the final results and their combined uncertainty is evaluated. A comparison to the established literature values is carried out in section 5.6 for the different virial coefficients, while the comparison of secondary results from the DCGT measurements is carried out directly in the corresponding sections of the DCGT results.

5.1. DCGT results
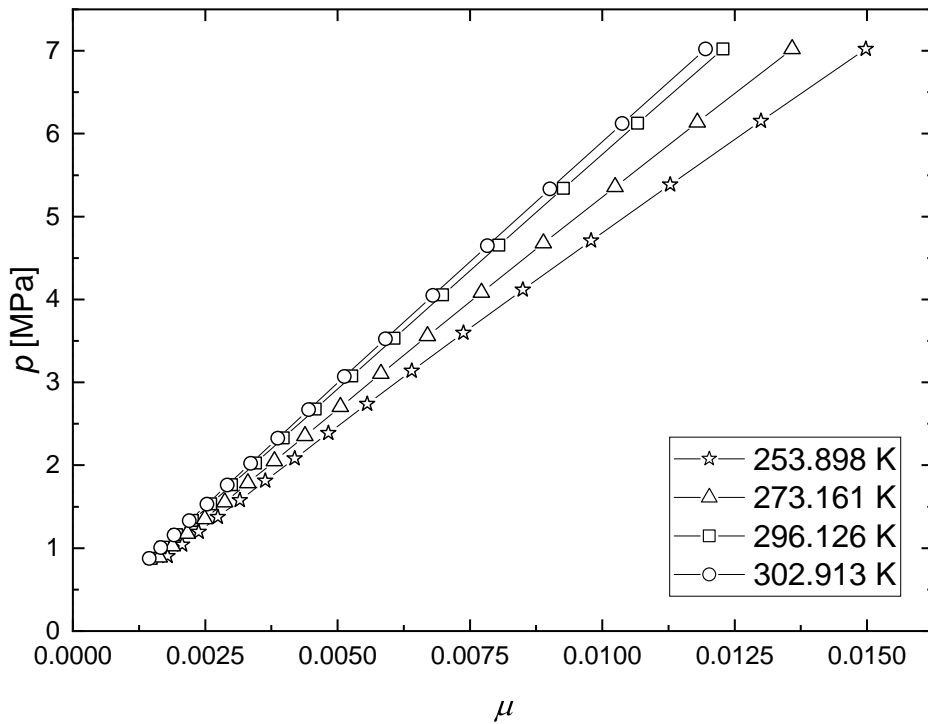
Figure 5.1.: Averaged pressure and capacitance data at the indicated temperatures. The solid lines are guides to the eye and do not represent a fit function.

The DCGT results of this section are important in different ways. The effective compressibilities of the different capacitors, which will be reported in section 5.1.1, can be compared to the values retrieved from the RUS measurements (see section 4.1.3). Thermodynamic temperatures, which will be presented in section 5.1.2, are part of the project "Real-K" (see

section 2.1). There, the capabilities of DCGT as a practical, primary thermometer are explored for temperatures above the triple point of water. The molar polarizability (section 5.1.3) and the DCGT virial coefficients (section 5.1.4) are required to evaluate the dielectric expansion experiments in section 5.4. Furthermore, it should be emphasized again that in contrast to the expansion evaluation, the DCGT results are not influenced by the pressure deformation of the measuring cells or their thermal expansion. Also, the DCGT results only depend on the different temperature of the gas-handling system by means of the small head correction.

For the evaluation, the capacitance and pressure data is fitted by the following polynomial $p_r = A_1^* \mu_r + A_2^* \mu_r^2 + A_3^* \mu_r^3 + A_4^* \mu_r^4$, whose coefficients are compared to the DCGT working equation 3.22. Details on the required fit order were given in section 3.6. Generally, the fitting may be carried out in different ways. First, each isothermal measurement can be fitted individually, and the average value of the desired property is calculated. This is particularly helpful to assess the repeatability of the experiments. The second approach is to perform a fit on the averaged data, whereas the pressures of the individual isotherms are corrected to the average isothermal temperature T_{iso}. The p and μ values of the individual isotherms are then averaged, and a single fit to this average data is performed. The averaged values of p and μ for the four temperatures are summarized in table J.1 in the appendix J and are visualized in figure 5.1. The fit coefficients A_1^* to A_4^* are summarized in table J.2 in appendix J as well together with their standard uncertainty from the fit routine. The coefficients A_1 to A_4 as defined in the DCGT working equation 3.22 can be calculated from the coefficients A_1^* to A_4^* by the simple relations:

$$A_1 = A_1^*; \; A_2 = \frac{A_2^*}{A_1^2}; \; A_3 = \frac{A_3^*}{A_1^3}; \; A_4 = \frac{A_4^*}{A_1^4} \tag{5.1}$$

These DCGT coefficients, which are required for the final data evaluation, are summarized in table 5.2. Their uncertainty needs to be investigated as well to assess the uncertainty of the properties, which are going to be determined from these coefficients in the next sections. The regulations for the assignment of uncertainty to measurements as well as the propagation of uncertainty are defined in the GUM [7]. However, the standard GUM does not include the propagation of uncertainty from measured data to fit coefficients. That is why Monte-Carlo simulations, which are described in the supplement 1 to the GUM, were performed [107]. The methodology is in detail shown in the following and will be used in the next two sections on the results of the expansion experiments as well. In case of the DCGT evaluation, contributions that influence the pressure and the capacitance data have to be taken into account. The first step is the generation of an ideal data set, which is carried out by fitting the averaged data summarized in table J.1. In turn, ideal pressures p are then calculated from the fit coefficients and the actually measured values of μ. The basic idea is to statistically vary either p or μ within a suitable interval that is defined by the standard uncertainty of the input property. The used random numbers are normally distributed in case

T_{iso} [K]	253.898	273.161	296.126	302.913
A_1 [10^8Pa]	5.099 375	5.486 820	5.948 512	6.085 060
A_2 [10^9Pa^{-1}]	-12.7203	-9.5140	-6.6549	-5.9734
A_3 [10^{16}Pa^{-2}]	2.807	2.276	1.817	1.725
A_4 [10^{25}Pa^{-3}]	6.63	5.61	4.65	3.27
statistical scattering of pressures - p_{MC}				
$u(A_1)$ [10^8Pa]	0.000 073	0.000 080	0.000 086	0.000 086
$u(A_2)$ [10^9Pa^{-1}]	0.0132	0.0138	0.0140	0.0138
$u(A_3)$ [10^{16}Pa^{-2}]	0.035	0.033	0.034	0.038
$u(A_4)$ [10^{25}Pa^{-3}]	2.52	2.78	2.94	2.95
statistical scattering of capacitance - μ_{MC}				
$u(A_1)$ [10^8Pa]	0.000 040	0.000 052	0.000 066	0.000 062
$u(A_2)$ [10^9Pa^{-1}]	0.0058	0.0073	0.0086	0.0081
$u(A_3)$ [10^{16}Pa^{-2}]	0.013	0.018	0.021	0.020
$u(A_4)$ [10^{25}Pa^{-3}]	0.89	1.18	1.47	1.42
systematic pressure uncertainty - p_{syst}				
$u(A_1)$ [10^8Pa]	0.000 075	0.000 080	0.000 087	0.000 089
$u(A_2)$ [10^9Pa^{-1}]	0.0009	0.0008	0.0007	0.0007
$u(A_3)$ [10^{16}Pa^{-2}]	<0.001	<0.001	<0.001	<0.001
$u(A_4)$ [10^{25}Pa^{-3}]	<0.01	<0.01	<0.01	<0.01

Table 5.2.: DCGT fit coefficients of the polynomial fit of fourth order to the averaged data for corresponding average values of the four measured temperatures and the contributions of propagated uncertainty.

the uncertainty contribution underlies a Gaussian distribution which is the case here. For rectangular distributions, equally distributed random numbers would be used. The scattered data is fitted and the fit coefficients are stored in a table. This process is repeated typically several hundred times. While the average value of these fit coefficients is identical to the one of the ideal data, the standard uncertainty of all these fit coefficients is a measure for the propagation of uncertainty from the scattered input property.

In this thesis, the Monte-Carlo simulations are embedded in a Microsoft Excel template using VBA macros. The random numbers used to scatter the data are supplied by an algorithm generating a series of pseudo random numbers. Not only does the next number in the series rely on the previous number, the series of numbers is repeated, which happens after more than one million iterations. That is why the starting value of the random number generator is initialized by a value taken from the system operating clock.

To assess the number of iterations required for the Monte-Carlo simulation to provide a reliable result on the standard uncertainty of the fit coefficient, the development of the standard uncertainty of this fit coefficient can be plotted over the corresponding number of samples. According to the law of big numbers, this value is going to be stable after a certain number of iterations. In figure 5.2, this is exemplified by the example of the A_1^* coefficient at 253 K, when each of the pressures p_r used for the fitting of the data is varied with a normal distribution function and a standard uncertainty of 5 ppm. While the standard uncertainty significantly changes in the beginning, it converges to a stable value after around 300 samples.
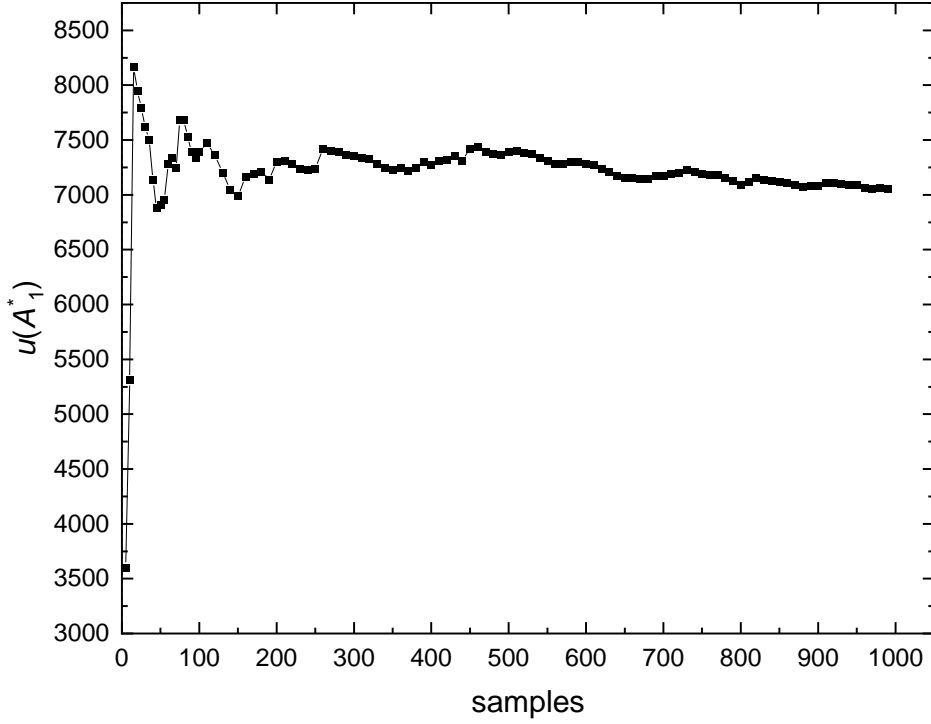
Figure 5.2.: Development of the standard uncertainty of the A_1^* fit coefficient at $253\,\mathrm{K}$ for a variation in p_r with a relative standard uncertainty of $5\,\mathrm{ppm}$ in dependance of the number of Monte-Carlo samples.

For the simulations performed in this work, typically 700 calculations were carried out.

As layed out in section 4.2, the uncertainties of the pressure measurement have three different categories. Category III inhibits the statistical scattering of the pressures and amounts to $5\,\mathrm{ppm}$ over the entire pressure range (see table 4.5). Uncertainties of the fit coefficients arising from this contribution are labeled by p_{MC}. The second purely statistical component that needs to be processed by the Monte-Carlo simulation is the uncertainty of the capacitance bridge. The relative uncertainty for the determination of capacitance ratios was assessed in section 4.3 to be $u_{\mathrm{r}}\left(\frac{C(p)}{C(0)}\right) = 5.4 \times 10^{-8}$. The propagation of this uncertainty via the relative change of capacitance $\gamma = \frac{C(p)-C(0)}{C(0)}$ to the absolute uncertainty of the actual DCGT working variable $\mu = \frac{\gamma}{\gamma+3}$ is:

$$u(\mu) = \frac{(1-\mu)^2}{3}\left(\frac{3}{1-\mu} - 2\right) \cdot u_{\mathrm{r}}\left(\frac{C(p)}{C(0)}\right) \tag{5.2}$$

This defines the scattering interval for μ, which is typically in between $1.2\,\mathrm{ppm}$ at $7\,\mathrm{MPa}$ and $10\,\mathrm{ppm}$ at $1\,\mathrm{MPa}$. Contributions arising from this component are marked with μ_{MC}.

The remaining contributions of uncertainty to the pressure, which are of category I and category II (see table 4.5 in section 4.2), cause systematic deviations of all interpolated pressures during the isotherm measurement. Scattering the isotherm pressures randomly is, thus, not a viable option. Instead, the following approach is taken. The relative uncertainty

of category I is identical for both calibration points with the pressure balance causing an identical relative shift. On top, the category II contributions cause additional shifts that are different for both calibration points. To assess the uncertainty, the ideal pressures are first shifted by the category I contribution which is 10.25 ppm for Digi_1. On top, the maximum split between category II contributions is taken into account as a worst case estimate assuming none at 7 MPa and 9.49 ppm at 1 MPa. This can be described by multiplication of each pressure with the following function:

$$p = p_{\text{ideal}} \cdot \left(1 + \left(13.97 - \frac{3.72}{6} \left(\frac{p_{\text{ideal}}}{10^6} - 1 \right) \right) 10^{-6} \right) \tag{5.3}$$

These pressures are fitted together with the μ values, whereas the difference between the retrieved fit coefficients and the ideal initial fit coefficients defines the propagated uncertainty. Contributions arising from this procedure are labeled by p_{syst}.

The results of these previously described efforts are summarized in table 5.2 for the four measured temperatures. The simulation is based on the fit coefficients of the polynomial A_1^* to A_4^*. The propagation of their uncertainty to the DCGT coefficients A_1 to A_4 given in table 5.2 is based on equation 5.1:

$$
\begin{aligned}
u_{\text{r}}(A_1) &= u_{\text{r}}(A_1^*) \\
u_{\text{r}}(A_2) &= u_{\text{r}}(A_2^*) + 2u_{\text{r}}(A_1) \\
u_{\text{r}}(A_3) &= u_{\text{r}}(A_3^*) + 3u_{\text{r}}(A_1) \\
u_{\text{r}}(A_4) &= u_{\text{r}}(A_4^*) + 4u_{\text{r}}(A_1)
\end{aligned}
\tag{5.4}
$$

Consideration of the contribution of A_1^* does not actually change the significant numbers of the uncertainties of the higher fit coefficients since the one of A_1^* is very low compared to the others.

5.1.1. Effective compressibility of the capacitors

As already explained, precise values of the effective compressibility κ_{eff} are essential to evaluate the capacitance data. To validate the values retrieved from the RUS measurements shown in section 4.1.3, a DCGT evaluation is carried out to determine κ_{eff} for the individual capacitors. In principal, κ_{eff} may be calculated from the fit coefficient A_1 of the DCGT working equation 3.22 by:

$$\kappa_{\text{eff}} = 3 \left(\frac{1}{A_1} - \frac{A_\epsilon}{RT_{\text{iso}}} \right) \tag{5.5}$$

Values retrieved directly from this fit typically suffer larger uncertainties due to the required higher fit orders that increase the uncertainties of the A_1 term. Furthermore, this

(a) C_1

(b) C_2

(c) C_3

(d) C_4
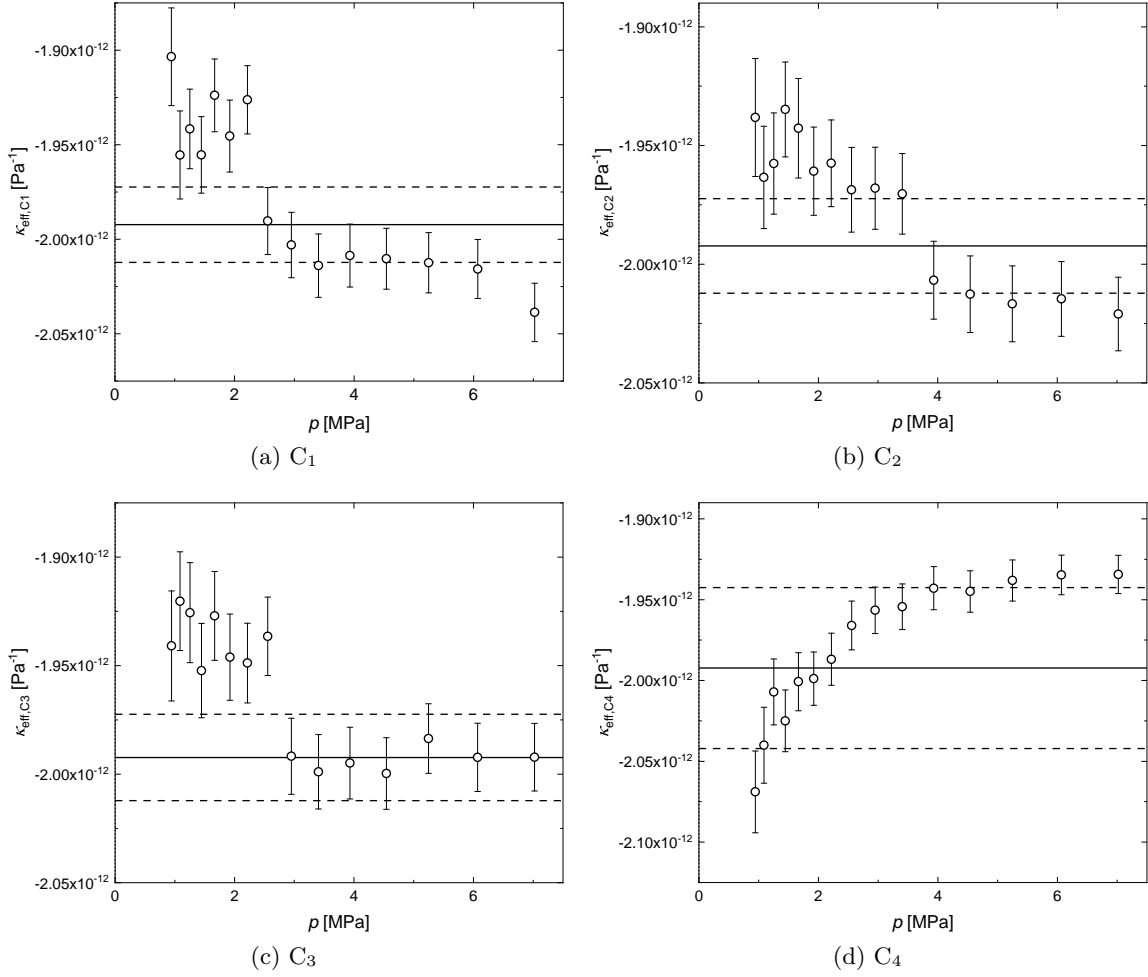
Figure 5.3.: Effective compressibilities of the four capacitors retrieved from the helium isotherm number 18 at the triple point of water. Precise DCGT virial coefficients for He were taken from reference [1] to correct the data to ideal pressures. The error bars are combined standard uncertainties of κ_{eff} from the DCGT data. The solid line marks the value determined from the RUS measurements. The dashed lines mark the final assigned uncertainty of κ_{eff} (1 % for C_1 to C_3; 2.5 % for C_4).

equation shows why it is beneficial to evaluate the helium data rather than the argon data. Since the molar polarizability A_ϵ of helium is a factor of eight smaller than argons, the measurements are much more sensitive to the influence of κ_{eff}. The consequence is that the reachable relative standard uncertainties for κ_{eff} are in the order of 1 % for helium, while they are in the order of 6.5 % for argon. Another reason to evaluate helium is that for helium the very precise DCGT virial coefficients published by Gaiser *et al.* can be used to calculate the contributions of the higher terms [1]. These contributions are then subtracted from the measured pressures resulting in a corrected ideal pressure p_{corr}. In this way, a precise value of κ_{eff} can be retrieved for each data point by:

$$\kappa_{\text{eff}} = 3 \left(\frac{\mu}{p_{\text{corr}}} - \frac{A_\epsilon}{RT_{\text{iso}}} \right) \tag{5.6}$$

The corresponding results are plotted in figure 5.3. Capacitors C_1 to C_3 behave similar and show a step in κ_{eff} at different pressures. The origin of this behavior is not fully clear. Eventually, the changes in pressure cause a small temporary tilt or eccentricity of the capacitor that influences the measured capacitance. Such an effect would have to be reversed upon evacuation since the capacitance in vacuum before and after the expansion was checked and agrees on the level of the uncertainty of the capacitance ratio measurement as described in section 4.1.3. The value determined from the RUS measurements still mostly lies within the expanded standard uncertainty (plotted is the standard uncertainty). However, capacitor C_4 is different. Instead of a step like behavior, the compressibility appears to be constant for higher pressures until around 3.5 MPa. The deviations to the RUS value in this range are in the order of 2.5 % and are beyond the expanded standard uncertainty. With lower values κ_{eff} decreases steadily, in contrast to the previously observed step like behavior. It crosses the RUS value but continues to depart from it. Again, the origin of this behavior is not fully understood, whereas it is plausible for C_4 to behave different from the other capacitors since the gas is always expanded into this one. Additionally, the evacuation may induce mechanical stress as well. The qualitative trend shown here can be reproduced with the data for helium at room temperature whereas the pressure at which the steps emerge are similar but not entirely identical. For this thesis, the effects are included in the uncertainty budget of κ_{eff} in section 4.1.3.

The error bars in the plots were calculated including the error propagation by:

$$u(\kappa_{\text{eff}}) = 3 \sqrt{\left(\frac{u(\mu)}{p_{\text{corr}}} \right)^2 + \left(\mu \frac{u(p_{\text{corr}})}{p_{\text{corr}}^2} \right)^2 + \left(\frac{u(A_\epsilon)}{RT_{\text{iso}}} \right)^2 + \left(\frac{A_\epsilon u(T)}{RT_{\text{iso}}^2} \right)^2} \tag{5.7}$$

$u(\mu)$ and $u(p_{\text{corr}})$ include the type A uncertainty of the capacitance and pressure measurement in form of the standard uncertainty of the corresponding measuring signal for the averaging time of 30 minutes for each capacitor at each data point. The uncertainty of p_{corr} also contains the propagated uncertainties of the correction utilizing the DCGT virial coefficients.

5.1.2. Thermodynamic temperatures

The thermodynamic temperatures T_{DCGT} of the DCGT data can be retrieved from the fit coefficient A_1 by the formula:

$$T_{\text{DCGT}} = \frac{A_\epsilon}{R \left(\frac{1}{A_1} - \frac{\kappa_{\text{eff}}}{3} \right)} \tag{5.8}$$
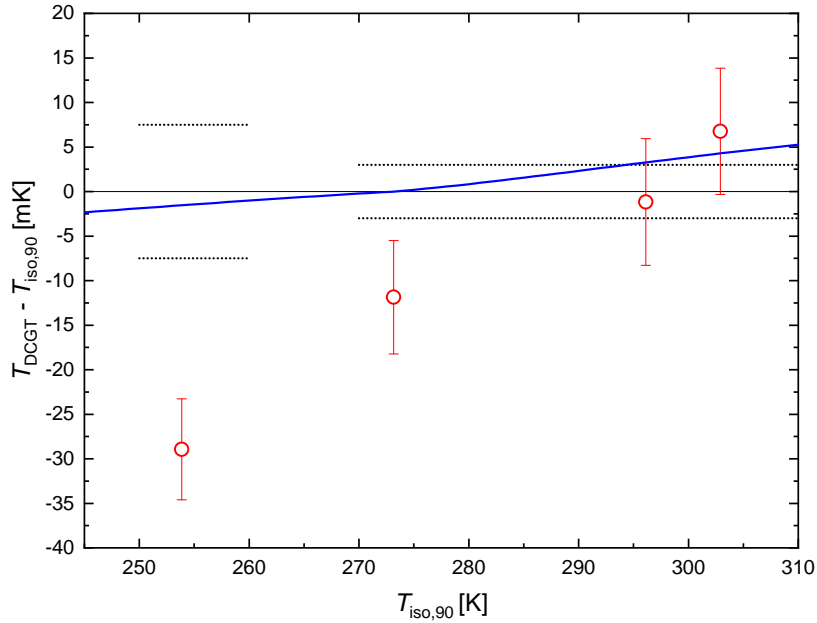
Figure 5.4.: Differences ΔT between the thermodynamic temperatures from the DCGT and the ones measured with the CSPRT (red circles). The dotted line represents the uncertainty of the CSPRT whereas the solid blue line indicates the difference between thermodynamic and ITS-90 temperature.

For the molar polarizability of argon, the value of Gaiser *et al.* $A_\epsilon = 4.140\,686\,\mathrm{cm\,mol^{-3}}$ with a relative standard uncertainty of 2.4 ppm was inserted [37]. To compare these temperatures to the temperatures T_iso measured with the $25.5\,\Omega$ platinum standard thermometer, the differences between thermodynamic temperature and the ITS-90 temperature have to be taken into account. The deviations of "T-T_{90}" are topic of ongoing investigations and may for now be best corrected by the functions given in reference [108]. The resulting temperatures are summarized in table 5.3, where ΔT is the difference between T_DCGT and $T_\mathrm{iso,90}$ including the correction "T-T_{90}".

$T_\mathrm{iso,90}$ [K]	T_DCGT [K]	$u(T_\mathrm{DCGT,90})$ [mK]	$T - T_{90}$ [mK]	ΔT [mK]
253.897	253.869	5.7	-1.5	-27.4
273.162	273.150	6.4	0	-11.9
296.126	296.125	7.1	3.3	-4.2
302.913	302.919	7.1	4.3	2.5

Table 5.3.: Comparison of the temperatures $T_\mathrm{iso,90}$ measured with the CSPRT and the ones retrieved from the DCGT data. The temperature differences ΔT include the correction "$T - T_{90}$".

These deviations are plotted in figure 5.4 together with the corresponding uncertainties. At the two highest temperatures the values agree well within the standard uncertainty. At the triple point of water the values overlap by their expanded standard uncertainties. For 253 K, the deviations are slightly outside of the range of expanded uncertainties, whereas the uncertainty of the temperature measurement at 253 K is 7.5 mK (see section 4.4 for details).

5. Results

The trend of rising temperature deviations for departing from ambient temperature especially at 253 K is a consequence of the temperature gradients over the measuring cells described in section 4.1.1. Since the capacitors essentially average the measuring signal over the length of the inner electrode, these gradients lead to the reported deviations. As explained in 4.1.1 the effect is increased for the measurement at 253 K because the Fluke 2100 temperature controller that stabilizes the bath thermostat could not be used here. Essentially, the problem of temperature gradients is attributed to a compromise that had to be found during the construction of the apparatus. Since the primary goal of the apparatus is the determination of virial coefficients, the size of the measuring cells was increased during the planning phase to minimize the influence of the volume of the gas-handling system. At this point, parts of the system were already manufactured so that the dimension of the vacuum cell could not be changed. The only option was to make the cells longer, which decreased the distance between measuring cells and the colder CF-200 flange. Though these effects play obviously a role for properties that are retrieved from the first DCGT fit coefficient A_1, it will be shown that they only have a minor influence on the virial coefficients. Overall, the effect of gradients is included in the uncertainty of the CSPRT and seems to be on an appropriate level. The combined uncertainties $u_c(T_{\mathrm{DCGT}})$ of the temperatures in table 5.3 and figure 5.4 were calculated in accordance with the GUM by:

$$u_c(T_{\mathrm{DCGT}}) = \sqrt{\left(\frac{\partial T_{\mathrm{DCGT}}}{\partial A_\epsilon}u(A_\epsilon)\right)^2 + \left(\frac{\partial T_{\mathrm{DCGT}}}{\partial A_1}u(A_1)\right)^2 + \left(\frac{\partial T_{\mathrm{DCGT}}}{\partial \kappa_{\mathrm{eff}}}u(\kappa_{\mathrm{eff}})\right)^2} \quad (5.9)$$

The derivatives in formula 5.8 are the sensitivity coefficients and given by:

$$
\begin{aligned}
\frac{\partial T_{\mathrm{DCGT}}}{\partial A_\epsilon} &= \frac{T_{\mathrm{DCGT}}}{A_\epsilon} \\
\frac{\partial T_{\mathrm{DCGT}}}{\partial A_1} &= \frac{T_{\mathrm{DCGT}}^2 R}{A_\epsilon A_1^2} \\
\frac{\partial T_{\mathrm{DCGT}}}{\partial \kappa_{\mathrm{eff}}} &= \frac{T_{\mathrm{DCGT}}}{3\left(\frac{1}{A_1} - \frac{\kappa_{\mathrm{eff}}}{3}\right)}
\end{aligned}
\quad (5.10)
$$

T_{DCGT} [K]	253.869	273.150	296.125	302.919
A_ϵ [mK]	0.61	0.66	0.71	0.73
κ_{eff} [mK]	0.86	1.00	1.17	1.23
$A_1 - p_{\mathrm{syst}}$ [mK]	3.71	4.10	4.44	4.54
$A_1 - p_{\mathrm{MC}}$ [mK]	3.64	3.98	4.29	4.26
$A_1 - \mu_{\mathrm{MC}}$ [mK]	2.01	2.57	3.26	3.08
$\boldsymbol{u(T_{\mathrm{DCGT}})}$ **[mK]**	**5.7**	**6.4**	**7.1**	**7.1**

Table 5.4.: Uncertainty contributions to the thermodynamic temperatures retrieved from the DCGT data evaluation.

From these coefficients, the different contributions can be calculated and are summarized

in table 5.4. At this point the uncertainty is dominated by the pressure measurement. For conventional DCGT measurements this component can potentially be decreased by utilizing a precise pressure balance at the cost of manual operation.

5.1.3. Molar polarizability of argon

The assessment of the molar polarizability A_ϵ is best carried out by evaluation of the measurements performed at 296 K since temperature gradients that could distort the results are minimized here. The results presented in the previous section as well as in section 4.1.1 indicated that this problem occurs for temperatures departing from ambient temperature. For noble gases, this procedure is valid since A_ϵ is not temperature dependent. To assess the molar polarizabilities from the fitted data, the fit coefficient A_1 is used to give:

$$A_\epsilon = \left(\frac{1}{A_1} - \frac{\kappa_{\text{eff}}}{3} \right) RT \tag{5.11}$$

Here, it is important to correct the measured ITS-90 temperature T_{iso} to the thermodynamic temperature T as shown in the previous section. From the averaged pressure and capacitance data $A_\epsilon = 4.140\,748 \times 10^{-6}\,\text{m}^3\,\text{mol}^{-1}$ is determined with a combined relative standard uncertainty of 25 ppm. Gaiser *et al.* published a value for the molar polarizability of $4.140\,686 \times 10^{-6}\,\text{m}^3\,\text{mol}^{-1}$ with a relative uncertainty of 2.4 ppm in 2018 [37]. The relative deviation to this benchmark value is 14 ppm demonstrating the capabilities of this apparatus for this purpose as well.

The combined uncertainty $u_c(A_\epsilon)$ was calculated by:

$$u_c(A_\epsilon) = \sqrt{ \left(\frac{\partial A_\epsilon}{\partial T} u(T) \right)^2 + \left(\frac{\partial A_\epsilon}{\partial k_{\text{eff}}} u(\kappa_{\text{eff}}) \right)^2 + \left(\frac{\partial A_\epsilon}{\partial A_1} u(A_1) \right)^2 } \tag{5.12}$$

The calculation of the partial derivatives is straight forward and, thus, not explicitly shown here again. All components contributing to the combined uncertainty are summarized in table 5.5. To test the repeatability, A_ϵ was also derived for each individual isothermal measurement. The deviations of these values to the average value are visualized in figure

contribution	absolute	relative
κ_{eff}	$1.6 \times 10^{-11}\,\text{m}^3\,\text{mol}^{-1}$	4.0 ppm
T	$4.2 \times 10^{-11}\,\text{m}^3\,\text{mol}^{-1}$	10.1 ppm
$A_1 - p_{\text{syst}}$	$6.1 \times 10^{-11}\,\text{m}^3\,\text{mol}^{-1}$	14.6 ppm
$A_1 - p_{\text{MC}}$	$5.1 \times 10^{-11}\,\text{m}^3\,\text{mol}^{-1}$	12.3 ppm
$A_1 - \mu_{\text{MC}}$	$4.6 \times 10^{-11}\,\text{m}^3\,\text{mol}^{-1}$	11.0 ppm
$\boldsymbol{u_c(A_\epsilon)}$	**10.2**	**24.6**

Table 5.5.: Uncertainty contributions to the molar polarizability of argon retrieved from the DCGT data evaluation at 296 K in absolute and relative units.

5.5. The corresponding standard uncertainty of the average value is 15 ppm confirming the assessed uncertainty which was given under the assumption of a single measurement.
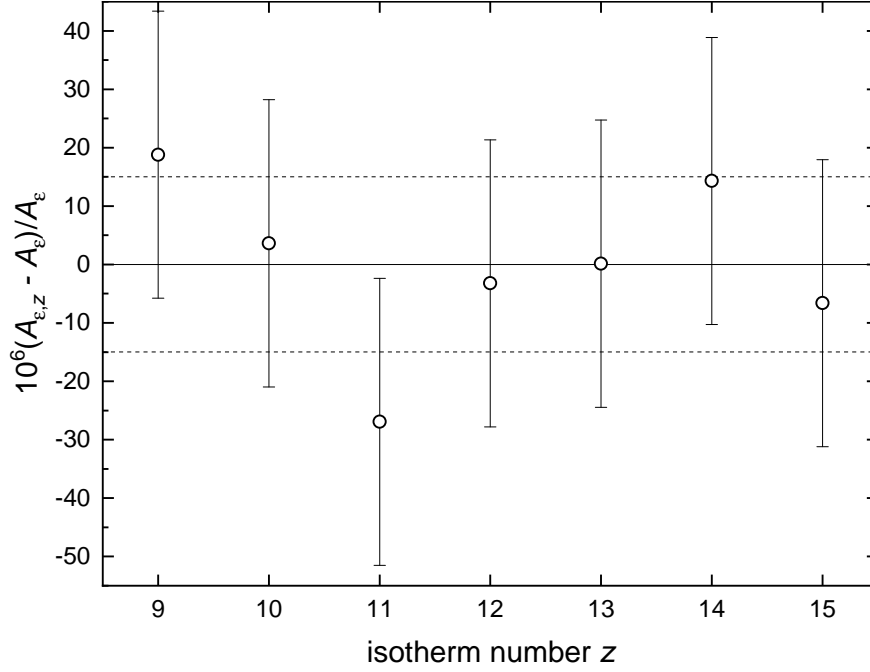
Figure 5.5.: The black circles show the deviations of the the the molar polarizabilities of argon for the seven isotherms measured at 296 K from the average value in ppm. The error bars are the combined uncertainties. The solid line marks the average value with the dashed lines indicating the corresponding standard uncertainty of the mean value.

5.1.4. DCGT virial coefficients

The calculation of the DCGT virial coefficients is carried out based on the working equation 3.22 by:

$$
\begin{aligned}
B_{\mathrm{DCGT}} &= (RT_{\mathrm{iso}})\left(A_2 + \frac{\kappa_{\mathrm{eff}}}{3}\left(1 + \frac{B(T)}{A_\epsilon}\right)\right) \\
C_{\mathrm{DCGT}} &= (RT_{\mathrm{iso}})^2\left(A_3 - \frac{\kappa_{\mathrm{eff}}}{3RT_{\mathrm{iso}}}\left(2A_\epsilon - 3B_{\mathrm{DCGT}} - \frac{1}{A_\epsilon}\left(2B_{\mathrm{DCGT}}^2 + C(T)\right)\right)\right)
\end{aligned}
\tag{5.13}
$$

It is necessary to include values for the density virial coefficients $B(T)$ and $C(T)$ in the two small correction terms. In this case, experimental values of Gilgen *et al.* that were reanalyzed by Jäger *et al.* were chosen [29, 67]. However, the demands for their uncertainty is rather low. A relative uncertainty of 5 % in $B(T)$ would lead to a contribution of 0.002 % for the relative uncertainty of B_{DCGT}, while 10 % in $C(T)$ contribute less than 0.004 % to the uncertainty of C_{DCGT}. In principal, also the values determined by the Burnett expansion in section 5.3 could be applied. The results for the four different temperatures are summarized in table 5.6 for B_{DCGT} and C_{DCGT} together with their relative combined standard uncertainties and

the relevant contributions to the uncertainty. Furthermore, the repeatability in [%] which was retrieved from the values of the individual isotherms (see figure 5.6 and 5.7) is given and in excellent agreement with the assessed combined uncertainty. Components that are not included for B_{DCGT} since their contribution is less than $0.005\,\%$ are κ_{eff}, A_ϵ, $B(T)$ and T_{iso}. For C_{DCGT}, components that contribute less than $0.01\,\%$ are not listed, which includes κ_{eff}, A_ϵ, $C(T)$ and B_{DCGT}. In contrast to B_{DCGT}, a small contribution of the temperature uncertainty is included at $253\,\mathrm{K}$ for C_{DCGT}. Based on equation 5.13, the propagation of uncertainty can be calculated as shown in the previous sections. It can be seen from table 5.6 that the two main contributions to the DCGT virial coefficients arise from the statistical scattering of pressure and capacitance, while the absolute pressure and temperature are of minor importance.

T_{iso} [K]	253.898	273.161	296.126	302.913
B_{DCGT} $[10^6\mathrm{m}^3\mathrm{mol}^{-1}]$	-26.844	-21.602	-16.380	-15.040
$u_{\mathrm{r}}(B_{\mathrm{DCGT}})$ [%]	0.11	0.16	0.25	0.27
repeatability [%]	*0.07	0.07	0.14	**0.10
component and contribution to uncertainty for B_{DCGT}				
$A_2 - p_{\mathrm{MC}}$ [%]	0.10	0.15	0.21	0.23
$A_2 - \mu_{\mathrm{MC}}$ [%]	0.05	0.08	0.13	0.14
$A_2 - p_{\mathrm{syst}}$ [%]	0.01	0.01	0.01	0.01
C_{DCGT} $[10^9\mathrm{m}^6\mathrm{mol}^{-2}]$	1.2501	1.1733	1.1008	1.0939
$u_{\mathrm{r}}(C_{\mathrm{DCGT}})$ [%]	1.34	1.66	2.21	2.50
repeatability [%]	*0.66	0.52	0.86	**0.98
component and contribution to uncertainty for C_{DCGT}				
$A_3 - p_{\mathrm{MC}}$ [%]	1.26	1.45	1.89	2.22
$A_3 - \mu_{\mathrm{MC}}$ [%]	0.46	0.81	1.14	1.15
$A_3 - p_{\mathrm{syst}}$ [%]	0.01	0.01	0.01	0.01
T_{iso} [%]	0.01	0.01	0.01	0.01

Table 5.6.: Second and third DCGT virial coefficients and their combined relative standard uncertainties as well as the repeatability from the individual isotherms at the four measured temperatures. The main contributions to the uncertainty are listed in the lower part. * repeatability based on two measurements ** repeatability based on three measurements

(a) 253.898 K

(b) 273.161 K

(c) 296.126 K

(d) 302.913 K
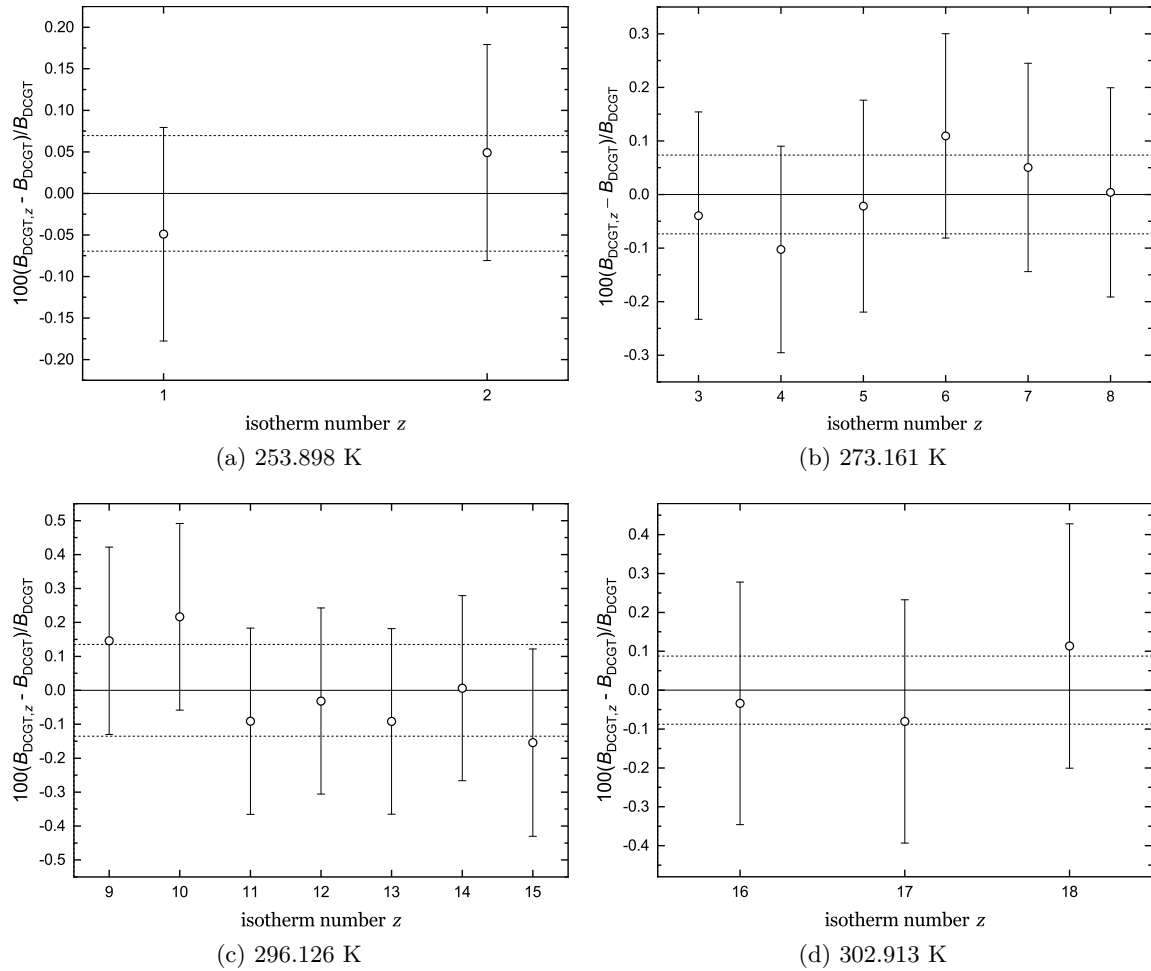
Figure 5.6.: Relative deviations of the individual values of the second DCGT virial coefficient from the average value at the indicated temperatures in %. The error bars represent the combined standard uncertainties. The standard uncertainty of the average values is indicated by the dashed lines.

(a) 253.898 K

(b) 273.161 K

(c) 296.126 K

(d) 302.913 K
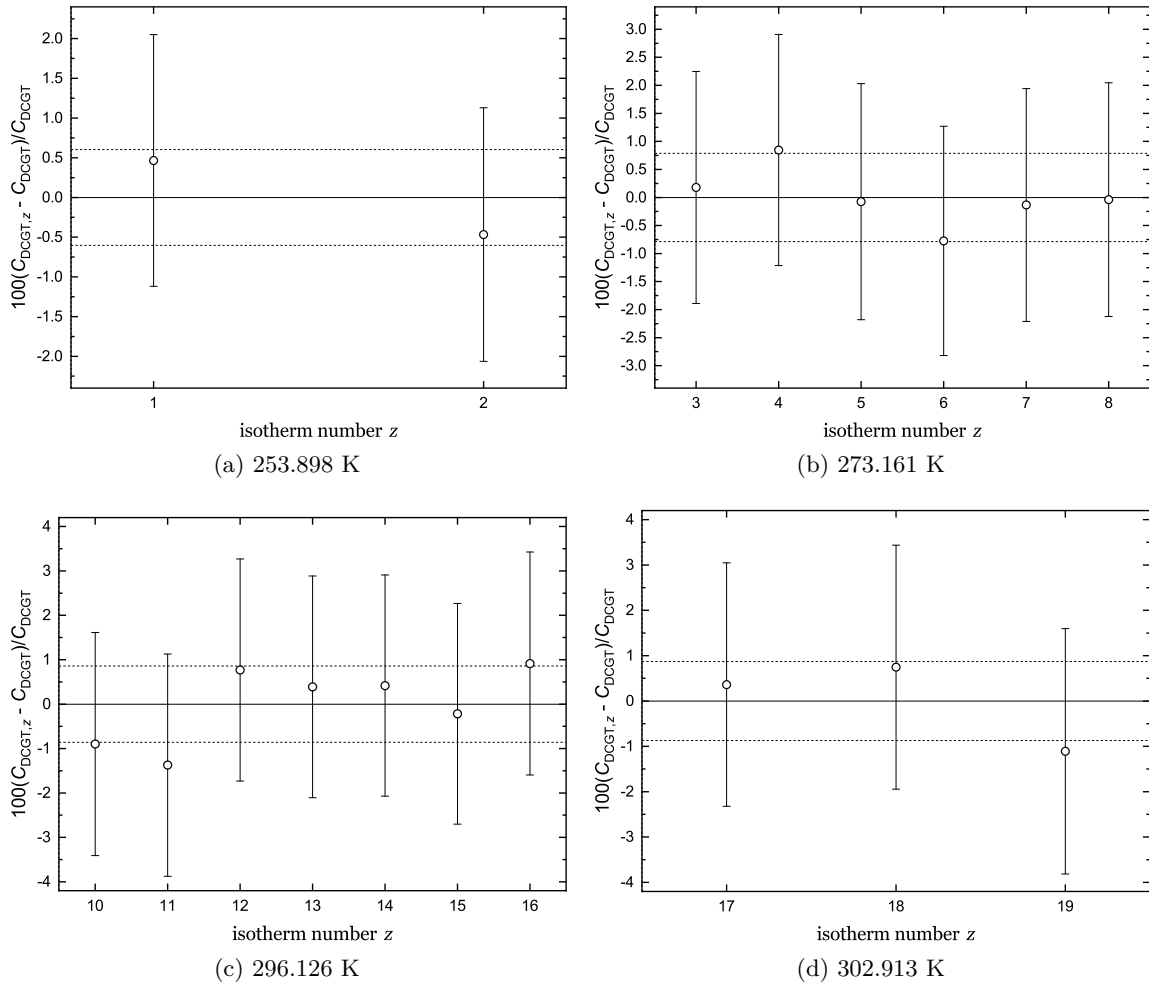
Figure 5.7.: Relative deviations of the individual values of the third DCGT virial coefficient from the average value at the indicated temperatures in %. The error bars represent the combined standard uncertainties. The standard deviation of the average values is indicated by the dashed lines.

5.2. The apparatus constant

The key assumption of the expansion experiments is that the volume ratio defining the pressure and capacitance ratios is constant over temperature and pressure. Appropriate working equations were retrieved in sections 3.3.2 and 3.4.2 to include the effect of pressure deformation. The inclusion of the thermal expansion of the cells will be treated later in this section. In principal, the pressure and capacitance data may simply be fitted with a polynomial and evaluated directly by the working equations 3.53 given in section 3.5. In both cases, the first coefficient of the polynomial fit delivers the apparent apparatus constant $Q_{\Delta T}$ as defined in equation 3.37. A second approach is to determine $Q_{\Delta T}$ with the lowest possible uncertainty and constraint the constant term of the fit function. It will be shown that the uncertainties of density (section 5.3) and dielectric virial coefficients (section 5.4) determined in this manner are roughly a factor of two smaller. To reach the stated uncertainties of the virial coefficients, the volume ratio needs to be known with a relative uncertainty in the order of 5 ppm. Obviously this is not possible by means of dimensional measurements for the complex volumes. Instead, a different strategy is followed in this work.

First, the volume ratio at constant temperatures Q (see definition in equation 3.37) is determined by measurements at $T_{\text{iso}} \approx T_{\text{GHS}}$. One option would be to utilize an average value of the individual isotherms that were measured with argon at 296 K. This has several drawbacks. Argon is the gas under investigation and should not be used to calibrate the apparatus, though this option is in principle viable. Another problem is that the uncertainty of the first fit coefficient rises with higher fit orders, but it was shown in section 3.6 that these are required in particular for the evaluation of the pressure ratios since the fourth density virial coefficient still has a significant influence. Furthermore, the lowest measured pressure is 1 MPa, which means that the extrapolation to zero pressure is vulnerable to statistical scattering. In principal, the capacitance data may be utilized instead since here the required fit order is lower. However, in this work precise measurements with helium were carried out instead. The advantage of helium is that the virial coefficients can be precisely determined by *ab initio* calculations. Knowing them, the working equations 3.32 and 3.45, which include pressure deformation at isothermal conditions, can be fully constrained for all terms except Q and P_{ratio} or F_{ratio}, respectively. While the uncertainties of Q that can be reached from the determination with a fit are in the order of 12 ppm due to the extrapolation, the uncertainty of a single measurement is now dominated by the statistical scattering of pressure and capacitance date and results in relative uncertainties in the order of 7 ppm. From the five isothermal measurements with helium (isotherm numbers 20 to 24) at 296 K, the apparatus constant Q at isothermal conditions was determined to be $Q = 1.1513434$. Calculated values for the required virial coefficients were taken from references [43] for $b_{\epsilon}(T)$, [6] for $c_{\epsilon}(T)$, [109] for $B(T)$, [26] for $C(T)$ and [110] for $D(T)$. An average value of the pressure and capacitance ratios was used and allowed to assign a relative standard uncertainty of 5 ppm.

The second step is to determine $Q_{\Delta T}$ for the measuring temperature with Q as base value,

which is in principle possible by equation 3.37. Again, the determination of the partial volume ratios Q_A and Q_B with sufficient uncertainty is not possible with dimensional measurements. Still, the values given for Q_A and Q_B in table 4.1 can be used to simulate the principle behavior of $Q_{\Delta T}$. The development over the temperature ratio T_{ratio} (assuming a constant temperature of the gas-handling system) can be sufficiently described by a linear function in the temperature with the residuals being less than $1\,\text{ppm}$ for all temperatures measured in this work. Until this point, the thermal expansion of the volume of the measuring cells in the order of $48 \times 10^{-6}\,\text{K}^{-1}$ was not considered. This effect is not relevant for the data evaluation with free fits since it only influences $Q_{\Delta T}$ but not the higher orders. For free fits, it is ,thus, automatically included in the data evaluation by the working equation 3.53. However, to constraint $Q_{\Delta T}$ it has to be included. The difference in the absolute value of $Q_{\Delta T}$ can be in the order $5\,\text{ppm}$ for $253\,\text{K}$. But more importantly, repeating the simulation including this effect shows that the temperature dependence can still be described by a linear function with the residuals being less than $1\,\text{ppm}$. Since the reference value of Q was already determined at ambient temperature, only the slope β_Q needs to be assessed. This was done by additional measurements of helium at the triple point of water (isotherm number 19) whereas a relative uncertainty of $1\,\%$ can be assigned. The general equation to calculate the apparatus constant at a certain temperature (in the temperature range of this work) is finally given by:

$$Q_{\Delta T} = Q + \beta_Q \cdot (T_{\text{ratio}} - 1) = 1.1513434 - 0.0031315 \cdot (T_{\text{ratio}} - 1) \tag{5.14}$$

The corresponding uncertainty is calculated by:

$$u(Q_{\Delta T}) = \sqrt{(u(Q))^2 + (u(\beta_Q)(T_{\text{ratio}} - 1))^2 + (u(T_{\text{Ratio}})\beta_Q)^2 + (10^{-6} \cdot Q_{\Delta T})^2} \tag{5.15}$$

The last contribution to uncertainty takes the deviation from the linear behavior described in the previous text into account. The final values used to constrain the data as well as the corresponding uncertainties are summarized in table 5.7 for the measured temperatures.

T_{iso} [K]	253.898	273.161	296.126	302.913
$Q_{\Delta T}$	1.151 771 5	1.151 581 1	1.151 342 5	1.151 272 7
$u(Q_{\Delta T})$	0.000 007 3	0.000 006 4	0.000 005 8	0.000 006 0

Table 5.7.: Values and uncertainties of the apparent apparatus constant used to constrain the fit of the expansion experiments and determined by measurements with helium.

5.3. Density virial coefficients of argon

The calculation of the density virial coefficients is based on fitting the pressure ratios $P_{r,\text{ratio}} = \frac{p_r}{p_{r+1}}$ over the initial pressures p_r, as described in section 3.3, where r is the number of the expansion. A summary of the averaged pressures and corresponding ratios is given in table K.1 in appendix K. The used polynomial is $P_{r,\text{ratio}} = K_0 + K_1 \cdot p_r + K_2 \cdot p_r^2 + K_3 \cdot p_r^3$ for a free fit and $P_{r,\text{ratio}} - Q_{\Delta T} = K_1 \cdot p_r + K_2 \cdot p_r^2 + K_3 \cdot p_r^3$ for a constraint fit. For the latter, case $Q_{\Delta T}$ is calculated by equation 5.14 that was described in the previous section 5.2.

The fit coefficients of the averaged data are summarized in table 5.8 together with different contributions of uncertainty that are explained in the following. The propagation of

T_{iso} [K]	253.898	273.161	296.126	302.913
free fit				
K_0	1.151 754	1.151 547	1.151 312	1.151 234
K_1 $[10^{-9}\text{Pa}^{-1}]$	−1.838	−1.366	−0.967	−0.853
K_2 $[10^{-17}\text{Pa}^{-2}]$	2.61	3.208	3.515	3.010
K_3 $[10^{-24}\text{Pa}^{-3}]$	3.89	2.527	1.462	1.625
statistical scattering of pressures - p_{MC}				
$u(K_0)$	0.000 018	0.000 018	0.000 018	0.000 017
$u(K_1)$ $[10^{-9}\text{Pa}^{-1}]$	0.018	0.019	0.018	0.018
$u(K_2)$ $[10^{-17}\text{Pa}^{-2}]$	0.55	0.48	0.53	0.48
$u(K_3)$ $[10^{-24}\text{Pa}^{-3}]$	0.43	0.44	0.43	0.45
temperature instability of T_{GHS}				
$u(K_0)$	0.000 003	0.000 003	0.000 003	0.000 003
$u(K_1)$ $[10^{-9}\text{Pa}^{-1}]$	0.003	0.003	0.003	0.003
$u(K_2)$ $[10^{-17}\text{Pa}^{-2}]$	0.08	0.07	0.07	0.08
$u(K_3)$ $[10^{-24}\text{Pa}^{-3}]$	0.06	0.06	0.06	0.06
constraint fit				
$Q_{\Delta T}$	1.151 772	1.151 581	1.151 342	1.151 273
K_1 $[10^{-9}\text{Pa}^{-1}]$	−1.855	−1.398	−0.995	−0.891
K_2 $[10^{-17}\text{Pa}^{-2}]$	3.06	4.08	4.22	4.05
K_3 $[10^{-24}\text{Pa}^{-3}]$	3.53	1.83	0.92	0.79
statistical scattering of pressures - p_{MC}				
$u(K_1)$ $[10^{-9}\text{Pa}^{-1}]$	0.0044	0.0041	0.0043	0.0042
$u(K_2)$ $[10^{-17}\text{Pa}^{-2}]$	0.20	0.19	0.19	0.19
$u(K_3)$ $[10^{-24}\text{Pa}^{-3}]$	0.21	0.20	0.21	0.19
uncertainty of the apparatus constant - $Q_{\Delta T}$				
$u(K_1)$ $[10^{-9}\text{Pa}^{-1}]$	0.0072	0.0063	0.0058	0.059
$u(K_2)$ $[10^{-17}\text{Pa}^{-2}]$	0.19	0.17	0.16	0.16
$u(K_3)$ $[10^{-24}\text{Pa}^{-3}]$	0.15	0.14	0.13	0.13
temperature instability of T_{GHS}				
$u(K_1)$ $[10^{-9}\text{Pa}^{-1}]$	0.0006	0.0006	0.0006	0.0006
$u(K_2)$ $[10^{-17}\text{Pa}^{-2}]$	0.03	0.03	0.03	0.03
$u(K_3)$ $[10^{-24}\text{Pa}^{-3}]$	0.02	0.03	0.03	0.03

Table 5.8.: Fit coefficients of the Burnett expansions and the propagated uncertainties resulting from the listed components obtained by means of the simulations described in the text. $Q_{\Delta T}$ is calculated by equation 5.14.

the statistical uncertainty from the pressure measurement to the fit coefficients requires to perform Monte-Carlo simulations. This formalism was described in detail in section 5.1, whereas here, the initial pressure p_r and the corresponding pressure ratios $P_{\text{ratio},r} = \frac{p_r}{p_{r+1}}$ have to be investigated. An ideal data set is generated by fitting the averaged pressures and corresponding pressure ratios. The fit coefficients are used to calculate ideal pressure ratios. At this point an important step is to use the calculated ideal pressure ratios to, in turn, calculate the ideal pressures after the expansion. This is required to treat the statistical scattering of the pressures (category III in table 4.5) properly since the pressure p_r before and the pressure after the expansion p_{r+1} need to be scattered independently within their standard uncertainty of 5 ppm. After this, the pressure ratios are calculated again and fitted, the values of the fit coefficients are tabulated and the process is repeated with 700 samples. This routine covers the determination with a free fit. For the constraint fit, the simulation routine is identical except for the fit of the scattered data sets, which is carried out for $P_{\text{ratio},r} - Q_{\Delta T}$ over p_r without the coefficient K_0. These contributions are labeled as p_{MC} in table 5.8.

The second contribution (p_{syst} in table 5.8) that needs to be investigated for the free as well as for the constraint fit are the contributions of category I and II in table 4.5. As described in section 5.1, a worst case estimate is given by shifting both calibration points by the systematic contribution of category I, while the statistical contribution of category II is only applied to the calibration point at 1 MPa. The difference in the fit coefficients compared to the ideal fit coefficients is the measure for the propagated uncertainty. Since the relative change of K_0 is only in the order of 5×10^{-10} and the influence on the higher fit coefficients is less than 100 ppm, this component is neglected here. For the constraint fit, the uncertainty of the calculated apparent apparatus constant $Q_{\Delta T}$ needs to be taken into account. Therefore, $Q_{\Delta T}$ is changed by 5 ppm and the difference in the fit coefficient K_1 defines the propagated uncertainty.

Finally, the temperature instability of the gas-handling system causes statistical scattering of the pressures. It was estimated in section 4.7 that the remaining relative uncertainty of the pressure ratio after correction to isothermal conditions is 1 ppm. P_{ratio} was scattered within this interval in a Monte-Carlo simulation as well, whereas the resulting contribution is listed in table 5.8.

Determination of the second density virial coefficient   The second density virial coefficient $B(T_{\text{iso}})$ can be retrieved from the fit coefficients listed in table 5.8 by utilizing the working equation 3.53:

$$B(T_{\text{iso}}) = \frac{K_1}{K_0 - 1} \cdot \frac{RT_{\text{iso}}}{V_1} - T_{\text{ratio}} \frac{1 - V_1}{V1} \cdot B_{\text{GHS}} -$$
$$RT_{\text{iso}} \frac{V_2}{V_1} \cdot \lambda_{\text{B}} - RT_{\text{iso}} \frac{V_3}{V_1} \cdot \lambda_{\text{A}} - RT_{\text{iso}} \frac{V_4}{V_1} \cdot \lambda_{\text{GHS}} \tag{5.16}$$

where the coefficients V_1 to V_4 are defined in equation 3.54 in section 3.5. In case of the

T_{iso} [K]	253.898	273.161	296.126	302.913
Terms of equation 5.16				
a) $\frac{K_1}{K_0-1}$ $[10^{-6}\text{m}^3\text{mol}^{-1}]$	-27.24	-21.90	-16.94	-15.30
b) $\frac{K_1}{Q_{\Delta T}-1}$ $[10^{-6}\text{m}^3\text{mol}^{-1}]$	-27.48	-22.44	-17.41	-15.98
B_{GHS} $[10^{-6}\text{m}^3\text{mol}^{-1}]$	-0.927	-1.042	-1.215	-1.266
λ_{B} $[10^{-6}\text{m}^3\text{mol}^{-1}]$	0.158	0.170	0.185	0.190
λ_{A} $[10^{-6}\text{m}^3\text{mol}^{-1}]$	-0.237	-0.255	-0.276	-0.283
λ_{GHS} $[10^{-6}\text{m}^3\text{mol}^{-1}]$	-0.004	-0.004	-0.005	-0.005
Contributions to uncertainty				
a) $K_0 - p_{\text{MC}}$ $[10^{-6}\text{m}^3\text{mol}^{-1}]$	0.003	0.003	0.002	0.002
a) $K_1 - p_{\text{MC}}$ $[10^{-6}\text{m}^3\text{mol}^{-1}]$	0.268	0.297	0.317	0.321
a) $K_1 - T_{\text{GHS,MC}}$ $[10^{-6}\text{m}^3\text{mol}^{-1}]$	0.039	0.040	0.046	0.047
b) $K_1 - Q_{\Delta T}$ $[10^{-6}\text{m}^3\text{mol}^{-1}]$	0.106	0.101	0.101	0.106
b) $K_1 - p_{\text{MC}}$ $[10^{-6}\text{m}^3\text{mol}^{-1}]$	0.065	0.066	0.075	0.076
b) $K_1 - T_{\text{GHS,MC}}$ $[10^{-6}\text{m}^3\text{mol}^{-1}]$	0.009	0.009	0.010	0.010
B_{GHS} $[10^{-6}\text{m}^3\text{mol}^{-1}]$	0.005	0.005	0.006	0.007
λ_{A} $[10^{-6}\text{m}^3\text{mol}^{-1}]$	0.012	0.013	0.014	0.014
λ_{B} $[10^{-6}\text{m}^3\text{mol}^{-1}]$	0.008	0.008	0.009	0.009
Q_{B} $[10^{-6}\text{m}^3\text{mol}^{-1}]$	0.004	0.002	<0.001	0.001
Q_{A} $[10^{-6}\text{m}^3\text{mol}^{-1}]$	0.011	0.006	0.001	0.003
Q^* $[10^{-6}\text{m}^3\text{mol}^{-1}]$	0.001	0.001	0.001	0.001
Results of the free fit [a]				
B $[10^{-6}\text{m}^3\text{mol}^{-1}]$	-26.23	-20.77	-15.62	-13.93
$u(B)$ $[10^{-6}\text{m}^3\text{mol}^{-1}]$	0.272	0.300	0.321	0.325
$u_{\text{r}}(B)$ [%]	1.04	1.45	2.05	2.33
repeatability [%]	0.59^*	1.28	0.97	0.31^{**}
Results of the constraint fit [b]				
B $[10^{-6}\text{m}^3\text{mol}^{-1}]$	-26.48	-21.28	-16.10	-14.62
$u(B)$ $[10^{-6}\text{m}^3\text{mol}^{-1}]$	0.126	0.123	0.127	0.133
$u_{\text{r}}(B)$ [%]	0.48	0.58	0.79	0.91
repeatability [%]	$^*0.05$	0.35	0.70	$^{**}0.85$

Table 5.9.: Listed are the absolute values of the terms used to calculate $B(T_{\text{iso}})$ according to equation 5.16. Contributions marked with [a] contribute to the free fit exclusively, whereas these marked with [b] only contribute to the constraint fit. The main contributions to uncertainty are given. Final values of the second density virial coefficient for the free and constraint fit including their corresponding combined uncertainties are listed in the lower part including the repeatability, which is determined as the relative standard deviation of the individual isothermal measurements. * repeatability based on two measurements ** repeatability based on three measurements

constraint fit, the fit coefficient K_0 of equation 5.16 is replaced by the constraint apparatus constant $Q_{\Delta T}$. It can be seen from equation 5.16 that the second density virial coefficient B_{GHS} at the temperature of the gas-handling system already needs to be known. In case no literature values are available, the first measurement has, thus, to be performed for $T_{\text{iso}} = T_{\text{GHS}}$. The data can then be evaluated by the more simple working equation 3.32, which only takes the deformation of the cells into account. As described in section 4.1.1 and

visible from table 5.1, this isothermal restriction could not be met for all measurements at 296 K. That is why the working equation 5.16 given here is utilized together with values for $B(T_{\text{GHS}})$ that are taken from the reanalyzed data of Gilgen *et al.* by Jäeger *et al.* [29, 67]. The contributions from the terms of equation 5.16, the main contributions to uncertainty and the final values including their combined uncertainty are listed in table 5.9 for the free as well as for the constraint fits. The assignment of uncertainties to $B(T_{\text{iso}})$ follows the same pattern defined by the GUM shown in the previous sections. The partial derivatives of equation 5.16 are not shown explicitly here since they are very lengthy due to the complex coefficients V_1 to V_4. The individual components adding relevant uncertainty contributions may be taken from table 5.9. Contributions that were neglected since their influence is less than 0.005 % are the uncertainty of the absolute temperature T_{iso}, the deformation of the gas-handling system λ_{GHS} and the apparent apparatus constant $Q_{\Delta T}$ for the free fit. The contribution due to the temperature ratio T_{ratio} is included in the uncertainty of $Q_{\Delta T}$ for the constraint fit, while the influence in the working equation 5.16 is as well less than 0.005 %. The repeatability of the Burnett expansions is visualized in figure 5.8 by the results for the free and the constraint fits of the individual isotherms. Values obtained by both approaches deviate significantly but overlap within their expanded uncertainties. It is concluded that the additional fit parameter of the free fit potentially causes these deviations. The deviation to the value from the constraint fit can be reduced utilizing the approach by Nowak *et al.* [89, 90], which was shown in section 3.6. The order of the fit is reduced, whereas the fitting is exclusively carried out for lower density data.

It can be seen from table 5.9 that the main correction to the ideal fit coefficients arises from the different temperature of the gas-handling system and is in the order of 4 % to 8 %, while the relative corrections due to the deformation of the cells is typically less than 2 %. Regarding the main sources of uncertainty, the statistical scattering of the pressures can be identified for the free fits. The application of a constraint fit reduces this component by a factor of approximately three, while the leading uncertainty contribution results from the uncertainty of $Q_{\Delta T}$. All other components only have minor contributions. As already pointed out for the DCGT virial coefficients in section 5.1.4, the uncertainty of absolute pressures and temperatures is only of secondary importance.

At this point a determination of the third density virial coefficient C from the fit coefficient K_2 of the Burnett expansion is only possible at the temperature T_{GHS} of the gas-handling system via the working equation 3.32. This equation includes the pressure deformation of the measuring cells, while equations for other temperatures were not yet obtained due to the complexity of their derivation. Also, it can be seen from table 5.8 that the achievable uncertainties are comparably high due to the statistical scattering of the pressures. To give an estimate, an average value was derived from the three isotherms (numbers 9,10 and 15) with the lowest scattering in P_{ratio}. For a free fit, a value of $0.97 \times 10^{-10}\,\text{m}^6\,\text{mol}^{-2}$ with a relative standard uncertainty of 17 % can be obtained. The uncertainty can be lowered to 6 % by applying a constraint fit with the corresponding value of C being $1.12 \times 10^{-10}\,\text{m}^6\,\text{mol}^{-2}$.
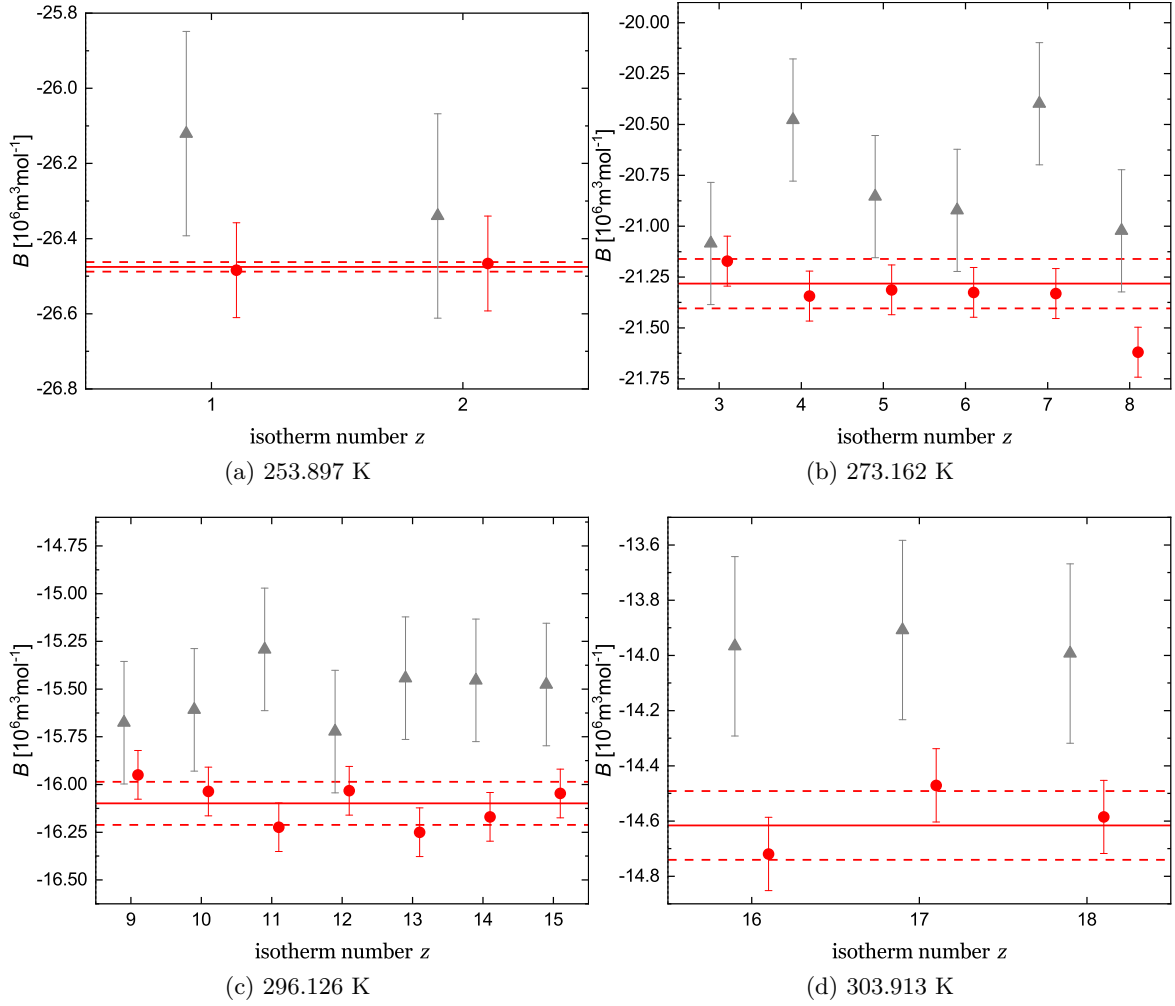
Figure 5.8.: Values of the second density virial coefficient for the individual isotherms measured at the indicated temperatures. Grey triangles denote values retrieved by a free fit, while solid red circles represent values obtained by a constraint fit. Error bars mark the combined standard uncertainty. The solid red line is the average value for a constraint fit, whereas the dashed line indicates the corresponding standard uncertainty.

5.4. Dielectric virial coefficients of argon

The calculation of the dielectric virial coefficients is based on fitting the ratios of Mosotti-terms $F_{r,\text{ratio}} = \frac{f_r}{f_{r+1}}$ over the initial Mosotti-term f_r, as described in section 3.4, where r is the number of the expansion. A summary of the averaged Mosotti-terms and corresponding ratios is given in table K.2 in appendix K. As explained in section 3.6, the used polynomials $F_{r,\text{ratio}} = D_0 + D_1 \cdot f_r + D_2 \cdot f_r^2$ for a free fit and $F_{r,\text{ratio}} - Q_{\Delta T} = D_1 \cdot f_r + D_2 \cdot f_r^2$ for a constraint fit are sufficient. In the latter case, the apparatus constant $Q_{\Delta T}$ is calculated by equation 5.14. The fit coefficients of the averaged data are summarized in table 5.10 together with propagated uncertainties based on the listed components. To treat the statistical scattering of the capacitance data, Monte-Carlo simulations are performed again. Therefore, the relative

T_{iso} [K]	253.898	273.161	296.126	302.913
free fit				
D_0	1.151 763	1.151 563	1.151 319	1.151 257
D_1	0.0409	0.0336	0.0190	0.016
D_2	−0.46	−0.71	−0.57	−0.63
statistical scattering of capacitance - f_{MC}				
$u(D_0)$	0.000 013	0.000 013	0.000 015	0.000 015
$u(D_1)$	0.0032	0.0035	0.0046	0.0047
$u(D_2)$	0.16	0.80	0.63	0.39
temperature instability of T_{GHS}				
$u(D_0)$	0.000 001	0.000 001	0.000 001	0.000 001
$u(D_1)$	0.0003	0.0004	0.0004	0.0004
$u(D_2)$	0.02	0.03	0.03	0.03
constraint fit				
$Q_{\Delta T}$	1.151 772	1.151 581	1.151 342	1.151 273
D_1	0.0386	0.028	0.012	0.01
D_2	−0.33	−0.38	−0.08	−0.25
statistical scattering of capacitance - f_{MC}				
$u(D_1)$	0.0009	0.0011	0.0014	0.0014
$u(D_2)$	0.08	0.10	0.14	0.15
uncertainty of the apparatus constant - $Q_{\Delta T}$				
$u(D_1)$	0.0021	0.0020	0.0020	0.0021
$u(D_2)$	0.12	0.12	0.14	0.15
temperature instability of T_{GHS}				
$u(D_1)$	0.0001	0.0001	0.0002	0.0002
$u(D_2)$	0.01	0.01	0.02	0.02

Table 5.10.: Fit coefficients of the dielectric expansions and the propagated uncertainties of the listed components to these coefficients.

standard uncertainty $u_{\text{r}}\left(\frac{C(p)}{C(0)}\right) = 5.4 \times 10^{-8}$ for the measurement of capacitance ratios needs to be converted to an absolute uncertainty of the Mosotti-term $f = \frac{\epsilon_{\text{r}}-1}{\epsilon_{\text{r}}+2}$, which is rearranged to give:

$$f = \frac{\epsilon_{\text{r}} - 1}{\epsilon_{\text{r}} + 2} = 1 - \frac{1(1 + \kappa_{\text{eff}}p)}{\gamma + 3 + 2\kappa_{\text{eff}}} \tag{5.17}$$

In equation 5.17, γ is the relative change of capacitance defined in equation 3.21, whose uncertainty is, thus, given by $u(\gamma) = (\gamma + 1)u_{\text{r}}\left(\frac{C(p)}{C(0)}\right)$. It can be seen from equation 5.17 that two further contributions arise for the uncertainty of f. The uncertainty of κ_{eff} would usually be treated as a systematic component since its value may be unknown but should be constant during the course of an isotherm. However, in this work indication is given in section 5.1.1 that κ_{eff} may eventually vary during the measurement. To give a worst case estimate, κ_{eff} is, therefore, also varied for each data point in the range of its uncertainty, which was assessed in section 4.1.3 to be 1 %. The contribution of the uncertainty of the pressure measurement is approximately three orders of magnitude smaller than the other

two and, thus, neglected here. With the remaining two components, the uncertainty of the Mosotti-term is given by:

$$u(f) = \sqrt{\left(\frac{\partial f}{\partial \gamma}u(\gamma)\right)^2 + \left(\frac{\partial f}{\partial \kappa_{\text{eff}}}u(\kappa_{\text{eff}})\right)^2} \tag{5.18}$$

The partial derivatives are given by:

$$\begin{aligned}
\frac{\partial f}{\partial \gamma} &= \frac{3(1 + \kappa_{\text{eff}}p)}{(\gamma + 3 + 2\kappa_{\text{eff}}p)^2} \\
\frac{\partial f}{\partial \kappa_{\text{eff}}} &= \frac{3p(\gamma + 3 + 2\kappa_{\text{eff}}p) - 6p(1 + \kappa_{\text{eff}})}{(\gamma + 3 + 2\kappa_{\text{eff}}p)^2}
\end{aligned} \tag{5.19}$$

For each data point, f_r as well as f_{r+1} are scattered in the uncertainty interval defined by equation 5.18. This process is valid for the data evaluation with a free fit. In analogy to the Monte-Carlo simulations for pressure data in the previous section, the constraint ratios $F_{\text{ratio},r} - Q_{\Delta T}$ are fitted over f_r. Also, the influence of the relative uncertainty of $Q_{\Delta T}$ of 5 ppm is investigated by changing $Q_{\Delta T}$ by this amount and repetition of the constraint fit. The last component that has to be treated by Monte-Carlo simulations is the temperature instability of the gas-handling system, which causes scattering of F_{ratio} in the order of 1 ppm (see section 4.7).

Determination of the second dielectric virial coefficient The second dielectric virial coefficient $b_\epsilon(T_{\text{iso}})$ can be retrieved utilizing the working equation 3.53:

$$\begin{aligned}
b_\epsilon(T_{\text{iso}}) =& \frac{D_1}{D_0 - 1} \cdot \frac{RT_{\text{iso}}}{V_1} - T_{\text{ratio}}\frac{1 - V_1}{V1} \cdot b_{\epsilon,\text{GHS}}- \\
& RT_{\text{iso}}\frac{V_2}{V_1} \cdot \lambda_{\text{B}} - RT_{\text{iso}}\frac{V_3}{V_1} \cdot \lambda_{\text{A}} - RT_{\text{iso}}\frac{V_4}{V_1} \cdot \lambda_{\text{GHS}}- \\
& \frac{V_5}{V_1} \cdot (B_{\text{DCGT,iso}} - T_{\text{Ratio}}B_{\text{DCGT,GHS}})
\end{aligned} \tag{5.20}$$

where the coefficients V_1 to V_5 are defined in equation 3.54 in section 3.5. In case of the constraint fit, the fit coefficient D_0 of equation 5.20 is replaced by the constraint apparatus constant $Q_{\Delta T}$. As already explained in the previous section for the density virial coefficients, usually a precise measurement at $T_{\text{ratio}} = 1$ has to be performed first to determine $b_{\epsilon\text{GHS}}$. For the reasons given in the previous section, the most recent calculated values by Garberoglio and Harvey are used here [43]. The contributions from the terms of equation 5.20, the main contributions to uncertainty and final results including their combined uncertainty are listed in table 5.11 for the free as well as for the constraint fits. To determine the combined uncertainty, the partial derivatives of equation 5.20 are required. Again, this simple yet lengthy task is not shown here, whereas the resulting contributions are shown in table 5.11.

T_{iso} [K]	253.898	273.161	296.126	302.913
Terms of equation 5.20				
a) $\frac{D_1}{D_0-1}$ [10^{-6}m^{3}mol^{-1}]	1.189	0.983	0.561	0.471
b) $\frac{D_1}{Q_{\Delta T}-1}$ [10^{-6}m^{3}mol^{-1}]	1.122	0.830	0.341	0.310
$b_{\epsilon,\mathrm{GHS}}$ [10^{-6}m^{3}mol^{-1}]	0.023	0.027	0.031	0.033
λ_{B} [10^{-6}m^{3}mol^{-1}]	0.157	0.170	0.185	0.189
λ_{A} [10^{-6}m^{3}mol^{-1}]	-0.237	-0.255	-0.276	-0.283
λ_{GHS} [10^{-6}m^{3}mol^{-1}]	-0.004	-0.004	-0.005	-0.005
B_{DCGT} [10^{-6}m^{3}mol^{-1}]	0.811	0.448	-0.002	-0.134
Contributions to uncertainty				
a) $D_1 - C_{\mathrm{MC}}$ [10^{-6}m^{3}mol^{-1}]	0.092	0.103	0.136	0.140
a) $D_1 - T_{\mathrm{GHS,MC}}$ [10^{-6}m^{3}mol^{-1}]	0.010	0.016	0.013	0.013
b) $D_1 - C_{\mathrm{MC}}$ [10^{-6}m^{3}mol^{-1}]	0.026	0.033	0.041	0.042
b) $D_1 - Q_{\Delta T}$ [10^{-6}m^{3}mol^{-1}]	0.060	0.058	0.059	0.062
b) $D_1 - T_{\mathrm{GHS,MC}}$ [10^{-6}m^{3}mol^{-1}]	0.004	0.004	0.004	0.004
$b_{\epsilon,\mathrm{GHS}}$ [10^{-6}m^{3}mol^{-1}]	0.002	0.003	0.003	0.003
λ_{A} [10^{-6}m^{3}mol^{-1}]	0.012	0.013	0.014	0.014
λ_{B} [10^{-6}m^{3}mol^{-1}]	0.008	0.008	0.009	0.009
λ_{GHS} [10^{-6}m^{3}mol^{-1}]	<0.001	0.001	0.001	0.001
Q_{B} [10^{-6}m^{3}mol^{-1}]	0.004	0.002	<0.001	0.001
Q_{A} [10^{-6}m^{3}mol^{-1}]	0.012	0.007	<0.001	0.002
Q^* [10^{-6}m^{3}mol^{-1}]	0.010	0.005	0.001	0.002
$B_{\mathrm{DCGT,iso}}$ [10^{-6}m^{3}mol^{-1}]	0.009	0.008	<0.001	0.006
$B_{\mathrm{DCGT,GHS}}$ [10^{-6}m^{3}mol^{-1}]	0.005	0.005	<0.001	0.006
Results of the free fit [a]				
b_ϵ [10^{-6}m^{3}mol^{-1}]	0.437	0.598	0.628	0.671
$u(b_\epsilon)$ [10^{-6}m^{3}mol^{-1}]	0.095	0.105	0.138	0.142
$u_{\mathrm{r}}(b_\epsilon)$ [%]	21.8	17.6	22.0	21.1
repeatability [%]	7.9*	12.6	16.7	8.0**
Results of the constraint fit [b]				
b_ϵ [10^{-6}m^{3}mol^{-1}]	0.370	0.445	0.409	0.510
$u(b_\epsilon)$ [10^{-6}m^{3}mol^{-1}]	0.070	0.070	0.074	0.077
$u_{\mathrm{r}}(b_\epsilon)$ [%]	18.9	15.7	17.1	15.1
repeatability [%]	3.4*	8.6	10.5	11.4**

Table 5.11.: Absolute values of the terms used to calculate $b_\epsilon(T_{\mathrm{iso}})$ according to equation 5.20. Contributions marked with [a] contribute to the free fit exclusively, whereas these marked with [b] only contribute to the constraint fit. The main contributions to uncertainty are given in the middle part of the table. Final values of the dielectric virial coefficient for the free and constraint fit including their corresponding combined uncertainties are listed in the lower part including the repeatability, which is determined as the relative standard deviation of the individual isothermal measurements. * repeatability based on two measurements ** repeatability based on three measurements

In contrast to the density virial coefficients, an additional component based on the second DCGT virial coefficients is required to describe the influence of the dead volumes at different temperature since, unlike the pressure, the dielectric constant is not equal in both thermal

regimes. This was extensively discussed in section 3.4.3. The correction to the ideal fit coefficient is of the same order of magnitude, but since the the DCGT virial coefficients can be measured very precisely the resulting contribution to the combined uncertainty of b_ϵ is rather small. The relative correction due to $b_{\epsilon,\mathrm{GHS}}$ is a little bit lower compared to the equivalent for the density virial coefficients which is a consequence of the less distinctive temperature dependence. The absolute values of the terms describing the deformation of the cells under pressure are equal for both expansion evaluations. For the second density virial coefficient, the relative correction of the ideal fit coefficient is less than $2\,\%$. In contrast, this effect leads to a relative correction of the ideal fit coefficient in the order of several ten percent for the dielectric expansion. This is a consequence of the very small absolute value of b_ϵ.

The dominating uncertainty contributions are identical to the Burnett expansion. In case a free fit is applied the statistical scattering of the capacitance defines the reachable uncertainty. With a constraint fit, the uncertainty of $Q_{\Delta T}$ becomes the dominating component, whereas the scattering is still of the same order of magnitude. The application of the constraint fit leads to a decrease in uncertainty by roughly a factor of two, which may as well be seen in table 5.11 for the absolute uncertainties. It should be noted that the relative uncertainty of b_ϵ is distorted since the values from the free fit are significantly larger leading to the impression of lower relative uncertainties. Besides these components, the pressure deformation coefficients gain importance. The influence of statistical scattering on the fit coefficient D_0 is not listed since its contribution is less than $0.001 \times 10^{-6}\,\mathrm{m^3\,mol^{-1}}$ for all temperatures. Again, the uncertainty of T_ratio does not contribute significantly to the uncertainty by means of the working equation 5.20, but it is included in the uncertainty of $Q_{\Delta T}$ for the constraint fit. The values of $b_\epsilon(T)$ for the individual isotherms and the two fit approaches are plotted in figure 5.9. Again, a systematic deviation between the values from the free fit and the ones from the constraint fit can be reported, whereas there are no discrepancies beyond the level of expanded uncertainties.

An attempt for the derivation of the third dielectric virial coefficient from the corresponding fit coefficient D_2 could in principal be made for the data at $296\,\mathrm{K}$. The required working equation 3.45 includes the deformation of the cells under pressure. However, the resulting uncertainties can be estimated from table 5.10 and are in the order of almost $100\,\%$. That is why at this stage no value is reported.
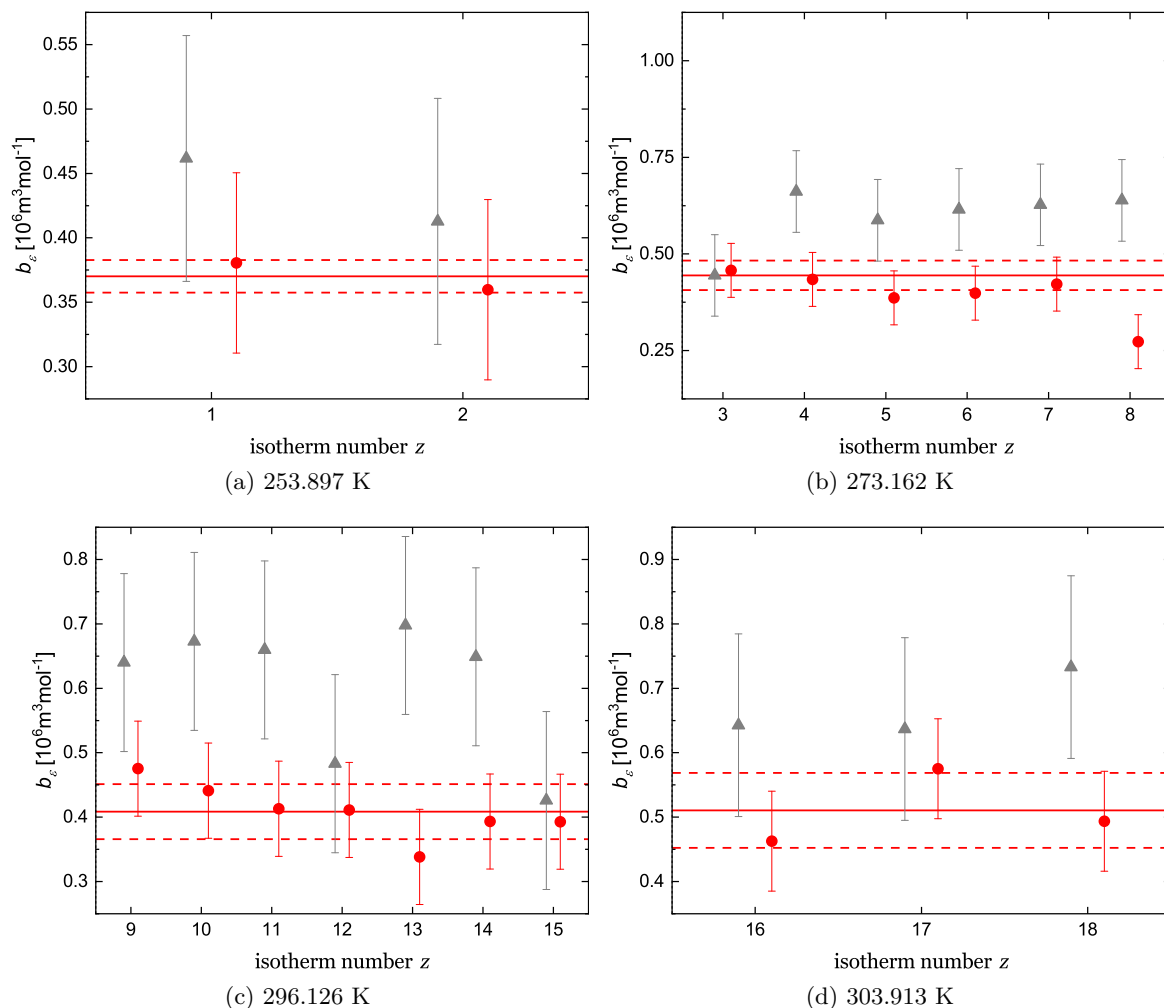
Figure 5.9.: Values of the second dielectric virial coefficient of argon for the individual isotherms measured at the indicated temperatures. Grey triangles denote values retrieved by a constraint fit, while the ones obtained from a constraint fit are marked by red circles. The error bars are the combined standard uncertainties. The average value and the corresponding standard uncertainty of the values from the constraint fit are visualized by the solid and dashed red lines.

5.5. Cross check of the measured virial coefficients

A major benefit of the approach shown in this thesis is that the different determined virial coefficients can be cross checked. As described in section 3.2, the second DCGT virial coefficient is defined by $B_{\mathrm{DCGT}}(T) = B(T) - b_\epsilon(T)$. These three properties were derived in the previous sections and are compared in table 5.12. The absolute deviations $B_{\mathrm{DCGT}}(T) - (B(T) - b_\epsilon(T))$ are visualized in figure 5.10. All values agree within their standard uncertainties except for the one calculated from the free fit at 302.913 K, which is slightly outside the 68.27 % level of confidence but very well within the expanded uncertainty. A certain trend can be seen for the calculated values from the constraint values that are all larger than the measured ones. This effect is attributed to the density virial coefficients since these are two orders of magnitude larger than the dielectric virials. The deviations shown here, thus, represent the ones that were already reported in section 5.3.

T_{iso} [K]	253.898	273.161	296.126	302.913
DCGT				
$B_{\mathrm{DCGT}}(T)$ [$10^{-6}\mathrm{m}^3\mathrm{mol}^{-1}$]	-26.844	-21.602	-16.380	-15.040
$u(B_{\mathrm{DCGT}}(T))$ [$10^{-6}\mathrm{m}^3\mathrm{mol}^{-1}$]	0.036	0.035	0.041	0.040
$u_{\mathrm{r}}(B_{\mathrm{DCGT}})$ [%]	0.11	0.16	0.25	0.27
expansion - free fit				
$B(T) - b_\epsilon(T)$ [$10^{-6}\mathrm{m}^3\mathrm{mol}^{-1}$]	-26.667	-21.370	-16.650	-15.126
$u(B(T) - b_\epsilon(T))$ [$10^{-6}\mathrm{m}^3\mathrm{mol}^{-1}$]	0.288	0.318	0.350	0.354
$u_{\mathrm{r}}(B(T) - b_\epsilon(T))$ [%]	1.07	1.47	2.13	2.36
ΔB_{DCGT} [$10^{-6}\mathrm{m}^3\mathrm{mol}^{-1}$]	-0.177	-0.232	-0.128	-0.436
$\Delta B_{\mathrm{DCGT}}/B_{\mathrm{DCGT}}$ [%]	0.66	1.07	0.78	2.90
expansion - constraint fit				
$B(T) - b_\epsilon(T)$ [$10^{-6}\mathrm{m}^3\mathrm{mol}^{-1}$]	-26.845	-21.727	-16.507	-15.126
$u(B(T) - b_\epsilon(T))$ [$10^{-6}\mathrm{m}^3\mathrm{mol}^{-1}$]	0.123	0.132	0.146	0.150
$u_{\mathrm{r}}(B(T) - b_\epsilon(T))$ [%]	0.46	0.61	0.89	1.00
ΔB_{DCGT} [$10^{-6}\mathrm{m}^3\mathrm{mol}^{-1}$]	0.001	0.125	-0.127	-0.864
$\Delta B_{\mathrm{DCGT}}/B_{\mathrm{DCGT}}$ [%]	<0.01	-0.58	-0.77	-0.57

Table 5.12.: Values and uncertainties (absolute and relative) of the second DCGT virial coefficient from the DCGT experiments as well as from the ones calculated by the results of the expansion experiments for free and constraint fits. The absolute and relative deviations between the values from the DCGT and the expansion experiments are listed as $\Delta B_{\mathrm{DCGT}} = B_{\mathrm{DCGT}} - (B(T) - b_\epsilon(T))$.
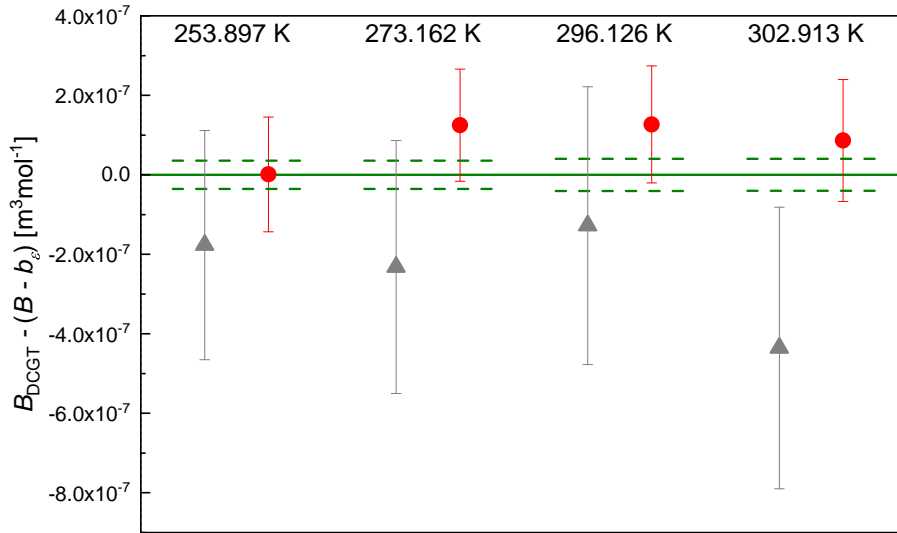
Figure 5.10.: Absolute differences between the directly determined values of $B_{\text{DCGT}}(T)$ (section 5.1.4) and the ones calculated from $B(T)$ (5.3) and $b_\epsilon(T)$ (5.4). Grey triangles denote virial coefficients retrieved from free fits, while red circles mark values determined by constraint fits. The error bars are the combined standard uncertainty of the calculated values, while the green dashed lines indicate the standard uncertainty of $B_{\text{DCGT}}(T)$.

5.6. Comparison to literature data

The comparison to the literature values starts with the density (subsection 5.6.1) and dielectric virial coefficients (subsection 5.6.2) since these values are required to calculate literature values of DCGT virial coefficients for subsection 5.6.3. It should be noted that not all available literature values are shown here, but only those who were considered to be relevant.

5.6.1. Comparison of the density virial coefficients to the literature

The second density virial coefficient of argon has a significant temperature dependance, which was shown in figure 3.1. In the measured temperature range, $B(T)$ increases from roughly $-26.5 \times 10^{-6} \, \text{m}^3 \, \text{mol}^{-1}$ at $253 \, \text{K}$ to $-14.6 \times 10^{-6} \, \text{m}^3 \, \text{mol}^{-1}$ at $303 \, \text{K}$. The sign of $B(T)$ switches at approximately $408 \, \text{K}$. To resolve the small differences to the literature data the comparison shown in figure 5.11 is carried out independently for the four measured temperatures.

Theoretical calculations include semi-classical computations by Mehl (published in Moldover *et al.* [31]), who gave an estimate of uncertainty. Furthermore, works by Jäger *et al.* and Wiebke *et al.* based on coupled cluster calculations (see section 3.1.1) both from 2011 are selected [29, 30]. Since both authors utilized a pair potential by Jäger *et al.* [111] in combination with a short range corrected three-body potential by Schwerdtfeger *et al.* [112], the good agreement between these two works is relativized. These authors did not assign an uncertainty to their computations, but Gaiser *et al.* estimated uncertainties for their values at the triple point of water, which are assumed here as well [1]. Uncertainties at other

5. Results
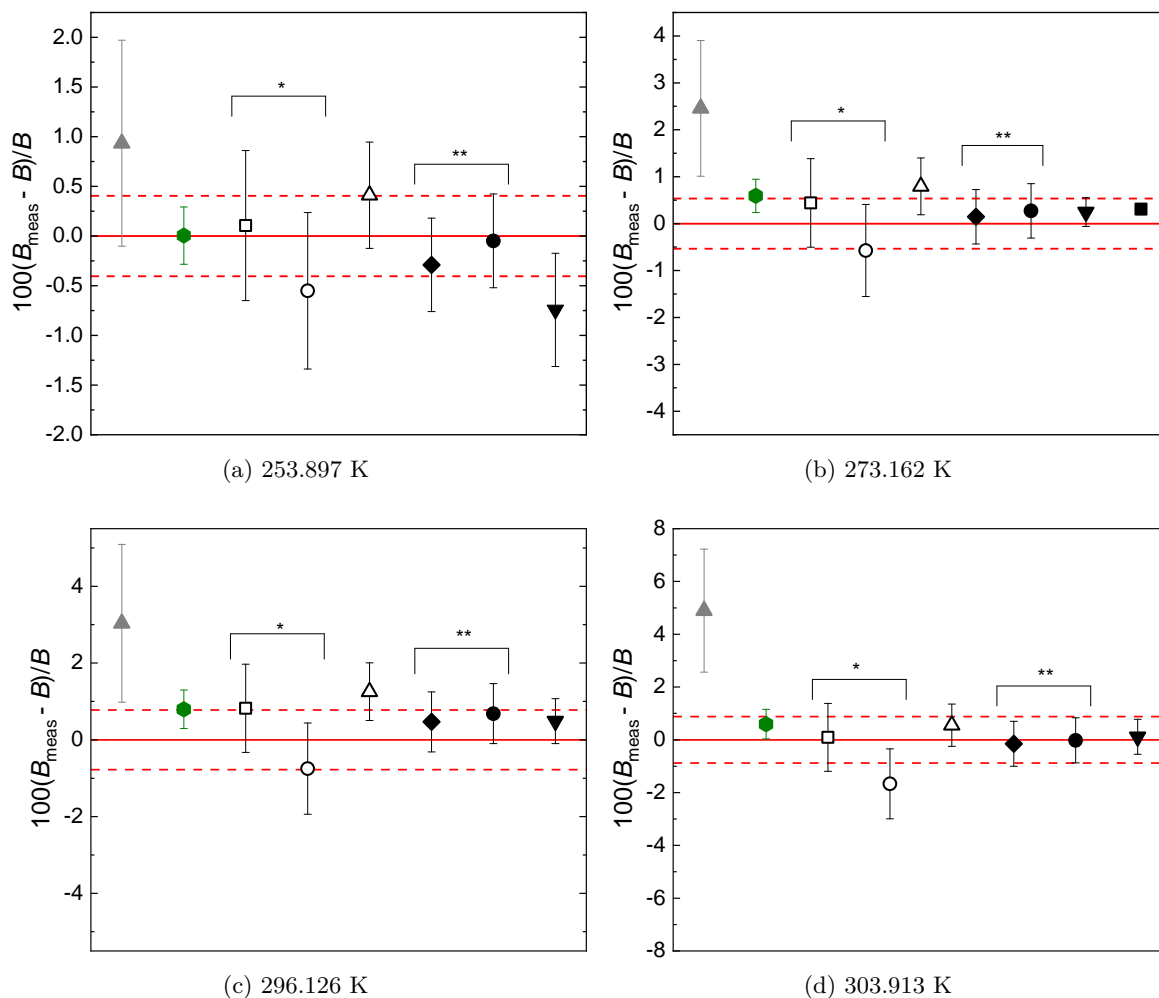
Figure 5.11.: Relative deviations to the value of $B_{\mathrm{meas}}(T)$ determined in section 5.3 by the constraint fit (—). The red dashed lines indicate the corresponding combined standard uncertainty. Values from the free fits (▲) and the ones calculated from the second DCGT virial coefficients (⬢) of section 5.1.4 and the dielectric virial coefficients obtained from the constraint fit in section 5.4 are shown. Literature values from **theory**: □ - Jäger *et al.* [29]; ○ - Wiebke *et al.* [30]; △ - values computed by Mehl published in Moldover *et al.* [31]. Literature values from **experiment**: ◆ - Tegeler *et al.* [88]; ● - Jäger *et al.* [29]; ▼ - values by McLinden published in Cencek *et al.* [32]; ■ - Gaiser *et al.* [1]. The error bars are combined uncertainties that sometimes had to be estimated or increased in case interpolation was required to obtain $B(T)$ at the measured temperature. See text for details. Values marked with * utilized the same potentials while these marked with ** rely on the same data by Gilgen *et al.* [67] and can, thus, not be seen as independent determinations.

temperatures are approximated assuming that these have the same temperature dependence as these stated by Mehl in [31]. A three-body potential for argon was published by Cencek *et al.* in 2013 together with values for $C(T)$ determined by coupled cluster calculations and an estimate of uncertainty [32].

253.898 K	273.161 K	296.126 K	302.913 K	reference
-26.23 ± 0.20	-20.77 ± 0.20	-15.62 ± 0.18	-13.93 ± 0.18	This work free fit
-26.48 ± 0.20	-21.28 ± 0.20	-16.10 ± 0.18	-14.62 ± 0.18	This work constraint fit
calculated values of $B(T)$ in $10^6\mathrm{m}^3\mathrm{mol}^{-1}$				
-26.45 ± 0.20	-21.19 ± 0.20	-15.97 ± 0.18	-14.60 ± 0.18	Jäger *et al.* [29]
-26.62 ± 0.21	-21.41 ± 0.21	-16.22 ± 0.19	-14.86 ± 0.19	Wiebke *et al.* [30]
-26.37 ± 0.14	-21.11 ± 0.13	-15.90 ± 0.12	-14.54 ± 0.12	Moldover *et al.* [31]
experimental values of $B(T)$ in $10^6\mathrm{m}^3\mathrm{mol}^{-1}$				
-26.55 ± 0.13	-21.25 ± 0.13	-16.02 ± 0.13	-14.64 ± 0.13	Tegeler *et al.* [67, 88]
-26.48 ± 0.13	-21.22 ± 0.13	-15.99 ± 0.13	-14.62 ± 0.13	Jäger *et al.* [29, 67]
-26.67 ± 0.15	-21.230 ± 0.065	-16.02 ± 0.09	-14.60 ± 0.10	Cencek *et al.* [32]
	-21.217 ± 0.014			Gaiser *et al.* [1]

Table 5.13.: Relevant calculated and experimentally determined values of the second density virial coefficient of argon from the literature for the indicated temperatures. The values by McLinden published in Cencek *et al.* had to be interpolated introducing additional uncertainty.

The most comprehensive experimental determination of the *p-ρ-T* behavior of argon was carried out by Gilgen *et al.* in 1994 utilizing a two-sinker densimeter (see 3.3). The data was reevaluated in 1999 by Tegeler *et al.* and in 2011 by Jäeger *et al.* with focus on the determination of density virial coefficients, which was exemplified in section 3.6. Furthermore, values determined from densimetry measurements of argon by McLinden are included in Cencek *et al.* [32] for different temperatures. Except for the triple point of water, these temperatures do not coincide with the ones measured in this thesis. That is why values of $B(T)$ were interpolated, whereas an additional uncertainty component for this procedure had to be introduced.

It was already explained in section 5.3 that the application of the free fit is error prone due to the higher fit order. The results can be optimized by reducing high pressure data points together with the fit order. Still, it is advisable to apply a constraint on the apparatus constant if possible. That is why the further discussion will be based on the value obtained from the constraint fit. Overall, all values plotted in figure 5.11 agree very well. In most cases, the literature values lie within the standard uncertainty of the values determined in this thesis. For the few exceptions, overlap by means of the standard uncertainties can still be reported. Especially in comparison to densimetry, this method may offer a complementary approach without the need to determine the absolute density while keeping competitive uncertainties. Regarding the uncertainties, a even more sophisticated approach is to calculate the density virial coefficients from the DCGT virial coefficients (section 5.1.4) and the dielectric virial coefficients (section 5.4). In this case, relative uncertainties for $B(T)$ between 0.3 % and 0.55 % can be obtained, although the relative uncertainties of $b_\epsilon(T)$ are in the order of 15 %.

This approach gains further importance for the higher virial coefficients. As pointed out in section 5.3, at this point a determination of $C(T)$ is only possible at ambient temperature. The comparison of this value to the established literature is shown in table 5.14. While the agreement to the established literature of $C(T)$ is on an acceptable level and well within

the standard uncertainty, the uncertainty of C_{DCGT} is significantly lower. Since the determination at temperatures different from ambient will introduce further contributions to the uncertainty, the calculation by $C(T) = C_{\mathrm{DCGT}}(T) + c_\epsilon(T) + 2b_\epsilon(T)B_{\mathrm{DCGT}}$ is advisable.

253.898 K	273.161 K	296.126 K	302.913 K	reference
calculated values of $C(T)$ in $10^{12}\mathrm{m}^6\mathrm{mol}^{-2}$				
1128 ± 28	1147 ± 23	1071 ± 19	1052 ± 18	Jäger *et al.* [29]
1208 ± 28	1130 ± 23	1056 ± 19	1038 ± 18	Wiebke *et al.* [30]
1234 ± 15	1152 ± 13	1077 ± 11	1057 ± 10	Moldover *et al.* [31]
experimental values of $C(T)$ in $10^{12}\mathrm{m}^6\mathrm{mol}^{-2}$				
1271 ± 50	1178 ± 50	1109 ± 50	1079 ± 50	Tegeler *et al.* [67, 88]
1234 ± 50	1153 ± 50	1074 ± 50	1054 ± 50	Jäger *et al.* [29, 67]
1235 ± 43	1153 ± 32	1080 ± 60	1061 ± 64	Cencek *et al.* [32]
		970 ± 165		This work free fit
		1119 ± 70		This work constraint fit

Table 5.14.: Relevant calculated and experimentally determined values of the third density virial coefficient of argon from the literature for the indicated temperatures. The values by McLinden published in Cencek *et al.* had to be interpolated introducing additional uncertainty.

5.6.2. Comparison of the dielectric virial coefficients to the literature

T [K]	$b_\epsilon(T)$ $[10^{-6}\frac{\mathrm{m}^3}{\mathrm{mol}}]$	$u(b_\epsilon(T))$ $[10^{-6}\frac{\mathrm{m}^3}{\mathrm{mol}}]$	reference
242.95	0.449	0.017	Huot *et al.* 1991 [6]
303.15	0.298	0.022	Huot *et al.* 1991 [6]
407.60	0.024	0.073	Huot *et al.* 1991 [6]
323.00	0.429*	0.012	Achtermann *et al.* 1991 [50]
303.00	0.417*	0.012	Achtermann *et al.* 1993 [49]
303.00	0.297*	0.024	Bose *et al.* 1988 [115]
322.85	0.174	0.029	Bose *et al.* 1970 [114]
322.15	0.094	0.048	Orcutt *et al.* 1967 [113]
323.15	0.532	0.024	Orcutt *et al.* 1965 [5]
373.15	0.701	0.097	Orcutt *et al.* 1965 [5]
373.15	0.605	0.024	Orcutt *et al.* 1965 [5]
423.15	0.556	0.024	Orcutt *et al.* 1965 [5]
423.15	0.749	0.024	Orcutt *et al.* 1965 [5]

Table 5.15.: Overview of experimentally determined values of b_ϵ of argon shown in figure 5.12. Values marked with * were obtained from optical experiments at a wavelength of 632.99 nm.

Since the temperature dependence of the second dielectric virial coefficient is much less distinctive and the relative uncertainties are much higher than these of the density virial coefficients, a comparison to other values can be carried out by means of the absolute values over a suitable temperature range. An overview of the relevant theoretical and experimental literature values is shown in figure 5.12 together with the values determined by the constraint
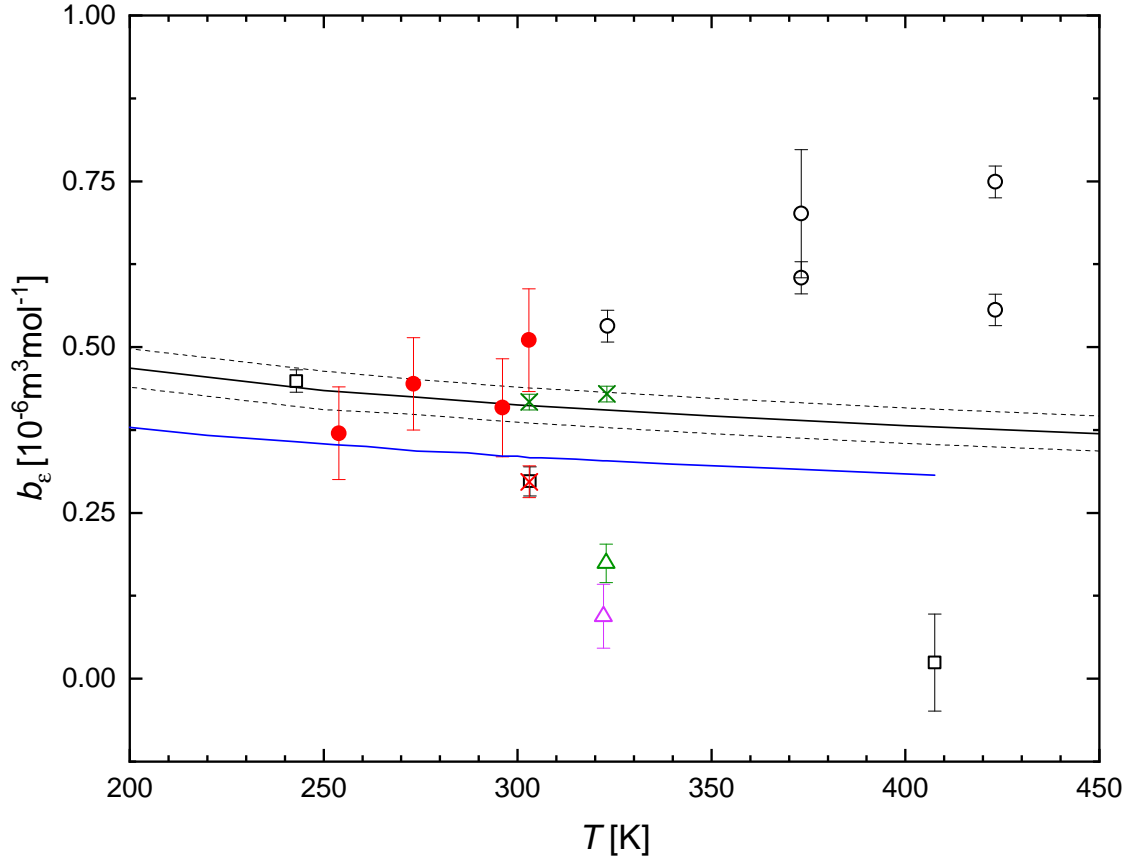
Figure 5.12.: Overview of theoretical calculations and experimental values of the second dielectric virial coefficient of argon as a function of temperature. For the experimental results, same symbols indicate that the same method was used. The black dashed line indicates the estimated expanded uncertainty. **Theory:** —— Garberoglio and Harvey 2020 [43]; —— Rizzo *et al.* 2002 [45]; Results indistinguishable to Garberoglio and Harvey on the scale of this plot were reported by Vogel *et al.* and Song *et al.* [44, 48]. **Experimental:** ● - this work (constraint fit); ○ - Orcutt and Cole 1965 [5]; □ - Huot and Bose 1991 [6]; △ - Orcutt 1967 [113]; △ - Bose and Cole 1970 [114]; × - Bose *et al.* 1970 [114]; × - Achtermann *et al.* 1991, 1993 [49, 50]

fit from section 5.4 in this work.

Among the theoretical work, three provide almost coinciding results in the temperature range of interest for this work. An older publication by Vogel *et al.* from 2010 and two very recent publications by Garberoglio and Harvey as well as Song and Luo [43, 44, 48]. The agreement is a consequence of utilizing the same interaction induced pair polarizability that was developed by Vogel *et al.* in their work. Both of the latter works utilized a more recent pair potential by Patkowski *et al.* [116] from 2017 compared to Vogel *et al.*. However, since the second dielectric virial coefficient is dominated by the influence of the pair polarizability on the one hand, and since the pair potential was already very well developed by 2010, these three works can not be viewed as independent confirmations of the calculation. They are still relevant since Vogel *et al.* and Song *et al.* used a semi-classical approach with different

253.898 K	273.161 K	296.126 K	302.913 K	reference
$b_\epsilon(T)$ in $10^{-6}\mathrm{m}^3\mathrm{mol}^{-1}$				
0.437 ± 0.095	0.598 ± 0.105	0.628 ± 0.138	0.671 ± 0.142	This work free fit
0.370 ± 0.059	0.445 ± 0.065	0.409 ± 0.073	0.510 ± 0.076	This work constraint fit
calculated values of $b_\epsilon(T)$ in $10^{-6}\mathrm{m}^3\mathrm{mol}^{-1}$				
0.433 ± 0.029	0.425 ± 0.027	0.415 ± 0.026	0.412 ± 0.027	Garberoglio *et al.* 2020 [43]
0.433 ± 0.024	0.424 ± 0.024	0.414 ± 0.023	0.411 ± 0.023	Song *et al.* 2020 [44]
0.433	0.424	0.414	0.411	Vogel *et al.* 2010 [48]
0.352	0.343	0.336	0.333	Rizzo *et al.* 2002 [45]

Table 5.16.: Overview of determined values of b_ϵ in $10^{-6}\frac{\mathrm{m}^3}{\mathrm{mol}}$ at the four measured temperatures as well as calculated values from the literature including the uncertainty estimates provided for the two recent publications.

levels of quantum mechanical corrections, while Garberoglio and Harvey used a path integral method including higher levels of quantum mechanics (see also section 3.1.3). The matching results indicate that both approaches can be used to calculate the second dielectric virial coefficients. Garberoglio and Harvey stated that quantum effects first start to play a role for temperatures below 100 K [43]. This will be of particular interest when new pair polarizabilities, which are part of the "Quantum Pascal" project (see section 2.2), are available. In figure 5.12 the values of Garberoglio *et al.* are shown since these technically include higher levels of quantum mechanics. Furthermore, they gave an estimate of uncertainty, which is based on a uncertainty estimate for the pair polarizability of Vogel *et al.* that was apparently part of a private communication [43]. It should be noted that Song and Luo estimated an uncertainty for their values as well, which is approximately equal to the one by Garberoglio and Harvey since it is based on a similar estimate of the relative uncertainty of the pair polarizability of Vogel *et al.* of 5.4 %. Another independent theoretical calculation by Rizzo *et al.* from 2002 is shown in the plot as well. It has a roughly constant absolute offset compared to the other calculations, which corresponds to almost 20 % at the triple point of water and is far beyond the uncertainties estimated by Garberoglio *et al.* as well as Song et al. [43, 44]. These authors concluded that the calculation by Rizzo *et al.* must have been doubtful in parts for the applied quantum mechanical corrections. A summary of the calculated values at the four temperatures measured in this thesis is given table 5.16

The experimental work shown in figure 5.12 and summarized in table 5.15 is scattered widely. Though, often no rigorous uncertainties are given, the stated uncertainties are partially clearly too optimistic and display the experimental difficulties. To knowledge of the author, expansion experiments are at this point the only viable access to $b_\epsilon(T)$ with reasonable uncertainties. The last work in this field was carried out almost three decades ago. Relevant experiments that should be highlighted were carried out by Huot *et al.*, whereas their value at 408 K is significantly below the established values [6]. They used an approach developed by Buckingham [117], which is described in detail in appendix G.2 similar to the cyclic expansion described in this appendix as well. Achtermann *et al.* published very precise assessments of the refractive index virial coefficients at a wavelength of 632.99 nm for 303 K

and 323 K. The difference between the dielectric and refractive index virial coefficients (see appendix D for their relation) is typically in the order of a few percent. The difference was for instance calculated for helium at this wavelength by Puchalski *et al.* to be 2.5 %. Thus, the value is included here especially due to the attributed low uncertainty. Another optical measurement at the same wavelength was performed by Bose *et al.* in 1977. This value at 303 K coincides perfectly with the measurement of Huot and Bose at this temperature. Orcutt and Cole utilized the dielectric expansion method described in section 3.4 in 1965. Unfortunately, the values are higher than the calculations and more precise experiments that were carried out later. The differences are far outside the stated uncertainties. There are several possible sources that can lead to this deviations. First, the behavior of the utilized plate capacitors under pressure may be an issue. This also accounts for the deformation of the vessels under pressure. As shown in section 5.4, the influence of this correction can be in the order of several ten percent. Both effects are systematic leading to shifted values. Errors in their correction remain completely undetected for repetitions of the experiment. An additional modification of the method, the cyclic expansion described in appendix G.2, was used in 1967 by the same authors to decrease the uncertainties. This data point in turn is significantly lower than the ones reported previously. Since a new experimental setup was used, again, the systematic effects described previously could explain the deviation. A second work utilizing the cyclic expansion and the same apparatus was published in 1970 by Bose and Cole. The value is in reasonable agreement with the first one, which again indicates a systematic error source from the used apparatus.

Generally, the retrieved values in this work agree very well with the theory of Garberoglio and Harvey [43] and, thus, also with the calculations of Vogel *et al.* [48] and Song and Luo [44]. The values at 273 K (six isotherms) and 296 K (seven isotherms) lie within the estimated expanded uncertainty of the theoretical calculations [43]. The values at 253 K (two isotherms) and 303 K (three isotherms) still agree on the level of their standard uncertainty. It should be noted at this point that the uncertainties assigned to the results of this work correspond to the uncertainty of a single isotherm measurement and could potentially be decreased by statistical means. Furthermore, the values obtained in this thesis confirm the highly precise optical measurements by Achtermann *et al.* [49, 50]. Overall, it can be concluded that the theory of Rizzo *et al.* is erroneous [45]. The results by Huot *et al.* seem to agree very well at 243 K but deviate on the level of four standard uncertainties at 303 K and 408 K [6]. This indicates that eventually a systematic temperature effect has lead to these deviations. This also accounts to the other works shown in figure 5.12 and table 5.15 which are prior to 1970. They are not taken into account for comparison since their large deviations indicate undetected systematic errors. Still, there is one conclusion that can be drawn from these measurements. These advanced experimental methods, which were developed to minimize the relative uncertainty of the apparatus constant to the level of a few ppm [118], for instance the cyclic expansion [113] or the method of Buckingham [117] (see appendix G.2), can still result in systematically wrong results. It was shown in section 5.4 that the data evaluation is heavily influenced by effects due to pressure deformation, which is why the author assumes

that these are causing the deviations.

The experimental challenges are even more distinct for the third dielectric virial coefficient $c_\epsilon(T)$. At this point, no relevant theoretical calculations of $c_\epsilon(T)$ were published for argon, and only one experimental determination by Huot *et al.* [6] can be found in the literature. Gaiser *et al.* retrieved another value from the high pressure data measured by Lallemand *et al.* by the application of constraints for the molar polarizability and $b_\epsilon(T)$ [1, 51]. Achtermann *et al.* published precisely measured third refractive index virial coefficients of argon for a wavelength of 632.99 nm. Under the assumption that the influence of the frequency will only cause deviations to $c_\epsilon(T)$ in the order of a few percent, which is the case for $b_\epsilon(T)$, the values are listed together with the others in table 5.17. As explained in section 5.4, no estimate for the third dielectic virial coefficient are given within this thesis. However, the values are required to calculate the third DCGT virial coefficient in the next section.

T [K]	$c_\epsilon(T)$ [$10^{-12}\frac{\text{m}^6}{\text{mol}^2}$]	$u(c_\epsilon(T))$ [$10^{-12}\frac{\text{m}^6}{\text{mol}^2}$]	reference
242.95	-21.95	0.52	Huot *et al.* 1991 [6]
303.15	-17.80	9.77	Huot *et al.* 1991 [6]
407.60	-12.68	5.72	Huot *et al.* 1991 [6]
298.15	-22.40**	3.60	Lallemand *et al.* 1977 [1, 51]
323.00	-20.64*	0.48	Achtermann *et al.* 1991 [50]
303.00	-21.36*	0.48	Achtermann *et al.* 1993 [49]
interpolated values of $c_\epsilon(T)$ at the measured temperatures			
253.898	-18.03	2.7	interpolation
273.161	-19.10	2.9	interpolation
296.126	-20.38	3.1	interpolation
302.913	-20.75	3.1	interpolation

Table 5.17.: Experimentally determined values of c_ϵ including the stated uncertainty estimates. Values marked with * are refractive index virial coefficients at a wavelength of 632.99 nm. The value marked with ** was reevaluated by Gaiser *et al.*. In the lower part, interpolated values of $c_\epsilon(T)$ derived by the procedure described in the text are listed together with an estimated standard uncertainty of 15 %.

To retrieve values of $c_\epsilon(T)$ at the temperatures measured in this work, the following strategy is followed. The values by Achtermann *et al.* lie in between these of Huot *et al.* and Lallemand *et al.* confirming their magnitude to some extend. Still, since the frequency dependence of $c_\epsilon(T)$ is unclear, they are not used further. Instead, the three values by Huot *et al.* show an approximately linear behavior in temperature. This is used to interpolate a value at 298.15 K by Huot *et al.*. Since the uncertainties are comparable, the average value of this value and the one by Gaiser *et al.* based on the data of Lallemand *et al.* is calculated and selected as a base value, while the linear temperature dependence of Huot *et al.* is selected to calculate c_ϵ at the other temperatures. These calculated values are shown in the second part of table 5.17. A standard uncertainty of 15 % is estimated based on the scattering of the experimental values.

5.6.3. Comparison of the DCGT virial coefficients to the literature
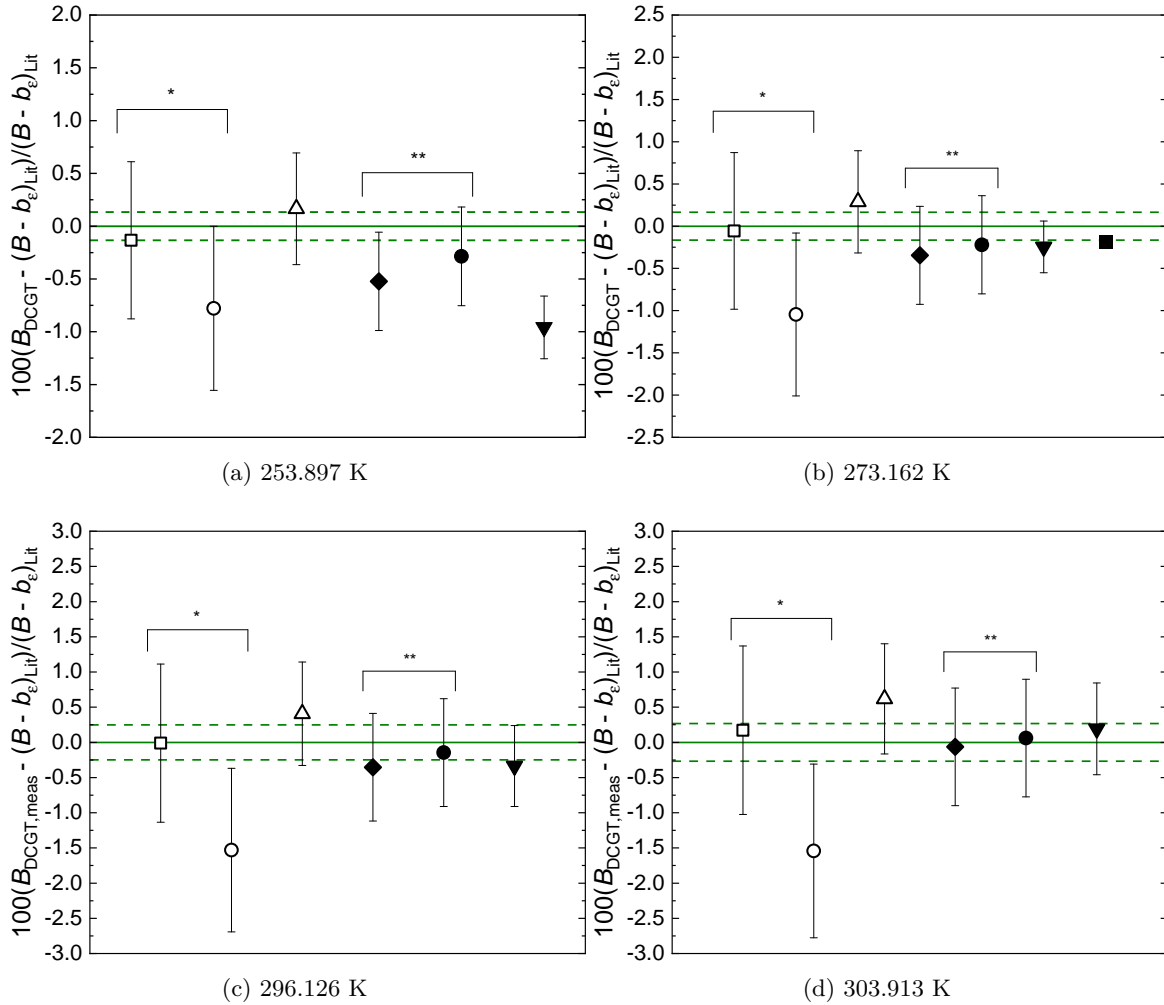
Figure 5.13.: Relative difference between the directly determined second DCGT virial coefficient $B_{\mathrm{DCGT,meas}}$ and values $(B - b_\epsilon)_{\mathrm{Lit}}$ that were calculated from literature values for $B(T)$ and $b_\epsilon(T)$ except for the directly determined very accurate value of Gaiser *et al.* (■) at $273\,\mathrm{K}$ [1]. The uncertainty of this value is below the size of the used symbol. —— value retrieved in this work. The green dashed lines mark the corresponding combined standard uncertainty. Values based on **theory:** □ - Jäger *et al.* [29]; ○ - Wiebke *et al.* [30]; △ - values computed by Mehl published in Moldover *et al.* [31]. Values based on **experiment:** ◆ - Tegeler *et al.* [88]; ● - Jäger *et al.* [29]; ▼ - values by McLinden published in Cencek *et al.* [32] The error bars are combined uncertainties, whereas sometimes uncertainties had to be estimated. Values for b_ϵ were taken from Garberoglio and Harvey [43]. Values marked with * utilized the same potentials while these marked with ** rely on the same data by Gilgen *et al.* [67] and can, thus, not be seen as independent determinations. See the text further details.

Highly precise experimental values of DCGT virial coefficients were published by Gaiser *et al.* with $B_{\mathrm{DCGT}} = -21.1609\,\mathrm{cm^3\,mol^{-1}}$ and $C_{\mathrm{DCGT}} = 1182.7\,\mathrm{cm^6\,mol^{-2}}$ at the triple point
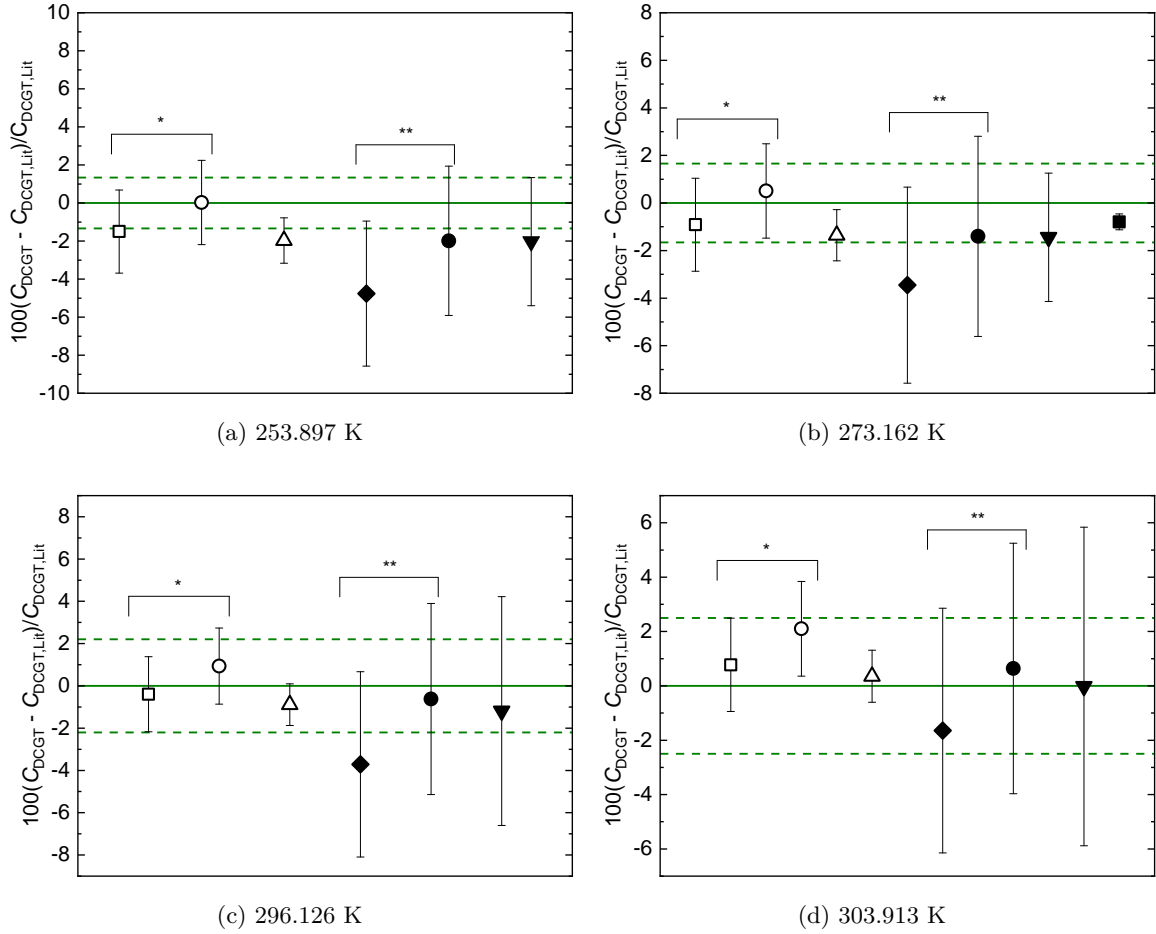
Figure 5.14.: Relative difference between the directly determined third DCGT virial coefficient $C_{\mathrm{DCGT,meas}}$ and values $C_{\mathrm{DCGT,Lit}}$ that were calculated from literature values for the density and dielectric virial coefficients except for the directly measured very accurate value of Gaiser *et al.* (■) at 273 K [1]. —— value retrieved in this work. The dashed green lines mark the corresponding combined standard uncertainty. Values based on **theory:** □ - Jäger *et al.* [29]; ○ - Wiebke *et al.* [30]; △ - combinations of the second density virial coefficient by Mehl published in Moldover *et al.* [31] with the third density virial coefficient by Cencek *et al.* [32]. Values based on **experiment:** ◆ - Tegeler *et al.* [88]; ● - Jäeger *et al.* [29]; ▼ - values by McLinden that were published in Cencek *et al.* [32]. The error bars are combined uncertainties, whereas sometimes uncertainties had to be estimated. Values for b_ϵ were taken from Garberoglio and Harvey [43] while c_ϵ had to be estimated from experimental data by Huot *et al.* and Lallemand *et al.* [6, 51]. Values marked with * utilized the same potentials, while these marked with ** rely on the same data by Gilgen *et al.* [67] and can, thus, not be seen as independent determinations. Further details on the assigned uncertainty, the evaluation of c_ϵ and interpolation of experimental values is given in the text.

of water based on measurements that were carried out in the frame of the determination of the Boltzmann constant [1]. That is why the corresponding relative standard uncertainties,

204 ppm for B_{DCGT} and 3336 ppm for C_{DCGT}, are extremely low. Other than that, there is a lack of directly determined DCGT virial coefficients. That is why a comparison is carried out by calculation of B_{DCGT} and C_{DCGT} by equations 3.23 from the most relevant density and dielectric virial coefficients in the literature, which were presented in the previous two sections 5.6.1 and 5.6.2. Details on their determination, valuation and uncertainty was given in these sections.

The relative deviations of the measured values to these calculated literature values are plotted in figure 5.13 for the second DCGT virial coefficient and in figure 5.14 for the third DCGT virial coefficient. Overall, an excellent agreement, which is typically well within the standard uncertainty, can be reported. For B_{DCGT}, the values by Wiebke *et al.* are systematically deviating not only from the measured values but also from the values of Jäger *et al.*. Since both authors utilized the same potentials, this deviation surprises to some extend but may as well display the difficulties in these calculations. The comparably low uncertainties of the calculated density virial coefficients (especially of $C(T)$) by Mehl published in [31] were confirmed on the level of uncertainty and for the indicated temperatures. This is an important aspect since the assignment of uncertainties to theoretical calculations is rather challenging. The experimentally achieved uncertainties of B_{DCGT} can compete with the ones of the values that were retrieved from accurate experimental determinations with densimeters. Since the uncertainty of the calculated DCGT virial coefficients is by far dominated by the uncertainty of $B(T)$ and $C(T)$, this direct comparison can be carried out. For C_{DCGT}, the uncertainties are actually below these of the established methods. This aspect can be exploited to precisely determine the third density virial coefficient.

6. Summary, conclusions and outlook

Summary   The previous chapters comprehensively covered the theoretical background, design, construction and first results of a compact and innovative apparatus capable of determining three different kinds of virial coefficients simultaneously in an automated manner. The novel working equations include the main corrections of cell deformation under pressure as well as dead volumes at different temperatures and, thus, provide important information for future work. They are the basis for a comprehensive uncertainty analysis for each of the three methods in accordance with the GUM and its first supplement. Validation of the performance was achieved by determination of the DCGT, second density and second dielectric virial coefficients of argon at temperatures of $254\,\mathrm{K}$, $273.16\,\mathrm{K}$, $296\,\mathrm{K}$ and $303\,\mathrm{K}$. The retrieved values were cross checked amongst each other and showed excellent agreement on the level of the standard uncertainty in comparison to other highly accurate experimental and theoretical data in the literature. The evaluation of the expansion experiments was shown to be rather complex, whereas reliable and precise results can be obtained utilizing a constraint on the apparatus constant from accurate measurements with helium. The obtained relative uncertainty on the level of $5\,\mathrm{ppm}$ for this volume ratio allowed to decrease the uncertainty in density and dielectric virial coefficients by a factor of two in comparison to their determination from a free fit. Based on Monte-Carlo simulations, it was shown that the dominating contribution of uncertainty is the statistical scattering of pressure and capacitance together with the uncertainty of $Q_{\Delta T}$. The reached relative standard uncertainties are in the order of $0.15\,\%$ to $0.3\,\%$ for B_{DCGT} and $1.5\,\%$ to $2.5\,\%$ for C_{DCGT}. For $B(T)$, relative standard uncertainties of $0.5\,\%$ to $0.9\,\%$ can be reported, while those of $b_\epsilon(T)$ are in the order of $15\,\%$. This work marks the first attempt for the determination of the latter since three decades. Compared to older publications, the detailed uncertainty budget appears to give an honest indication of the measuring performance, while stated uncertainties in the literature are mostly far too optimistic.

Generally, it was shown that the expansion experiments are vulnerable to systematic and hard to assess error sources. These effects are especially prominent for the dielectric expansion, while in case of the Burnett expansion additional care has to be taken with regard to the required fit order. At this point higher virial coefficients can only be obtained for equal temperatures of the measuring cells and the gas-handling system. In contrast, the data evaluation by means of DCGT offers a variety of advantages. Corrections due to the pressure deformation of the cells and the temperature of the gas-handling system do not have to be taken into account here making the underlying working equation less complex. Therefore, higher virial coefficients are easier to obtain, while, at the same time, the reachable

uncertainties of the DCGT virial coefficients are significantly lower than those of the density virial coefficients from the Burnett expansion. It was shown that the determined dielectric virial coefficients can be used to calculate the density virial coefficients from the DCGT virial coefficients to further decrease their uncertainty. The reachable orders of uncertainty are comparable to the most precise alternative methods.

To fully use the potential of this experimental approach, a few key considerations have to be taken into account. Ideally, the measurements should be performed at completely isothermal conditions. Furthermore, it has to be ensured that a reasonable number of measurements can be taken with the defined volume ratio between measuring and expansion volume to enable sufficient fit orders. The capacitors should be designed to have a low and easy to determine compressibility (for instance by using tungsten carbide for the electrodes). They should not be exposed to rapid pressure changes, while, at the same time, the expansion volume needs to be evacuated properly. It was shown that the main contributions to uncertainty of virial coefficients for all three methods arise from statistical scattering of data points from isothermal measurements. As a consequence, the temperature stability is very important, while, in contrast, the uncertainty of the absolute pressure and temperature measurement is only of secondary importance.

Conclusions This last aspect offers a certain potential for the commercialization of this approach with less expensive measuring equipment. Essentially, the precise measurement of changes in pressure, capacitance and temperature is required, while their absolute assessment is not dominating. This reduces the costs for the pressure and temperature measuring equipment. Monte-Carlo simulations showed that unfortunately the demands in capacitance measurement cannot be lowered. To the knowledge of the author, the used capacitance bridge is at this point the only commercially available but also cost intensive option with the required performance. As pointed out already, a highly accurate calibration of the apparatus constant would be required to reach the full potential of the method. Aspects that complicate the handling of such a system are the need to determine a suitable fit order for the data and the fact that the working equations are based on the Clausius-Mosotti equation, which does, for instance, not include polar molecules. It should also be pointed out that the determined second and third density virial coefficient, which were obtained by the measurements up to $7\,\mathrm{MPa}$ are only capable of describing the density well below $3\,\mathrm{MPa}$ with reasonable uncertainty. In contrast, a proper densimeter will always measure the exact density at the corresponding pressure and temperature.

Outlook The next step is to reduce the uncertainty of the constraint fits of the expansion data. Therefore, further measurements with helium over a broader temperature range will allow to determine the apparent apparatus constant at the individual measuring temperatures with lower uncertainty. After that, the operating temperature range will be extended. Therefore, the thermal stabilization of the gas-handling system will be improved by thermal anchoring to a thermostated copper block. Furthermore, the reported temperature gradients

inside the system will be decreased by adjustment of the fluid bath temperature and further thermal bridges inside the measuring chamber. This is required in particular to assess the potential of the method to be used as a compact and automated DCGT, which could become a practical direct realization of the unit kelvin. At the same time, these modifications will allow to assess the molar polarizability with lower uncertainty over a wider temperature range than possible at this point. This is important for the measurement of molecules, as for instance hydrogen, whose molar polarizability is temperature dependent. Experiments with hydrogen and mixtures are intended after the work on the noble gases (neon is to be measured) has finished. On the theoretical side, the derivation of an expression for the third density and dielectric virial coefficients for temperatures other than ambient is targeted. However, great care has to be taken since approximations are required to obtain solvable equations for these properties.

Bibliography

[1] C. Gaiser and B. Fellmuth, *The Journal of Chemical Physics* **150**, 134303 (2019).

[2] H. Luther, K. Grohmann, and B. Fellmuth, *Metrologia* **33**, 341 (1996).

[3] M. P. White and D. Gugan, *Metrologia* **29**, 37 (1992).

[4] E.S. Burnett, *Journal of Applied Mechanics* **3**, A136 (1936).

[5] R. H. Orcutt and R. H. Cole, *Physica* **31**, 1779 (1965).

[6] J. Huot and T. K. Bose, *The Journal of Chemical Physics* **95**, 2683 (1991).

[7] JCGM 100, *Evaluation of measurement data-Guide to the expression of uncertainty in measurement* (2008).

[8] O. Kunz and W. Wagner, *Journal of Chemical & Engineering Data* **57**, 3032 (2012).

[9] T. Zandt, W. Sabuga, C. Gaiser, and B. Fellmuth, *Metrologia* **52**, S305 (2015).

[10] M. R. Moldover, *Journal of Research of the National Institute of Standards and Technology* **103**, 167 (1998).

[11] C. Gaiser, B. Fellmuth, and W. Sabuga, *Nature Physics* **16**, 177 (2020).

[12] L. R. Pendrill, *Metrologia* **41**, S40 (2004).

[13] K. Jousten, J. Hendricks, D. Barker, K. Douglas, S. Eckel, P. Egan, J. Fedchak, J. Flügge, C. Gaiser, D. Olson, J. Ricker, T. Rubin, W. Sabuga, J. Scherschligt, R. Schödel, U. Sterr, J. Stone, and G. Strouse, *Metrologia* **54**, S146 (2017).

[14] I. Silander, C. Forssén, J. Zakrisson, M. Zelan, and O. Axner, *Optics Letters* **45**, 2652 (2020).

[15] I. Silander, T. Hausmaninger, C. Forssén, M. Zelan, and O. Axner, *Journal of Vacuum Science & Technology B* **37**, 042901 (2019).

[16] P. F. Egan, J. A. Stone, J. K. Scherschligt, and A. H. Harvey, *Journal of Vacuum Science & Technology A* **37**, 031603 (2019).

[17] W. E. Putnam and J. E. Kilpatrick, *The Journal of Chemical Physics* **21**, 951 (1953).

[18] J. O. Hirschfelder, C. F. Curtiss, and R. B. Bird, *Molecular theory of gases and liquids*, corr. print. with notes added. ed., Structure of matter series (Wiley, New York,NY, 1964).

[19] C. Gaiser, B. Fellmuth, N. Haft, A. Kuhn, B. Thiele-Krivoi, T. Zandt, J. Fischer, O. Jusko, and W. Sabuga, *Metrologia* **54**, 280 (2017).

[20] E. Bich, R. Hellmann, and E. Vogel, *Molecular Physics* **105**, 3035 (2007).

[21] W. Cencek, M. Przybytek, J. Komasa, J. B. Mehl, B. Jeziorski, and K. Szalewicz, *The Journal of Chemical Physics* **136**, 224303 (2012).

[22] M. Przybytek, W. Cencek, B. Jeziorski, and K. Szalewicz, *Physical Review Letters* **119**, 123401 (2017).

[23] B. Song, P. Xu, and M. He, *Molecular Physics* **119**, e1802525 (2020).

[24] P. Czachorowski, M. Lesiuk, M. Przybytek, M. Puchalski, and B. Jeziorski, *arXiv* , 2007.09767 (2020).

[25] G. Garberoglio and A. H. Harvey, *Journal of Research of the National Institute of Standards and Technology* **114**, 249 (2009).

[26] G. Garberoglio, M. R. Moldover, and A. H. Harvey, *Journal of Research of the National Institute of Standards and Technology* **116**, 729 (2011).

[27] K. R. S. Shaul, A. J. Schultz, and D. A. Kofke, *The Journal of Chemical Physics* **137**, 184101 (2012).

[28] K. R. Shaul, A. J. Schultz, D. A. Kofke, and M. R. Moldover, *Chemical Physics Letters* **531**, 11 (2012).

[29] B. Jäger, R. Hellmann, E. Bich, and E. Vogel, *The Journal of Chemical Physics* **135**, 084308 (2011).

[30] J. Wiebke, P. Schwerdtfeger, G. E. Moyano, and E. Pahl, *Chemical Physics Letters* **514**, 164 (2011).

[31] M. R. Moldover, R. M. Gavioso, J. B. Mehl, L. Pitre, M. de Podesta, and J. T. Zhang, *Metrologia* **51**, R1 (2014).

[32] W. Cencek, G. Garberoglio, A. H. Harvey, M. O. McLinden, and K. Szalewicz, *The Journal of Physical Chemistry A* **117**, 7542 (2013).

[33] C. J. F. Böttcher, *Theory of electric polarization Volume I Dielectrics in static fields*, second edition, completely revised. ed., Theory of electric polarization, Vol. volume 1 (Elsevier, Amsterdam and London and New York and Tokyo, 1973).

[34] M. Puchalski, K. Piszczatowski, J. Komasa, B. Jeziorski, and K. Szalewicz, *Physical Review A* **93**, 032515 (2016).

[35] G. Łach, B. Jeziorski, and K. Szalewicz, *Physical Review Letters* **92**, 233001 (2004).

[36] M. Puchalski, K. Szalewicz, M. Lesiuk, and B. Jeziorski, *Physical Review A* **101**, 022505 (2020).

[37] C. Gaiser and B. Fellmuth, *Physical Review Letters* **120**, 123203 (2018).

[38] A. Nicklass, M. Dolg, H. Stoll, and H. Preuss, *The Journal of Chemical Physics* **102**, 8942 (1995).

[39] C. Lupinetti and A. J. Thakkar, *The Journal of Chemical Physics* **122**, 44301 (2005).

[40] A. D. Buckingham and J. A. Pople, *Transactions of the Faraday Society* **51**, 1029 (1955).

[41] T. L. Hill, *The Journal of Chemical Physics* **28**, 61 (1958).

[42] R. Moszynski, T. G. Heijmen, and A. van der Avoird, *Chemical Physics Letters* **247**, 440 (1995).

[43] G. Garberoglio and A. H. Harvey, *Journal of Research of the National Institute of Standards and Technology* **125**, 125022 (2020).

[44] B. Song and Q.-Y. Luo, *Metrologia* **57**, 025007 (2020).

[45] A. Rizzo, C. Hättig, B. Fernández, and H. Koch, *The Journal of Chemical Physics* **117**, 2609 (2002).

[46] M. O. Bulanin, U. Hohm, Y. M. Ladvishchenko, and K. Kerl, *Zeitschrift für Naturforschung A* **49**, 890 (1994).

[47] W. Cencek, J. Komasa, and K. Szalewicz, *The Journal of Chemical Physics* **135**, 014301 (2011).

[48] E. Vogel, B. Jäger, R. Hellmann, and E. Bich, *Molecular Physics* **108**, 3335 (2010).

[49] H. J. Achtermann, J. G. Hong, G. Magnus, R. A. Aziz, and M. J. Slaman, *The Journal of Chemical Physics* **98**, 2308 (1993).

[50] H. J. Achtermann, G. Magnus, and T. K. Bose, *The Journal of Chemical Physics* **94**, 5669 (1991).

[51] M. Lallemand and D. Vidal, *The Journal of Chemical Physics* **66**, 4776 (1977).

[52] D. Gugan and G. W. Michel, *Metrologia* **16**, 149 (1980).

[53] C. Gaiser, T. Zandt, and B. Fellmuth, *Metrologia* **52**, S217 (2015).

[54] C. Gaiser, B. Fellmuth, and T. Zandt, *International Journal of Thermophysics* **35**, 395 (2014).

[55] B. Fellmuth, C. Gaiser, and J. Fischer, *Measurement Science and Technology* **17**, R145 (2006).

[56] K. H. Berry, *Metrologia* **15**, 89 (1979).

[57] T. W. Hänsch, *Metrology and fundamental constants: Metrologia e costanti fondamentali ; Varenna on Lake Como, Villa Monastero, 18-28 July 2006*, Proceedings of the International School of Physics "Enrico Fermi, Vol. course 166 (IOS Press, Amsterdam and Washington, DC and Bologna, Italy, 2007).

[58] P. M. C. Rourke, C. Gaiser, B. Gao, D. M. Ripa, M. R. Moldover, L. Pitre, and R. J. Underwood, *Metrologia* **56**, 032001 (2019).

[59] E. F. May, L. Pitre, J. B. Mehl, M. R. Moldover, and J. W. Schmidt, *Review of Scientific Instruments* **75**, 3307 (2004).

[60] J. W. Schmidt, R. M. Gavioso, E. F. May, and M. R. Moldover, *Physical Review Letters* **98**, 254504 (2007).

[61] E. F. May, M. R. Moldover, and J. W. Schmidt, *Physical Review A* **78**, 032522 (2008).

[62] N. Sakoda, K. Shindo, K. Motomura, K. Shinzato, M. Kohno, Y. Takata, and M. Fujii, *International Journal of Thermophysics* **33**, 6 (2012).

[63] N. Sakoda, K. Shindo, K. Shinzato, M. Kohno, Y. Takata, and M. Fujii, *International Journal of Thermophysics* **31**, 276 (2010).

[64] R. Kleinrahm and W. Wagner, *The Journal of Chemical Thermodynamics* **18**, 739 (1986).

[65] W. Wagner and R. Kleinrahm, *Metrologia* **41**, S24 (2004).

[66] M. O. McLinden, in *Volume properties*, edited by E. Wilhelm and T. M. Letcher (Royal Society of Chemistry, Cambridge, 2015) pp. 73–99.

[67] R. Gilgen, R. Kleinrahm, and W. Wagner, *The Journal of Chemical Thermodynamics* **26**, 399 (1994).

[68] R. Kleinrahm, X. Yang, M. O. McLinden, and M. Richter, *Adsorption* **25**, 717 (2019).

[69] M. Richter and M. O. McLinden, *Scientific Reports* **7**, 6185 (2017).

[70] K. Moritz, R. Kleinrahm, M. O. McLinden, and M. Richter, *Measurement Science and Technology* **28**, 127004 (2017).

[71] K. R. Hall and F. B. Canfield, *Physica* **33**, 481 (1967).

[72] K. R. Hall and F. B. Canfield, *Physica* **47**, 99 (1970).

[73] W. H. Mueller, T. W. Leland, and R. Kobayashi, *AIChE Journal* **7**, 267 (1961).

[74] F. B. Canfield, T. W. Leland, and R. Kobayashi, *Advances in Cryogenic Engineering* **8**, 146 (1963).

[75] Barkan E.S., *Journal of Engineering Physics* **44**, 651 (1983).

[76] J. C. Holste, M. Q. Watson, M. T. Bellomy, P. T. Eubank, and K. R. Hall, *AIChE Journal* **26**, 954 (1980).

[77] J. C. Holste, J. G. Young, P. T. Eubank, and K. R. Hall, *AIChE Journal* **28**, 807 (1982).

[78] M. Waxman and J. R. Hastings, *Journal of Research of the National Bureau of Standards* **75C**, 165 (1971).

[79] O. Kunz, *The GERG-2004 wide-range equation of state for natural gases and other mixtures*, GERG technical monograph, Vol. 15 (VDI-Verl., Düsseldorf, 2007).

[80] C.-A. Hwang, P. P. Simon, H. Hou, K. R. Hall, J. C. Holste, and K. N. Marsh, *The Journal of Chemical Thermodynamics* **29**, 1455 (1997).

[81] N. Sakoda, K. Shindo, K. Motomura, K. Shinzato, M. Kohno, Y. Takata, and M. Fujii, *International Journal of Thermophysics* **33**, 381 (2012).

[82] S. Cheng, F. Shang, W. Ma, H. Jin, N. Sakoda, X. Zhang, and L. Guo, *Journal of Chemical & Engineering Data* **64**, 1693 (2019).

[83] A. D. Buckingham and J. A. Pople, *Discussions of the Faraday Society* **22**, 17 (1956).

[84] M. Davies, ed., *Dielectric and Related Molecular Processes*, Dielectric and Related Molecular Processes (Royal Society of Chemistry, Cambridge, 1972).

[85] D. R. Johnston, G. J. Oudemans, and R. H. Cole, *The Journal of Chemical Physics* **33**, 1310 (1960).

[86] D. R. Johnston and R. H. Cole, *The Journal of Chemical Physics* **36**, 318 (1962).

[87] Å. Björck, *BIT Numerical Mathematics* **7**, 1 (1967).

[88] C. Tegeler, R. Span, and W. Wagner, *Journal of Physical and Chemical Reference Data* **28**, 779 (1999).

[89] P. Nowak, R. Kleinrahm, and W. Wagner, *The Journal of Chemical Thermodynamics* **28**, 1423 (1996).

[90] P. Nowak, R. Kleinrahm, and W. Wagner, *The Journal of Chemical Thermodynamics* **29**, 1137 (1997).

Bibliography

[91] C. Guenz, C. Gaiser, and M. Richter, *Measurement Science and Technology* **28**, 027002 (2017).

[92] T. Zandt, B. Fellmuth, C. Gaiser, A. Kuhn, A. Merlone, F. Moro, and B. Thiele-Krivoi, *International Journal of Thermophysics* **32**, 1355 (2011).

[93] A. M. Thompson and D. G. Lampard, *Nature* **177**, 888 (1956).

[94] T. J. Buckley, J. Hamelin, and M. R. Moldover, *Review of Scientific Instruments* **71**, 2914 (2000).

[95] J. Q. Shields, R. F. Dziuba, and H. P. Layer, *IEEE Transactions on Instrumentation and Measurement* **38**, 249 (1989).

[96] J. Q. Shields, R. F. Dziuba, R. E. Elmquist, and L. H. Lee, in *Proceedings of Conference on Precision Electromagnetic Measurements Digest* (IEEE, 27 June-1 July 1994) pp. 391–392.

[97] J. W. Schmidt and M. R. Moldover, *International Journal of Thermophysics* **24**, 375 (2003).

[98] C. Gaiser and B. Fellmuth, *Physica Status Solidi B* **253**, 1549 (2016).

[99] B. Fellmuth, J. Fischer, C. Gaiser, O. Jusko, T. Priruenrom, W. Sabuga, and T. Zandt, *Metrologia* **48**, 382 (2011).

[100] A. Koschine and J. K. Lehmann, *Measurement Science and Technology* **3**, 411 (1992).

[101] R. B. Wearn and N. G. Larson, *Deep Sea Research Part A. Oceanographic Research Papers* **29**, 111 (1982).

[102] B. Fellmuth, H. Bothe, N. Haft, and J. Melcher, *IEEE Transactions on Instrumentation and Measurement* **60**, 2522 (2011).

[103] C. Gaiser, *Properties of helium and gas thermometry*, Berichte aus der Physik (Shaker, Aachen, 2008).

[104] D. N. Homan, *Journal of Research of the National Bureau of Standards* **72C**, 161 (1968).

[105] H. Preston-Thomas, *Metrologia* **27**, 3 (1990).

[106] J. P. Paul Bramley, *Cal Lab The International Journalof Metrlogoy* **Oct-Nov-Dec**, 30 (2006).

[107] JCGM 101, *Evaluation of measurement data - Supplement 1 to the "Guide to the expression of uncertainty in measurements" - Propagation of distributions using a Monte Carlo method* (2008).

[108] J. Fischer, M. de Podesta, K. D. Hill, M. Moldover, L. Pitre, R. Rusby, P. Steur, O. Tamura, R. White, and L. Wolber, *International Journal of Thermophysics* **32**, 12 (2011).

[109] P. Czachorowski, M. Przybytek, M. Lesiuk, M. Puchalski, and B. Jeziorski, *Physical Review A* **102**, 042810 (2020).

[110] A. J. Schultz and D. A. Kofke, *Journal of Chemical & Engineering Data* **64**, 3742 (2019).

[111] B. Jäger, R. Hellmann, E. Bich, and E. Vogel, *Molecular Physics* **107**, 2181 (2009).

[112] P. Schwerdtfeger, B. Assadollahzadeh, and A. Hermann, *Physical Review B* **82**, 205111 (2010).

[113] R. H. Orcutt, *The Journal of Chemical Physics* **46**, 697 (1967).

[114] T. K. Bose and R. H. Cole, *The Journal of Chemical Physics* **52**, 140 (1970).

[115] T. K. Bose, K. Boudjarane, J. Huot, and J. M. St-Arnaud, *The Journal of Chemical Physics* **89**, 7435 (1988).

[116] K. Patkowski and K. Szalewicz, *The Journal of Chemical Physics* **133**, 094304 (2010).

[117] A. D. Buckingham, *The Journal of Chemical Physics* **52**, 5960 (1970).

[118] H. Sutter and R. H. Cole, *The Journal of Chemical Physics* **52**, 132 (1970).

[119] Lehmann Jochen, *Aufbau einer Apparatur zur Bestimmung der ersten, zweiten und dritten dielektrischen Virialkoeffizienten und Messungen an Ethen*, Phd thesis, Wilhelm-Pieck-Universität Rostock, Rostock (1982).

[120] T. K. Bose, J. M. St-Arnaud, H. J. Achtermann, and R. Scharf, *Review of Scientific Instruments* **57**, 26 (1986).

Appendices

A. Relation between density and pressure virial coefficients

To determine the relation between density and pressure virial coefficients, the equal compressibility factors Z are compared

$$Z = 1 + B(T)\rho_{\mathrm{m}} + C(T)\rho_{\mathrm{m}}^2 + ... = 1 + B_p(T)p + C_p(T)p^2 + ... \tag{A.1}$$

The pressure p is replaced by equation 3.2:

$$
\begin{aligned}
B(T)\rho_{\mathrm{m}} &+ C(T)\rho_{\mathrm{m}}^2 + ... = \\
&B_p(T)\rho_{\mathrm{m}}RT\left(1 + B(T)\rho_{\mathrm{m}} + C(T)\rho_{\mathrm{m}}^2 + ...\right) + \\
&C_p(T)\left(\rho_{\mathrm{m}}RT\left(1 + B(T)\rho_{\mathrm{m}} + C(T)\rho_{\mathrm{m}}^2 + ...\right)\right)^2 + ... = \\
&B_p(T)\rho_{\mathrm{m}}RT + B_p(T)B(T)\rho_{\mathrm{m}}^2RT + B_p(T)C(T)\rho_{\mathrm{m}}^3RT + ... \\
&+ C_p(T)\rho_{\mathrm{m}}^2(RT)^2\left(1 + 2B(T)\rho_{\mathrm{m}} + 2C(T)\rho_{\mathrm{m}}^2 + B^2(T)\rho_{\mathrm{m}}^2 + \right. \\
&\left. 2C(T)B(T)\rho_{\mathrm{m}}^3 + C^2(T)\rho_{\mathrm{m}}^4 + ...\right) = \\
&B_p(T)\rho_{\mathrm{m}}RT + B_p(T)B(T)\rho_{\mathrm{m}}^2RT + B_p(T)C(T)\rho_{\mathrm{m}}^3RT + ... \\
&+ C_p(T)\rho_{\mathrm{m}}^2(RT)^2 + 2C_p(T)B(T)\rho_{\mathrm{m}}^3(RT)^2 + 2C_p(T)C(T)\rho_{\mathrm{m}}^4(RT)^2 \\
&+ C_p(T)B^2(T)\rho_{\mathrm{m}}^4(RT)^2 + 2C_p(T)C(T)B(T)\rho_{\mathrm{m}}^5(RT)^2 + C_p(T)C^2(T)\rho_{\mathrm{m}}^6(RT)^2 + ...
\end{aligned}
\tag{A.2}
$$

Now, a comparison of coefficients of the particle densitiy reveals the relations given in equation 3.5 of section 3.1.1

$$
\begin{aligned}
\rho_{\mathrm{m}} &: B = B_p RT \\
\rho_{\mathrm{m}}^2 &: C = B^2 + C_p^2(RT)^2
\end{aligned}
\tag{A.3}
$$

B. Relation between dielectric and Mosotti virial coefficients

To determine the relation between dielectric and Mosotti virial coefficients, the equal correction factors of equations 3.12 and 3.13 are compared.

$$1 + b_\epsilon(T)\rho_\mathrm{m} + c_\epsilon(T)\rho_\mathrm{m}^2 + ... = 1 + b_\mathrm{CM}(T)f + c_\mathrm{CM}(T)f^2 + ... \tag{B.1}$$

The Clausius Mosotti Term *CM* is replaced by equation 3.12:

$$
\begin{aligned}
b_\epsilon(T)&\rho_\mathrm{m} + c_\epsilon(T)\rho_\mathrm{m}^2 + ... = \\
b_\mathrm{CM}(T)&A_\epsilon\rho_\mathrm{m}\left(1 + b_\epsilon\left(T\right)\rho_\mathrm{m} + c_\epsilon\left(T\right)\rho_\mathrm{m}^2 + ...\right) + \\
c_\mathrm{CM}(T)&\left(A_\epsilon\rho_\mathrm{m}\left(1 + b_\epsilon\left(T\right)\rho_\mathrm{m} + c_\epsilon\left(T\right)\rho_\mathrm{m}^2 + ...\right)\right)^2 + ... = \\
b_\mathrm{CM}(T)&A_\epsilon\rho_\mathrm{m} + b_\mathrm{CM}(T)b_\epsilon(T)A_\epsilon\rho_\mathrm{m}^2 + b_\mathrm{CM}(T)c_\epsilon(T)A_\epsilon\rho_\mathrm{m}^3 + \\
c_\mathrm{CM}(T)&\left(A_\epsilon\rho_\mathrm{m}\right)^2\left(1 + 2b_\epsilon(T)\rho_\mathrm{m} + 2c_\epsilon(T)\rho_\mathrm{m}^2 + b_\epsilon^2(T)\rho_\mathrm{m}^2 + \right. \\
&\left. 2b_\epsilon(T)c_\epsilon(T)\rho_\mathrm{m}^3 + c_\epsilon^2(T)\rho_\mathrm{m}^4 + ...\right) = \\
b_\mathrm{CM}(T)&A_\epsilon\rho_\mathrm{m} + b_\mathrm{CM}(T)b_\epsilon(T)A_\epsilon\rho_\mathrm{m}^2 + b_\mathrm{CM}(T)c_\epsilon(T)A_\epsilon\rho_\mathrm{m}^3 + \\
c_\mathrm{CM}(T)&\left(A_\epsilon\rho_\mathrm{m}\right)^2 + 2c_\mathrm{CM}(T)b_\epsilon(T)A_\epsilon^2\rho_\mathrm{m}^4 + c_\mathrm{CM}(T)b_\epsilon^2(T)A_\epsilon^2\rho_\mathrm{m}^4 + \\
2c_\mathrm{CM}(T)&c_\epsilon(T)b_\epsilon(T)A_\epsilon^2\rho_\mathrm{m}^5 + c_\mathrm{CM}(T)c_\epsilon^2(T)A_\epsilon^2\rho_\mathrm{m}^6 + ...
\end{aligned}
\tag{B.2}
$$

Now, a comparison of coefficients of the particle densitiy reveals:

$$
\begin{aligned}
\rho_\mathrm{m} &: b_\epsilon(T) = b_\mathrm{CM}(T)A_\epsilon \\
\rho_\mathrm{m}^2 &: c_\epsilon(T) = b_\epsilon^2(T) + c_\mathrm{CM}(T)A_\epsilon^2
\end{aligned}
\tag{B.3}
$$

C. Derivation of the virial equation of state

This chapter summarizes the derivation of the virial equation of state presented in [18]. Starting point is the partition function Z_N, which is related to the pressure p by the well known relationship:

$$p = kt \left(\frac{\partial \ln Z_N}{\partial V} \right)_T \tag{C.1}$$

For N identical particles with mass m the partition function is given by:

$$Z_{\mathrm{n}} = \frac{1}{N! h^{3N}} \int \int \exp \left(-\frac{1}{kT} \left(\sum_{i=0}^{N} \frac{p\prime_i^2}{2m} + \Phi(\boldsymbol{r}^N) \right) \right) d\boldsymbol{r}^N d\boldsymbol{p}\prime^N \tag{C.2}$$

In this formula, the bold symbols denote vector properties namely the spatial coordinate $\boldsymbol{r}$ and the momentum coordinate $\boldsymbol{p}\prime$. Furthermore, $\Phi(\boldsymbol{r}^N)$ is the total potential energy of all particles and h is the Planck constant. Integration over the momentum space of formula C.2 yields the following expression:

$$Z_{\mathrm{n}} = \frac{1}{N! \lambda^{3N}} \int \exp \left(-\frac{\Phi(\boldsymbol{r}^N)}{kT} \right) d\boldsymbol{r}^N \tag{C.3}$$

with $\lambda = h/(2\pi mkT)^{1/2}$. The challenge lies in the integration over the spatial coordinate of equation C.3 with the exponential term being the so called Boltzmann factor $W_N\left(\boldsymbol{r}^N\right)$. To solve the integral, the key idea is to split $W_N\left(\boldsymbol{r}^N\right)$ into a sum of products of so called U-functions $U_l\left(\boldsymbol{r}\right)$. These functions are given by different combinations of Boltzmann factors with l denoting the considered number of particles in a group for the corresponding U-function. They have the Form:

$$
\begin{aligned}
U_1\left(\boldsymbol{r}_i\right) =& W_1\left(\boldsymbol{r}_i\right) \\
U_2\left(\boldsymbol{r}_i, \boldsymbol{r}_j\right) =& W_2\left(\boldsymbol{r}_i, \boldsymbol{r}_j\right) - W_1\left(\boldsymbol{r}_i\right) W_1\left(\boldsymbol{r}_j\right) \\
U_3\left(\boldsymbol{r}_i, \boldsymbol{r}_j, \boldsymbol{r}_k\right) =& W_3\left(\boldsymbol{r}_i, \boldsymbol{r}_j, \boldsymbol{r}_k\right) - W_2\left(\boldsymbol{r}_i, \boldsymbol{r}_i\right) W_1\left(\boldsymbol{r}_k\right) - W_2\left(\boldsymbol{r}_j, \boldsymbol{r}_k\right) W_1\left(\boldsymbol{r}_i\right) \\
& - W_2\left(\boldsymbol{r}_k, \boldsymbol{r}_i\right) W_1\left(\boldsymbol{r}_j\right) + 2W_1\left(\boldsymbol{r}_i\right) W_1\left(\boldsymbol{r}_j\right) W_1\left(\boldsymbol{r}_k\right)
\end{aligned}
\tag{C.4}
$$

It can be shown that the Boltzmannfactor is $W_N\left(\boldsymbol{r}^N\right) = \sum \prod U_l(\boldsymbol{r})$, which may be

C. Derivation of the virial equation of state

inserted for the integration of equation C.3 resulting in:

$$Z_n = \frac{1}{\lambda^{3N}} \sum \prod_{l=1}^{N} \frac{(Vb_l)^{m_l}}{m_l!} \tag{C.5}$$

In this formula, V is the volume, m_l is the number of groups containing l particles and b_l are the so called cluster integrals, which are given by:

$$b_l = \frac{1}{Vl!} \int U_l\left(\boldsymbol{r}_1, \boldsymbol{r}_2, ..., \boldsymbol{r}_l\right) d\boldsymbol{r}_1 d\boldsymbol{r}_2 ... d\boldsymbol{r}_l \tag{C.6}$$

Solving equation C.5 is again complex and well described in reference [18]. The important end result after insertion in equation C.1 is:

$$\frac{p}{kT} = \frac{N}{V} - \sum_{k=1}^{\infty} \frac{k\beta_k}{k+1} \left(\frac{N}{V}\right)^{k+1} \tag{C.7}$$

In this formula, the β_k denote different combinations of the cluster integrals b_l. Lower orders are, for instance, given by:

$$
\begin{aligned}
\beta_1 &= 2b_2 \\
\beta_2 &= 3b_3 - 6b_2^2 \\
\beta_3 &= 4b_4 - 24b_2b_3 + \frac{80}{3}b_2^3
\end{aligned}
\tag{C.8}
$$

It is obvious that equation C.7 is very similar to the virial expansion defined in equation 3.2. Comparison of orders of particle density reveal the following relations between the density virial coefficients and the β_k for the lower orders:

$$
\begin{aligned}
B'(T) &= -\frac{1}{2}\beta_1 = -b_2 \\
C'(T) &= -\frac{2}{3}\beta_2 = -2b_3 + 4b_2^2 \\
D'(T) &= -\frac{3}{4}\beta_3 = -3b_4 + 18b_2b_3 - 20b_2^3
\end{aligned}
\tag{C.9}
$$

The prime indicates that these are the microscopic rather than the molar virial coefficients. Up to this point, the properties of the potential have not been further specified, which will be necessary now. A valid assumption that has to be made for the further evaluation is the assumption of additivity. This means that the force between any two particles shall not depend on the configuration of the remaining particles. The potential may then be rewritten as

148

$$\Phi(\boldsymbol{r}^N) = \frac{1}{2} \sum_{i=1}^{N-1} \sum_{j=2}^{N} \varphi_{ij}(\boldsymbol{r}_{ij}) \tag{C.10}$$

In this formula, $\varphi_{ij}(\boldsymbol{r}_{ij})$ denotes the interaction potential between two particles. Mayer and co-workers used the function

$$f_{ij}(\boldsymbol{r}_{ij}) = \exp\left(-\frac{\varphi_{ij}}{kT}\right) - 1 \tag{C.11}$$

to further simplify the problem. Unless the particles are so close that the interaction energy is significantly different from zero, this function is zero. With this formula, the cluster integrals b_l can be rewritten as follows:

$$b_1 = \frac{1}{V} \int d\boldsymbol{r_1} = 1$$
$$b_2 = \frac{1}{2V} \int \int f_{12} d\boldsymbol{r_1} d\boldsymbol{r_2} \tag{C.12}$$
$$b_3 = \frac{1}{6V} \int \int \int \left(f_{12}f_{13} + f_{12}f_{23} + f_{13}f_{23} + f_{12}f_{13}f_{23}\right) d\boldsymbol{r_1} d\boldsymbol{r_2} d\boldsymbol{r_3}$$

The big benefit of this notation is that the integrals of equation C.12 are reducible. As a consequence, some of the terms in the integrals can be rewritten as products of integrals. To illustrate the consequence, one may look at the integral b_3. The first three terms can now be expressed by means of b_2 leading to cancelation in such a way that $C'(T)$ does only contain three particle interactions. It can be shown that this is true for all orders of the virial coefficients. The most important correction to the ideal gas is, thus, the second density virial coefficient containing the two particle interaction.

At this point it is in principle possible to calculate the virial coefficients for a given potential by means of classical mechanics. Unfortunately, the integrals are complicated but solvable for very simple potentials. However, with realistic potentials they are mostly not solvable. For the noble gases used within this thesis, the valid assumption of an angle-independent potential allows at least to derive an analytical expression for the second order, which is given by [18]:

$$B'(T) = -2\pi \int_0^\infty \left(\exp\left(\frac{-\varphi(r)}{kT}\right) - 1\right) r^2 dr \tag{C.13}$$

However, the previous considerations do not take quantum mechanical contributions into account. Luckily, the derivation can be adapted with modest effort [18].

First, the classic partition function Z_N has to be replaced by the quantum mechanical one:

C. Derivation of the virial equation of state

$$Z_{N,\text{qm}} = \sum_n \exp\left(-\frac{E_n}{kT}\right) \tag{C.14}$$

The E_n are the energy levels of the system. Secondly, the Boltzmann factor needs to be replaced by the slater sum. For two particles, this is given by:

$$W_s(\boldsymbol{r}_1, \boldsymbol{r}_2) = 1 \pm \exp\left(-\frac{2\pi r_{12}}{\lambda^2}\right) \tag{C.15}$$

The plus sign in the previous applies for Bose-statistics, while the minus is for Fermi-statistics. Exchanging the two given quantities in the derivation given here and in appendix C is leading directly to the quantum mechanical result. The introduction of discrete energy levels and the need to distinguish between particles depending on the spin configuration represent basic principles of quantum mechanics. The main task in calculating the density virials lies now in the exact calculation of the energy levels, which is done by solving the Schrödinger equation.

$$
\begin{aligned}
B'(T) = \lambda^3 \Bigg(&\pm 2^{-\frac{5}{2}} - 2^{\frac{3}{2}} \sum_l (2l+1) \sum_n e^{\left(-\frac{E_{nl}}{kT}\right)} - \\
&\frac{2^{\frac{3}{2}}}{\pi} \sum_l (2l+1) \int_0^\infty e^{\left(-\frac{\hbar^2 \kappa^2}{2\mu_\text{m} kT}\right)} \left(\frac{d\delta_l}{d\kappa}\right) d\kappa \Bigg)
\end{aligned}
\tag{C.16}
$$

In this formula $\mu_\text{m} = m_1 m_2 / (m_1 + m_2)$ is the reduced mass and $\kappa = (2\mu_\text{m} E_n)^{\frac{1}{2}}/\hbar$. $E_n l$ are the discrete energy states of the system, $\delta_l(\kappa)$ is the phase-shift of the energy states, which is caused by scattering, and the summation is carried out over the angular momentum l of the two particle system.

D. The Lorentz-Lorenz equation and refractive virial coefficients

While the Clausius-Mosotti equation 3.12 of electrostatics can be used to describe the relation between ϵ and the molar particle density, frequency dependencies need to be included for optical experiments. This is done by the Lorentz-Lorenz equation:

$$\frac{n^2 - 1}{n^2 + 2} = A_n\left(\omega\right) \rho_\mathrm{m} \left(1 + b_n\left(\omega, T\right) \rho_\mathrm{m} + c_n\left(\omega, T\right) \rho_\mathrm{m}^2 + ...\right) \tag{D.1}$$

In this equation, n is the refractive index $A_n\left(\omega\right)$ is the dynamic molar polarizability (in some works it is referred to as refractivity) and $b_n\left(\omega, T\right)$,$c_n\left(\omega, T\right)$...are the refractive virial coefficients of second, third,... order. For the comparison of static and dynamic experiments, it is useful to declare static and dynamic terms of the involved properties:

$$A_n\left(\omega\right) = A_\epsilon + A_\mu + \Delta A_n\left(\omega\right) = A_\epsilon + A_\mu + \alpha_2\omega^2 + \alpha_4\omega^4 \tag{D.2}$$

$$b_n\left(\omega, T\right) = b_\epsilon\left(T\right) + \Delta b_n\left(\omega, T\right) \tag{D.3}$$

$$c_n\left(\omega, T\right) = c_\epsilon\left(T\right) + \Delta c_n\left(\omega, T\right) \tag{D.4}$$

In this notation, it becomes obvious that equation D.2 turns into the Clausius-Mosotti equation in the limit of zero frequency with $n^2 = \epsilon_\mathrm{r}\mu_\mathrm{r}$.

E. DCGT working equations

E.1. Derivation of the classic DCGT working equation

In the following derivation, the temperature dependence of the virial coefficients will not be indicated in the formulas to ease reading. Combination of the gas equation 3.2 and the Clausius-Mosotti equation 3.12 yields:

$$p = \frac{RT}{A_\epsilon} f \frac{(1 + B\rho_\mathrm{m} + C\rho_\mathrm{m}^2 + ...)}{(1 + b_\epsilon \rho_\mathrm{m} + c_\epsilon \rho_\mathrm{m}^2 + ...)} \tag{E.1}$$

In this formula, $f = \frac{\epsilon_\mathrm{r} - 1}{\epsilon_\mathrm{r} + 2}$ is used to substitute the Mosotti-term. Since the dielectric virials are typically two orders of magnitude smaller than the density virials, the denominator can be expanded into a Taylor series resulting in:

$$p = \frac{RT}{A_\epsilon} f \left(1 + B\rho_\mathrm{m} + C\rho_\mathrm{m}^2 + ... \right) \left(1 - b_\epsilon \rho_\mathrm{m} + (b_\epsilon^2 - c_\epsilon)\rho_\mathrm{m}^2 + ... \right) \tag{E.2}$$

Furthermore, the particle density in the small correction terms containing the virial coefficients is replaced by the approximation $\rho_\mathrm{m} = \frac{f}{A_\epsilon} \left(1 - b_\epsilon \frac{f}{A_\epsilon} \right)$:

$$p = \frac{RT}{A_\epsilon} f \left(1 + (B - b_\epsilon)\frac{f}{A_\epsilon} + \left(C - c_\epsilon + 2b_\epsilon^2 - 2Bb_\epsilon \right) \left(\frac{f}{A_\epsilon} \right)^2 + ... \right) \tag{E.3}$$

For an ideal capacitor that is not deformed under pressure, the Mosotti-term f can be expressed by means of the DCGT measuring quantity γ defined in equation 3.19 as the relative change of capacitance.

$$f = \frac{\epsilon_\mathrm{r} - 1}{\epsilon_\mathrm{r} + 2} = \frac{\gamma}{\gamma + 3} = \mu \tag{E.4}$$

The working quantity μ of the DCGT is equal to the Mosotti-term for vanishing deformation. For a real capacitor, this deformation needs to be taken into account. To obtain a suitable expression, μ is written as:

$$\mu = \frac{\epsilon_{\mathrm{r}} - 1 + \epsilon_{\mathrm{r}}\kappa_{\mathrm{eff}}p}{\epsilon_{\mathrm{r}} + 2 + \epsilon_{\mathrm{r}}\kappa_{\mathrm{eff}}p} = 1 + \frac{3(f-1)}{3 + \kappa_{\mathrm{eff}}p(1 + 2f)} \tag{E.5}$$

where ϵ_{r} is replaced by the rearranged equation E.4 $\epsilon_{\mathrm{r}} = -2 - \frac{3}{f-1}$. In the denominator the small correction Term $2f$ is approximated by 2μ, while the pressure p is approximated by the ideal formula $p = \frac{RT}{A_\epsilon}f$ resulting in

$$\mu = 1 + \frac{3(f-1)}{3 + \frac{\kappa_{\mathrm{eff}}RT}{A_\epsilon}f(1 + 2\mu)} \tag{E.6}$$

This equation can be rearranged for f:

$$\begin{aligned} f &= \frac{\mu}{1 + \frac{\kappa_{\mathrm{eff}}RT}{3A_\epsilon}\left(1 - \mu + 2\mu^2\right)} \\ &\approx \frac{\mu}{1 + \frac{\kappa_{\mathrm{eff}}RT}{3A_\epsilon}} \end{aligned} \tag{E.7}$$

where μ can be neglected in the denominator term containing κ_{eff} since it is typically much smaller than one. Now, f in the linear term of equation E.3 is replaced by this expression, while in the higher orders containing the virials f is approximated by μ resulting in:

$$p = \frac{1}{\frac{A_\epsilon}{RT} + \frac{\kappa_{\mathrm{eff}}}{3}}\mu\left(1 + (B - b_\epsilon)\frac{\mu}{A_\epsilon} + \left(C - c_\epsilon + 2b_\epsilon^2 - 2Bb_\epsilon\right)\left(\frac{\mu}{A_\epsilon}\right)^2 + \ldots\right) \tag{E.8}$$

This working equation allows the fit of data points of pressure and capacitance and has been used typically for the determination of temperatures of less than $50\,\mathrm{K}$. Since the temperature is retrieved from the linear term, the approximations in the higher orders are reasonable. However, for the derivation of virial coefficients another working equation needs to be retrieved.

E.2. Derivation of a DCGT working equation for higher temperatures and virial coefficients

The derivation of this working equation essentially starts the same way as the previous one. However, since also the third virial coefficients shall be determined, it is necessary to include also the fourth virial coefficients into this derivation. To ease readibility, the temperature dependence of the virial coefficients is not indicated in the formulas. Furthermore, the Clausius-Mossoti equation is substituted as follows:

$$f = A_\epsilon \rho_m \left(1 + b_\epsilon \rho_m + c_\epsilon \rho_m^2 + d_\epsilon \rho_m^3 + ...\right)$$
$$= A_\epsilon \rho_m \left(1 + x\right) \tag{E.9}$$

With this, the molar particle density in the gas equation can be replaced leading to:

$$p = \frac{RTf}{A_\epsilon(1+x)} \left(1 + \frac{B}{\left(\frac{A_\epsilon}{y}(1+x)\right)} + \frac{C}{\left(\frac{A_\epsilon}{f}(1+x)\right)^2} + \frac{D}{\left(\frac{A_\epsilon}{f}(1+x)\right)^3} + ...\right)$$
$$= \frac{RTf'}{(1+x)} \left(1 + B\left(\frac{f'}{(1+x)}\right) + C\left(\frac{f'}{(1+x)}\right)^2 + D\left(\frac{f'}{(1+x)}\right)^3 + ...\right) \tag{E.10}$$

To ease reading, $\frac{f}{A_\epsilon}$ is substituted by f'. Replacing the particle density in the Clausius-Mosotti equation leads to:

$$(1+x) = 1 + b_\epsilon \frac{f'}{(1+x)} + c_\epsilon \left(\frac{f'}{(1+x)}\right)^2 + d_\epsilon \left(\frac{f'}{(1+x)}\right)^3 + ... \tag{E.11}$$

Up to this point no approximations were made, while in the simpler derivation the particle density was replaced by the ideal Clausius-Mosotti equation. But, to linearize the problem, it is necessary to approximate the terms containing $(1+x)$ in the denominator. This is done by expanding these terms into a Taylor series, where due to the smallness of the dielectric virial coefficients only linear orders are considered starting with the Clausius-Mosotti equation:

$$(1+x) = 1 + b_\epsilon f'(1-x) + c_\epsilon f'^2(1-2x) + d_\epsilon f'^3(1-3x) \tag{E.12}$$

This equation can be rearranged for x giving:

$$x = \frac{b_\epsilon f' + c_\epsilon f'^2 + d_\epsilon f'^3}{1 + b_\epsilon f' + 2c_\epsilon f'^2 + 3d_\epsilon f'^3} \tag{E.13}$$

The denominator is again approximated by a Taylor series that is trunctuated after the linear term resulting in:

$$x = \left(b_\epsilon f' + c_\epsilon f'^2 + d_\epsilon f'^3\right)\left(1 - b_\epsilon f' - 2c_\epsilon f'^2 - 3d_\epsilon f'^3\right)$$
$$= b_\epsilon f' - b_\epsilon^2 f'^2 + c_\epsilon f'^2 - 3b_\epsilon c_\epsilon f'^3 + d_\epsilon f'^3 - 2c_\epsilon^2 f'^4 - 4b_\epsilon d_\epsilon f'^4 - 5c_\epsilon d_\epsilon f'^5 - 3d_\epsilon^2 f'^6 \tag{E.14}$$

To make use of this result, the denominator terms containing $(1+x)$ in equation E.10 are

also developed into a Taylor series, where terms up to second order are included. Then, x is inserted and terms up to order four in the Mosotti-term f are considered.

$$
\begin{aligned}
p =\;& RTf'\left(1 - x + x^2\right)\left(1 + Bf'\left(1 - x + x^2\right) + Cf'^2\left(1 - 2x + 3x^2\right) + Df'^3\left(1 - 3x + 6x^2\right)\right) \\
=\;& RTf'\left(1 + (B - b_\epsilon)y' + (C - c_\epsilon + 2b_\epsilon^2 - 2b_\epsilon B)f'^2 + \right. \\
& \left. (D - d_\epsilon - 2b_\epsilon^3 + 5b_\epsilon^2 B + 5b_\epsilon c_\epsilon - 2Bc_\epsilon - 3b_\epsilon C)f'^3 + \ldots\right) \\
=\;& RT\frac{f}{A_\epsilon}\left(1 + (B - b_\epsilon)\frac{f}{A_\epsilon} + (C - c_\epsilon + 2b_\epsilon^2 - 2b_\epsilon B)\left(\frac{f}{A_\epsilon}\right)^2 + \right. \\
& \left. (D - d_\epsilon - 2b_\epsilon^3 + 5b_\epsilon^2 B + 5b_\epsilon c_\epsilon - 2Bc_\epsilon - 3b_\epsilon C)\frac{f}{A_\epsilon}^3 + \ldots\right)
\end{aligned}
$$

$$(\text{E.15})$$

This formula does include the dielectric virial coefficients in the higher orders that were neglected previously. To adapt this equation to real measurement conditions, the deformation of the capacitor under pressure needs to be taken into account again. Starting from equation E.5, the pressure in the small correction term $\kappa_{\text{eff}}p(1 + 2\mu)$ is replaced by $\frac{fRT}{A_\epsilon}\left(1 + (B - b_\epsilon)\frac{\mu}{A_\epsilon} + C\left(\frac{\mu}{A_\epsilon}\right)^2\right)$ rather than by the ideal term resulting in:

$$
\mu = 1 + \frac{3(f - 1)}{3 + \kappa_{\text{eff}}\frac{RTf}{A_\epsilon}\left(1 + (B - b_\epsilon)\frac{\mu}{A_\epsilon} + C\left(\frac{\mu}{A_\epsilon}\right)^2\right)(1 + 2\mu)}
$$

$$(\text{E.16})$$

In the correction terms containing the virial coefficients, the exact Mosotti-term f is approximated by μ. Rearrangement for f yields:

$$
\begin{aligned}
f =\;& \frac{\mu}{1 - \frac{\kappa_{\text{eff}}RT}{3A_\epsilon^3}(\mu - 1)(1 + 2\mu)(A_\epsilon^2 + A_\epsilon(B - b_\epsilon)\mu + c_\epsilon\mu^2)} \\
=\;& \frac{\mu}{1 + \frac{\kappa_{\text{eff}}RT}{3A_\epsilon} + \frac{\kappa_{\text{eff}}RT}{3A_\epsilon}\left(\mu\left(1 + \frac{(B - b_\epsilon)}{A_\epsilon}\right) + \mu^2\left(\frac{C}{A_\epsilon^2} + \frac{(B - b_\epsilon)}{A_\epsilon} - 2A_\epsilon^2\right) + \mu^3\left(\frac{C}{A_\epsilon^2} - \frac{2(B - b_\epsilon)}{A_\epsilon}\right) - \mu^4\left(\frac{2C}{A_\epsilon^2}\right)\right)}
\end{aligned}
$$

$$(\text{E.17})$$

The denominator is expanded into a Taylor series for small values of μ up to the linear order resulting in:

$$f = \frac{\mu}{1 + \frac{\kappa_{\text{eff}}RT}{3A_\epsilon}} - \frac{\mu^2 \frac{\kappa_{\text{eff}}RT}{3A_\epsilon}\left(1 + \frac{(B-b_\epsilon)}{A_\epsilon}\right)}{\left(1 + \frac{\kappa_{\text{eff}}RT}{3A_\epsilon}\right)^2} +$$

$$\frac{\mu^3 \left(\frac{\kappa_{\text{eff}}RT}{3A_\epsilon}\right)^2 \left(\left(1 + \frac{(B-b_\epsilon)}{A_\epsilon}\right)^2 + \frac{\kappa_{\text{eff}}RT}{3A_\epsilon}\left(2 - \frac{(B-b_\epsilon)}{A_\epsilon} - \frac{C}{A_\epsilon^2}\right)\right)}{\left(1 + \frac{\kappa_{\text{eff}}RT}{3A_\epsilon}\right)^3}$$

$$\text{(E.18)}$$

Insertion of this expression in equation E.15 results in the given expression:

$$p = A_1\mu\left(1 + A_1 A_2 \mu + A_1^2 A_3 \mu^2 + A_1^3 A_4 \mu^3 + ...\right)$$

$$A_1 = \frac{1}{\frac{A_\epsilon}{RT} + \frac{\kappa_{\text{eff}}}{3}}$$

$$A_2 = \frac{1}{RT}(B - b_\epsilon) - \frac{\kappa_{\text{eff}}}{3}\left(1 + \frac{B}{A_\epsilon}\right)$$

$$A_3 = \frac{1}{(RT)^2}\left(C - c_\epsilon - 2b_\epsilon(B - b_\epsilon)\right)$$

$$+ \frac{\kappa_{\text{eff}}}{3}\frac{1}{RT}\left(2A_\epsilon - 3(B - b_\epsilon) - \frac{1}{A_\epsilon}(2(B - b_\epsilon)^2 + C)\right)$$

$$+ \left(\frac{\kappa_{\text{eff}}}{3}\right)^2\left(3 + \frac{1}{A_\epsilon}(B - b_\epsilon) + \frac{1}{A_\epsilon^2}((B - b_\epsilon)^2 - C)\right)$$

$$A_4 = \frac{1}{(RT)^3}\left(D - d_\epsilon - 3b_\epsilon C - 2Bc_\epsilon + 5b_\epsilon c_\epsilon + 5b_\epsilon^2 B - 2b_\epsilon^3\right)$$

$$+ \frac{\kappa_{\text{eff}}}{(RT)^2}\left(4A_\epsilon(B - b_\epsilon) - 2(B - b_\epsilon)^2 - 6b_\epsilon(B - b_\epsilon) + 3(C - c_\epsilon)\right)$$

$$+ \frac{\kappa_{\text{eff}}}{(RT)^2}\frac{1}{A_\epsilon}\left(6b_\epsilon(B - b_\epsilon)^2 + (B - b_\epsilon)(3c_\epsilon - 5C)\right)$$

$$+ \left(\frac{\kappa_{\text{eff}}}{3}\right)^2\frac{1}{RT}\left(7(B - b_\epsilon) + \frac{1}{A_\epsilon}4(B - b_\epsilon)^2 + \frac{1}{A_\epsilon^2}\left(3(B - b_\epsilon)^3 - 2C(B - b_\epsilon)\right)\right)$$

$$\text{(E.19)}$$

F. Burnett expansion working equations

F.1. Ideal Burnett expansion working equation

The pressure ratio between the rth expansion and expansion $r + j$ from volume V_A into volumes $V_A + V_B$ may in accordance with equation 3.2 and utilizing the conservation of the number of particles be written as:

$$\frac{p_r}{p_{r+j}} = \frac{RT\rho_{\text{m},r}(1 + B\rho_{\text{m},r} + C\rho_{\text{m},r}^2 + D\rho_{\text{m},r}^3 + ...)}{RT\rho_{\text{m},r+j}(1 + B\rho_{\text{m},r+j} + C\rho_{\text{m},r+j}^2 + D\rho_{\text{m},r+j}^3 + ...)} \tag{F.1}$$

Assuming that the volumes remain constant independent of the pressure, the molar particle densities are only defined by the two volumes V_A and V_B:

$$\frac{\rho_{\text{m},r+j}}{\rho_{\text{m},r}} = \left(\frac{V_A}{V_A + V_B}\right)^j = Q^{-j} \tag{F.2}$$

In this formula, Q denotes the apparatus constant. Combining equations F.1 and F.2 results in:

$$\frac{p_r}{p_{r+j}} = \frac{RT\rho_{\text{m},r}(1 + B\rho_{\text{m},r} + C\rho_{\text{m},r}^2 + D\rho_{\text{m},r}^3)...)}{RT\rho_{\text{m},r}Q^{-j}\left(1 + B\rho_{\text{m},r}Q^{-j} + C\rho_{\text{m},r}^2 Q^{-2j} + D\rho_{\text{m},r}^3 Q^{-3j} + ...\right)} \tag{F.3}$$

To derive a proper expression for the data evaluation, first, equation 3.2 is inverted to give $\rho_{\text{m,r}}$ as a function of pressure:

$$\rho_{\text{m},r} = \frac{p_r}{RT}\left(1 - \frac{Bp_r}{RT} + \frac{2B^2 - C}{(RT)^2}p_r^2 + ...\right) \tag{F.4}$$

Furthermore $\frac{1}{p_{r+j}}$ is expanded into a Taylor series:

$$\frac{1}{p_{r+j}} = \frac{1}{RT\rho_{\text{m},r}Q^{-j}}\left(1 - BQ^{-j}\rho_{\text{m},r} + (C - B^2)Q^{-2j}\rho_{\text{m},r}^2 + ...\right) \tag{F.5}$$

Combining equations F.4 and F.5 with equation F.3, results in the final expression given in section 3.3.1:

$$\frac{p_r}{p_{r+j}} = Q^j + (Q^j - 1)\frac{B}{RT} \cdot p_r + \frac{(Q^j - Q^{-j})}{RT}(B^2 - C) \cdot p_r^2 + ...) +$$
$$\frac{1}{(RT)^3}\left[\left(\frac{1}{Q^j} - \frac{1}{Q^{2j}}\right)(BC - B^3) + \left(Q^j - \frac{1}{Q^{2j}}\right)(D - 3CB - 2B^3)\right] \cdot p_r^3 + ...$$

$$(F.6)$$

F.2. Isothermal Burnett expansion with deformation

Derivation of the working equation for the Burnett method with deformation of the cells starts with relation 3.31, which may be written as:

$$\frac{p_r V_A(1 + \lambda_A p_r)}{(1 + B_p p_r + C_p p_r^2 + D_p p_r^3 + ...)} = \frac{p_{r+1}(V_A + V_B)(1 + \lambda_{AB} p_{r+1})}{(1 + B_p p_{r+1} + C_p p_{r+1}^2 + D_p p_{r+1}^3 + ...)} \tag{F.7}$$

To ease the work, a combined compressibility κ_{AB} taking the deformation of cells A and B combined into account is defined. Fitting of the final equation will be carried out in the form of pressure ratios $P_{\text{ratio},r} = \frac{p_r}{p_{r+1}}$ over p_r. Substitution with $P_{\text{ratio},r}$ and rearrangement of equation F.7 results in:

$$\frac{P_{\text{ratio},r} V_A(1 + \lambda_A p_r)}{\left(1 + \lambda_{AB}\frac{p_r}{P_{\text{ratio},r}}(V_A + V_B)\right)} = \frac{(1 + B_p p_r + C_p p_r^2 + D_p p_r^3 ...)}{\left(1 + B_p\frac{p_r}{P_{\text{ratio},r}} + C_p\left(\frac{p_r}{P_{\text{ratio},r}}\right)^2 + D_p\left(\frac{p_r}{P_{\text{ratio},r}}\right)^3 + ...\right)} \tag{F.8}$$

Solving equation F.8 without approximations is only possible for orders up to the third pressure virial coefficient. These results are exact since including higher orders would not change the result for the second and third order virial coefficients but only higher virial coefficients. The terms of equation F.8 are multiplied out and can be arranged in the following way:

$$0 = P_{\text{ratio},r}^2 + P_{\text{ratio},r} \cdot \frac{p_r^2(V_A\lambda_A B_p - C_p V_B) - p_r B_p V_B - (V_A + V_B)}{V_A(1 + \lambda_A p_r)} +$$
$$p_r^3 C_p(\lambda_A V_A - \lambda_{AB}(V_A + V_B)) - p_r^2 B_p \lambda_{AB}(V_A + V_B) - p_r \lambda_{AB}(V_A + V_B) \tag{F.9}$$

This binomial equation can be solved for $P_{\text{ratio},r}$, and the result may be arranged in a series of powers of p_r:

$$P_{\text{ratio},r} = \frac{(V_A + V_B)}{V_A} + \frac{B_p V_B + \lambda_{AB} V_A - \lambda_A (V_A + V_B)}{V_A} \cdot p_r +$$
$$\left(\frac{\lambda_{AB} V_A (B_p - \lambda_{AB})}{(V_A + V_B)} + \frac{(V_A + V_B)(\lambda_A^2 - \lambda_A B_p)}{V_A} + \frac{C_p(V_B^2 + 2 V_A V_B)}{V_A(V_A + V_B)} \right) \cdot p_r^2$$

$$\text{(F.10)}$$

The formula is simplified by using the introduced apparatus constant $Q = \frac{(V_A + V_B)}{V_A}$:

$$P_{\text{ratio},r} = Q + [B_p(Q-1) + \lambda_{AB} - \lambda_A Q] \cdot p_r +$$
$$\left[\frac{\lambda_{AB}(B_p - \lambda_{AB})}{Q} + Q(\lambda_A^2 - \lambda_A B_p) + C_p(Q - \frac{1}{Q}) \right] \cdot p_r^2 +$$
$$\left[D_p \left(Q - \frac{1}{Q^2} \right) + C_p \left(\frac{B_p(Q-1)}{Q^2} + 2\frac{\lambda_{AB}}{Q^2} - \lambda_A(Q + \frac{1}{Q}) \right) + \right.$$
$$\frac{B_p \lambda_{AB}}{Q^2} (\lambda_{AB}(Q-3) - B_p(Q-1)) + B_p \lambda_A \left(\lambda_A Q + \frac{\lambda_{AB}}{Q} \right) +$$
$$\left. \frac{\lambda_{AB}^2}{Q} \left(\frac{2\lambda_{AB}}{Q} - \lambda_A \right) - \lambda_A^3 Q \right] \cdot p_r^3 + \dots$$

$$\text{(F.11)}$$

Equation F.11 also contains the term for the fourth pressure virial coefficient D_p. It has been calculated by approximating the term $D_p \left(\frac{p_s}{P_{\text{ratio},r}} \right)^3 \approx D_p \left(\frac{p_s}{Q} \right)^3$ in equation F.8 and repeating the steps above. Though a determination of the fourth virial coefficients is beyond the experimental capabilities of the apparatus, the term is important for cross checks with constraints, especially for helium, whose virial coefficients can be precisely calculated.

Since the density virial coefficients are the target quantity, the used pressure virial coefficients are replaced according to the definitions in equation 3.5. Furthermore, the combined compressibility is replaced by $\lambda_{AB} = \frac{\lambda_A}{Q} + \kappa_B(1 - \frac{1}{Q})$ so the final result only contains the compressibility of cell B λ_B. This results in the final expression given in section 3.3.2:

$$\frac{p_r}{p_{r+1}} = Q + (Q-1) \left(\frac{B}{RT} + \frac{1}{Q}(\lambda_B - \lambda_A(Q+1)) \right) \cdot p_r +$$
$$\left[\frac{C - B^2}{(RT)^2} \left(Q - \frac{1}{Q} \right) + Q\lambda_A(\lambda_A - \frac{B}{RT}) + \right.$$
$$\left. \frac{1}{Q} \left(\frac{B}{RT} \left(\frac{\lambda_A}{Q} + \lambda_B \left(1 - \frac{1}{Q} \right) \right) - \left(\frac{\lambda_A}{Q} + \lambda_B \left(1 - \frac{1}{Q} \right) \right)^2 \right) \right] \cdot p_r^2 + \dots$$

$$\text{(F.12)}$$

To compare the final working equation retrieved in section 3.3.4 to this result, the derivation has been repeated including the volumes of the gas-handling system and their deformation as depicted in figure 3.5. Thus, the starting equation is:

$$\frac{p_r\left(V_{\mathrm{A}}(1+\lambda_{\mathrm{A}}p_r)+V_{\mathrm{DA}}(1+\lambda_{\mathrm{GHS}}p_r)\right)}{(1+B_pp_r+C_pp_r^2+D_pp_r^3+...)}=$$
$$\frac{p_{r+1}(V_{\mathrm{A}}(1+\lambda_{\mathrm{A}}p_{r+s})+V_{\mathrm{B}}(1+\lambda_{\mathrm{B}}p_{r+1})+(V_{\mathrm{DA}}+V_{\mathrm{DB}})(1+\lambda_{\mathrm{GHS}}p_{r+1}))}{(1+B_pp_{r+1}+C_pp_{r+1}^2+D_pp_{r+s}^3+...)} \tag{F.13}$$

Since the gas-handling system is made of the same tubing, the pressure deformation coefficient λ_{GHS} is valid for both volumes V_{DA} and V_{DB}. Solving this equation delivers the same fit coefficient $K_0 = Q$ for the constant term. The second fit coefficient K_1 is the linear term multiplied by p_r and is best displayed in the form:

$$\frac{K_1}{K_0-1}=B_p+\lambda_{\mathrm{A}}\left[\frac{1}{1+Q_{\mathrm{A}}}-\frac{Q^*\left(1-\frac{1}{Q}\right)}{1+Q_{\mathrm{B}}}\right]+\lambda_{\mathrm{B}}\left[\frac{1}{Q(1+Q_{\mathrm{B}})}\right]+$$
$$\lambda_{\mathrm{GHS}}\left[\frac{1}{Q(1+\frac{1}{Q_{\mathrm{B}}})}-\frac{1}{1+\frac{1}{Q_{\mathrm{A}}}}+\left(\frac{1}{Q}-1\right)\frac{Q^*Q_{\mathrm{A}}}{1+Q_{\mathrm{B}}}\right] \tag{F.14}$$

Q^*, Q_{A} and Q_{B} are the volume ratios defined in equation 3.37.

F.3. Burnett expansion with dead volumes

Starting point is equation 3.35, where the pressure is replaced with the pressure ratio before and after the expansion $P_{\mathrm{ratio},r}=\frac{p_r}{p_{r+1}}$

$$\frac{p_rV_{\mathrm{A}}}{T_{\mathrm{iso}}(1+B_{p,\mathrm{iso}}p_r+...)}+\frac{p_rV_{\mathrm{DA}}}{T_{\mathrm{GHS}}(1+B_{p,\mathrm{GHS}}p_r+...)}=$$
$$\frac{p_r(V_{\mathrm{A}}+V_{\mathrm{B}})}{P_{\mathrm{ratio},r}T_{\mathrm{iso}}(1+B_{p,\mathrm{iso}}\frac{p_r}{P_{\mathrm{ratio},r}}+...)}+\frac{p_r(V_{\mathrm{DA}}+V_{\mathrm{DB}})}{P_{\mathrm{ratio},r}T_{\mathrm{GHS}}(1+B_{p,\mathrm{GHS}}\frac{p_r}{P_{\mathrm{ratio},r}}+...)} \tag{F.15}$$

To further develop this equation into a suitable working equation, the help of the program "Mathematica" is required. First, equation F.15 is solved for $P_{\mathrm{ratio},r}$. The resulting bulky expression is then displayed as a series in powers of p_r with the result being:

$$P_{\mathrm{ratio},r}=K_0+K_1p_r+K_2p_r^2+...$$
$$K_0=1+\frac{T_{\mathrm{iso}}V_{\mathrm{DB}}+T_{\mathrm{GHS}}V_{\mathrm{B}}}{T_{\mathrm{iso}}V_{\mathrm{DA}}+T_{\mathrm{GHS}}V_{\mathrm{A}}}$$
$$K_1=\frac{(B_{p,\mathrm{iso}}-B_{p,\mathrm{GHS}})(T_{\mathrm{GHS}}V_{\mathrm{B}}+T_{\mathrm{iso}}V_{\mathrm{DB}})T_{\mathrm{GHS}}V_{\mathrm{A}}}{(T_{\mathrm{iso}}V_{\mathrm{DA}}+T_{\mathrm{GHS}}V_{\mathrm{A}})^2}+ \tag{F.16}$$
$$\frac{B_{p,\mathrm{GHS}}T_{\mathrm{GHS}}V_{\mathrm{B}}+B_{p,\mathrm{iso}}T_{\mathrm{GHS}}V_{\mathrm{A}}-B_{p,\mathrm{GHS}}T_{\mathrm{GHS}}V_{\mathrm{A}}+B_{p,\mathrm{GHS}}T_{\mathrm{iso}}V_{\mathrm{DB}}}{T_{\mathrm{GHS}}V_{\mathrm{A}}+T_{\mathrm{iso}}V_{\mathrm{DA}}}-$$
$$\frac{(B_{p,\mathrm{iso}}-B_{p,\mathrm{GHS}})T_{\mathrm{GHS}}(V_{\mathrm{A}}+V_{\mathrm{B}})}{T_{\mathrm{GHS}}(V_{\mathrm{A}}+V_{\mathrm{B}})+T_{\mathrm{iso}}(V_{\mathrm{DA}}+V_{\mathrm{DB}})}$$

This formula is rather bulky. Though some of the terms can be simplified to some extend, the clearest simplification is achieved when the following quotient is calculated:

$$
\frac{K_1}{K_0 - 1} = B_{p,\mathrm{GHS}} +
$$

$$
(B_{p,\mathrm{iso}} - B_{p,\mathrm{GHS}}) \left(\frac{1}{1 + \frac{T_{\mathrm{iso}}}{T_{\mathrm{GHS}}} \frac{V_{\mathrm{DA}}}{V_{\mathrm{A}}}} - \frac{1}{1 + \frac{T_{\mathrm{iso}}}{T_{\mathrm{GHS}}} \frac{V_{\mathrm{DB}}}{V_{\mathrm{B}}}} + \frac{1}{1 + \frac{T_{\mathrm{iso}}}{T_{\mathrm{GHS}}} \frac{(V_{\mathrm{DA}}+V_{\mathrm{DB}})}{(V_{\mathrm{A}}+V_{\mathrm{B}})}} \right)
$$

$$(F.17)$$

F.4. Final Burnett working equation with combined deformation and dead volumes

Starting from equation 3.39, the following assumptions are made to achieve a solvable equation. Considered virial coefficients are of second order only. In the terms describing the deformation of the cells after the expansion, the pressure is approximated by $\frac{p_r}{Q_{\Delta T}}$. Furthermore, the equation is expressed by means of the pressure ratio before and after the expansion $P_{\mathrm{ratio}} = \frac{p_r}{p_{r+1}}$.

$$
\frac{p_r V_{\mathrm{A}}(1 + \lambda_{\mathrm{A}} p_r)}{T_{\mathrm{iso}}(1 + B_{p,\mathrm{iso}} p_r)} + \frac{p_r V_{\mathrm{DA}}(1 + \lambda_{\mathrm{GHS}} p_r)}{T_{\mathrm{GHS}}(1 + B_{p,\mathrm{GHS}} p_r)} =
$$
$$
\frac{p_r(V_{\mathrm{A}}(1 + \lambda_{\mathrm{A}} \frac{p_r}{Q_{\Delta T}}) + V_{\mathrm{B}}(1 + \lambda_{\mathrm{B}} \frac{p_r}{Q_{\Delta T}}))}{P_{\mathrm{ratio}} T_{\mathrm{iso}}(1 + B_{p,\mathrm{iso}} \frac{p_r}{P_{\mathrm{ratio}}})} + \frac{p_r(V_{\mathrm{DA}} + V_{\mathrm{DB}})(1 + \lambda_{\mathrm{GHS}} \frac{p_r}{Q_{\Delta T}})}{P_{\mathrm{ratio}} T_{\mathrm{GHS}}(1 + B_{p,\mathrm{GHS}} \frac{p_r}{P_{\mathrm{ratio}}})}
$$

$$(F.18)$$

Solving the equation for P_{ratio} as a function of p_r and expanding the result as a series of powers of p_r results in: $P_{\mathrm{ratio}} = K_0 + K_1 p_r + K_2 p_r^2 + ...$ K_0 is consistently equal to $Q_{\Delta T}$.

$$
K_0 = 1 + \frac{T_{\mathrm{iso}} V_{\mathrm{DB}} + T_{\mathrm{GHS}} V_{\mathrm{B}}}{T_{\mathrm{iso}} V_{\mathrm{DA}} + T_{\mathrm{GHS}} V_{\mathrm{A}}}
$$

$$(F.19)$$

The other coefficients are very long functions, which is why only the final expression utilized for the evaluation of the data $\frac{K_1}{K_0 - 1}$ is shown here:

$$\frac{K_1}{K_0 - 1} = B_{p,\text{iso}} \left[\frac{1}{1 + \frac{T_{\text{iso}}}{T_{\text{GHS}}} \frac{(V_{\text{DB}}+V_{\text{DA}})}{(V_{\text{B}}+V_{\text{A}})}} + \frac{1}{1 + \frac{T_{\text{GHS}}}{T_{\text{iso}}} \frac{V_{\text{B}}}{V_{\text{DB}}}} - \frac{1}{1 + \frac{T_{\text{GHS}}}{T_{\text{iso}}} \frac{V_{\text{A}}}{V_{\text{DA}}}} \right] +$$

$$B_{p,\text{GHS}} \left[\frac{2}{1 + \frac{T_{\text{iso}}}{T_{\text{GHS}}} \frac{V_{\text{DB}}}{V_{\text{B}}}} + \frac{1}{1 + \frac{T_{\text{GHS}}}{T_{\text{iso}}} \frac{V_{\text{B}}}{V_{\text{DB}}}} - \frac{1}{1 + \frac{T_{\text{iso}}}{T_{\text{GHS}}} \frac{V_{\text{DA}}}{V_{\text{A}}}} - \frac{1}{1 + \frac{T_{\text{iso}}}{T_{\text{GHS}}} \frac{(V_{\text{DB}}+V_{\text{DA}})}{(V_{\text{B}}+V_{\text{A}})}} \right] +$$

$$\lambda_{\text{B}} \left[\frac{1}{Q_{\Delta T} \left(1 + \frac{T_{\text{iso}}}{T_{\text{GHS}}} \frac{V_{\text{DB}}}{V_{\text{B}}}\right)} \right] +$$

$$\lambda_{\text{A}} \left[\frac{\frac{1}{Q_{\Delta T}} - 1}{\left(\frac{V_{\text{B}}}{V_{\text{A}}} + \frac{T_{\text{iso}}}{T_{\text{GHS}}} \frac{V_{\text{DB}}}{V_{\text{A}}}\right)} - \frac{1}{1 + \frac{T_{\text{GHS}}}{T_{\text{iso}}} \frac{V_{\text{DA}}}{V_{\text{A}}}} \right] +$$

$$\lambda_{\text{GHS}} \left[\frac{\frac{1}{Q_{\Delta T}} - 1}{\left(\frac{V_{\text{DB}}}{V_{\text{DA}}} + \frac{T_{\text{GHS}}}{T_{\text{iso}}} \frac{V_{\text{B}}}{V_{\text{DA}}}\right)} + \frac{1}{Q_{\Delta T} \left(1 + \frac{T_{\text{GHS}}}{T_{\text{iso}}} \frac{V_{\text{B}}}{V_{\text{DB}}}\right)} - \frac{1}{1 + \frac{T_{\text{GHS}}}{T_{\text{iso}}} \frac{V_{\text{A}}}{V_{\text{DA}}}} \right]$$

$$(F.20)$$

By means of the volume ratios defined in equation 3.37 and the temperature ratio $T_{\text{ratio}} = \frac{T_{\text{iso}}}{T_{\text{GHS}}}$ equation F.20 can be expressed by:

$$\frac{K_1}{K_0 - 1} = B_{p,\text{iso}} \left[\frac{1}{1 + \frac{1}{T_{\text{ratio}} Q_{\text{B}}}} - \frac{1}{1 + \frac{1}{T_{\text{ratio}} Q_{\text{A}}}} + \frac{1}{1 + T_{\text{ratio}} \frac{(Q_{\text{B}}+Q_{\text{A}}Q^*)}{(1+Q^*)}} \right] +$$

$$B_{p,\text{GHS}} \left[1 + \frac{1}{1 + T_{\text{ratio}} Q_{\text{B}}} - \frac{1}{1 + T_{\text{ratio}} \frac{Q_{\text{B}}+Q_{\text{A}}Q^*}{1+Q^*}} - \frac{1}{1 + T_{\text{ratio}} Q_{\text{A}}} \right] +$$

$$\lambda_{\text{B}} \left[\frac{1}{Q_{\Delta T}} \left(\frac{1}{1 + T_{\text{ratio}} Q_{\text{B}}} \right) \right] +$$

$$\lambda_{\text{A}} \left[\left(\frac{1}{Q_{\Delta T}} - 1 \right) \frac{Q^*}{1 + T_{\text{ratio}} Q_{\text{B}}} - \frac{1}{1 + T_{\text{ratio}} Q_{\text{A}}} \right] +$$

$$\lambda_{\text{GHS}} \left[\frac{1}{Q_{\Delta T}} \left(\frac{Q_{\text{A}} Q^*}{Q_{\text{B}} + \frac{1}{T_{\text{ratio}}}} + \frac{1}{1 + \frac{1}{T_{\text{ratio}} Q_{\text{B}}}} \right) - \frac{1}{1 + \frac{1}{T_{\text{ratio}} Q_{\text{A}}}} - \frac{Q_{\text{A}} Q^*}{Q_{\text{B}} + \frac{1}{T_{\text{ratio}}}} \right]$$

$$(F.21)$$

After converting the pressure virial coefficients to the density virial coefficients, this is the final result given in section 3.3.4

G. Dielectric expansion working equations

G.1. Ideal dielectric expansion

The ratio of the Mosotti-term between the rth expansion and expansion $r + j$ from volume V_A into volumes $V_A + V_B$ may in accordance with equation 3.12 be written as:

$$\frac{f_r}{f_{r+j}} = \frac{A_\epsilon \rho_{\text{m},r} \left(1 + b_\epsilon \rho_{\text{m},r} + c_\epsilon \rho_{\text{m},r}^2 + ...\right)}{A_\epsilon \rho_{\text{m},r+j} \left(1 + b_\epsilon \rho_{\text{m},r+j} + c_\epsilon \rho_{\text{m},r+j}^2 + ...\right)} \tag{G.1}$$

Combination with the apparatus constant defined by the volume ratio $\frac{\rho_{\text{m},r+j}}{\rho_{\text{m},r}} = \left(\frac{V_A}{V_A+V_B}\right)^j = Q^{-j}$ results in:

$$\frac{f_r}{f_{r+j}} = \frac{A_\epsilon \rho_{\text{m},r} \left(1 + b_\epsilon \rho_{\text{m},r} + c_\epsilon \rho_{\text{m},r}^2 + ...\right)}{A_\epsilon \rho_{\text{m},r} Q^{-j} \left(1 + b_\epsilon \rho_{\text{m},r} Q^{-j} + c_\epsilon \rho_{\text{m},r}^2 Q^{-2j} + ...\right)} \tag{G.2}$$

The denominator of the right side is expanded into a Taylor series

$$\frac{1}{\left(1 + b_\epsilon \rho_{\text{m},r} Q^{-j} + c_\epsilon \rho_{\text{m},r}^2 Q^{-2j} + ...\right)} = 1 - b_\epsilon Q^{-j} \rho_{\text{m},r} + Q^{-2j}(b_\epsilon^2 - c_\epsilon)\rho_{\text{m},r}^2 + ... \tag{G.3}$$

To derive a proper expression for the data evaluation, equation 3.12 is inverted to give $\rho_{\text{m},r}$ as a function of the Mosotti-term:

$$\rho_{\text{m},r} = \frac{f_r}{A_\epsilon} \left(1 - \frac{b_\epsilon f_r}{A_\epsilon} + \frac{2b_\epsilon^2 - c_\epsilon}{A_\epsilon^2} f_r^2 + ...\right) \tag{G.4}$$

Inserting equations G.3 and G.2 into equation G.2 results in the final expression given in 3.4.1:

$$\frac{f_r}{f_{r+j}} = Q^j + \frac{(Q^j - 1)}{A_\epsilon} b_\epsilon f_j + \frac{(Q^j - Q^{-j})}{A_\epsilon^2} \left(c_\epsilon - b_\epsilon^2\right) f_j^2 + ... \tag{G.5}$$

G.2. Improvements to the dielectric expansions

Improvements to the procedure described in section 3.4.1 were implemented rather quickly. Orcutt and Cole published a system with three vessels of equal volume and each one equipped with a capacitor of same capacity in 1967 [113]. The setup is shown in figure G.1. Expansions were carried out in a cyclic manner. For instance, cells A and B are filled and the gas is expanded into cell C. After this, cell A is evacuated and the gas is expanded from B and C into it. The last turn is the expansion from A and C into the evacuated cell B. Thus, the gas was expanded once into each cell and one cycle is completed. If the volumes are defined as $V_A = V(1 + \delta_A)$, $V_B = V(1 + \delta_B)$ and $V_C = V(1 + \delta_C)$, it can be shown (see appendix G.2.1) that the ratio of the densities $Q_{\text{cycle},3}$ is:

$$Q_{\text{cycle},3} = \frac{\rho_{r+3}}{\rho_r} = \left(\frac{2}{3}\right)^3 \left(1 + \frac{1}{4}\left(\delta_A\delta_B + \delta_B\delta_C + \delta_C\delta_A\right) - \frac{1}{8}\delta_A\delta_C\delta_C + ...\right) \tag{G.6}$$

under the auxialary condition that $\delta_A + \delta_B + \delta_C = 0$. Deviations from the ideal density ratio are thus automatically only a second order effect, which allows to determine $Q_{\text{cycle},3}$ with relative uncertainties of a few ppm. The exact determination of δ_A, δ_B and δ_C and, thus, the apparatus constant is carried out by additional pressure measurements. The procedure is shown in appendix G.2.2. Knowing $Q_{\text{cycle},3}$ and the molar polarizability A_ϵ, the data can be evaluated by the following working equation [118]:
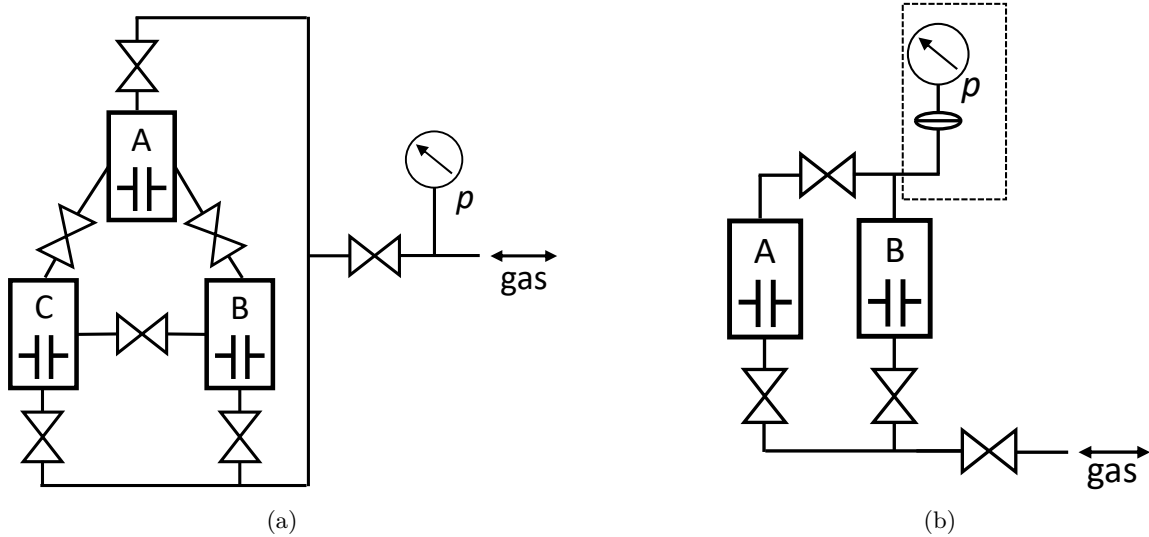
Figure G.1.: Schemes of the setups used by Orcutt and Cole (a) for the cyclic expansion with three cells [113] and as proposed by Buckingham *et al.* (b) and adapted later by Koschine *et al.* with two cells [100, 117]. The pressure measurement in scheme (b) was introduced by Koschine *et al.* to also determine density virial coefficients.

$$f_r - \frac{f_{r+3}}{Q_{\text{cycle},3}} = \frac{b_\epsilon(t)}{A_\epsilon}(1 - Q_{\text{cycle},3}) \cdot f_r^2 +$$

$$\left(\frac{c_\epsilon(T)}{A_\epsilon^2}(1 - Q_{\text{cycle},3}^2) - \frac{2b_\epsilon^2(T)}{A_\epsilon^2}(1 - Q_{\text{cycle},3}) \right) \cdot f_r^3 + ... \tag{G.7}$$

Dielectric virial coefficients retrieved by this method are believed to be a factor 2 - 5 times more accurate than the ones obtained with the standard method [84]. The published relative uncertainties of the second dielectric virial coefficients measured with this method are typically less than $10\,\%$ [113, 114, 118]. Another big advantage of this method is the implicit detection of errors in case constant and linear terms different from zero arise in the polynomial used to fit the data [100]. Experiments with three vessels were not published any more after 1970 probably for two reasons. Koschine *et al.* have shown that a cyclic expansion is also possible by utilizing only two vessels in 1992 reducing the experimental complexity [100, 119]. Their setup is shown in figure G.1. The additionally installed differential pressure transducer allowed to measure the density virial coefficients as well. The working equation is identical to the one for the three vessel cyclic expansion G.7, but the apparatus constant $Q_{\text{cycle},3}$ has to be replaced by $Q_{\text{cycle},2}$. For the two volumes being $V_A = V + \delta$ and $V_B = V - \delta$, it is given by:

$$Q_{\text{cycle},2} = \frac{1}{4}\left(1 - \left(\frac{\delta}{V}\right)^2\right) \tag{G.8}$$

A method to determine the small correction term $\frac{\delta}{V}$ from additional pressure measurements is shown in appendix G.2.2. The vanish of three cell expansions may as well be due to an idea of Buckingham *et al.* published in 1970 [117]. Their method requires only two cells with matched volumes and matched capacitances as well. The sum of both capacitances is measured for cell A being filled and cell B being evacuated. The gas is then expanded into cell B and the sum of capacitances is measured again. Using the nomenclature $V_A = V(1 + \delta_V)$ and $V_B = V(1 - \delta_V)$ for the volumes as well as $C_A = C(1 + \delta_C)$ and $C_B = C(1 - \delta_C)$ for the capacitances, it can be shown that the change in the sum of capacitance Δ_A is [6]:

$$\frac{\Delta_A}{C(\epsilon_{\text{r,A}} - 1)} = (\delta_V - \delta_C) - \frac{b_\epsilon(T) + A_\epsilon}{6A_\epsilon}(\epsilon_{\text{r,A}} - 1) +$$

$$\left(\frac{4b_\epsilon^2(T) - 3c_\epsilon(T) + 2b_\epsilon(T)A_\epsilon + A_\epsilon^2}{36A_\epsilon^2} \right)(\epsilon_{\text{r,A}} - 1)^2 -$$

$$\left(\frac{c_\epsilon(T) + 2A_\epsilon b_\epsilon(T) + A_\epsilon^2}{36A_\epsilon^2} \right)\delta_V(\epsilon_{\text{r,A}} - 1)^2 \tag{G.9}$$

with $\epsilon_{\text{r,A}}$ denoting the dielectric constant for the expansion from A to B. After that, the process is repeated, but with cell B being filled and gas being expanded into cell A.

$$\frac{\Delta_B}{C(\epsilon_{\mathrm{r,B}} - 1)} = -\ (\delta_V - \delta_C) - \frac{b_\epsilon(T) + A_\epsilon}{6A_\epsilon}(\epsilon_{\mathrm{r,B}} - 1) +$$

$$\left(\frac{4b_\epsilon^2(T) - 3c_\epsilon(T) + 2b_\epsilon(T)A_\epsilon + A_\epsilon^2}{36A_\epsilon^2}\right)(\epsilon_{\mathrm{r,B}} - 1)^2 - \tag{G.10}$$

$$\left(\frac{c_\epsilon(T) + 2A_\epsilon b_\epsilon(T) + A_\epsilon^2}{36A_\epsilon^2}\right)\delta_V(\epsilon_{\mathrm{r,B}} - 1)^2$$

in this case Δ_B denotes the change of the sum of capacitances for the expansion from B into A and $\epsilon_{\mathrm{r,B}}$ is the corresponding dielectric constant. By summation of equations G.9 and G.10, the linear term of the deviations cancels resulting in [6]:

$$\frac{\Delta_A}{C(\epsilon_{\mathrm{r,A}} - 1)} + \frac{\Delta_B}{C(\epsilon_{\mathrm{r,B}} - 1)} = -\left(\frac{b_\epsilon(t) + A_\epsilon}{6A_\epsilon}\right)\left((\epsilon_{\mathrm{r,A}} - 1) + (\epsilon_{\mathrm{r,B}} - 1)\right) +$$

$$\frac{1}{2}\left(\frac{4b_\epsilon^2(T) - 3c_\epsilon(T) + 2b_\epsilon(T)A_\epsilon + A_\epsilon^2}{36A_\epsilon^2}\right)\left((\epsilon_{\mathrm{r,A}} - 1) + (\epsilon_{\mathrm{r,B}} - 1)\right)^2 + ... \tag{G.11}$$

Fitting the left handside of equation G.11 over $(\epsilon_{\mathrm{r,A}} - 1) + (\epsilon_{\mathrm{r,B}} - 1)$ with a polynomial of appropriate order allows to retrieve the dielectric virial coefficients from the fit coefficients. Due to the matched volumes and skillful arrangement of the equation, neither the absolute volumes or apparatus constants nor the small deviations are included in the working equation in first orders. Dielectric virial coefficients measured in this manner have similar uncertainties as the one from the cyclic expansions. This method was successfully used for the determination of the dielectric virial coefficients of noble gases [3, 6].

Though the improvements made from the standard dielectric expansion method are promising, they all require to have precisely matched volumes. Since an automated pressure measurement has to be carried out for the determination of the density virial coefficients and the DCGT evaluation, this requirement could not be met within the frame of this work. Further details on the design of the current apparatus are given in chapter 4. Eventually, it could be possible to adapt the method of Buckingham to the system by expanding gas for instance between two equally sized cells, whereas gas is expanded from cell A including the dead volume of the pressure sensor at a different temperature into another cell B. The inverse expansion is then carried out from cell B and the dead volume into cell A. This has not been done within the framework of this thesis for two reasons. Preliminary experiments with equal sized cells have shown that it is only possible to carry out around 8 expansions before the uncertainty of the pressure measuring equipment is getting too high. 8 data points are not even enough to fit a polynomial of third order, while a fourth order fit is required due to the influence of the higher density virials. For the exclusive evaluation of the dielectric virials the, fit order may actually be sufficient, but it is at this point unclear how the dead volume can be included in the working equation.

It should be noted that the dielectric method has also been transferred to optical experiments [50, 120]. Instead of the Clausius-Mosotti equation, the Lorentz-Lorenz equation is used to derive the working equation (see also appendix D). The particle density is assessed via measurements of the refractive index with appropriate spectrometers.

G.2.1. The three cell cyclic expansion by Orcutt and Cole

The ratio of density ρ_r and after ρ_{r+3} one expansion cycle including in total three expansions may be written as:

$$\frac{\rho_{r+3}}{\rho_r} = \frac{V_A + V_B}{V_A + V_B + V_C} \cdot \frac{V_B + V_C}{V_A + V_B + V_C} \cdot \frac{V_C + V_A}{V_A + V_B + V_C} \tag{G.12}$$

following the declaration of the volumes as $V_A = V(1 + \delta_A)$, $V_B = V(1 + \delta_B)$ and $V_C = V(1 + \delta_C)$ this results in:

$$\frac{\rho_{r+3}}{\rho_r} = \frac{V(2 + \delta_A + \delta_B) \cdot V(2 + \delta_B + \delta_C) \cdot V(2 + \delta_C + \delta_A)}{V^3(3 + \delta_A + \delta_B + \delta_C)} \tag{G.13}$$

The denominator is simplified by the additional postulation that the sum of volume deviations shall be zero $\delta_A + \delta_B + \delta_C = 0$

$$\frac{\rho_{r+3}}{\rho_r} \cdot 3^3 = 8 + 8(\delta_A + \delta_B + \delta_C) + 6(\delta_A\delta_B + \delta_B\delta_C + \delta_C\delta_A) + 2(\delta_A^2 + \delta_B^2 + \delta_C^2) +$$
$$(\delta_A^2\delta_b + \delta_A^2\delta_C + \delta_A\delta_C^2 + \delta_B^2\delta_A + \delta_B^2\delta_C + \delta_C^2\delta_B) + 2\delta_A\delta_B\delta_C \tag{G.14}$$

This expression can be written as:

$$\frac{\rho_{r+3}}{\rho_r} \cdot 3^3 = 8 + 2(\delta_A + \delta_B + \delta_C)^2 + 2(\delta_A\delta_B + \delta_B\delta_C + \delta_C\delta_A) +$$
$$(\delta_A + \delta_B + \delta_C)(\delta_A\delta_B + \delta_B\delta_C + \delta_C\delta_A) - \delta_A\delta_B\delta_C \tag{G.15}$$

which leads to the final simplification due to the demanded restriction $\delta_A + \delta_B + \delta_C = 0$.

$$\frac{\rho_{r+3}}{\rho_r} = \left(\frac{2}{3}\right)^3 \left(1 + \frac{1}{4}(\delta_A\delta_B + \delta_B\delta_C + \delta_A\delta_C) - \frac{1}{8}\delta_A\delta_B\delta_C\right) \tag{G.16}$$

It shall be noted that in the original publication the two last terms in the above equation have exactly opposite signs [113]. Eventually, this lead to a slightly different reassessment of the working equation in a later publication [118].

G.2.2. The two cell cyclic expansion by Koschine and Lehmann - correction to the apparatus constant

In the following, the determination of the corrections to the apparatus constant is shown by the example of the two cell cyclic expansion [100]. Let cell A with volume $V_A = V + \delta_V$ be filled with n_{A1} moles of gas at a pressure p_{A1}, while cell B with volume $V_B = V - \delta_V$ is evacuated. This initial condition can be written as:

$$p_{A1} = \frac{n_{A1}RTZ_{A1}}{V_A} \tag{G.17}$$

after the expansion this changes to

$$p_{A2} = \frac{n_{A1}RTZ_{A1}}{V_A + V_B} \tag{G.18}$$

With the volumes defined as in the text above, the ratio of both pressures can be written as:

$$\frac{p_{A2}}{p_{A1}} = \frac{Z_{A2}}{Z_{A1}} \frac{V + \delta_V}{2V} = \frac{1}{2} \frac{Z_{A2}}{Z_{A1}} (1 + \frac{\delta_V}{V}) \tag{G.19}$$

The same procedure is repeated with cell B being filled initially and expansion into cell A:

$$\frac{p_{B2}}{p_{B1}} = \frac{1}{2} \frac{Z_{B2}}{Z_{B1}} (1 - \frac{\delta_V}{V}) \tag{G.20}$$

Multiplication of equation G.19 with the inverted ratio of equation G.20 leads to:

$$\frac{p_{A2}p_{B1}}{p_{A1}p_{B2}} = \frac{Z_{A2}Z_{B1}}{Z_{A1}Z_{A2}} \frac{1 + \frac{\delta_V}{V}}{1 - \frac{\delta_V}{v}} \tag{G.21}$$

By choosing the same starting pressures, the compressibility factors cancel and the formula may be simplified to:

$$\frac{p_{A2}p_{B1}}{p_{A1}p_{B2}} \approx 1 + 2\frac{\delta_V}{V} \tag{G.22}$$

Thus, the small correction term $\frac{\delta_V}{V}$ can be determined by simple pressure ratios. Since the influence on the apparatus constant is of quadratic order, relative uncertainties in the pressure measurement in the order of 10^{-4} are already sufficient. The apparatus constant can, then, be calculated by the given equation G.8 $Q_{\text{cycle},2} = \frac{1}{4} \left(1 - \left(\frac{\delta_V}{V}\right)^2\right)$

G.3. Dielectric expansion with deformation of the cells

Derivation of the working equation for the dielectric expansion method with deformation of the cells starts with relation 3.44, which may be written as:

$$\frac{f_r V_A \left(1 + \lambda_A p_r\right)}{f_{r+1}(V_A + V_B)\left(1 + \lambda_{AB} p_{r+1}\right)} = \frac{1 + b_{CM} f_r + c_{CM} f_r^2 + ...}{1 + b_{CM} f_{r+1} + c_{CM} f_{r+1}^2 + ...} \tag{G.23}$$

In analogy to the derivation given in section F.2, the combined compressibility λ_{AB} taking the deformation of both cells into account is used. Though the pressure is measured in this experiment, it is replaced in the following step, so others can apply the equation to experiments, where the pressure is not assessed at the same time. The idealized relation $p = \frac{fRT}{A_\epsilon}$ is used to rewrite f_r and f_{r+1} in the small correction terms. Furthermore, the ratios of Mosotti-terms $F_{\text{ratio},r} = \frac{f_r}{f_{r+1}}$ are used to replace f_{r+1}:

$$\frac{F_{\text{ratio},r} V_A \left(1 + \lambda_A \frac{f_r RT}{A_\epsilon}\right)}{(V_A + V_B)\left(1 + \lambda_{AB} \frac{f_1 RT}{F_{\text{ratio},r} A_\epsilon}\right)} = \frac{1 + b_{CM} f_r + c_{CM} f_r^2 + ...}{1 + b_{CM} \frac{f_r}{F_{\text{ratio},r}} + c_{CM} \left(\frac{f_r}{F_{\text{ratio},r}}\right)^2 + ...} \tag{G.24}$$

Following the routine given for the evaluation of equation F.8, this equation can be multiplied out and solved for $F_{\text{ratio},r}$. The result can be arranged as a series in powers of f_r and is:

$$\begin{aligned}
F_{\text{ratio},r} = {} & \frac{(V_A + V_B)}{V_A} + \frac{b_{CM} V_B + \frac{RT}{A_\epsilon}(\lambda_B V_A - \lambda_A(V_A + V_B))}{V_A} \cdot f_r + \\
& \left[c_{CM} \frac{V_B^2 + 2V_A V_B}{(V_A + V_B)V_A} + \frac{\lambda_A RT}{A_\epsilon^2}(\lambda_A RT - b_{CM} A_\epsilon)\frac{(V_A + V_B)}{V_A} + \right. \\
& \left. \frac{\lambda_{AB} RT}{A_\epsilon^2}(b_{CM} A_\epsilon - \lambda_{AB} RT)\frac{V_A}{(V_A + V_B)} \right] \cdot f_r^2
\end{aligned} \tag{G.25}$$

This expression is simplified by substitution with the apparatus constant Q.

$$\begin{aligned}
F_{\text{ratio},r} = {} & Q + \left(b_{CM}(Q-1) + \frac{RT}{A_\epsilon}(\lambda_{AB} - \lambda_A Q)\right) \cdot f_r + \\
& \left[c_{CM}(Q - \frac{1}{Q}) + \frac{\lambda_A RT}{A_\epsilon^2}(\lambda_A RT - b_{CM} A_\epsilon)Q + \right. \\
& \left. \frac{\lambda_{AB} RT}{Q A_\epsilon^2}(b_{CM} A_\epsilon - \lambda_{AB} RT) \right] \cdot f_r^2 + ...
\end{aligned} \tag{G.26}$$

To retrieve the dielectric virial coefficients, the Mosotti virial coefficients are replaced by the relations given in equation 3.14. Furthermore, the combined compressibility is replaced by $\lambda_{AB} = \frac{\lambda_A}{Q} + \lambda_B(1 - \frac{1}{Q})$ so the final result only contains the compressibility of cell B λ_B. This results in the final expression:

$$F_{\text{ratio},r} = Q + (Q-1)\left(\frac{b_\epsilon}{A_\epsilon} + \frac{RT}{A_\epsilon}\frac{1}{Q}(\lambda_\text{B} - \lambda_\text{A}(Q+1))\right)\cdot f_r +$$
$$\left[\frac{c_\epsilon - b_\epsilon^2}{A_\epsilon^2}\left(Q - \frac{1}{Q}\right) + \frac{Q\lambda_\text{A}RT}{A_\epsilon^2}(\lambda_\text{A}RT - b_\epsilon) + \right.$$
$$\left.\frac{(RT)^2}{QA_\epsilon^2}\left(\frac{b_\epsilon}{RT}\left(\frac{\lambda_\text{A}}{Q} + \lambda_\text{B}\left(1 - \frac{1}{Q}\right)\right) - \left(\frac{\lambda_\text{A}}{Q} + \lambda_\text{B}\left(1 - \frac{1}{Q}\right)\right)^2\right)\right]\cdot f_r^2 + .. \tag{G.27}$$

Rearrangement of this equation leads to the final form given in section 3.4.3

G.4. Dielectric expansions with dead volumes

Carrying on the discussion from section 3.4.3, the Mosotti-terms at T_GHS are directly linked to the ones at T_iso by means of the DCGT data evaluation. The ansatz in equation 3.48 is simplified by neglecting the small corrections due to κ_eff for this assessment. Furthermore, $\mu_r \approx f_r$, when the influence of the compressibility is neglected. With these assumptions, equation 3.48 can be written as:

$$T_\text{iso}f_{r,\text{iso}}\left(1 + \frac{B_\text{DCGT,iso}}{A_\epsilon}f_{r,\text{iso}}\right) = T_\text{GHS}f_{r,\text{GHS}}\left(1 + \frac{B_\text{DCGT,GHS}}{A_\epsilon}f_{r,\text{GHS}}\right) \tag{G.28}$$

Solving this equation for $f_{r,\text{GHS}}$ yields:

$$f_{r,\text{GHS}} = \frac{A_\epsilon}{2B_\text{DCGT,GHS}}\left(\sqrt{\frac{T_\text{iso}}{T_\text{GHS}}\frac{4B_\text{DCGT,GHS}}{A_\epsilon}f_{r,\text{iso}}(1 + \frac{B_\text{DCGT,iso}}{A_\epsilon}f_{r,\text{iso}}) + 1} - 1\right) \tag{G.29}$$

Replacing $f_{r,\text{GHS}}$ with this expression in the starting equation 3.47 results in a non-solvable equation. That is why equation G.29 is expanded into a Taylor series that is truncated after the quadratic term:

$$f_{r,\text{GHS}} = \frac{T_\text{iso}}{T_\text{GHS}}\cdot f_{r,\text{iso}} + \frac{B_\text{DCGT,iso}T_\text{iso}T_\text{GHS} - B_\text{DCGT,GHS}T_\text{iso}^2}{T_\text{GHS}^2 A_\epsilon}\cdot f_{r,\text{iso}}^2 + ... \tag{G.30}$$

Using this expression and after incorporation of $F_{\text{ratio,iso}} = \frac{f_{r,\text{iso}}}{f_{r+1,\text{iso}}}$, consequent substitution results in:

$$\frac{f_{r,\text{iso}}V_A}{(1 + b_{\text{CM,iso}}f_{r,\text{iso}})} - \frac{f_{r,\text{iso}}(V_A + V_B)}{F_{\text{ratio,iso}}(1 + b_{\text{CM,iso}}\frac{f_{r,\text{iso}}}{F_{\text{ratio,iso}}})} =$$

$$\frac{\left(\frac{T_{\text{iso}}}{T_{\text{GHS}}} \cdot \frac{f_{r,\text{iso}}}{F_{\text{ratio,iso}}} + \frac{B_{\text{DCGT,iso}}T_{\text{iso}}T_{\text{GHS}} - B_{\text{DCGT,GHS}}T_{\text{iso}}^2}{T_{\text{GHS}}^2 A_\epsilon} \cdot \frac{f_{r,\text{iso}}^2}{Q_{\Delta T}^2}\right)(V_{DA} + V_{DB})}{\left(1 + b_{\text{CM,GHS}}\left(\frac{T_{\text{iso}}}{T_{\text{GHS}}} \cdot \frac{f_{r,\text{iso}}}{F_{\text{ratio,iso}}} + \frac{B_{\text{DCGT,iso}}T_{\text{iso}}T_{\text{GHS}} - B_{\text{DCGT,GHS}}T_{\text{iso}}^2}{T_{\text{GHS}}^2 A_\epsilon} \cdot \frac{f_{r,\text{iso}}^2}{Q_{\Delta T}^2}\right)\right)} \quad \text{(G.31)}$$

$$-\frac{\left(\frac{T_{\text{iso}}}{T_{\text{GHS}}} \cdot f_{r,\text{iso}} + \frac{B_{\text{DCGT,iso}}T_{\text{iso}}T_{\text{GHS}} - B_{\text{DCGT,GHS}}T_{\text{iso}}^2}{T_{\text{GHS}}^2 A_\epsilon} \cdot f_{r,\text{iso}}^2\right)V_{DA}}{\left(1 + b_{\text{CM,GHS}}\left(\frac{T_{\text{iso}}}{T_{\text{GHS}}} \cdot f_{r,\text{iso}} + \frac{B_{\text{DCGT,iso}}T_{\text{iso}}T_{\text{GHS}} - B_{\text{DCGT,GHS}}T_{\text{iso}}^2}{T_{\text{GHS}}^2 A_\epsilon} \cdot f_{r,\text{iso}}^2\right)\right)}$$

considering only the orders for the second virial coefficients. In order for equation G.31 to be solvable for $F_{\text{ratio},r}$ as a function of $f_{r,\text{iso}}$, $F_{\text{ratio},r}^2$ had to be replaced by the apparent apparatus constant $Q_{\Delta T}^2$, which will be the first fit coefficient of the final form. The solution can be described by:

$$F_{\text{ratio},r} = D_0 + D_1 f_r + D_2 f_r^2 + \dots$$

$$D_0 = 1 + \frac{T_{\text{iso}}V_{DB} + T_{\text{GHS}}V_B}{T_{\text{iso}}V_{DA} + T_{\text{GHS}}V_A} = Q_{\Delta T}$$

$$D_1 = b_{\text{CM,iso}} + (b_{\text{CM,GHS}}T_{\text{iso}} + b_{\text{CM,iso}}T_{\text{GHS}})\frac{(T_{\text{GHS}}V_B + T_{\text{iso}}V_{DB})}{T_{\text{GHS}}(T_{\text{GHS}}V_A + T_{\text{iso}}V_{DA})} +$$

$$(b_{\text{CM,GHS}}T_{\text{iso}} - b_{\text{CM,iso}}T_{\text{GHS}})\frac{(V_A + V_B)}{T_{\text{GHS}}(V_A + V_B) + T_{\text{iso}}(V_{DA} + V_{DB})} - \quad \text{(G.32)}$$

$$(b_{\text{CM,GHS}}V_A + b_{\text{CM,iso}}V_{DA})\frac{T_{\text{iso}}(T_{\text{GHS}}(V_A + V_B) + T_{\text{iso}}(V_{DA} + V_{DB}))}{(T_{\text{iso}}V_{DA} + T_{\text{GHS}}V_A)^2} +$$

$$\frac{(B_{\text{DCGT,GHS}}T_{\text{iso}} - B_{\text{DCGT,iso}}T_{\text{GHS}})}{A_\epsilon} \cdot \frac{T_{\text{iso}}}{T_{\text{GHS}}} \cdot$$

$$\frac{T_{\text{GHS}}(V_A + V_B) + T_{\text{iso}}(V_{DA} + V_{DB})}{T_{\text{GHS}}(T_{\text{GHS}}V_A + T_{\text{iso}}V_{DA})^2} \cdot \left(V_{DA} - \frac{V_{DA} + V_{DB}}{Q_{\Delta T}^2}\right)$$

A comparison with equation 3.36 shows, that the coefficient D_0 corresponds to the apparent apparatus constant $Q_{\Delta T}$ as well and converges to the ideal apparatus constant Q for equalizing the temperatures. Instead of the D_1 term, it is again beneficial to calculate the ratio $\frac{D_1}{D_0 - 1}$:

$$\frac{D_1}{D_0 - 1} = b_{\text{CM,iso}} \left(1 + \frac{V_\text{A} + \frac{T_\text{iso}}{T_\text{GHS}} V_\text{DA}}{V_\text{B} + \frac{T_\text{iso}}{T_\text{GHS}} V_\text{DB}} \right) + b_{\text{CM,GHS}} \frac{T_\text{iso}}{T_\text{GHS}} -$$

$$(b_{\text{CM,GHS}} V_\text{A} + b_{\text{CM,iso}} V_\text{DA}) \frac{T_\text{iso}}{T_\text{GHS}} \left(\frac{1}{V_\text{B} + \frac{T_\text{iso}}{T_\text{GHS}} V_\text{DB}} + \frac{1}{V_\text{A} + \frac{T_\text{iso}}{T_\text{GHS}} V_\text{DA}} \right)$$

$$\left(b_{\text{CM,GHS}} \frac{T_\text{iso}}{T_\text{GHS}} - b_{\text{CM,iso}} \right) \frac{(V_\text{A} + V_\text{B})(V_\text{A} + \frac{T_\text{iso}}{T_\text{GHS}} V_\text{DA})}{(V_\text{B} + \frac{T_\text{iso}}{T_\text{GHS}} V_\text{DB})(V_\text{A} + V_\text{B} + \frac{T_\text{iso}}{T_\text{GHS}} (V_\text{DA} + V_\text{DB}))} +$$

$$\frac{(B_{\text{DCGT,GHS}} T_\text{iso} - B_{\text{DCGT,iso}} T_\text{GHS})}{A_\epsilon} \cdot \frac{T_\text{iso}}{T_\text{GHS}} \frac{(V_\text{A} + V_\text{B} + \frac{T_\text{iso}}{T_\text{GHS}} (V_\text{DA} + V_\text{DB}))}{(V_\text{B} + \frac{T_\text{iso}}{T_\text{GHS}} V_\text{DB})(V_\text{A} + \frac{T_\text{iso}}{T_\text{GHS}} V_\text{DA})} \cdot$$

$$\left(V_\text{DA} - \frac{V_\text{DA} + V_\text{DB}}{Q_{\Delta T}^2} \right)$$

$$(\text{G.33})$$

With the volume ratios defined in equation 3.37 and the temperature ratio $T_\text{ratio} = \frac{T_\text{iso}}{T_\text{GHS}}$, equation G.33 can be simplified to the expression given in section 3.4.3:

$$F_{\text{ratio},r} = D_0 + D_1 \cdot f_r + D_2 \cdot f_r^2 + \dots$$

$$D_0 = Q_{\Delta T}$$

$$\frac{D_1}{D_0 - 1} = b_{\text{CM,iso}} \left[\frac{1}{1 + T_\text{ratio} Q_\text{A}} - \frac{1}{1 + T_\text{ratio} Q_\text{B}} + \frac{1}{1 + T_\text{ratio} \frac{(Q_\text{B} + Q_\text{A} Q^*)}{(1 + Q^*)}} \right] +$$

$$b_{\text{CM,GHS}} T_\text{ratio} \left[1 + \frac{1}{1 + T_\text{ratio} Q_\text{B}} - \frac{1}{1 + T_\text{ratio} Q_\text{A}} - \frac{1}{1 + T_\text{ratio} \frac{(Q_\text{B} + Q_\text{A} Q^*)}{(1 + Q^*)}} \right] +$$

$$\frac{(B_{\text{DCGT,iso}} - T_\text{ratio} B_{\text{DCGT,GHS}})}{A_\epsilon} \left[\left(\frac{1}{Q_{\Delta T}^2} - 1 \right) \left(\frac{1}{1 + \frac{1}{T_\text{ratio} Q_\text{A}}} + \frac{Q_\text{A} Q^*}{\frac{1}{T_\text{ratio}} + Q_\text{B}} \right) + \right.$$

$$\left. \frac{1}{Q_{\Delta T}^2} \left(\frac{1}{1 + \frac{1}{T_\text{ratio} Q_\text{B}}} + \frac{\frac{Q_\text{B}}{Q^*}}{\frac{1}{T_\text{ratio}} + Q_\text{A}} \right) \right]$$

$$(\text{G.34})$$

G.5. Final working equation for dielectric expansions

As previously described, the equation is solved for $F_{\text{ratio,iso}}$ with the help of the program "Mathematica" (Wolfram Research) and the result is rearranged as $F_{\text{ratio,iso}} = D_0 + D_1 f_{r,\text{iso}} + D_2 f_{r,\text{iso}}^2 + \dots$. The term $D_0 = Q_{\Delta T}$ is equivalent to all previous results. To display the result required for the data evaluation in this thesis, the term $\frac{D_1}{D_0 - 1}$ is depicted:

$$
\begin{aligned}
\frac{D_1}{D_0 - 1} = {}& b_{\mathrm{CM,iso}} \left[\frac{1}{1 + \frac{T_{\mathrm{iso}}}{T_{\mathrm{GHS}}} \cdot \frac{V_{\mathrm{DB}}}{V_{\mathrm{B}}}} - \frac{1}{1 + \frac{T_{\mathrm{iso}}}{T_{\mathrm{GHS}}} \cdot \frac{V_{\mathrm{DA}}}{V_{\mathrm{A}}}} + \frac{1}{1 + \frac{T_{\mathrm{iso}}}{T_{\mathrm{GHS}}} \cdot \frac{(V_{\mathrm{DA}}+V_{\mathrm{DB}})}{(V_{\mathrm{A}}+V_{\mathrm{B}})}} \right] + \\[2ex]
& b_{\mathrm{CM,GHS}} \cdot \frac{T_{\mathrm{iso}}}{T_{\mathrm{GHS}}} \left[1 + \frac{1}{1 + \frac{T_{\mathrm{iso}}}{T_{\mathrm{GHS}}} \cdot \frac{V_{\mathrm{DB}}}{V_{\mathrm{B}}}} - \frac{1}{1 + \frac{T_{\mathrm{iso}}}{T_{\mathrm{GHS}}} \cdot \frac{V_{\mathrm{DA}}}{V_{\mathrm{A}}}} - \frac{1}{1 + \frac{T_{\mathrm{iso}}}{T_{\mathrm{GHS}}} \cdot \frac{(V_{\mathrm{DA}}+V_{\mathrm{DB}})}{(V_{\mathrm{A}}+V_{\mathrm{B}})}} \right] + \\[2ex]
& \lambda_{\mathrm{B}} \cdot \frac{R T_{\mathrm{iso}}}{A_\epsilon Q_{\Delta T}} \left[\frac{1}{1 + \frac{T_{\mathrm{iso}}}{T_{\mathrm{GHS}}} \cdot \frac{V_{\mathrm{DB}}}{V_{\mathrm{B}}}} \right] + \\[2ex]
& \lambda_{\mathrm{A}} \cdot \frac{R T_{\mathrm{iso}}}{A_\epsilon Q_{\Delta T}} \left[\left(\frac{1}{Q_{\Delta T}} - 1 \right) \left(\frac{1}{\frac{V_{\mathrm{B}}}{V_{\mathrm{A}}} + \frac{T_{\mathrm{iso}}}{T_{\mathrm{GHS}}} \cdot \frac{V_{\mathrm{DB}}}{V_{\mathrm{A}}}} \right) - \frac{1}{1 + \frac{T_{\mathrm{iso}}}{T_{\mathrm{GHS}}} \cdot \frac{V_{\mathrm{DA}}}{V_{\mathrm{A}}}} \right] + \\[2ex]
& \lambda_{\mathrm{GHS}} \cdot \frac{R T_{\mathrm{iso}}}{A_\epsilon Q_{\Delta T}} \left[\frac{1}{Q_{\Delta T}} \left(\frac{1}{\frac{V_{\mathrm{DB}}}{V_{\mathrm{DA}}} + \frac{T_{\mathrm{GHS}}}{T_{\mathrm{iso}}} \frac{V_{\mathrm{B}}}{V_{\mathrm{DA}}}} + \frac{1}{1 + \frac{T_{\mathrm{GHS}}}{T_{\mathrm{iso}}} \cdot \frac{V_{\mathrm{B}}}{V_{\mathrm{DB}}}} \right) - \right. \\[2ex]
& \left. \frac{1}{\frac{V_{\mathrm{DB}}}{V_{\mathrm{DA}}} + \frac{T_{\mathrm{GHS}}}{T_{\mathrm{iso}}} \cdot \frac{V_{\mathrm{B}}}{V_{\mathrm{DA}}}} - \frac{1}{1 + \frac{T_{\mathrm{GHS}}}{T_{\mathrm{iso}}} \cdot \frac{V_{\mathrm{A}}}{V_{\mathrm{DA}}}} \right] + \\[2ex]
& \frac{B_{\mathrm{DCGT,GHS}}}{A_\epsilon} \cdot \frac{T_{\mathrm{iso}}}{T_{\mathrm{GHS}}} \left[\left(1 - \frac{1}{Q_{\Delta T}^2} \right) \left(\frac{1}{1 + \frac{T_{\mathrm{GHS}}}{T_{\mathrm{iso}}} \cdot \frac{V_{\mathrm{A}}}{V_{\mathrm{DA}}}} + \frac{1}{\frac{V_{\mathrm{DB}}}{V_{\mathrm{DA}}} + \frac{T_{\mathrm{GHS}}}{T_{\mathrm{iso}}} \cdot \frac{V_{\mathrm{B}}}{V_{\mathrm{DA}}}} \right) - \right. \\[2ex]
& \left. \frac{1}{Q_{\Delta T}^2} \left(\frac{1}{1 + \frac{T_{\mathrm{GHS}}}{T_{\mathrm{iso}}} \cdot \frac{V_{\mathrm{B}}}{V_{\mathrm{DB}}}} + \frac{1}{\frac{V_{\mathrm{DA}}}{V_{\mathrm{DB}}} + \frac{T_{\mathrm{GHS}}}{T_{\mathrm{iso}}} \cdot \frac{V_{\mathrm{A}}}{V_{\mathrm{DB}}}} \right) \right] + \\[2ex]
& \frac{B_{\mathrm{DCGT,iso}}}{A_\epsilon} \left[\left(\frac{1}{Q_{\Delta T}^2} - 1 \right) \left(\frac{1}{1 + \frac{T_{\mathrm{GHS}}}{T_{\mathrm{iso}}} \cdot \frac{V_{\mathrm{A}}}{V_{\mathrm{DA}}}} + \frac{1}{\frac{V_{\mathrm{DB}}}{V_{\mathrm{DA}}} + \frac{T_{\mathrm{GHS}}}{T_{\mathrm{iso}}} \cdot \frac{V_{\mathrm{B}}}{V_{\mathrm{DA}}}} \right) - \right. \\[2ex]
& \left. \frac{1}{Q_{\Delta T}^2} \left(\frac{1}{1 + \frac{T_{\mathrm{GHS}}}{T_{\mathrm{iso}}} \cdot \frac{V_{\mathrm{B}}}{V_{\mathrm{DB}}}} + \frac{1}{\frac{V_{\mathrm{DA}}}{V_{\mathrm{DB}}} + \frac{T_{\mathrm{GHS}}}{T_{\mathrm{iso}}} \cdot \frac{V_{\mathrm{A}}}{V_{\mathrm{DB}}}} \right) \right] +
\end{aligned}
$$

$$(\mathrm{G.35})$$

H. Temperature stability of the gas-handling system

(a) isotherm 2

(b) isotherm 6

(c) isotherm 14
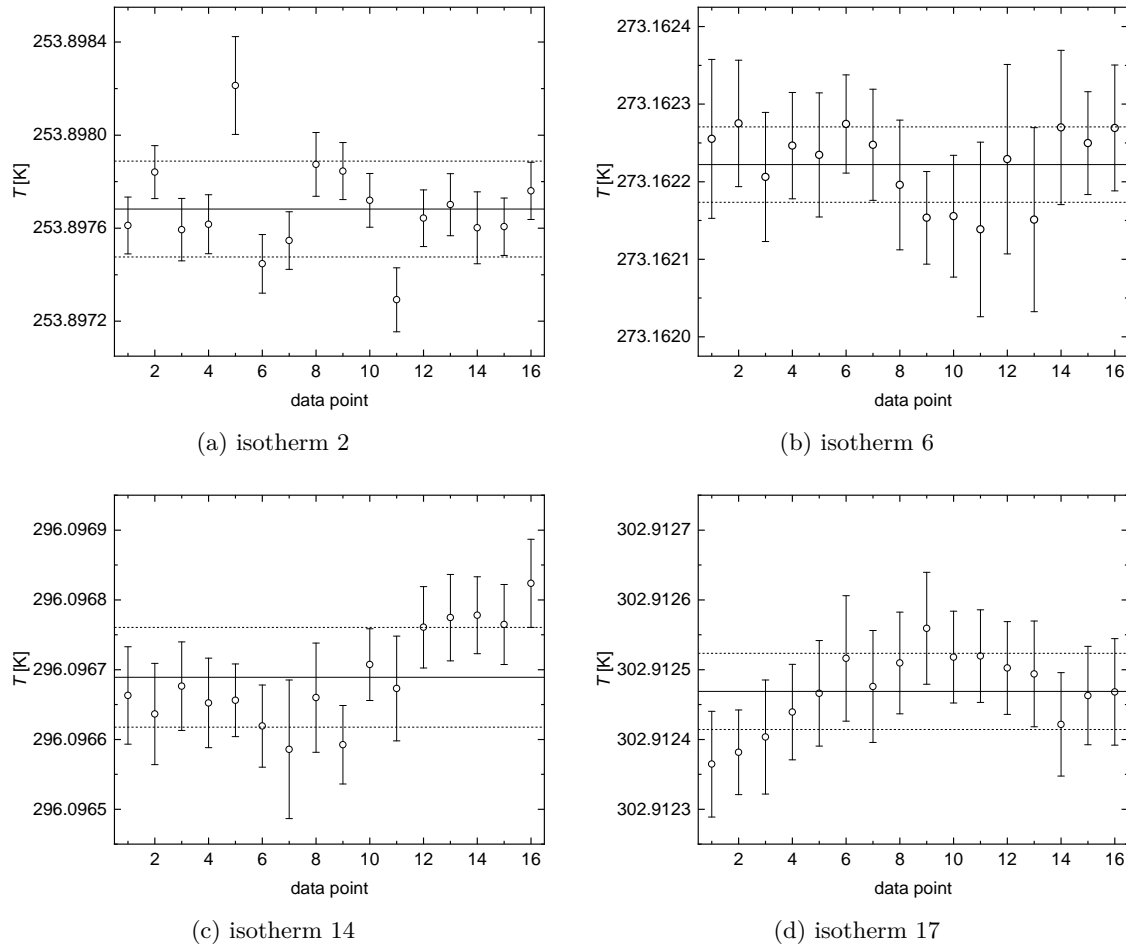
(d) isotherm 17

Figure H.1.: Examples of the temperature stability of the gas-handling system during an isotherm measurement for each temperature. The isotherm numbers are defined in table 5.1 and are the same as in figure 4.3. Data point 1 corresponds to the starting pressure of 7 MPa. At each data point, the temperature was measured for 2 hours with the error bars indicating the corresponding standard uncertainty of these averaged temperatures. The solid lines indicate the average value of temperature over the whole isotherm measurement, while the dashed line shows the corresponding standard deviation. The depicted temperature is the internal temperature of Digi1.

I. Linearity of the pressure sensors

A two point calibration of the pressure sensors can only be performed if they have a linear characteristic or one that can be described by two parameters. To demonstrate this for the used pressure sensors, the data sets plotted in figure 4.11 were used to calculate the absolute deviations to the pressure balance for four distinct temperatures utilizing the the temperature sensitivity coefficients β_{Digi_1} and β_{Digi_1}. The results are visualized in figures I.1 for Digi1 and in I.2 for Digi2.
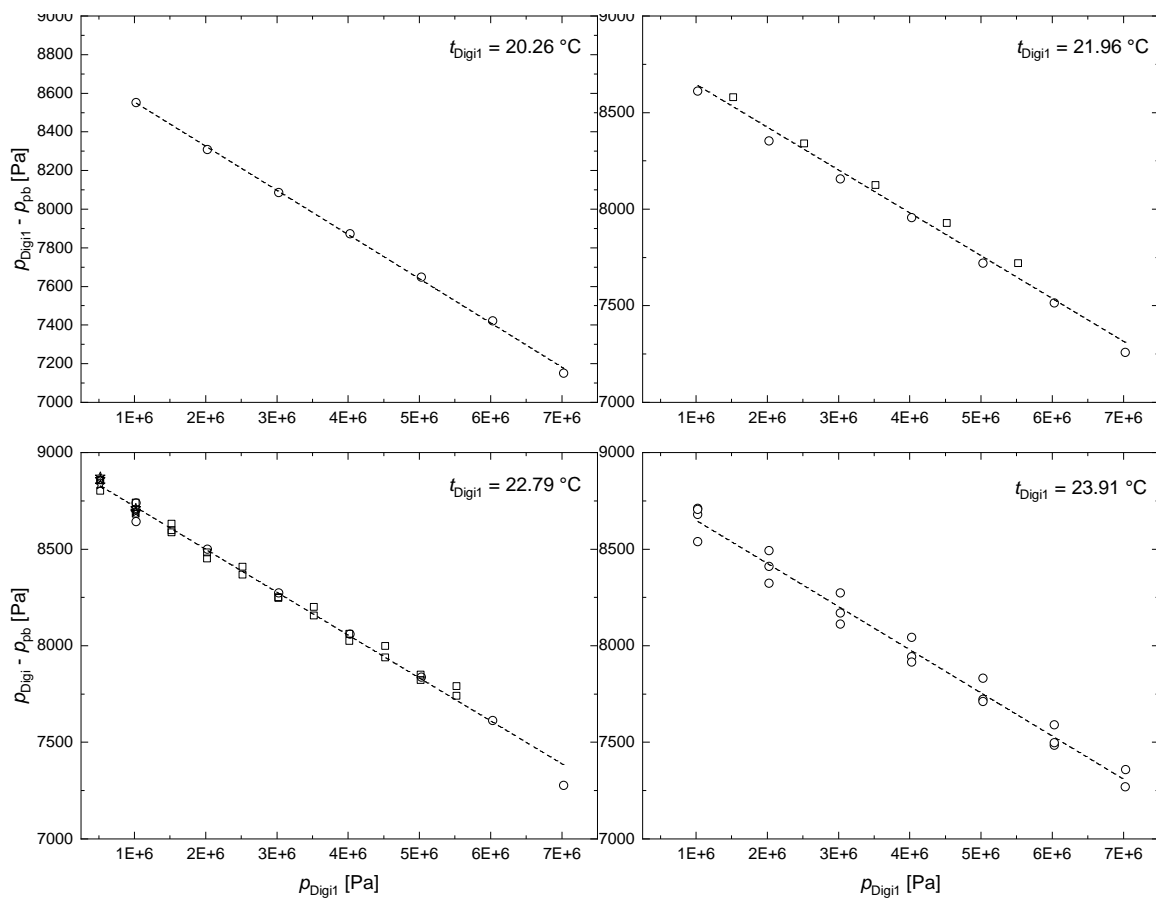
Figure I.1.: Linearity of Digi_1 depicted for four different sensor temperatures measured with three different pressure balances "Ruska 4" (open circles), "Ruska 5" (open stars) and "Ruska 6" (open cubes). Dashed lines are linear fits applied to the data.

Figure I.2.: The characteristic curve of Digi$_2$ depicted for four different sensor temperatures measured with three different pressure balances "Ruska 4" (open circles), "Ruska 5" (open stars) and "Ruska 6" (open cubes). Dashed lines are polynomial fits of second order applied to the data.

J. DCGT results

J.1. Average pressure and capacitance values of argon

Table J.1 summarizes the corrected and averaged pressure and capacitance data of the DCGT evaluation of argon.

$T_{\text{iso}} = 253.8975\,\text{K}$

data point	p_r [Pa]	μ	data point	p_r [Pa]	μ
1	7 022 767.2	0.014 977 13	9	2 387 512.3	0.004 824 71
2	6 152 329.6	0.012 997 91	10	2 080 491.4	0.004 188 29
3	5 385 715.4	0.011 280 73	11	1 812 158.7	0.003 635 91
4	4 710 996.6	0.009 790 84	12	1 577 794.3	0.003 156 41
5	4 117 698.0	0.008 498 08	13	1 373 277.4	0.002 740 22
6	3 596 532.3	0.007 376 26	14	1 194 889.0	0.002 378 93
7	3 139 266.4	0.006 402 78	15	1 039 391.7	0.002 065 29
8	2 738 458.1	0.005 557 93	16	903 920.3	0.001 793 02

$T_{\text{iso}} = 273.1613\,\text{K}$

data point	p_r [Pa]	μ	data point	p_r [Pa]	μ
1	7 021 651.2	0.013 585 86	9	2 354 716.5	0.004 386 23
2	6 135 591.9	0.011 794 41	10	2 050 190.4	0.003 808 51
3	5 358 806.0	0.010 239 45	11	1 784 485.7	0.003 306 93
4	4 677 996.1	0.008 889 72	12	1 552 779.9	0.002 871 44
5	4 081 625.7	0.007 718 12	13	1 350 816.9	0.002 493 34
6	3 559 533.7	0.006 701 05	14	1 174 871.4	0.002 165 04
7	3 102 801.7	0.005 818 14	15	1 021 643.7	0.001 879 99
8	2 703 534.1	0.005 051 66	16	888 244.6	0.001 632 48

$T_{\text{iso}} = 296.1256\,\text{K}$

data point	p_r [Pa]	μ	data point	p_r [Pa]	μ
1	7 022 759.9	0.012 281 79	9	2 329 811.8	0.003 975 15
2	6 123 995.1	0.010 666 16	10	2 027 228.1	0.003 452 51
3	5 338 904.1	0.009 263 11	11	1 763 583.4	0.002 998 62
4	4 653 176.0	0.008 044 80	12	1 533 921.7	0.002 604 39
5	4 054 284.1	0.006 986 75	13	1 333 940.5	0.002 262 00
6	3 531 397.3	0.006 067 91	14	1 159 861.1	0.001 964 64
7	3 075 060.5	0.005 269 97	15	1 008 374.1	0.001 706 37
8	2 676 962.9	0.004 576 98	16	876 567.5	0.001 482 07

$T_{\text{iso}} = 302.9126\,\text{K}$

data point	p_r [Pa]	μ	data point	p_r [Pa]	μ
1	7 022 723.0	0.011 949 42	9	2 324 100.3	0.003 870 10
2	6 121 117.2	0.010 378 50	10	2 021 950.2	0.003 361 46
3	5 334 226.9	0.009 014 21	11	1 758 759.0	0.002 919 68
4	4 647 400.7	0.007 829 26	12	1 529 580.1	0.002 535 99
5	4 047 954.6	0.006 800 12	13	1 330 062.1	0.002 202 74
6	3 524 911.5	0.005 906 28	14	1 156 420.0	0.001 913 28
7	3 068 680.9	0.005 129 98	15	1 005 329.9	0.001 661 86
8	2 670 869.7	0.004 455 72	16	873 887.7	0.001 443 50

Table J.1.: Averaged pressure and capacitance data at the four different temperatures.

J.2. Fit coefficients of the averaged DCGT isotherm fits

Table J.2 summarizes the fit results of the polynomial fit to the DCGT data of argon.

T_{iso} [K]	253.898	273.161	296.126	302.913
A_1^* [10^8Pa]	5.099 375	5.486 820	5.948 512	6.085 060
$u(A_1^*)$ [10^8Pa]	0.000 014	0.000 024	0.000 025	0.000 042
A_2^* [10^9Pa]	-3.3076	-2.8642	-2.3548	-2.2118
$u(A_2^*)$ [10^9Pa]	0.0005	0.0010	0.0012	0.0002
A_3^* [10^{10}Pa]	3.722	3.759	3.824	3.888
$u(A_3^*)$ [10^{10}Pa]	0.006	0.013	0.017	0.030
A_4^* [10^{10}Pa]	4.48	5.08	5.82	4.48
$u(A_4^*)$ [10^{10}Pa]	0.22	0.52	0.73	1.32

Table J.2.: Fit coefficients and their standard uncertainty of the polynomial fit of fourth order to the averaged data for corresponding average values of the four measured temperatures.

K. Data of the expansion experiments

The averaged pressures and Mosotti-terms as well as their corresponding ratios are given in table K.1 (pressure data) and table K.2 (dielectric expansions). The values are visualized in figure K.1. Both values are plotted over the measured pressure to illustrate the convergence towards $Q_{\Delta T}$ (see section 5.2). Due to the required correction to the temperature T_{GHS} described in section 4.7, the ratios are not identical with the ratio of two consecutive pressures or Mosotti-Terms. Furthermore, the values are, therefore, slightly different compared to the ones given in table J.1 for the DCGT data.

(a) 253.897 K

(b) 273.162 K

(c) 296.126 K

(d) 303.913 K
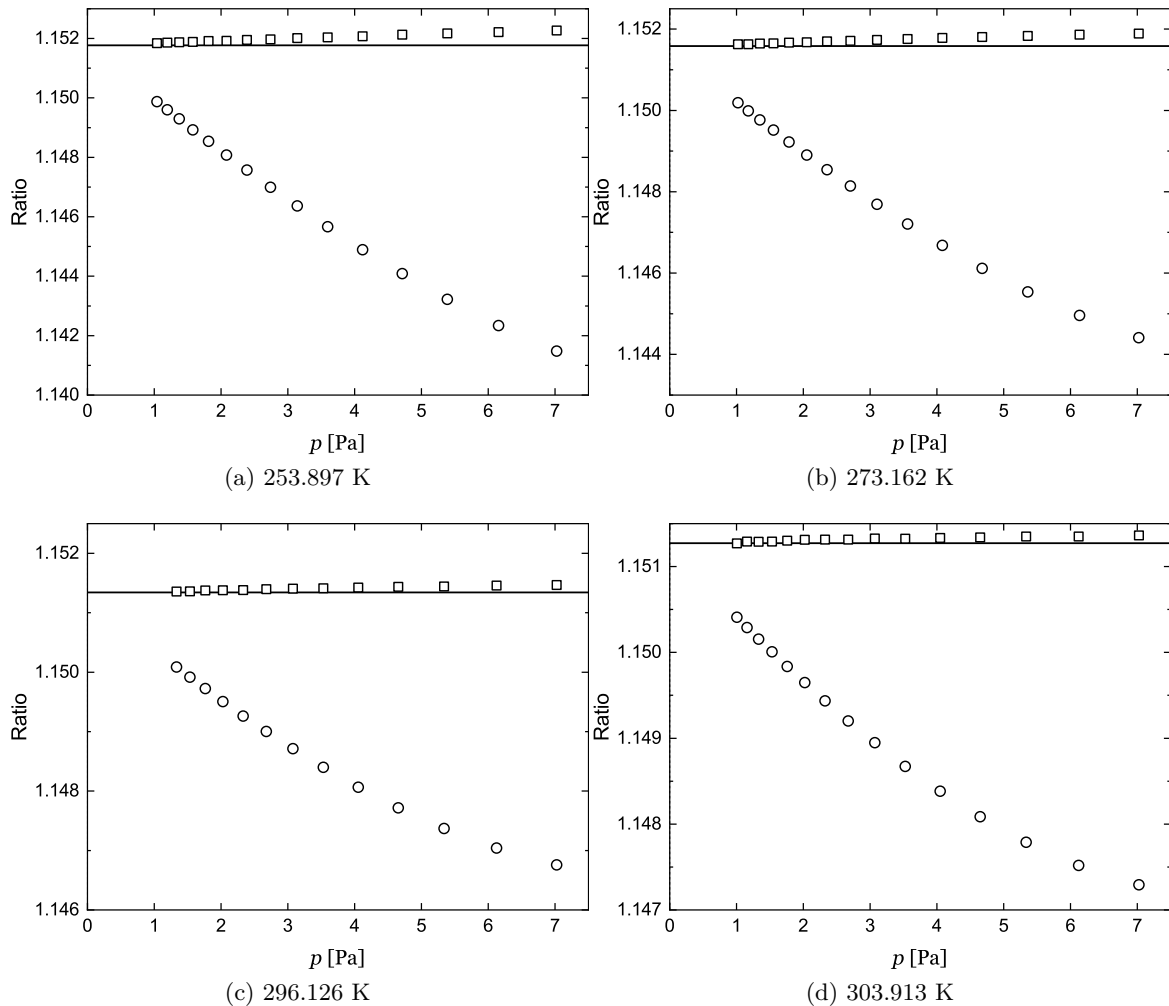
Figure K.1.: Pressure ratios (open circles) and ratios of Mosotti-terms (open squares) of argon plotted over the measured pressures at the indicated temperatures. The solid line indicates the apparent apparatus constant $Q_{\Delta T}$.

$\boldsymbol{T}_{\mathrm{iso}} = 253.8975\,\mathrm{K}$

data point	p_r [Pa]	$P_{\mathrm{ratio},r}$	data point	p_r [Pa]	$P_{\mathrm{ratio},r}$
1	7 022 765.7	1.141 481	9	2 387 515.5	1.147 571
2	6 152 331.7	1.142 340	10	2 080 492.8	1.148 075
3	5 385 713.6	1.143 222	11	1 812 157.5	1.148 542
4	4 711 003.5	1.144 086	12	1 577 792.8	1.148 927
5	4 117 706.1	1.144 893	13	1 373 275.6	1.149 294
6	3 596 547.6	1.145 663	14	1 194 885.2	1.149 603
7	3 139 269.1	1.146 366	15	1 039 387.9	1.149 873
8	2 738 462.4	1.146 990			

$\boldsymbol{T}_{\mathrm{iso}} = 273.1613\,\mathrm{K}$

data point	p_r [Pa]	$P_{\mathrm{ratio},r}$	data point	p_r [Pa]	$P_{\mathrm{ratio},r}$
1	7 021 455.4	1.144 413	9	2 354 549.8	1.148 541
2	6 135 385.8	1.144 959	10	2 050 035.4	1.148 904
3	5 358 595.5	1.145 538	11	1 784 339.1	1.149 226
4	4 677 804.1	1.146 118	12	1 552 645.4	1.149 517
5	4 081 436.1	1.146 680	13	1 350 693.5	1.149 767
6	3 559 345.3	1.147 205	14	1 174 757.7	1.149 990
7	3 102 621.2	1.147 692	15	1 021 539.0	1.150 188
8	2 703 363.9	1.148 141			

$\boldsymbol{T}_{\mathrm{iso}} = 296.1256\,\mathrm{K}$

data point	p_r [Pa]	$P_{\mathrm{ratio},r}$	data point	p_r [Pa]	$P_{\mathrm{ratio},r}$
1	7 022 794.3	1.146 758	8	2 676 982.6	1.149 003
2	6 124 009.7	1.147 042	9	2 329 828.6	1.149 263
3	5 338 945.9	1.147 370	10	2 027 272.5	1.149 506
4	4 653 211.2	1.147 719	11	1 763 595.0	1.149 725
5	4 054 314.3	1.148 066	12	1 533 931.0	1.149 916
6	3 531 421.8	1.148 399	13	1 333 947.9	1.150 088
7	3 075 084.8	1.148 714			

$\boldsymbol{T}_{\mathrm{iso}} = 302.9126\,\mathrm{K}$

data point	p_r [Pa]	$P_{\mathrm{ratio},r}$	data point	p_r [Pa]	$P_{\mathrm{ratio},r}$
1	7 022 691.2	1.147 293	9	2 324 097.4	1.149 436
2	6 121 103.7	1.147 519	10	2 021 947.8	1.149 649
3	5 334 227.9	1.147 788	11	1 758 756.6	1.149 836
4	4 647 397.1	1.148 085	12	1 529 577.0	1.150 008
5	4 047 958.3	1.148 383	13	1 330 057.8	1.150 156
6	3 524 908.1	1.148 672	14	1 156 416.0	1.150 290
7	3 068 684.1	1.148 949	15	1 005 325.8	1.150 409
8	2 670 867.6	1.149 202			

Table K.1.: Averaged pressures and pressure ratios of the Burnett expansion.

$T_\mathrm{iso} =253.8975\,\mathrm{K}$

data point	f_r	$F_{\mathrm{ratio},r}$	data point	f_r	$F_{\mathrm{ratio},r}$
1	0.014 981 85	1.152 270	9	0.004 826 30	1.151 951
2	0.013 002 04	1.152 217	10	0.004 189 67	1.151 921
3	0.011 284 33	1.152 169	11	0.003 637 12	1.151 914
4	0.009 794 00	1.152 126	12	0.003 157 46	1.151 882
5	0.008 500 82	1.152 071	13	0.002 741 13	1.151 873
6	0.007 378 67	1.152 039	14	0.002 379 72	1.151 862
7	0.006 404 88	1.152 011	15	0.002 065 98	1.151 845
8	0.005 559 76	1.151 970			

$T_\mathrm{iso} =273.1613\,\mathrm{K}$

data point	f_r	$F_{\mathrm{ratio},r}$	data point	f_r	$F_{\mathrm{ratio},r}$
1	0.013 590 14	1.151 889	9	0.004 387 47	1.151 699
2	0.011 798 10	1.151 862	10	0.003 809 56	1.151 678
3	0.010 242 60	1.151 834	11	0.003 307 83	1.151 668
4	0.008 892 45	1.151 804	12	0.002 872 21	1.151 651
5	0.007 720 45	1.151 782	13	0.002 493 99	1.151 645
6	0.006 703 04	1.151 756	14	0.002 165 60	1.151 629
7	0.005 819 84	1.151 736	15	0.001 880 47	1.151 626
8	0.005 053 12	1.151 713			

$T_\mathrm{iso} =296.1256\,\mathrm{K}$

data point	f_r	$F_{\mathrm{ratio},r}$	data point	f_r	$F_{\mathrm{ratio},r}$
1	0.012 286 51	1.151 468	8	0.004 578 78	1.151 397
2	0.010 670 25	1.151 457	9	0.003 976 71	1.151 383
3	0.009 266 84	1.151 444	10	0.003 453 97	1.151 379
4	0.008 047 93	1.151 436	11	0.002 999 80	1.151 376
5	0.006 989 47	1.151 423	12	0.002 605 41	1.151 362
6	0.006 070 27	1.151 413	13	0.002 262 89	1.151 357
7	0.005 272 03	1.151 406			

$T_\mathrm{iso} =302.9126\,\mathrm{K}$

data point	f_r	$F_{\mathrm{ratio},r}$	data point	f_r	$F_{\mathrm{ratio},r}$
1	0.011 954 12	1.151 363	9	0.003 871 65	1.151 315
2	0.010 382 60	1.151 351	10	0.003 362 81	1.151 312
3	0.009 017 79	1.151 349	11	0.002 920 86	1.151 301
4	0.007 832 37	1.151 340	12	0.002 537 01	1.151 291
5	0.006 802 83	1.151 334	13	0.002 203 62	1.151 288
6	0.005 908 63	1.151 325	14	0.001 914 05	1.151 292
7	0.005 132 03	1.151 328	15	0.001 662 52	1.151 269
8	0.004 457 50	1.151 315			

Table K.2.: Averaged Mosotti-terms and corresponding ratios of the dielectric expansion.

Lebenslauf

Name: Christian Heinz Günz

Geburtsdatum: 27.06.1989

Ausbildung

2000 - 2008   Bertolt-Brecht Gymnasium Schwarzenberg

                             Abschluss: Abitur

10/2008 - 10/2011   Bachelorstudium Technische Physik

                             Technische Universität Ilmenau

03/2011 - 09/2011   Praktikum und Anfertigung der Bachelorarbeit am

                             Helomholtz-Zentrum Dresden Rossendorf

                             Abschluss: Bachelor of Science

                             Titel der Arbeit: *Untersuchung seltenerddotierter*

                             SiO_2-Dünnschichten für Downconversion Anwendungen

                             in der Photovoltaik

10/2011 - 06/2014   Masterstudium Technische Physik

                             Technische Universität Ilmenau

                             Schwerpunkte: Ober- und Grenzflächenphysik

                             Halbleiter- / Mikro- und Nanoelektronik

                             Abschluss: Master of Science

                             Titel der Arbeit: *Temperature dependence of Kohn*

                             anomalies on single-crystalline graphite

Berufliche Tätigkeit:

12/2010 - 09/2012   insgesamt 13 Monate wissenschaftliche Hilfskraft im

                             Fachgebiet Experimentalphysik I, TU Ilmenau

11/2012 - 07/2014   insgesamt 15 Monate wissenschaftliche Hilfskraft im

                             Fachgebiet Technische Physik I, TU Ilmenau

seit 12/2014   wissenschaftlicher Mitarbeiter an der

                             Physikalisch-Technischen Bundesanstalt,

                             Arbeitsgruppe 7.43 Kryo- und Primärthermometrie